

British Geological Survey  
Engineering Geology and Geophysics Group

Technical Report WN/95/37

**Methods for the recognition of geological  
weakness zones and other surface  
discontinuities caused by underground  
mining in Carboniferous terrain**

**Final Report. Part 1: Text**

D Beamish, R C Flint, P G Greenwood, P D Jackson  
P I Meldrum, R J Peart, M G Raines and C Williams

The **Final Report** comprises the volumes - **Part 1: Text**  
**Part 2 : Figures**

*Bibliographic Reference :*

Beamish, D, Flint R C, Greenwood, P G, Jackson, P D  
Meldrum, P I, Peart, R J, Raines, M G, Williams, C  
Methods for the recognition of geological weakness  
zones and other surface discontinuities caused by  
underground mining in Carboniferous terrain.  
*British geological Survey,*  
*Technical Report, WN/95/37*

Research funded in part by the  
Commission of the European  
Communities European Coal and  
Steel Community.  
EC Contract No. 7220/AF/136

British Geological Survey, Keyworth, Nottingham, NG12 5GG

©NERC copyright 1996



This report has been generated from a scanned image of the document with any blank pages removed at the scanning stage.

Please be aware that the pagination and scales of diagrams or maps in the resulting report may not appear as in the original

## SUMMARY

Since March 1992 the British Geological Survey (BGS) has collaborated in a CEC part-funded project under the leadership of Dr Clasen of Saarberg, Saarbrueken, Germany. The aim of this project was to determine the most efficient combination of surface geophysical techniques to be used in combination with airborne optical scanning data for the routine detection of shallow faults. Such features, when reactivated following undermining, may become the locii of damaging subsidence, but where they can be traced in advance of mining operations then remedial measures (such as underpinning etc) may be undertaken. This final report outlines the geophysical methods applied and describes our most significant results. Conclusions are drawn concerning the relative efficiencies of each technique and possible complementary applications.

We have applied an extensive range of geophysical techniques ranging from conventional galvanic resistivity through a novel application of natural gamma surface mapping to state-of-the-art Ground Probing Radar (GPR) and RESCAN microprocessor controlled resistivity mapping. A total of 14 Test Sites were investigated using one or more of a total of 14 techniques. The Test Sites are traversed by faults that are either projected from underground mapping or suggested by linears identified in optical scanning data. These sites display a variety of fault styles and throw and variable overburden conditions.

In the present study the faults have been located both directly and indirectly. Direct detection requires that at least one of the physical properties of the rock have been sufficiently altered during and/or after faulting to generate a geophysical response along the fault plane. Indirect fault detection involves the mapping of abrupt lithological displacements and is aided in areas like those studied here where there occur rapid alternations of contrasting lithologies (eg sandstones and shales). Only GPR and, to a much lesser extent, RESCAN and Very Low Frequency electromagnetics (VLF) have been successful in the direct location of faults. With the exception of seismic refraction all of the techniques applied have been successful to varying degree in the indirect detection.

Clearly the "ideal" technique for routine application should be efficient in operation and be capable of both direct and indirect mapping. In the present work only GPR and VLF have satisfied these criteria. In addition these techniques have been shown to be largely complementary, with GPR yielding high detail of shallow (< 6 m) stratigraphy and structure while VLF allows rapid mapping of resistivity variations (reflecting gross structure) down to about 30 m. Magnetometry may also be applicable since some weakly magnetic horizons were identified in the study areas and there is also a suggestion at one site of the deposition within a fault zone of epithermal magnetic material. This technique should be investigated further.





This page is blank

## Contents

Page	Summary
1.	Introduction
2.	The target areas, test sites and their geological setting
3.	Outline of the geophysical techniques applied
3.1	Ground probing radar
3.2	Galvanic resistivity
3.2.1	Vertical electrical sounding
3.2.2	Resistivity mapping
3.2.3	RESCAN
3.3	Spontaneous potential
3.4	Very Low Frequency electromagnetics (VLF)
3.4.1	Background to geological mapping using VLF
3.4.2	VLF in a one-dimensional (1-D) environment
3.4.3	Depth of investigation
3.4.4	Introduction to the Saarbrueken VLF surveys
3.4.5	Two-dimensional (2-D) modelling and inversion of VLF data
3.4.6	Overview of VLF in 2-D and three-dimensional (3-D) environments
3.4.7	3-D VLF modelling
3.4.8	Use of rotational invariants to map structure
3.4.9	Summary of 3-D modelling results
3.4.10	VLF interpretation in areas of complex geology
3.4.11	Karous-Hjelt filtering
3.5	Ground conductivity
3.6	Seismic
3.6.1	Seismic refraction
3.6.2	Azimuthal seismic
3.6.3	Seismic tomography
3.7	Magnetometry
3.8	Natural gamma
3.8.1	Borehole logging
3.8.2	Surface mapping
4.	Discussion of results
4.1	Test site 1.1
4.2	Test site 1.2
4.3	Test site 1.3
4.4	Test site 1.4
4.5	Test site 1.5
4.6	Test site 1.6
4.7	Test site 2.1
4.8	Test site 2.3
4.9	Hahnwald traverse

- 4.10 Test site 2.5
- 4.11 Test site 3.1
- 4.12 Test site 3.2
- 4.13 Test site 3.2 EXT
- 4.14 Magnetic susceptibility testing of typical local rock types

- 5. Conclusions
- 6. Acknowledgements
- 7. References
- 8. Appendix A (Listing of Project Reports and other publications)
- 9. Appendix B (RESCAN focussed surface array)

## List of Figures

Figure 1a.	Location map for Saarland.
Figure 1b.	Location map for Target Areas 1 to 3.
Figure 2.	Location map for Test Sites 1.1 to 1.6.
Figure 3.	Location map for Test Sites 2.1 to 2.5.
Figure 4.	Location map for Test Sites 3.1 to 3.2 and 3.2 (Ext).
Figure 1 <i>res.</i>	Electrode arrays used for the resistivity surveys.
Figure 2 <i>rsc.</i>	The 2D electrode grid used for RESCAN surveys, and the definition of the 'half Schlumberger' mapping technique.
Figure 1 <i>vlf.</i>	Depth of investigation of VLF EM fields.
Figure 2 <i>vlf.</i>	Azimuths of VLF transmitters relative to Test Areas 1, 2, and 3.
Figure 3 <i>vlf.</i>	Synthetic VLF model for non-dipping target.
Figure 4 <i>vlf.</i>	Synthetic VLF model for dipping target.
Figure 5 <i>vlf.</i>	Principal components of the VLF field.
Figure 6 <i>vlf.</i>	VLF modelling. Model 1: apparent resistivity and phase.
Figure 7 <i>vlf.</i>	VLF modelling. Model 1: Z field ratios.
Figure 8 <i>vlf.</i>	VLF modelling. Model 2: apparent resistivity and phase, $E_y$ polarisation.
Figure 9 <i>vlf.</i>	VLF modelling. Model 2: Z field ratios, $E_y$ polarisation.
Figure 10 <i>vlf.</i>	VLF modelling. Model 2: apparent resistivity and phase, $E_x$ polarisation.
Figure 11 <i>vlf.</i>	VLF modelling. Model 3: Z field ratios, $E_x$ polarisation.
Figure 12 <i>vlf.</i>	VLF modelling. Model 3: apparent resistivity and phase, $E_y$ polarisation.
Figure 13 <i>vlf.</i>	VLF modelling. Model 3: Z field ratios, $E_y$ polarisation.
Figure 14 <i>vlf.</i>	VLF modelling. Model 3: apparent resistivity and phase, $E_x$ polarisation.
Figure 15 <i>vlf.</i>	VLF modelling. Model 3: Z field ratios, $E_x$ polarisation.
Figure 16 <i>vlf.</i>	VLF modelling. Model 1: use of rotational invariants.
Figure 17 <i>vlf.</i>	VLF modelling. Model 2: use of rotational invariants.
Figure 18 <i>vlf.</i>	VLF modelling. Model 3: use of rotational invariants.
Figure 6.	Test Site 1.1. Geological section: boreholes BK1.11, BK1.12, and BK1.13.
Figure 1 <i>gpr.</i>	Test Site 1.1. GPR profiles for line 0. 25 MHz antennae.
Figure 2 <i>gpr.</i>	Test Site 1.1. GPR profiles for line 0. 50 MHz antennae.
Figure 5.	Test Site 1.1. Geophysical grid, borehole locations, and interpretation.
Figure 2 <i>res.</i>	Test Site 1.1. Interpretation of VES 1, 2, and 3.
Figure 9 <i>rsc.</i>	Test Site 1.1. Plan (partial) of site showing location of RESCAN survey grid.
Figure 10 <i>rsc.</i>	Test Site 1.1. Apparent resistivity data, showing projected position of the fault.
Figure 19 <i>vlf.</i>	Test Site 1.1. Line 10S. Karous-Hjelt filtering of VLF M-field response over cultural feature.
Figure 3 <i>gpr.</i>	Test Site 1.2. GPR profiles for line 20S. 25 MHz antennae.
Figure 4 <i>gpr.</i>	Test Site 1.2. GPR profiles for line 20S. 50 MHz antennae.
Figure 7.	Test Site 1.2. Geophysical grid, borehole locations, and interpretation.
Figure 8.	Test Site 1.2. Geological section: boreholes BK1.21, BK1.22, BK1.23 and BK1.24.
Figure 5 <i>gpr.</i>	Test Site 1.2. GPR profiles for line 20N. 25 MHz antennae.
Figure 6 <i>gpr.</i>	Test Site 1.2. GPR profiles for line 20N. 50 MHz antennae.
Figure 3 <i>res.</i>	Test Site 1.2. Interpretation of VES 1, 2, and 3.
Figure 29 <i>rsc.</i>	Test Site 1.2. Plan (partial) of site showing location of RESCAN grid.

Figure 7 <i>resc.</i>	Test Site 1.2. RESCAN apparent resistivity map for three overlapping sections.
Figure 27 <i>resc.</i>	Test Site 1.2. Grids a, b, and c. Apparent resistivity traverse
Figure 28 <i>resc.</i>	Test Site 1.2. Grids a, b, and c. Focussing balance factors.
Figure 1 <i>em.</i>	Test Site 1.2. Horizontal and vertical dipole conductivity contours.
Figure 2 <i>em.</i>	Test site 1.2. Composite horizontal and vertical dipole conductivity and GPR section for line 0.
Figure 3 <i>em.</i>	Test Site 1.2. Composite horizontal and vertical dipole conductivity and GPR section for line 20S.
Figure 4 <i>em.</i>	Test Site 1.2. Composite horizontal and vertical dipole conductivity and GPR section for line 60S and possible geological section.
Figure 5 <i>em.</i>	Test Site 1.2. Composite horizontal and vertical dipole conductivity and GPR section for line 20N and proven geology.
Figure 6 <i>em.</i>	Test Site 1.2. Composite of conductivity profiles and Rescan images of part of line 20N.
Figure 1 <i>sei.</i>	Test Sites 1.2 and 1.4. Plots of horizontal velocity versus depth.
Figure 2a,b <i>sei.</i>	Test Site 1.2. Setup BK1.24/1.21. Hydrophone data. (a) Raypath coverage. (b) Straight ray, 10% anistropy correction.
Figure 1 <i>gam.</i>	Test Site 1.2. Natural gamma logs for boreholes BK1.21 to BK1.24.
Figure 4 <i>res.</i>	Test Site 1.3. Interpretation of VES 1, and 2.
Figure 9.	Test Site 1.4. Geophysical grid, borehole locations, and interpretation.
Figure 7 <i>gpr.</i>	Test Site 1.4. GPR profile for line 30S. 50 MHz antennae.
Figure 10.	Test Site 1.4. Geological section: boreholes BK1.43, BK1.44
Figure 30 <i>resc.</i>	Test Site 1.4. Plan (partial) of site showing location of RESCAN grid.
Figure 8 <i>resc.</i>	Test Site 1.4. Resistivity imaging using pole-dipole 'half Schlumberger' measurements made under computer control. Pseudo and 1D corrected XZ sections show different responses over a fault identified by GPR.
Figure 7 <i>em.</i>	Test Site 1.4. Composite horizontal and vertical dipole conductivity and GPR section for line 30S.
Figure 2 <i>gam.</i>	Test Site 1.4. Natural gamma logs for boreholes BK1.43 to BK1.44.
Figure 11.	Test Sites 1.5 and 1.6. Geophysical grid, trench locations, and interpretation.
Figure 8 <i>gpr.</i>	Test Site 1.5. GPR profile for line 10S. 25 MHz antennae.
Figure 9 <i>gpr.</i>	Test Site 1.5. GPR profile for line 10S. 50 MHz antennae.
Figure 12.	Test Site 1.5. Trenches 1, 2, and 3, line 10S.
Figure 10 <i>gpr.</i>	Test Site 1.5. GPR profile for line 10S (eastern end). 50 MHz antennae.
Figure 11 <i>gpr.</i>	Test Site 1.5. GPR profile for line 0. 25 MHz antennae.
Figure 13.	Test Site 1.5. Trench 4, line 0.
Figure 5 <i>res.</i>	Test Site 1.5. Interpretation of VES 1, and 2.
Figure 12 <i>gpr.</i>	Test Site 1.6. GPR profile for line 0. 25 MHz antennae.
Figure 13 <i>gpr.</i>	Test Site 1.6. GPR profile for line 0. 50 MHz antennae.
Figure 14.	Test Site 1.6. Trenches 5 and 6, line 10S.
Figure 14 <i>gpr.</i>	Test Site 1.6. GPR profile for line 20S. 25 MHz antennae.
Figure 15 <i>gpr.</i>	Test Site 1.6. GPR profile for line 40S and line 20N (Test Site 1.5). 25 Mhz antennae.
Figure 16 <i>gpr.</i>	Test Site 1.6. GPR profile for line 40S and line 20N (Test Site 1.5). 50 MHz antennae.

- Figure 15. Test Site 2.1. Geophysical grid, trench and borehole locations, and interpretation. May 1992 survey.
- Figure 16. Test Site 2.1. Geophysical grid, trench and borehole locations, and interpretation. December 1992 survey.
- Figure 17. Test Site 2.1. Exploratory trenches T1, T1a, and T2.
- Figure 17 *gpr*. Test Site 2.1. GPR profile for line 16S. 50 MHz antennae.
- Figure 18 *gpr*. Test Site 2.1. GPR profile for line 0. 50 MHz antennae.
- Figure 19 *gpr*. Test Site 2.1. GPR profile for line 30N. 50 MHz antennae.
- Figure 18. Test Site 2.1. Geological section: boreholes B1, B2, B3.
- Figure 20 *gpr*. Test Site 2.1. GPR profile for line ROAD. 50 MHz antennae.
- Figure 6 *res*. Test Site 2.1. Interpretation of VES 1, 2, and 3.
- Figure 7 *res*. Test Site 2.1. Schlumberger array resistivity contours.
- Figure 8 *res*. Test Site 2.1. Gradient array resistivity contours.
- Figure 9 *res*. Test Site 2.1. Gradient array resistivity profiles (logarithmic scale).
- Figure 10 *res*. Test Site 2.1. Gradient array detail over proven fault trace.
- Figure 31 *rsc*. Test Site 2.1. Plan (partial) of site showing location of RESCAN grid.
- Figure 3 *rsc*. Test Site 2.1. Half Schlumberger apparent resistivity maps for AB=3m.
- Figure 1 *rsc*. Test Site 2.1. Geological sections constrained by boreholes B1 and B2 and Trench T1.
- Figure 4 *rsc*. Test Site 2.1. Variable response from different depths of investigation (proportional to AB).
- Figure 5 *rsc*. Test Site 2.1. Smooth inversion of resistivity data illustrating the 3D nature of the geological structure.
- Figure 20 *rsc*. Apparent resistivity traverses.
- Figure 21 *rsc*. Test Site 2.1. Line 7. Focussed balance factors.
- Figure 22 *rsc*. Test Site 2.1. Line 7. Normalised W-E balance factors.
- Figure 23 *rsc*. Idealised model of a vertical face.
- Figure 24 *rsc*. Vertical interface model results, Focussed balance factors.
- Figure 25 *rsc*. Vertical interface model results, Normalised W-E balance factors.
- Figure 26 *rsc*. Test Site 2.1. Inferred surface location of fault trace.
- Figure 20 *vlf*. Test Site 2.1. VLF R-field (Interuran data) profiles and proved fault trace.
- Figure 8 *em*. Test Site 2.1. Apparent conductivity contours (EM31 horizontal dipole).
- Figure 1 *mag*. Test Site 2.1. Total field magnetic profiles.
- Figure 2 *mag*. Test Site 2.1. Magnetic model line 85W.
- Figure 3 *gam*. Test Site 2.1. Natural gamma surface mapping.
- Figure 21 *gpr*. Test Site 2.3. GPR profile for line 0. Comparison of 25, 50, and 100 MHz antennae frequencies.
- Figure 20. Test Site 2.3. Geological section: boreholes BK2.31 and BK2.32.
- Figure 22 *gpr*. Test Site 2.3. GPR profiles for lines 0, 10S, and 20S. 50 MHz antennae.
- Figure 11 *res*. Test Site 2.3. Interpretation of VES 1, and 2.
- Figure 32 *rsc*. Test Site 2.3. Plan (partial) of site showing location of RESCAN grid.
- Figure 6 *rsc*. Test Site 2.3. Apparent resistivity maps for two depths of investigation.
- Figure 21 *vlf*. Test Site 2.3. Modelled resistivity cross sections for lines 0, 10S, and 20S.
- Figure 22 *vlf*. Test Site 2.3. Occam inversion: levels of fit of models to observed data.
- Figure 19. Test Site 2.3. Geophysical grid, borehole locations, and interpretation.
- Figure 23 *vlf*. Test Site 2.3. Coincident GPR and VLF resistivity cross sections for line 10S.
- Figure 3 *mag*. Test Site 2.3. Total field magnetic profiles.



Figure 4 <i>mag</i> .	Test Site 2.3. Total field magnetic contours.
Figure 23 <i>gpr</i> .	Test Site Hahnwald. GPR profile for line Hahnwald.
Figure 12 <i>res</i> .	Hahnwald track. Interpretation of VES 1, and 2.
Figure 21.	Test Site Hahnwald. Hahnwald traverse and interpretation.
Figure 24 <i>gpr</i> .	Test Site 2.5. GPR profile for line Fence.
Figure 25 <i>gpr</i> .	Test Site 3.1. GPR profile for line 80W. 50 MHz antennae.
Figure 22.	Test Site 3.1. Geophysical grid and interpretation.
Figure 14 <i>res</i> .	Test Site 3.1. Interpretation of VES 1, 2, 3, and 4.
Figure 13 <i>res</i> .	Test Site 3.1. Line 80W. Dipole-dipole resistivity data.
Figure 11 <i>rsc</i> .	Test Site 3.1. Plan (partial) of site showing location of RESCAN survey grid.
Figure 12 <i>rsc</i> .	Test Site 3.1. Apparent resistivity data, showing projected position of the fault.
Figure 24 <i>vlf</i> .	Test Site 3.1. VLF-R and VLF-Z field data for 16 kHz transmitter.
Figure 25 <i>vlf</i> .	Test Site 3.1. VLF-R and VLF-Z field data for 24 kHz transmitter.
Figure 26 <i>vlf</i> .	Test Site 3.1. Invariant mapping: 16 kHz and 24 kHz transmitters.
Figure 27 <i>vlf</i> .	Test Site 3.1. VLF-Z field data using banded contour scale.
Figure 23.	Test Sites 3.2 and 3.2 (Ext). Geophysical grid and interpretation.
Figure 26 <i>gpr</i> .	Test Site 3.2. GPR profile for line 100E. 50 MHz antennae.
Figure 16 <i>res</i> .	Test Site 3.2. Interpretation of VES 1, 2, 3, and 4.
Figure 15 <i>res</i> .	Test Site 3.2. Line 0. Dipole-dipole resistivity data.
Figure 13 <i>rsc</i> .	Test Site 3.2. Plan (partial) of site showing location of RESCAN survey grid.
Figure 14 <i>rsc</i> .	Test Site 3.2. RESCAN apparent resistivity map for three overlapping sections.
Figure 28 <i>vlf</i> .	Test Site 3.2. VLF-R and VLF-Z field data for 16 kHz transmitter.
Figure 29 <i>vlf</i> .	Test Site 3.2. VLF-R and VLF-Z field data for 24 kHz transmitter.
Figure 30 <i>vlf</i> .	Test Site 3.2. VLF-R (phase) for 16 and 24 kHz transmitters and VLF-Z
Figure 27 <i>gpr</i> .	Test Site 3.2 (Ext). GPR profile for line 50EX. 50 MHz antennae. (converted magnitude and phase) for 16 kHz transmitter.
Figure 15 <i>rsc</i> .	Focussed currents over a conductive/resistive boundary (schematic).
Figure 16 <i>rsc</i> .	Electrode configuration (schematic) for a 'double laterolog' focussed array proposed by Jackson (1981).
Figure 17 <i>rsc</i> .	RESCAN electrode grid and focussed array positions.
Figure 18 <i>rsc</i> .	Adjacent grids.
Figure 19 <i>rsc</i> .	Model grid used in simulations of the focussed array.

### List of Tables

Table 1	Summarising the BGS geophysical field activities
Table 2	Electrical properties of some common materials



## 1. INTRODUCTION

This Final Report summarises the geophysical activities and main findings of the British Geological Survey (BGS) in support of a CEC part-funded project under the leadership of Dr Clasen of Saarberg, Germany. The primary aim of the project was to define the most efficient combination of surface geophysical techniques to be used routinely in conjunction with airborne optical scanning to detect near surface fault zones and other lines of tectonic weakness in advance of mining operations. Such features are frequently the locii of damaging subsidence following undermining unless remedial measures such as underpinning etc are taken in advance.

The project has run for 3.5 years, from 1 March 1992 to 31 August 1995. In this period BGS teams comprising between 2 and 5 geophysicists have applied an extensive range of geophysical techniques during 5 visits to field areas in the Saarland. The BGS Project Leader has also attended 2 Project Technical Meetings in Germany and we have hosted one such meeting in the UK. Data processing, interpretation and reporting and the development of advanced 3-D resistivity modelling software has continued throughout the project. In addition to undertaking our own programme of field work we have also advised on the geophysical data acquired by both our collaborators (DSR (Gesellschaft für Dekontaminierung, Sanierung, Rekultivierung mbH) and DFA (Fertigungs und Anlagenbau Gesellschaft mbH)) and by various geophysical contractors employed by Saarberg.

The report starts with brief accounts of the target areas investigated and their geological setting. This is followed by an outline of the physical principles of the geophysical techniques applied in the present study together with a description of the methods of data reduction, modelling, interpretation and presentation.

Emphasis has been placed on the Ground Probing Radar (GPR) and Very Low Frequency (VLF) electromagnetic (EM) techniques. GPR has been shown to be the most efficient means of locating the "weakness zones" at the reconnaissance scale and in addition yields detailed structural/stratigraphic information on these zones. GPR will most likely be of immediate interest for follow up work. VLF is also likely to assume a major role in routine fault detection. As part of the current Project a BGS EM specialist (Dr Beamish) has undertaken a comprehensive numerical modelling study of the detectability of blind conductive features of variable orientation with respect to VLF transmitter locations. He reaches important conclusions concerning the relative effectiveness of the VLF-R (electric field) and VLF-Z (magnetic field) modes and the enhancement of anomaly recognition and definition through the combination of VLF data obtained using two or more different VLF transmitters. An outline of Dr Beamish's work is included with this report since his findings will be of value in guiding future VLF surveys for fault detection.

Then follows a discussion of our most significant results on a site by site and technique by technique basis, including an attempt to integrate the findings of the different techniques where possible. Finally conclusions are drawn as to the relative merits of each of the geophysical techniques and the general findings of the project.

## 2. THE TARGET AREAS, TEST SITES AND THEIR GEOLOGICAL SETTING

BGS field activities have been confined to the three Target Areas shown in Figures 1a and 1b which depicts a zone some 15 km north of Saarbrueken. Target Area 1 is centred on a steep sided valley with up to 4 m thickness of clayey overburden; conversely, Target Areas 2 and 3 occupy upland areas with

generally less than 0.5 m of soil and weathered rock. Within each Target Area geophysical grids were established at up to six Test Sites (see Figures 2 to 4) traversed either by faults projected from underground mapping or by well defined photolinears recognised in the optical scanning data. Table 1 summarises the BGS field activities.

**Table 1 Summarising the BGS geophysical field activities**

SITE	GPR	RCN <sup>1</sup>	EM31	VLFR	VLFM	MAG	RST <sup>2</sup>	VES	SP	NATy	γLOG	ST <sup>3</sup>	SR <sup>4</sup>	AZS <sup>5</sup>
1.1	X	X	X		X	X		X						
1.2	X	X	X		X	X		X			X	X	X	X
1.3	X							X						
1.4	X	X	X					X			X	X		
1.5	X							X					X	
1.6	X												X	X
2.1	X	X	X			X	X	X		X				
2.3	X	X	X	X	X	X	X	X						
2.5	X		X			X	X	X						
HWT <sup>4</sup>	X						X	X						
SWT <sup>5</sup>	X													
3.1	X	X		X	X	X	X	X	X					
3.2	X	X		X	X	X	X	X	X					
3.2 EX	X			X	X	X								

RCN<sup>1</sup> RESCAN

ST<sup>3</sup> SEISMIC TOMOGRAPHY

AZS<sup>5</sup> AZIMUTHAL SEISMIC

SWT<sup>5</sup> STANGEWALD TRAVERSE

RST<sup>2</sup> RESISTIVITY TRAVERSING (ASSORTED ARRAYS)

SR<sup>4</sup> SEISMIC REFRACTION

HWT<sup>4</sup> HAHNWALD TRAVERSE

The local lithologies are molasse deposits of Upper Carboniferous age comprising an alternating sequence of shales and laterally impersistent sandstones with intercalations of conglomerates, tonsteins and coal seams, the latter of which attain thicknesses up to 3.5 m. Structurally these rocks occupy part of the northern limb of a major anticlinal feature within the south-west trending Saar-Nahe Basin. The dip is to the north/north-west at between 10° and 25°. Normal faulting along a series of largely north-west striking planes (and occasional reversed faulting) have resulted in a horst and graben tectonic pattern; important faults

traversing the Target Areas (and their respective throws) are the Vogelsborn (125 m) and Berschweiler (70 m) in Target Area 1, the Hahnwiese (60 m) in Target Area 2 and the 50 m broad west-north-west trending Merchweiler-Gotzenberg shear zone (200 m) in Target Area 3.

Block faulting of shallow dipping layers results in a significant horizontal displacement of their subcrop. For instance, at Test Site 2.1, lithologies on the west (downthrown) side of the Hahnwiese Fault subcrop some 120 m further south than their counterpart horizons on the east side. The geophysical mapping of such displacements is clearly a useful means of locating fault zones indirectly, especially where the fault plane itself is not characterised by a sufficiently contrasting physical property to enable its direct detection.

Geophysical logs from the Wiesbach 1 borehole (immediately north of Target Area 2) indicate that a natural gamma and resistivity contrast approximately in the ratios 3:1 and 1:4 exist between the local shale and sandstone sequences respectively. These are strong contrasts and hence the different units should be clearly defined by at least natural gamma and resistivity/conductivity mapping. In addition to these techniques ground probing radar, magnetometry, spontaneous potential traversing and various seismic methods were also applied on an experimental basis.

### 3. OUTLINE OF THE GEOPHYSICAL TECHNIQUES APPLIED

#### 3.1 Ground Probing Radar

The Ground Probing Radar (GPR) technique is similar in principle to sonar methods. In the present work we used the Pulse Ekko IV GPR equipment manufactured by Sensors and Software INC.; this system employs an impulse technique where short duration pulses of electromagnetic (EM) radiation are generated by a static antenna (transmit) and the reflections of these impulses from buried features are received by a second antenna (receive).

Reflections occur at sub-surface interfaces across which there is a contrast in electrical impedance. At the frequencies normally used for GPR ( $> 25$  MHz) electrical impedance is dominated by changes in the relative permittivity or dielectric constant ( $K$ ) of the ground. Generally speaking the strength of the reflected signals is proportional to the degree of contrast of dielectric properties across the interface, the larger the contrast the stronger the signal reflected back to the ground surface. Table 2, from Davis and Annan (1989), indicates typical values of  $K$  and other important GPR parameters (conductivity ( $\sigma$ ), EM transmission velocity ( $v$ ) and attenuation ( $\alpha$ )) for a range of commonly encountered materials.

Table 2 indicates the likelihood of a clear reflection from the contact between the local sandstones and shales, especially where the sandstone is porous and saturated or very tight. Water has both a high dielectric constant and it also controls the conductivity of most rocks; hence water content is one of the most important factors in determining the GPR properties of geological materials. Discrete reflections - or a characteristic pattern of reflections - may also occur within individual sandstone and shale units due to grain size grading during deposition and post depositional variations in compaction. These processes can result in a variable

moisture content within an apparently uniform lithology and such subtle features have been detected by only the GPR technique during the present work.

**Table 2      Electrical properties of common materials**

Material	K	$\sigma$ (mS/m)	$v$ (m/ns)	$\alpha$ (dB/m)
Air	1	0	0.3	0
Distilled water	80	0.01	0.033	$2 \times 10^{-3}$
Fresh water	80	0.5	0.033	0.1
Sea water	80	$3 \times 10^4$	0.01	$10^3$
Dry sand	3-5	0.01	0.15	0.01
Saturated sand	20-30	0.1-1.0	0.06	0.03-0.3
Limestone	4-8	0.5-2	0.12	0.4-1
Shales	5-15	1-100	0.09	1-100
Silts	5-30	1-100	0.07	1-100
Clays	5-40	2-1000	0.06	1-300
Granite	4-6	0.01-1	0.13	0.01-1
Dry salt	5-6	0.01-1	0.13	0.01-1
Ice	3-4	0.01	0.16	0.01

The thickness of ground that can be examined by GPR is related to attenuation of the EM radiation, the rate of attenuation being largely controlled by the conductivities of the earth materials present and the frequency of the transmitted impulses. A rough guide to penetration depth ( $d$ ) is:

$$d_{\max} < 35 / \sigma$$

where  $\sigma$  is the conductivity in mS/m (milliSiemens per metre).

Increased penetration generally results with the use of lower frequencies, but this in turn will result in some loss of target resolution. In the present work we used centre frequencies of 25 MHz, 50 MHz and 100 MHz which yield resolution limits of about 2 m, 1 m, and 0.5 m respectively. However, objects much smaller than these dimensions may still produce diffraction and interference patterns and hence may be located although they will not be uniquely identifiable.

Penetration depth is also a function of the separation between the transmit and receive antennae: a 3 m separation was used for the 25 MHz transmission, 2 m for the 50 MHz transmission and 1 m for the 100 MHz transmission.

In the present surveys the antennae (at a constant separation) were orientated perpendicular to the traverse direction and moved along the survey line at a station interval of either 0.25 m (for the 50 MHz and 100 MHz frequencies) or 0.5 m (for the 25 MHz frequency). The antennae



were held stationary for a few seconds at each observation point while reflections from successive transmitted pulses were stacked, digitally stored and subsequently displayed on the computer screen as the survey progressed.

Data collected by the Pulse Ekko IV system are recorded raw, i.e. no filtering, gain or processing of any nature is applied before storage on the computer. This simplifies procedures in the field and minimises the risk of irretrievable data distortion through operator error. Following the initial selection of geometrical factors for the chosen antennae array (primarily spacing and station interval) and other appropriate parameters via the control console, the survey can proceed with little further intervention by the operator.

The initial processing step is to dewow each trace, whereby a time domain filter is applied to remove very low frequency components. These are associated with either inductive phenomena or possible dynamic range limitations of the instrumentation. An automatic time zero shift correction has been applied; this correction adjusts the time datum and aligns each trace in the section. Simple horizontal and vertical filtering comprising respectively trace to trace averaging of adjacent traces, and a moving two point down-trace average were applied to minimise random noise and enhance the continuity of individual reflectors. At Test Area 1 where considerable radio frequency (RF) interference was experienced it was necessary to apply additional time domain filtering to minimise the disruptive effect.

Where topography is significant (showing relief of more than about 1 m along a traverse) then a topographic correction has been applied. This "hangs" the time datum of each trace onto the measured topographic profile and hence aligns the observed reflections into their correct spatial position. All the sections were plotted using automatic gain control (AGC). This gain attempts to equalise the amplitude of all signals by applying a gain which is inversely proportional to the received signal strength. Hence all parts of the signal, including noise, are amplified and relative amplitude information is not preserved.

The processed results are plotted in section form as two way travel time (TWT) (ie the time taken for passage of the signal from transmitter to reflecting horizon and back to the receiver) against traverse position. The numerals along the horizontal axis refer to the distance in metres along a particular traverse, the measuring point being taken as mid-way between the two antennae. The left hand vertical axis indicates the TWT in nanoseconds (nS) while the right hand axis shows the corresponding depth in metres. The velocity of 0.07 m/ns used for this conversion was determined experimentally in the field using common mid point stacks (CMP) made at Test Sites 1.1, 1.2, 1.4, and 2.3. The vertical velocity values derived from these stacks is an apparent value ie. it does not reflect the true velocity of electromagnetic energy through any single lithology except where that particular lithology is of uniform composition for the entire depth tested by the experimental array. In practice the velocity obtained by CMP tests is a weighted average value encompassing the velocities of all materials penetrated as the antennae separation is increased. Hence there is no clear distinction of individual velocities for the sandstone and shale units in the current work since in the relatively shallow depths investigated by GPR both these units will exhibit facies changes and intercalation.

The GPR sections are plotted with a vertical exaggeration of approximately 1.5. The two earliest "reflections" seen in all the sections (at a TWT of about 0 nS and a few tens of nS) represent the direct air-wave and ground-wave arrivals respectively, and are not true reflections.

### 3.2 Galvanic resistivity

In the galvanic electrical (or direct current) method, electric current is introduced into the ground through a pair of electrodes and the resulting potential difference established between a neighbouring pair of electrodes is measured. The value of apparent resistivity of the volume of ground influencing the current flow is obtained by a calculation involving the measured current and potential drop and a geometrical factor that varies with the electrode pattern and separations used. In the rare case of homogenous ground this value of apparent resistivity is equal to the actual or specific resistivity of that ground; more often, however, it represents a weighted average value of all the influencing lithologies.

The electrical resistivity of rock is determined principally by its water content; other influencing factors being the quality (or saltiness) of this water, the clay content or state of weathering and, rarely, the presence of metallic lustre minerals. Resistivity surveys were applied in the present study to map both the distribution (in 3-D) of rock types characterised by their resistivities and to define linear low resistivity anomalies that could reflect the enhanced porosity/saturation and clay content of fault zones.

Our resistivity measurements were made using the battery powered ABEM SAS300 Terrameter with auxiliary booster. The transmitted pulse is switched DC at about 0.2 Hz; this waveform facilitates rejection of tellurics, spontaneous potentials and electrode polarization effects (thus metal stakes can be used for both current and potential electrodes). The equipment incorporates a signal averaging system whereby numerous pulses are applied to the ground at each observation and the measured value of resistance is continuously averaged and accepted when it appears stable. Using this system reliable measurements may be obtained with current as low as 0.2 mA, but for most of the present work it was possible to maintain current output in the range 50 to 200 mA.

Resistivity measurements were made in both the sounding and profiling modes. These two different approaches and the wide variety of electrode arrays employed are discussed briefly below.

#### 3.2.1 Vertical Electrical Sounding (VES)

VES are used to map the vertical distribution of resistivities and hence rock types. It is common practice to start any electrical survey in an unknown area with a series of VES to establish the geoelectrical conditions. The sounding data can also be used to determine the optimum electrode separations for use in subsequent profiling or traversing arrays.

Electrical soundings were made using the Schlumberger array (Figure 1 *res*) in which the

current electrodes are expanded in line about a fixed central point and successively deeper sections of the earth are investigated. The inner potential electrodes are moved further apart only when the diminishing potential drop becomes difficult to measure accurately. Electrode separation in the present study was constrained by fences and rugged topography etc and never exceeded 200m; hence the depths investigated by this technique are rarely more than 15 m or so.

The apparent resistivity value, calculated for each current electrode position, is plotted against half the current electrode separation ( $AB/2$ ). The resulting VES graph may be interpreted quantitatively in terms of layer resistivity and thickness, assuming the layers to be both uniform and horizontal. In the absence of control data the interpretation is often best restricted to a qualitative appraisal of variations ( eg the depth and thickness of the most significant lithologies) from one sounding location to the next.

Electrical sounding data has been interpreted using either RESIST87 or an interactive inversion process that matches, to a required tolerance, the observed data with that calculated over a model of "minimum structure" ie a smoothly varying resistivity distribution. RESIST87 includes an inversion process that allows certain layer parameters to be fixed or constrained within limits. This process facilitates the comparison of adjacent soundings but it should be noted that, in the absence of geological control, the interpretations may not be realistic. The "minimum structure" model may be more appropriate in the absence of borehole control for this approach is objective. Where this technique has been used the models satisfying the observed data have been plotted on a diagram common to each Test Site, thereby facilitating direct comparison of possible geo-electrical structures in each area and high-lighting any variations. The depth scale of these models is shown in both logarithmic- (to accommodate the full investigated depth) and linear form (to detail variations in the top 15 m).

### 3.2.2 Resistivity mapping

In contrast to the VES technique, resistivity mapping or profiling is used to locate lateral resistivity variations. In general terms this is achieved by maintaining the current electrode separation at a constant value and moving the entire array, at fixed measuring intervals, across the area of interest. There exist numerous different arrangements of current and potential electrodes and for each is claimed some special advantage in terms of depth of investigation, target resolution and determination of dip, signal to noise ratio, efficiency of operation etc. In the present work we used four different profiling arrays; these are shown diagrammatically in Figure 1 *res* and described briefly with a mention of their advantages below.

*Schlumberger array:* the electrodes are set in-line with the outer current electrodes much further apart than the potential electrodes. The close spacing of these inner electrodes permits the measurement of a more uniform potential field and permits efficient surveying with a three man crew.

*Gradient array:* the current electrodes are set a relatively large distance apart and the potential electrodes are traversed within the central 3/5 of this distance where, in homogenous ground,



the electric field remains uniform. Adjacent lines can also be surveyed so that a rectangular grid of measurements is achieved from one current electrode set-up; this is especially beneficial in areas where high electrode contact resistance is a problem. The current electrode separation is the main controllable parameter governing the depth of investigation; this is chosen so that most current will flow within the depth range of interest (say the top 20 m in the present case); at the same time, it is important logistically that as large an area as possible be covered with each set-up. It is necessary to keep the potential electrode separation as small as possible in order to maximize the resolving power of this array. In the present work a separation of 2 m was found to be adequate while the measuring interval was usually set at the same value. In addition to the logistical advantages of the gradient array outlined above, it is widely recognised as the array best able to indicate the lateral position and dip of a target.

*Dipole - dipole array:* the current and potential electrode spacing is maintained at a distance "a" and measurements are made with potential pairs at successively greater distances (usually integer multiples, "n" of "a") from the current electrodes. The depth of investigation increases with increasing separation of the dipole pairs. The measuring or plotting point is taken to be at the intersection of lines drawn at  $45^\circ$  from the midpoint of the electrode pairs involved. In this manner the results, usually contoured, are presented as a pseudo-section which, in a very generalised way, does indicate resistivity variations with depth. In the present work "a" was set at 2 m and "n" values of 1 to 6 were used, with a station interval of 2 m. The dipole-dipole array has been shown to respond relatively well to narrow, steeply dipping conductors while it also yields some indication of depth and depth extent.

The dipole-dipole data have been inverted automatically using RES2DECO to produce a smooth (minimum structure) resistivity distribution (the model), the calculated values for which match those observed within user determined limits. The software uses a finite difference forward modelling subroutine to calculate the apparent resistivity values and a non linear least squares optimisation technique for the inversion routine. The results of the dipole-dipole traverses are presented as observed data (top), followed by the calculated values (next) for the model shown (third). The lower section shows the model resistivity distribution at natural scale.

*Pole-pole array:* with this array only one potential and one current electrode at a constant separation are moved along the traverse at regular intervals, the remote or "infinite" current and potential electrodes being fixed some 300 m normal to the traverse and on opposite sides of this. We used a pole-pole separation of 2 m and a station interval of 2 m. Maximum depth penetration and anomaly symmetry is claimed for this array.

### 3.2.3 RESCAN

#### *Introduction*

The BGS RESCAN computer controlled resistivity system was used to map with high resolution the shallow 3-D resistivity structure of faults proved earlier with complementary geophysical techniques (principally GPR). The objectives of these RESCAN surveys were twofold: to elucidate the geological nature of the faults and to facilitate the design (in terms of



array type and dimensions) of the optimum surface resistivity technique for the routine delineation of shallow faults in the environments encountered here.

At each survey site stainless steel electrodes were set at 1m interval over a 2-D array of dimensions 19m by 10m (thereby employing a total of 220 electrodes), straddling the proved fault trace. These electrodes were addressed sequentially, as directed by the computer software, and were in turn either current senders, potential measurers or passive. The 3-D data sets for a variety of different arrays were acquired by progressively increasing the depth of investigation within the 2-D array (by increasing either the separation of the current dipole or  $AB/2$ , the distance between the mobile current electrode and the centre of the potential dipole) thus gradually investigating the 3-D volume. Our present investigations were confined to the upper 10m or so with a lateral resolution of about 1m.

#### *Choice of electrode arrays*

We have found in earlier work that the selection of the electrode array is crucial if a realistic estimate of the true earth resistivity distribution is to be obtained from the surface measurements of apparent-resistivity. In some cases we have found that there is little need for further interpretation, since the observed resistivity distribution can match quite closely the lithological distribution.

Previous investigations of faulted mudrock (Jackson et al., 1991) highlighted some advantages of using two adaptations of the Schlumberger electrode array, namely the gradient array and the half Schlumberger array (see Figures 1 *res* and 2 *rsc*). In comparison with other commonly used arrays these two electrode configurations yield a relatively simple fault response. For instance, the Wenner array exhibits a response as each of the four electrodes pass over a faulted contact, the full Schlumberger array exhibits three responses while the half Schlumberger array and the gradient array exhibit respectively only two- and one such response. Thus the half Schlumberger and gradient arrays are most suited to mapping the resistivity distribution of 3-D geological structures since, by minimising the complexity of the electrode response, both these arrays facilitate the direct comparison of measured apparent resistivity with the geology.

A well known problem in apparent resistivity mapping is the phenomenon of current gathering or dispersion due to respectively conductive or resistive 3-D structures; these effects result in mapped apparent resistivities that do not faithfully reflect the true resistivity distribution. Focussed resistivity methods have been developed by the oil industry for use in borehole logging where it is required to penetrate that portion of the borehole wall invaded by highly conductive drilling muds. The technique utilises additional current sources to counteract the tendency of the measuring current to be distorted by the presence of conductive (or resistive) heterogeneities. Thus focussing offers the possibility of counteracting the current gathering effects outlined above.

The 'Microlaterolog' developed by Doll (1952) is a focussing device that has been used successfully for resistivity mapping on the earth's surface. Jackson (1981) showed that a derivative of this tool (employing discrete electrodes) functioned almost as well as the original borehole device (with its continuous ring electrodes) and hence made a nearly ideal surface

mapping device. With the advent of computer controlled resistivity surveying this modified focussing approach is made practicable and it was tested at several of the present sites. The resulting data will be used to aid the interpretation of the complementary 3-D surveys. Examples of focussed data (and its interpretation) from Test Sites 1.2 and 2.1 are presented in the main body of this report while further details of the technique are described in Appendix B.

As noted above, the half Schlumberger array is particularly suitable for investigating sub-vertical faults under a thin cover of drift. The three mobile electrodes of the half Schlumberger array can have four orientations within the rectangular grid, as shown in Figure 2rsc. The use of these four array styles allows coverage of the whole grid without loss at the edges. In addition, where overlapping coverage is provided by different styles, particularly at small AB spacings, the two halves of the Schlumberger array data can be compared. We believe that significant differences between these two halves indicate a 'current gathering' response to the 3-D geology which changes as the current electrode is moved.

#### *Interpretation and inversion of 3-D resistivity data*

Proprietary numerical techniques have been modified and used to create XZ cross-sections of apparent resistivity and corrected resistivity from the field survey data. Modelling facilities have also been tailored to accommodate complex geological models and to enable complete surveys to be simulated. The modelling output is in an identical format to the field data (XZ sections) and hence ready comparisons may be made.

A 1-D correction has been applied (Jackson et al., 1994), this procedure was first used before the advent of personal computers. Although this technique is now rarely used it is ideal for data processing prior to numerical modelling and inversion. It converts the apparent resistivities to conductances. Starting at the shallowest depth of investigation, it corrects the next deeper conductance using the one above, then moves down one level and repeats the process, finally converting the corrected conductances back to corrected resistivities.

Present research utilising forward modelling schemes within iterative inversion processes appear to be showing success in tomographic processing of resistivity surveys (Ramirez et al., 1991; Sasaki, 1992). This approach has now largely superseded back-projection techniques, particularly for the 2-D case. We are developing tomographic inversion schemes based on the use of smoothness constrained inversion (Sasaki, 1992) as a means of improving the stability of the solution, rather than damping it as in the Marquart-Levenberg formulation (eg. Ramirez et al., 1991), the popular choice until recently.

The RESCAN system provides substantial over-sampling which is of benefit to the inversion process which seeks to strike a balance between the 'smoothness' of the resistivity model and the 'goodness of fit' between the measured- and simulated field data. The 'smoothness' of the model is a mathematical constraint rather than a geological one, as it seeks to limit wild swings between adjacent model parameters. For example, two adjacent cells having resistivity values of  $1\text{E}+10\text{ohm-m}$  and  $1\text{E}-10\text{ohm-m}$  could provide a slightly better fit than if both cells had resistivities of approximately  $1\text{ohm-m}$ , which could be 'correct'.

The inversion scheme, as outlined above, is rapidly becoming the method of choice for resistivity inversion applied to sub-surface imaging (eg Sasaki, 1992; 1994). We have implemented a scheme which uses a 3-D finite difference method for the forward model (Jackson et al., 1992), along the following lines (Jackson et al., 1995):

The inversion concerns a data set of  $N$  measurements  $\mathbf{Res}(N)$  and a corresponding set of simulated values  $\mathbf{Mes}(N)$  which have been calculated for a given resistivity model  $\mathbf{x}(M)$  having  $M$  independent parameters. The objective of the inversion is to minimise the misfit between the data ( $\mathbf{Res}(N)$ ) and the values ( $\mathbf{Mes}(N)$ ) derived from the model ( $\mathbf{x}$ ) in a least squares sense and to minimise the roughness of the model ( $\mathbf{x}(M)$ ).

This scheme reduces to the well known equation:

$$[\mathbf{A}^T \mathbf{A} + \lambda (\mathbf{R}^T \mathbf{R})] \mathbf{x} = \mathbf{A}^T \mathbf{b}$$

where:

$\mathbf{R}$  is a matrix which defines the 'roughness' of the model  $\mathbf{x}$

$\mathbf{x}$  is the unknown resistivity vector

$\mathbf{b}$  (a vector) is a weighted function of the data mismatch eg  $(\mathbf{Res}(i) - \mathbf{Mes}(i))^2 / \sigma^2(i)$

$\mathbf{A}_{ij} = \mathbf{J}_{ij} / \sigma(i)$  where  $\sigma(i)$  is the standard deviation of the  $i$ th measured resistance datum and  $\mathbf{J}_{ij}$  is the Jacobian partial derivative of the  $i$ th measurement  $\mathbf{Mes}(i)$  w.r.t. the  $j^{\text{th}}$  resistivity parameter  $\mathbf{x}(j)$ .

This is a non-linear problem and the solution requires an iterative process, plus a means of defining  $\lambda$ . The standard deviation of the errors can be seen to be prominent being incorporated into both matrix  $\mathbf{A}$  and vector  $\mathbf{b}$ .

### 3.3 Spontaneous potential

Numerous natural electrical potentials exist in the ground. At least two of these (the streaming potential of fluids moving through narrow pores and the potential established by virtue of the variation of electrolytic concentration in contrasting lithologies) are associated with faulting. The natural potentials over a grid are measured with reference to a fixed point. A non-polarising electrode (a porous pot containing saturated copper sulphate solution) is fixed at this reference point and the potential between this and a mobile non-polarising electrode is read from a high impedance voltmeter connected between the two electrodes. Measurements were made every 5 m.

### 3.4 Very Low Frequency electromagnetics (VLF)

#### 3.4.1 Background to geological mapping using VLF

The use of VLF radio fields in the general context of geological mapping has been recently and extensively reviewed by McNeill and Labson (1991). In the summary of their review, the authors note that (despite disadvantages) the advantages inherent to the method have made the VLF technique by far the most popular electromagnetic (EM) technique in current use.

The VLF technique makes use of one or more distant radio transmitters operating between 15 kHz and 30 kHz. The limited bandwidth means that, although several transmitters may be used at different frequencies, a main attribute of the method is that of a single frequency EM sounding. The lack of bandwidth is compensated for by the fact that the instrumentation is very portable and cost-effective. An extensive surveying capability is provided by a single, roving operator.

The VLF method was developed as an inductive sounding technique measuring the amplitude (and subsequently phase) relationship between the vertical (secondary) magnetic field  $Z$  relative to the horizontal primary field  $H$ . This method, referred to here as VLF-Z, relies on wavefield interaction with two-dimensional (2D) and three-dimensional (3D) resistivity structure. The technique has since been extended to include a measure of the induced horizontal electric field component  $E$ . This VLF-R measurement provides a surface impedance value (e.g.  $E/H$ ), usually expressed as apparent resistivity and phase, using short (e.g. 5 m to 10 m) electric dipoles.

The VLF-R measurement, although appropriate for 1-D application, contains only marginal information on the vertical resistivity structure (Fischer et al. 1983) because, in effect, only a single frequency is available. These factors suggest that the strength of the VLF method lies predominantly in the definition of lateral gradients in the subsurface e.g. fault-mapping.

Both VLF-Z and VLF-R measurements were undertaken during the current Project, and significant advances have been made in applying the VLF technique to fault-mapping. These advances are largely in the field of 2D inversion and 3D forward modelling as described below.

### **3.4.2 VLF in a one-dimensional (1-D) environment**

In a 1-D resistivity environment (no lateral resistivity gradients) the VLF-Z measurement returns a zero value for both components (in-phase and in-quadrature) of the  $Z/H$  ratio since no secondary currents (along lateral boundaries) are induced. The VLF-R measurement always provides apparent resistivity and phase values that are the same for all transmitter frequencies i.e. over all directions of the inducing field.

If the subsurface is also vertically uniform over the depth scale corresponding to the depth of investigation (see below), the apparent resistivity will be equal to the true (uniform) resistivity of the material and the phase value will be  $45^\circ$ . All transmitters used will provide essentially the same values.

If the subsurface can be approximated by two layers (within the depth of investigation) then it is generally assumed that a conductor above an insulator provides phase angles of  $< 45^\circ$  while an insulator above a conductor provides phase angles of  $> 45^\circ$  (Arcone 1979).

### **3.4.3 Depth of investigation**

The depth of investigation is an important parameter for all electrical and electromagnetic



methods. The incident plane-wave VLF field decays with depth exponentially depending on the frequency and the subsurface resistivity. For the uniform subsurface case, the decay scale lengths are shown in Figure 1 *vlf* for six environments ranging from the resistive (500 ohm.m) to the conductive (10 ohm.m). A frequency of 20 kHz was used. As can be seen in Figure 1 *vlf*, attenuation increases with decreasing resistivity. A convenient method for expressing attenuation in EM methods is the skin-depth which is defined as the depth at which the field has attenuated to 1/e (approximately 37%) of its surface value. In practical units, the skin-depth ( $\delta$ ) is defined as:

$$\delta = 500(\rho/f)^{1/2}$$

where:  $\delta$  is in m,  $\rho$  is resistivity in ohm.m and  $f$  is frequency in hertz. Substituting a typical VLF frequency of 20 kHz provides a VLF "rule-of-thumb" of  $\delta = 3.6(\rho)^{1/2}$  in metres.

An effective penetration depth is a depth below which resistivity changes have little influence on the response measured at the surface. According to Spies (1989) a reasonable estimate for the depth of investigation of plane-wave methods is about 1.5 skin-depths. Using our VLF rule-of-thumb, VLF depths of investigation range from 17 m in a conductive (10 ohm.m) environment, through to 54 m in a "typical" 100 ohm.m environment, and down to 121 m in a resistive (500 ohm.m) environment.

The best way to "view" the above analysis is to consider that the VLF, single-frequency sounding, provides information on a scale-length-from the surface-(maximum contribution to the response) and over a hemisphere (centred on the sounding location) with a radius equal to the depth of investigation. The contribution to the surface response decreases exponentially with distance from the sounding location.

#### 3.4.4 Introduction to the Saarbrücken VLF surveys

The present VLF surveys were conducted as both profile and grid measurements. A summary of the VLF transmitter (Tx) directions and Tx output powers that could be received in the vicinity of Saarbrücken is shown in Figure 2 *vlf*. Commercially-available VLF survey equipment was used. DFA surveys employed the Geonics 16R and BGS surveys used the Scintrex IGS-2. To obtain good signal/noise the two primary transmitters used in the surveys were Rugby (303°) operating at 16 kHz and Carlisle (320°) operating at 19 kHz. Clearly the small azimuthal separation of 17° between these two transmitters does not allow full "orthogonal" investigation of response characteristics of fault trends.

If an "average" Tx direction of 311° is assumed then faults of this same azimuth (131° or 311°) will respond in a TE mode sense i.e. induced current flow parallel to strike. Structures with an orthogonal strike of 41° or 221° will respond in a TM mode sense i.e. induced current flow perpendicular to strike.

A few VLF surveys were also undertaken using both Rugby, UK (303°, 16 kHz) and Cutler, USA (265°, 24 kHz). The azimuthal difference of only 38° again precludes a full "orthogonal"

investigation of fault trends.

Prior to geological interpretation it is important that plotted profiles of VLF data be examined for the possible influences of cultural features (distortion). All man-made metallic features such as fences and pipelines are immersed in the same VLF wave-field as the subsurface. Where such cultural features are long and continuous, they have the capability of re-radiating the VLF field and acting as "line-source" anomalies. Such shallow and at-surface features can provide far larger VLF field perturbations than geological resistivity gradients. They are usually identified as being highly linear (spatially) and with a constant amplitude/phase characteristic. They are also generally associated with field-boundaries and tracks.

### 3.4.5 Two-dimensional (2-D) modelling and inversion of VLF data

Although extensive VLF data sets have been successfully used for *mapping* purposes, modelling and interpretation techniques which assess the third (i.e. depth) dimension appear limited. Using data from the present study, Beamish (1994) investigated the use of a new generation of regularised two dimensional inversion methods to VLF data. Given a suitable profile of VLF-R measurements, the work demonstrates an automatic method for the construction of a resistivity cross-section. The technique called Occam inversion (Constable et al., 1987) attempts to overcome the limited vertical resolution of VLF data by finding a resistivity distribution with the minimum amount of structure that fits the observations.

In order to carry out successful 2-D modelling and inversion, it is necessary that the data conform to one (or both) of the two principal modes. Basically the azimuths of VLF transmitter direction and geological strike must be either parallel (TE mode) or perpendicular (TM mode).

The methodology of 2-D inversion applied to VLF data is described by Beamish (1994). Tests were carried out using synthetic data. The procedure used was to define a simple, concealed resistivity anomaly and calculate the surface VLF response. These data were then inverted (starting from a uniform distribution) to allow an assessment of the structural resolution that might be achieved by automatic inversion.

Figure 3 *vlf* shows an example of the synthetic VLF modelling and inversion carried out. The target is a concealed conductive (5 ohm.m) slab (dash lines) immersed in a uniform region of 100 ohm.m. Using only 11 observations at 5 m separation across the 50 m traverse, the Occam inversions returned the contoured resistivity distributions shown. The upper diagram is the result of inverting single frequency (16 kHz) TE mode data. The lower diagram is the result of inverting TE mode data for two VLF frequencies (16 kHz and 24 kHz) jointly. The resolution obtained can be summarised as follows. The first reflecting horizon (the upper surface of the conductive zone) is the best resolved feature. Subsequent deeper resolution is more limited. The most conductive feature of the model may be displaced downwards from the "true" centre and inwards from the "true" edge. The resolution through the lower part of the model section is very limited.

Figure 4 *vlf* shows a second similar example in which the target is a concealed and dipping

conductive zone. The resistivity distributions obtained by inversion of single and two frequency VLF-R data sets are shown contoured. The upper diagram is the result of inverting single frequency (16 kHz) TM mode data. The lower diagram is the result of inverting TM mode data for two VLF frequencies (16 kHz and 24 kHz) jointly.

As indicated in Figures 3 *vlf* and 4 *vlf*, complete resolution of "true" structure cannot be achieved by single-frequency VLF profiling. The data has weak vertical resolution (below first wavefield contact) and strong lateral resolution. The results obtained by simulation modelling and inversion are a reflection of these two attributes combined. The synthetic modelling studies revealed that the region of "first wavefield contact" with an anomalous region produces the greatest resolution. Thereafter, with increasing depth, resolution decreases and the "base" of a structure is imaged, by the Occam inversion, as a smooth, long-wavelength gradient.

### 3.4.6 Overview of VLF in 2-D and three-dimensional (3-D) environments

The main interpretational difficulty with the VLF method stems from the directional polarisation of the incident field. The principal components of the primary VLF field are illustrated in Figure 5 *vlf*. In VLF sounding, electric and magnetic fields are always measured at right angles ( $E_x$  and  $H_y$  in Figure 5 *vlf*). The VLF magnetic receiver coil is first rotated about a vertical axis until maximum  $H$  signal is obtained. Two electrodes are then positioned perpendicular to the direction of  $H_{max}$  and are used to record  $E_x$ . As noted by Fischer et al. (1983), the electric field is simply measured at a right angle to the  $H_{max}$  direction and no effort is made to find the direction for which this field would reach a maximum amplitude.

The directional nature of the VLF measurement has profound implications for the manner in which the primary field couples with general 2-D and 3-D structures and the method of interpretation. The way VLF interacts with 2-D structure is discussed by Fischer et al. (1983) and by McNeill and Labson (1991). The assumption of infinite strike (which defines the 2-D case) provides two decoupled modes involving separate combinations of the field components. The TE-mode (or E-polarisation, electric field parallel to strike) involves surface fields  $E_x$ ,  $H_y$  and  $H_z$ . The TM-mode (or H-polarisation, magnetic field parallel to strike) involves the surface fields  $H_x$ ,  $E_y$  and  $E_z$ .

The two principal modes of induction when the VLF transmitter direction is either parallel to the geological strike (TE mode) or perpendicular to geological strike (TM mode) are illustrated in Figure 5 *vlf*. When VLF measurements can be obtained in one, or both, of these modes, interpretation can proceed in a straightforward manner, and 2-D forward modelling and inversion become possible (Beamish, 1994). An important consideration in a 2-D context is the joint information provided by VLF-R and VLF-Z measurements. As discussed above, an  $H_z$  field is absent from the TM mode response and can therefore be used as a means of "mode-identification".

Interpretational difficulties are experienced when field data are collected at azimuths which do not provide either of the two principal modes and/or the subsurface structures are complex and three dimensional. The literature provides very little information on the practical aspects of



geological interpretation when the "common" case of non-principal mode(s) are measured. In large part this stems from the fact that such information can only be obtained through three dimensional EM modelling. To clarify the interpretation of "difficult" VLF data sets a 3-D modelling study at VLF frequencies was undertaken. Although 3-D subsurface bodies are used, "elongate" bodies also allow approximate 2-D behaviour to be observed towards the centre of the body where "edge-effects" are minimal.

### 3.4.7 3-D VLF modelling

Recent advances in 3-D plane-wave modelling using difference equations are described by Mackie et al. (1993). Their algorithm is described as a robust and efficient finite difference scheme that computes the surface fields of general 3-D models using the minimum residual relaxation method. 3-D model construction is via a 3-D "core" (in x, y and z) with 2-D extensions (e.g. in x,z and y,z) at the edges of the core with both 3-D core and 2-D extensions underlain by a 1-D "base". All three model elements are constructed using a staggered grid that conforms with skin-depth requirements.

For the VLF modelling carried out here a frequency of 16 kHz was used throughout. The background material (in which the anomalous bodies are embedded) has a resistivity of 100 ohm.m. This provides a background skin-depth of 40 m. Only conductive (10 ohm.m) anomalies are considered here. The skin-depth within the anomalous conductive region is 12.5 m. The central core comprised 32 x 32 x 15 blocks with the central 100 m x 100 m of the core (in x,y) made up of blocks with lateral dimensions of 5 m. The 15 blocks making up the vertical distribution were assigned initial (0 m -10 m) block thicknesses of 2.5 m, thereafter increasing in thickness with depth. Complex surface field values were converted to apparent resistivity and phase for display.

In the following study all the bodies are electrically-thin (in either thickness or width) at VLF frequencies. Such near-surface bodies respond galvanically rather than inductively. The principal EM response perturbation in such cases occurs in amplitude (apparent resistivity) with only minor perturbations in the VLF-R phase and in the VLF-Z field. Although such field variations are too small to be readily detected by field surveys, the modelling procedure is highly accurate (1 %). The modelled EM field perturbations, although small, can be contoured to provide an accurate mapping of the response. The small perturbations are presented here as a guide to the response patterns that would be anticipated from larger scale bodies with a larger inductive response. Banded contours, which emphasise the changes in spatial gradient, are used to display the field parameters obtained.

#### *Model 1 (3dv2)*

This model was designed to illustrate the field behaviour of elongate anomalies with strike directions in the same (principal) directions of VLF transmitters. The environment corresponds to the 2D case, providing "ideal" TE- and TM-mode behaviour with end-effects added due to the finite strike length of the bodies.

The two bodies are directed E-W and N-S and are identical apart from orientation. Each has a



length of 40 m, a width of 5 m and a thickness of only 5 m. The bodies are "concealed" and extend from 2.5 to 7.5 m in depth. Since the bodies are "electrically thin" and shallow the secondary fields generated will be largely galvanic i.e. the main anomaly will be generated in amplitude (apparent resistivity).

The centre line of Body 1 (E-W) extends from (-40, 22.5 m) to (0, 22.5 m) and Body 2 (N-S) extends from (25.25, 0 m) to (25.25, -40 m). Apparent resistivity and phase behaviour is shown for Ex-polarisation (E-field polarised E-W) in Figure 6 *vlf*. In this polarisation Body 1 (E-W) responds in a TE mode and Body 2 (N-S) in a TM-mode. A N-S profile across the centre of Body 1 reveals 2D type behaviour with a central *minimum* of 70 ohm.m "outlining" the anomaly. Through the central modelled region, the apparent resistivity returns slowly to its background value (100 ohm.m). The finite length of the body is revealed by a concentric *increase* in apparent resistivity at the body ends.

Body 2 is responding largely in the TM mode (Ex current flow is perpendicular to the N-S axis of the body). A smaller amplitude anomaly with a much decreased "half-width" is observed.

The associated phase variations also shown in Figure 6 *vlf*, comprise a range of only  $4^\circ$  since the bodies are responding galvanically. It is arguable whether such variations could be detected in a field survey using an instrument with a phase resolution of the order of  $1^\circ$ . Despite the small level of the anomaly, the general pattern of phase behaviour is similar to that of the amplitude variations.

Again since the response is largely galvanic, the VLF-Z field ratios shown in Figure 7 *vlf* are extremely small ( $<0.5\%$ ) and could not be detected by a field survey. Despite their small magnitude, the results demonstrate the existence of an Hz field for Body 1 responding in a TE-mode (Ex current flow parallel to strike) and the lack of an Hz field from Body 2 responding in the TM mode (Ex current flow perpendicular to strike). Small amplitude 3D edge-effects from Body 2 are also apparent.

The modelling results obtained using the orthogonal polarisation (Ey-polarisation) are a simple transposition of those shown with Body 1 (E-W) responding in a TM mode and Body 2 (N-S) responding in a TE mode sense.

#### *Model 2 (3dv17)*

This model is designed to illustrate the field behaviour of a single elongate anomaly whose strike axis is rotated by  $17^\circ$  and  $73^\circ$  from the principal directions. The conductive body has a strike length of 62 m (-30 m to +30 m, along the y-axis), a width between 5 m and 10 m and is concealed. The body extends from 2.5 m to 20 m in depth. The (x,y) coordinates of the centre body end points are (-7.25, 30 m) and (7.25, -30 m).

#### *17 degree rotation from a TE mode response*

The VLF-R results shown in the Ey-polarisation of Figure 8 *vlf* represent a  $17^\circ$  rotation of strike from the direction of induction (transmitter due north/south). The anomaly pattern is similar to that observed for the Te mode response of Body 1 in the previous example (Figure 6

vlf). In Model 2 the central minimum contour of 60 ohm.m provides an outline of the concealed anomaly with the correct strike. End effects provide a localised increase in apparent resistivity to 120 ohm.m.

Phase angles for Ey-polarisation are defined in the second phase quadrant ( $90^{\circ}$  to  $180^{\circ}$ ). The phase response is again small due to the electrically-thin nature of the body which results in a largely galvanic response. The gradient anomaly pattern does however indicate that the true strike of the body is less well-identified in the VLF-R phase response.

Again since the response is largely galvanic, the VLF-Z field ratios, shown in Figure 9 vlf are small. The gradients generated however do indicate the correct strike orientation of the conductor.

#### *17 degree rotation from a TM-mode response*

The Ex-polarisation results for Model 2 define an anomaly strike direction that is  $17^{\circ}$  from the TM -mode. The VLF-R results are shown in Figure 10 vlf. The anomaly pattern is similar to that observed for the TM -mode response of Body 2 in the previous example (Figure 6 vlf). In the present case, the central minimum contour of 50 ohm.m outlines the concealed body. The gradient anomaly pattern in phase provides a central "low" that is closely associated with the strike of the body.

The anomaly rotation away from a true TM -mode provides a VLF-Z response as shown in Figure 11 vlf. The Z/H amplitudes are reduced by a factor of 2 from the previous case (Figure 9 vlf). The strike of the anomaly is not well-defined.

#### *Model 3 (3dv34)*

This model is designed to illustrate the field behaviour of a single elongate anomaly whose strike axis is rotated by  $34^{\circ}$  and  $56^{\circ}$  from the principal VLF directions. The conductive body has a central strike length of 67 m (-30 m to 30 m, along the y-axis) and a width of between 5 m and 10 m. The body is again concealed and extends from 2.5 m to 20 m in depth. The (x,y) coordinates of the centre body end points are (-15 m, 30 m) and (15 m, -30 m).

#### *34 degree rotation from a TE mode response*

The VLF-R results shown in the Ey-polarisation of Figure 12 vlf represent a  $34^{\circ}$  rotation of strike from a VLF transmitter due north/south. The results shown indicate that the 3-D response attributes, in both amplitude and phase, map the body ends very well. In the absence of such terminations (e.g. a 2-D case) the results indicate that the strike would be overestimated by the central resistivity low and would be poorly defined in the phase response.

The corresponding VLF-Z results shown in Figure 13 vlf are surprising. The anomaly pattern generated by a  $34^{\circ}$  rotation from the principal TE mode direction appears to map the strike direction adequately. The VLF-Z anomaly is generated by excess currents induced along the resistivity gradients provided by the body. It appears that even with a strike deviation of  $34^{\circ}$  from the principal TE mode, sufficient TE mode behaviour is generated to map the anomalous structure.

### 34 degree rotation from a TM mode response

The Ex-polarisation results for Model 3 define an anomaly strike direction that is  $34^\circ$  from the principal TM mode. The VLF-R results are shown in Figure 14 vlf. In this case the central minimum contour of 40 ohm.m outlines the concealed body while the associated phase low of  $43^\circ$  appears to underestimate the strike direction. Complex patterns of high values (both amplitude and phase) are generated by the ends of the 3-D body.

The response being considered can also be understood as a  $56^\circ$  rotation from the TE mode direction which generates the VLF-Z field. The VLF-Z response is shown in Figure 15 vlf. As with the corresponding case of Model 2 (Figure 11 vlf), the strike of the anomaly is poorly defined.

### 3.4.8 Use of rotational invariants to map structure

In a recent paper (Guerin et al., 1994) the use of invariants for correcting VLF field polarisation effects is discussed. The use of invariants follows from the standard procedures of tensor magnetotellurics (MT) in which 4 components (Ex, Ey, Hx and Hy) of the horizontal fields are measured and a tensor impedance (Z) relationship of the form :

$$\begin{pmatrix} E_x \\ \\ E_y \end{pmatrix} = \begin{pmatrix} Z_{xx} + Z_{xy} & \\ & \\ Z_{yx} + Z_{yy} & \end{pmatrix} \begin{pmatrix} H_x \\ \\ H_y \end{pmatrix}$$

is used. In the VLF method, Ex and Ey are provided by two different transmitters, and the two measurements can only provide the off-diagonal components Zxy and Zyx.

In MT the use of rotationally invariant parameters of the impedance tensor has been suggested in an attempt to minimise multidimensional effects. Berdichevsky and Dmitriev (1976) proposed two different rotationally-invariant averages of the tensor as  $Z_{av} = (Z_{xy} - Z_{yx}) / 2$  where "av" denotes an average, and a determinant average :  $Z_{det} = (Z_{xx}Z_{yy} - Z_{xy}Z_{yx})^{1/2}$ . A third invariant, the geometric mean  $Z_{gm} = (-Z_{xy}Z_{yx})^{1/2}$  is more suitable for VLF applications.

All three invariants are independent of the measurement directions. In our model studies all three invariants have been found to give very similar results and we here concentrate on the use of the geometric mean (Zgm). In terms of the measured VLF quantities of apparent resistivity ( $\rho$ ) and phase ( $\Phi$ ) we have  $\rho_{gm} = (\rho_{xy} \cdot \rho_{yx})^{1/2}$  and  $\Phi_{gm} = (\Phi_{xy} + \Phi_{yx})$ . If both  $\Phi_{xy}$  and  $\Phi_{yx}$  are defined in the first quadrant ( $0^\circ$  to  $90^\circ$ ) then  $\Phi_{gm}$  is defined in the range  $0^\circ$  to  $180^\circ$  with a value of  $90^\circ$  representing a uniform half-space response.

The ability of  $\rho_{gm}$ ,  $\Phi_{gm}$  to map structure provided by the three test models is now considered. The two polarisations (Ex and Ey) used to obtain the invariant represent stimulation of the models by two orthogonal VLF transmitters.

#### Model 1 (3dv2)

This model is characterised by two elongate anomalies with strike directions in the same

(principal) directions as the two VLF transmitters. In this "simple" situation, the invariant response, as shown in Figure 16 *vlf*, provides an "ideal" mapping of the anomalies associated with *both* conductive bodies. Both anomalies have the same half-width in amplitude and the four ends (of the two bodies) are identified by a similar increase in phase (above  $90^\circ$ ) and an associated low outlining each body.

#### *Model 2 (3dv17)*

This model is characterised by a single body with a strike rotated by  $17^\circ$  and  $73^\circ$  from the principal directions provided by the two VLF transmitters. In this case the invariant response, shown in Figure 17 *vlf*, provides a relatively simple mapping of the true strike and extent of the body. The interpretation of the invariant is more straightforward than an assessment of the individual maps provided by the two transmitters. The invariant phase in particular "simplifies" to a low value ( $<90^\circ$ ) above the body with an increase ( $>90^\circ$ ) defining the terminating ends.

#### *Model 3 (3dv34)*

This model is characterised by a single body with a strike rotated by  $34^\circ$  and  $56^\circ$  from the principal directions provided by the two VLF transmitters. In this case the invariant response, shown in Figure 18 *vlf*, again provides a straightforward mapping of true strike and extent of the body. A very similar anomaly mapping to the previous case (Model 2, Figure 17 *vlf*) occurs in both amplitude and phase.

### **3.4.9 Summary of 3D modelling results**

The first model (3dv2) considered the case of a VLF transmitter providing a principal (TE or TM) mode of induction. In this case the VLF-R results provide anomaly mapping in both TE (current parallel to strike) and TM (current perpendicular to strike) modes. The TM mode response produces a spatially more compact anomaly than that of the TE mode.

The use of VLF-R invariant mapping, employing two orthogonal transmitters, simplified interpretation as shown in Figure 16 *vlf*. The invariant amplitude displays an absence of 3-D end-effects while the invariant phase moves to high values in response to body termination points.

A VLF-Z response only occurs in the TE mode response. For the models studied, 3-D contributions to the VLF-Z response are minor.

The second two models (3dv17 and 3dv34) examined body strike rotations of  $17^\circ$  and  $34^\circ$  from both principal directions (i.e. VLF transmitters to the south/north and west/east). For both strike rotations and for both modes similar conclusions apply to the VLF-R response. The apparent resistivity mapping appears to approximately identify the 2-D strike of the body. The phase response is more complicated and, for the models studied, appears to be dominated by 3-D body end-effects. Clearly for the smaller rotation of  $17^\circ$  the results obtained are "closer" to the case of "principal direction" behaviour of model 3dv2.

For the rotations considered the use of invariant mapping provides an important simplification



for interpretation purposes. Again the invariant amplitude displays an absence of 3-D end-effects and the phase "identifies" the body termination points. Overall the invariant is seen to provide correct strike and body extent information.

It is noteworthy that the VLF-Z response for the rotation angles of  $17^\circ$  and  $34^\circ$  from principal TE mode identifies the correct body strike. Additional studies confirm that this behaviour is repeated for the rotation range from  $0^\circ$  to  $45^\circ$  from the principal TE mode direction. With increasing rotation angle, the magnitude of the VLF-Z anomaly decreases.

The VLF-Z response behaviour for rotations above  $45^\circ$  from TE mode is illustrated by the rotations of  $17^\circ$  and  $34^\circ$  from the principal TM mode direction. These results also relate to  $73^\circ$  and  $54^\circ$  rotations from the principal TE mode. In both of these cases the magnitude of the VLF-Z response rivals that of the previous case (rotations of less than  $45^\circ$ ) but the body strike direction is inaccurate.

#### 3.4.10 VLF interpretation in areas of complex geology

The parameters measured by VLF-R and VLF-Z can show a complex dependence on the combination of geological strike or trend encountered and the VLF transmitter azimuth used. A VLF-R response will always be present even for homogenous ground. The VLF-Z response will be zero for homogenous ground and may show a complex dependence on the azimuth combination in all other situations. As an aid to the interpreter it is important to measure *both* VLF-R and VLF-Z parameters; even in "simple" situations it will *confirm* that the structural resistivity style is indeed simple.

When attempting to detect the trend of resistivity gradients associated with geological structure the interpreter is required to "identify" TE and/or TM mode behaviour of the field parameters measured. This identification is made possible if two (or more) azimuthally distinct VLF transmitters are used. An azimuth separation which approaches  $90^\circ$  is most beneficial to the interpretation. As shown in the 3-D modelling, VLF-R data from two (or more) transmitters also allows the use of invariant mapping of both amplitude and phase which may simplify interpretation. Examples of the use of invariant mapping at Test Sites 3.1 and 3.2 are given below.

#### 3.4.11 Karous-Hjelt filtering

The in-phase component of the vertical secondary magnetic field of the VLF-Z data collected at Test Sites 1.1 and 1.2 has been subjected to a filtering process similar to that described by Karous and Hjelt (1983), using BGS software VLFCDI (Pedley, 1992). The data was first reversed in sign to satisfy the convention adopted in this procedure. The output from VLFCDI is a pseudo-section in which the horizontal axis represents locations along the profile, the vertical axis represents pseudo-depth and the contours (colours) represent current density. Ogilvy and Lee (1991) show that the technique yields a reliable indication of conductor depth and an indication of conductor quality and dip direction for single, steeply dipping conductors. This work was extended to include the VLF data (16kHz, originating from Rugby, UK) obtained by our collaborators, DFA GmbH, in Target Area 1.

### 3.5 Ground conductivity

Electrical conductivity quantifies the ease with which an electrical current can flow through a material and is measured in millisiemens per metre (mS/m), formerly millimhos per metre. The method uses a time-varying electromagnetic field as an energy source to measure an apparent conductivity whose value depends only on the coil separation and the distribution of ground resistivities. As it is an induction method there is no requirement for electrode contact with the ground and hence the technique is logistically superior to galvanic resistivity. Additional advantages include the absence of electrode effects and the fact that the ground adjacent to the transmitter or receiver coils does not make a disproportionate contribution to the measured signal.

By definition it can be seen that conductivity is the inverse of resistivity and the two parameters show a relationship of the form:  $1 \text{ mS/m} = 1000 \text{ ohm.m}$ . Hence data from conductivity and resistivity surveys are directly comparable.

The conductivity measuring equipment used in the present work was a Geonics EM31; this is a single operator battery powered terrain conductivity meter. It comprises a transmitter and receiver at either end of a 3.66 m rigid boom, with a central console housing the analogue meter and operator controls. When the transmitting coil is energised with an alternating current (9.8 kHz frequency) the resultant primary magnetic field induces small eddy currents in the ground. These currents subsequently produce a secondary magnetic field which is sensed by the receiver coil. The coil spacing is a small fraction of the skin depth and hence at the frequency employed the out of phase response is linearly related to the apparent conductivity of the ground and this is indicated directly by the instrument. This apparent conductivity represents a weighted average of ground conductivity within the sensing range of the instrument.

The depth of investigation is governed by the coil orientation and ranges between about 2.75 m (vertical coil, horizontal dipole) and 6 m (horizontal coil, vertical dipole). Thus by conducting surveys at the two possible coil orientations a qualitative assessment of the shallow conductivity structure can be made.

In addition to fault detection (either direct, by locating linear conductive features or indirect by the delineation of abrupt lithological displacements), rapid reconnaissance conductivity surveys prior to GPR traversing can quickly highlight those shallow conductive zones where radar penetration will be severely limited.

### 3.6 Seismic

#### 3.6.1 Seismic refraction

The shallow seismic refraction technique is used to determine both the thickness and sonic velocity of discrete lithologies and the presence of sub-vertical fault zones (characterised by anomalously low velocity extending into the refracting layer) to depths of about 30 m. Seismic

velocity (compressional) ranges between about 330 m/s in dry, unconsolidated deposits to 7 000 m/s in dense, fresh, ultrabasics. Thus a knowledge of the local seismic velocities allows the prediction to some extent of the lithologies present.

The technique requires the precise timing of the passage through the ground of an impulse generated artificially. Typically the source is the impact of a sledge hammer on a steel or thick nylon plate and the passage of the various resultant wave fronts is recorded by geophones implanted inline in the ground. Knowing the arrival times and the geometry of the geophone array, the velocity of the impulse through the ground can be calculated. Where the velocity of successively deeper layers increases in discrete steps (which is commonly the case in nature) then a plot of first arrival time against geophone distance from the impact point yields a series of more-or-less straight line segments from which can be calculated both layer velocity and thickness. Observations using the same geophone spread but with an impact at the opposite end (reverse shooting) allows calculation of refractor dip and topography. Additional intra- and mid-spread shots yield the additional control required for the time-delay and Generalised Reciprocal (Palmer, 1980) methods of interpretation that can reveal details of the refractor depths below each geophone and indicate variations of refractor velocity along the seismic line.

In the present study we used a Terraloc Mk III seismometer with a sledge hammer and nylon plate energy source. Triggering was achieved through a geophone immediately adjacent to the nylon plate. At each site nine "shots" were made into a single spread of 24 geophones at 2 m separation; the shot points were at 50 m, 25 m and 2 m offset from each end, at the spread centre and 12.5 m on either side of centre. Typically, stacking between 5 and 8 records at each site yielded good quality data. All geophone sites were optically levelled and the results incorporated into the subsequent interpretation.

#### *Data reduction and interpretation*

First arrival picking and subsequent analyses of the time-distance data was undertaken using VIEWSEIS. The simplest interpretation available is the Time Intercept Method; this yields layer thicknesses (accurate to about  $\pm 10\%$ ) and velocities in the vicinity of each shot point and, by interpolation, a much simplified cross section. More detailed mapping of the relief of refracting layers is possible with the Delay Time (Reciprocal) Method which requires arrival times at geophones from impacts at both ends of the spread. The most sophisticated approach is the Generalised Reciprocal Method which allows very detailed mapping of refractor relief and also indicates lateral refractor velocity variations. The interpretations presented in this report have combined all three approaches.

#### **3.6.2 Azimuthal seismic**

A Bolt airgun was suspended at one metre intervals between depths of 28 m and 7 m in borehole 1.22 at Test Site 1.2 and the first arrival times were recorded by geophones placed on the surface at a 45° interval around the circumference of concentric circles of varying radii (2 m, 5 m, 10 m etc) extending from the borehole. Triggering was achieved through a hydrophone suspended immediately above the airgun. It was anticipated that sub-vertical fractures (low velocity zones) would be detected by increased travel times of those seismic paths crossing



such features. It was planned to extend the experiment to the 75 m radii but unfortunately the borehole collapsed following rupture of the thin corrugated plastic casing and measurements were achieved only at the above short radii and to distances of 15 m, 20 m and 25 m from a depth of only 1.5 m (below which depth the hole was collapsed). The set-up was then moved to borehole 1.23 also at Test Site 1.2 but after observations on the 75 m radius (again at 45° intervals) at only three depths (28 m, 24 m and 20 m) problems with the air gun seating resulted in continual pressure loss and this work was abandoned.

#### *Seismic fan shooting*

A similar experiment to that described above except that the seismic source (sledge hammer and nylon plate) was on the ground surface and the azimuthal increment between geophones was reduced to only 10°. The geophones were placed at two radii, 20 m and 50 m. Triggering was through a geophone immediately adjacent to the nylon plate. The fan shooting technique was used in the early days of refraction prospecting to locate and trace both salt domes (high velocity) and gold bearing placer deposits (low velocity features) through observation of the variation in travel time to various positions on the arc.

#### *Data reduction and presentation*

First arrivals were picked manually using VIEWSEIS and these times were either plotted against the respective azimuths or as polar diagrams (fan shooting).

### **3.6.3 Seismic tomography**

Seismic tomographic imaging requires that a large number of observations of travel time are made between a seismic source and a receiver (or more often, a group of receivers). The source and receivers are usually located in adjacent boreholes which may be as far apart as 100 m, and, as in the present work, additional complementary data can be obtained by installing a string of geophones on the surface linking the boreholes. The source is repeatedly moved up or down in the borehole following each set of observations and in this manner a very large number of ray-paths are achieved (in excess of 2 000/site in some of the present work). The direct ray geometries (ie the straight path linking source and receiver) and the related travel times are inverted to produce a velocity distribution of the inter-borehole zone that best fits the observed data.

For the present work we used an in-house high voltage (4 kV) sparker as the source. This was particularly suitable as the dominant frequency (some 2 kHz) promotes high target resolution while this source has ample power for the rather short distances between the boreholes in the present study (maximum 30 m). A string of ten hydrophones, one metre separate, was suspended in the adjacent borehole while 24 standard compressional wave geophones at intervals of either 1 m or 1.5 m were planted on the surface. Coverage was obtained with the source at every one metre interval in one borehole to a hydrophone at every one metre interval in the adjacent borehole. Additionally coverage between the source at every one metre interval in both holes and every geophone was obtained. The data were recorded using two ABEM Terraloc Mk III 24 channel seismometers with common (electrical) triggering; these instruments promote signal/noise enhancement by stacking multiple shots. In the present area



seismic transmission was good and one shot only was usually sufficient to obtain a very clear seismogram.

#### *Data reduction and interpretation*

The travel times between source and receiver pairs were picked manually using VIEWSEIS software and a \*.TIM file was created. Using a screen editor this was converted to a \*.DAT file that was suitable for input to DIVINE, a seismic tomography package. Three additional input files are required for DIVINE, these defining: receiver positions (\*.REC), source positions (\*.SHO) and travel times for each source-receiver pair (\*.DIV).

Additional file types were generated to assist the interpretation. For example, a \*.VEL file was produced that is similar to the \*.DIV file but contains an extra column listing the ray velocity calculated using simple straight path geometry between source and receiver. The velocities obtained here were used to constrain the tomographic inversion so that only realistic values were output. A further supplementary routine was written to extract the most nearly horizontal raypaths from the \*.VEL files and output these and the associated velocities to a \*.PR file.

The original intention to combine both hydrophone and geophone data in the tomographic inversion was unfortunately frustrated on two counts. DIVINE is able to accommodate a maximum number of raypaths of only 1311, considerably fewer than the 2000 or so typically achieved in the present work. We considered using only alternate raypaths but it was then observed that the velocities interpreted using hydrophone and geophone data independently were markedly different ie the two data sets were fundamentally incompatible. Analysis of the waveforms yielded by the two types of detectors indicated responsive frequencies of 125 Hz and 900 Hz for geophones and hydrophones respectively. Not only are the geophones employed relatively low frequency devices, but a large proportion of the high frequency component of seismic energy will be further lost in the relatively porous overburden in which they are emplaced. The combination of low frequency responsive geophones with a high frequency source has resulted in weak and ambiguous registration of first arrivals which probably accounts for the discrepancies observed between the two data sets. The geophones employed were further unsuitable in that, given the low velocities prevailing in the overburden (700 m/s - 2 000 m/s), the dominant wavelength detected would be of the order of 20 m to 30 m which is far too large to resolve the expected target (a narrow fault zone). For these reasons the geophone and hydrophone data were not combined.

Initially a straight ray tomogram was produced for each site together with a diagram showing the ray paths and a contour plot of the ray coverage density. The results from these tomograms were disappointing as they all showed the same general convex pattern at the top and bottom of the image in the region of minimum ray coverage. The presence of this feature at all sites suggests that it is an artefact due to either or both the array configuration and processing.

To determine if the tomograms (inversions) were consistent with the field data further processing was undertaken. First, the velocities of the tomogram were compared with the calculated velocities in the \*.VEL (velocity for each raypath) files. In all cases good agreement was observed after adjusting the constraints on the inversion process. Secondly, a line graph

was produced for each site using the \*.PR files (velocity for each horizontal raypath), plotting the velocity of horizontal rays against their depth and thus obtaining an approximate velocity/depth structure in the vicinity of each borehole. Again the results were consistent with the velocities produced by the inversion process.

It is well known that velocity anisotropy can seriously degrade the resolution and appearance of seismic tomograms and hence various anisotropy corrections were applied to the present data. The programme ANISO was written; this assumes that vertical rays are slower than horizontal rays by a certain percentage. For rays intermediate between vertical and horizontal a sinusoidal scaling factor is applied to determine the proportion of the maximum anisotropy to be applied. The program used the \*.DIV files to produce a \*.ATY file. This has exactly the same format as a \*.DIV file but the travel times are corrected by the relevant anisotropy factor. For each site a \*.ATY file was produced for anisotropy corrections of 5%, 10%, 15%, 20%, 25%, 30% and 40%. It was found that generally the value of 15% gave the most realistic correction.

### 3.7 Magnetometry

Magnetometry records local variations in the earth's magnetic field and these in turn reflect contrasting magnetic susceptibilities. The susceptibility of rocks, a measure of how strongly magnetised they become in the inducing earth's field, is determined almost entirely by their content of ferrimagnetic minerals, principally magnetite and ilmenite. Quite subtle changes in the content of these auxiliary minerals result in the very large susceptibility variations displayed by rocks and hence magnetometry, probably the most cost effective geophysical technique, can be a very sensitive tool of geological mapping. Hence its application in the present work where we are seeking abrupt displacements of lithological units of contrasting susceptibility. In addition, fault zones are occasionally defined as linear features of either enhanced or depressed magnetic intensity, the first case resulting from the deposition of hydrothermal minerals and the latter from the oxidation of magnetic minerals in the shattered zone.

During the present work a Scintrex IGS-2 proton precession magnetometer was used; this records the absolute value with a sensitivity of 1 nT, approximately 1/50 000 part of the earth's field strength. This instrument can also measure the vertical gradient of the magnetic field over a 1 m sensor separation, and with this additional information we can immediately identify shallow (strong gradient) sources which usually have a cultural origin. Diurnal variations were monitored (and corrections subsequently applied) by repeated base station readings at approximately half-hourly intervals.

#### *Magnetic susceptibility observations*

Borehole cores encompassing a wide variety of representative local lithologies (including some from Project boreholes) were tested with a Kappameter in Saarbergwerke's core store near Saarbruecken. The Kappameter is a direct reading instrument, displaying the value of magnetic susceptibility in SI units ( $\times 10^{-3}$ ).

### 3.8 Natural gamma logging and mapping

#### 3.8.1 Borehole logging

All six vertical boreholes in Test Sites 1.2 and 1.4 were logged using the hand winched S. I. E. T450 logger employing a 2 cu in detector crystal. The logs were run from the bottom to the top of the hole at 1 m/minute using a time constant (integrating period) of 1 s.

Natural gamma logs are well able to differentiate between shales/clays (high natural activity) and clean sandstones (low activity) and the main purpose of our logging was to identify any uniform horizons extending between adjacent boreholes that were likely to behave as a geophysical unit ie those layers possessing common physical characteristics. This information would be used to constrain the tomographic inversions.

#### 3.8.2 Surface mapping

The S.I.E. T450 borehole logger was used to map the surface distribution of natural gamma activity at Test Site 2.1 only. In a novel application of this instrument the probe was mounted in a padded rigid plastic sheath to protect it from mechanical shock and dragged along the survey lines from a stationary point at the end of each line. The speed was maintained at 3 m/min and the integrating period set at 5 s, resulting in an averaged value for each 25 cm length of traverse. The analogue records were subsequently digitised and sampled at 1 m interval with each value being ascribed an X,Y coordinate according to line number and distance from the base line. The statistical variation in count-rate, monitored at the end of each traverse, ranged between 3 cps and 5 cps over a 5 min interval. While this is an appreciable proportion of the total range of values observed, the observations are nevertheless repeatable and consistent from line to line.

## 4. DISCUSSION OF RESULTS

### 4.1 Test Site 1.1

#### *GPR*

The projected Berschweiler Fault intersects Line 0 in the vicinity of 50 m and boreholes BK1.11 and BK1.13 located respectively 5 m west and east of this position proved major horizontal discontinuities in the shale and clay formations with a downthrow to the west. The geological logs for boreholes BK1.11, BK1.12 and BK1.13 (Figure 6) provide excellent control for the 25 Mhz and 50 MHz GPR sections (Figures 1 *gpr* and 2 *gpr*). The 50 MHz section shows increased resolution of shallow layers but marginally reduced penetration compared to the 25 MHz section. This is because the shorter wavelength associated with the higher frequency is able to resolve thin, shallow beds, whilst the longer wavelength of the lower frequency responds to deeper, thicker horizons. Thus to the east of the fault the 25 MHz section reveals one horizon (compared with two on the 50 Mhz section) and to the west two reflectors are identified (compared with at least three using the 50 Mhz antennae). It appears that the 25 MHz frequency has responded primarily to the thicker shale lithologies; these are also evidenced in the 50 MHz frequency which has additionally responded to thinner sandy clay

and sandy shale horizons. This comparison of responses shows the advantage of using both the 25 MHz and 50 MHz antennae.

#### VES

The three soundings made at this Test Site indicate very little variation in geo-electrical properties in the uppermost 15 m (see Figures 5 and 2 *res*) and hence fail to indicate the presence of the proved intervening fault.

#### RESCAN

A single electrode grid was established here, centred on Line 0 (Figure 9 *rsc*). The resistivity distributions mapped at three increasing depths (ABs of 3 m, 7 m and 11 m) shown in Figure 10 *rsc* reveal an overall marginal increase in apparent resistivity with depth. The proved fault trace appears to bound the zone of relatively high resistivity seen at depth in the southern part of the grid and may also coincide with the poorly defined salient of low resistivity immediately east of this. The resistivity distribution revealed here appears initially to be at variance with the logs of Boreholes BK1.11 and BK1.13 which indicate a thicker shallow clay-rich horizon in the former borehole (ie towards the west side of the grid). Thus it is likely that the high resistivity zone in the west reflects primarily the deeper 2 m thick clayey sandstone horizon mapped only in Borehole BK1.11.

#### VLF

The in-phase response of both VLF frequencies observed here display the classical cross-over anomaly directly above a conductor; the pseudo-section of Figure 19 *vlf* (19 kHz) indicates that this conductor is both shallow and near vertical. The corresponding 16 kHz pseudo-section (not shown) suggests that the conductor extends to the surface but this is thought to reflect the coarser observation interval used (5 m compared to 2 m). The VLF responses diminish southwards across the grid, with the weakest signatures seen on Line 20S; this is thought to reflect increased depth of burial of the (assumed) cultural feature in this direction.

The in-phase profile also indicates a weak conductor at about 22 m, this extends across the grid, parallel to the Berschweiler Fault but some 25 m east of its projected location.

#### Ground conductivity

The monotonous conductivity responses recorded at this Test Site have failed to indicate the proved fault. Either the technique has failed to penetrate the recent alluvial deposits or the lithologies juxtaposed by the fault movement lack sufficient conductivity contrast for their discrimination. The latter possibility is supported by the VES observations.

### 4.2 Test Site 1.2

#### GPR

The characteristic GPR response that we now associate with faulting appears on Line 20 S at about 80 m; Figures 3 *gpr* and 4 *gpr* show respectively the 25 Mhz and 50 Mhz sections. However, it is apparent that at this Test Site the Berschweiler Fault is not identified as a single, well defined linear feature extending across the survey grid, but rather as a series of en echelon displacements, as depicted in Figure 7. The shallow and thick clay and shale at this site, proved



by boreholes BK1.21 to BK1.24 (Figure 8), have restricted the depth of investigation to some 3 m (50 Mhz) and 6 m (25 Mhz). Extensive lateral displacements of these shallow lithologies and the underlying and interbedded sandstones is indicated by all GPR sections from this site while the borehole logs (Figure 8) confirm the lateral impersistence of most of the horizons across the short (20 m) inter-borehole distances.

Figures 5 *gpr* and 6 *gpr* clearly show the effect of EM attenuation at both 25 Mhz and 50 MHz by the shallow conductive lithologies on Line 20 N, which traverse includes three of the four boreholes subsequently drilled at this site. The radar sections also illustrate the lateral impersistence/displacements of these horizons.

In our Periodic Report (January to June 1994) we suggested a non linear alignment of the Berschweiler Fault (depicted as a yellow line in Figure C of that Report). A reappraisal of the GPR sections in conjunction with the results of the seismic tomography survey of January 1995, has resulted in the alternative alignment of the supposed Berschweiler Fault shown in Figure 7. It has proved impossible to correlate GPR features between adjacent lines to produce a single, continuous trace for the inferred position of the Fault, because of the complex distribution of near surface lithologies. For example on Line 0 the best defined GPR feature occurs at 83 m with only a weak anomaly at 95 m (the projected intersection of the straight line from the anomalous GPR features detected on Lines 60 S to 20 S). A similar pattern is repeated on Line 20 N.

#### VES

VES2 indicates a resistive lithology extending to about 6 m depth at 114 on Line 20 S (Figure 3 *res*). The prominent GPR reflector at about this depth extending between 88 and 136 (Figure 3 *gpr*) may correspond to the contact between this resistive unit and underlying more conductive lithologies. A similar correlation may be possible for the shallower GPR reflector (between 2 m and 4 m depth) and the relatively low resistivity units interpreted for VES2.

VES1 at 29 m on Line 20 S shows only a very thin resistive surface layer, in agreement with the trend suggested by the GPR sections (Figures 3 *gpr* and 4 *gpr*). VES3 shows practically identical shallow (15 m) layering to VES1 and yet was located only 30 m from VES2; this fact either attests to the geological complexity of this Test Site or indicates the presence of a fault between sites 2 and 3.

#### RESCAN

Three overlapping grids centred on Line 20 N (Figure 29 *rsc*) provided coverage from 64 W to 100 W. Figure 7 *rsc* shows the distribution of apparent resistivity at the shallowest depth of investigation (AB=3 m) measured using the half-Schlumberger array. The prominent low resistivity feature centred at 80 W is approximately coincident with (and shares a common north-westerly trend with) a GPR feature characteristic of faulting (Figures 5 *gpr*, 6 *gpr* and 7) and thus may represent direct evidence of faulting. Similarly, the sub-parallel conductive zone towards the east side of the grid may reflect an en echelon disturbance. The contrast in ambient apparent resistivity at about 90 W probably reflects the presence of shallow conductive shale (proved in boreholes BK1.23 and BK1.22) to the east of this point. The thin overburden at this site permitted the use of an array providing high lateral resolution resulting in clear anomaly



definition.

The corresponding focussed array analysis is illustrated in Figures 27 *rsc* and 28 *rsc*. Both focussed apparent resistivity and pole-pole profiles reveal the conductive zone between stations 76 W and 84 W on Line 20 N. However the crossovers between the profiles of normalised east and west balance factors indicate that this conductive zone comprises two discrete narrow features (of average width 2.5 m) separated by a more resistive band (not resolved with the standard RESCAN measurements described above). Thus a succession of near-surface resistivity discontinuities is indicated at this site and these may be ascribed to direct evidence of sub-parallel faulting.

#### *Ground conductivity*

Figure 1 *em* shows colour contoured plots of the horizontal and vertical dipole conductivity obtained on the six traverse lines at this Test Site (Figure 7); noise spikes associated with the track and a built-up area in the north west of the grid have been respectively smoothed and edited out. Two distinct anomalies are shown. The first, located in the central and eastern half of the site, trends north west (generally parallel to the projected Berschweiler Fault) and comprises alternating medium to high conductivities (respectively  $> 12$  mS/m and  $> 20$  mS/m for the horizontal and vertical dipole observations). This feature is most pronounced in the deeper penetrating vertical dipole plot. The second anomalous zone, of very restricted area, comprises low conductivities (respectively  $< 7.5$  mS/m and  $< 12.5$  mS/m for the horizontal and vertical dipole measurements) to the west of approximately station 85 on all traverse lines. The distribution of shallow conductivities thus outlined is largely in agreement with the indications of the three VES described above.

Closer examination of the individual conductivity profiles, however, suggests a more complex geological environment comprising at least three distinct conductivity zones:

a. Several profiles are characterised by small step-like features, consistent from line to line, that could reflect en-echelon faulting. The composite diagram of conductivity profiles and GPR section (50 Mhz) for Line 0 (Figure 2 *em*) shows these step-like features occurring on the downthrown side of the fault between stations 60 W and 80 W.

Similarly, in Figure 3 *em*, the composite diagram for Line 20 S, step-like features on the conductivity profiles (especially horizontal dipole) can be correlated with characteristic GPR patterns and could be indicative of en-echelon faulting. The vertical dipole data indicates increasing conductivity between stations 56 and the characteristic GPR fault anomaly at about 82. As this increase is not mirrored by the shallower penetrating horizontal dipole data, it is assumed that a change in facies to a more clayey sediment occurs across this interval below a depth of approximately 2 m. The steep decline in conductivity between stations 82 and 92 correlates with the pronounced GPR response associated with faulting.

b. Figure 4 *em* shows a hypothetical geological section that could account for the saw-tooth nature of the two conductivity profiles. This model suggests a sequence of shale overlying sandstone that has suffered faulting along south west dipping en echelon planes. Conductivity

minima are assumed to be located over the thickest/shallowest sandstones while conductivity highs reflect thick shales. Some corroborating evidence for such a model is provided by the GPR section of Figure 4 *em* which displays numerous dislocated reflectors and characteristic pattern zonation. For instance between about 80 and 140 the GPR shows very limited penetration (thick conductive shale) while beyond 144 the abrupt occurrence of the deep (6 m) reflector (indicating enhanced radar penetration) coincides with the zone of low conductivity (assumed shallow/thick sandstone).

c. The conductivity profiles of Line 20 N (Figure 5 *em*) show a prominent central zone of enhanced conductivity between 40 and 80; this could indicate a narrow faulted block in which occurs either a shallowing or thickening of a conductive layer. The dominant response is yielded by vertical dipole observations and hence the anomaly does not have a superficial origin. Borehole BK 1.23 near the centre of this feature proved shallow thick shales while two further boreholes to the west (in zones of reduced conductivity) proved increasing shallow sand content. Hence the conductivity feature, which does not show strong line to line consistency, may reflect only local facies variations. However, the western limit of the conductive feature (at about 80) does show some correlation with a characteristic GPR fault response (Figure 5 *em*).

A RESCAN survey was made over the western edge of the prominent conductivity feature. With the resistivity array configuration used, depths of investigation of about 3 m and 5 m (ie comparable to the EM31 depths of investigation) are achieved with AB spacings of 7 m and 9 m respectively. Figure 6 *em* shows close correspondence between the two data sets.

## SEISMIC

### *Seismic refraction*

A seismic refraction profile on Line 20 N indicated a refracting layer, of velocity about 2 200 m/s, lying about 5 m below surface and with relief of about 0.8 m. Numerous local depressions are indicated on the surface of the refractor but none of these appear especially significant, nor are they associated with reduced velocity indicative of faulting.

### *Azimuthal seismic*

*Source in Bk 1.22:* the shallow (1.5 m) source experiment yielded marginally increased travel times for all three radii towards 315°, suggesting the presence of a north west trending low velocity zone (fault?) passing within 15 m of borehole Bk 1.22.

*Source in Bk 1.23:* experiments with the source at depths of 20 m and 24 m and detectors at 75 m radius indicated largest time delays at azimuths of 225° and 270°, suggesting the presence of a south west trending low velocity zone passing through the borehole. An alternative explanation requires north west trending fractures between the source and geophones.

### *Seismic tomography*

The computed velocity/depth distribution (assuming horizontal straight rays) between adjacent

borehole sites is shown in Figure 1 *sei*. The rapid increase in velocity through shallow depths seen between sites BK1.22/BK1.23 and BK1.21/BK1.22 is consistent with reduced weathering and increased compaction with depth. The high velocities ( $> 3.3$  km/s) recorded below about 20 m at these two sites reflect the presence of a hard sandstone. The dramatic shallow increase in velocity is not observed between sites BK1.21/BK1.24, largely because the deeper standing water level in BK1.24 precluded hydrophone observations in the top 7 m.

BK1.24/1.21 : The raypath coverage for this tomogram is shown in Figure 2a *sei*. The thick shale/mudstone sequence recorded in Bk 1.24 (see Figure 8) is reflected in the tomogram by the relatively low velocities adjacent to this borehole (Figure 2b *sei*). Similarly, low velocities (combined with a low velocity gradient) are implied by the velocity/depth distribution at this site shown in Figure 1 *sei*. All the tomograms (ie both uncorrected and with an anisotropy correction of between 5% and 15% applied) from this site are markedly assymetrical, the strong lateral variation in velocity distribution being further highlighted by a low-velocity south west dipping salient at about 12 m. This dataset provides the strongest indication of faulting obtained with the current seismic tomography work and were the anomalous GPR feature detected on Lines 60 S to 20 S projected in a straight line it would not only support the present tomographic indication, but also largely parallel the Berschweiler Fault projected from their mine workings by Saarbergwerke.

The tomogram between sites BK1.21/1.22 displays a hiatus at a depth of about 14 m; spatially this correlates approximately with the projection of an anomalous GPR feature and may well indicate faulting. Further evidence of this may be provided by the velocity/depth plot for this site (Figure 1 *sei*) that indicates an anomalous distribution (ie a zone of reduced velocity at depth). The tomogram between sites BK1.22 and BK1.23 is largely symmetrical with no evidence of abrupt discontinuities or discrete low velocity features indicative of faulting.

#### *Natural gamma borehole logging*

The responses have been somewhat attenuated by the plastic borehole casing and contained water; nevertheless, consistent data reflecting geological contrasts have been observed.. In Figure 1 *gam* for example, the contact between sandstone and shales at about 13 m depth in borehole Bk 1.24 is well defined by an increase in counts of about 50%. Elsewhere, minor discrepancies between the geological description and gamma logs highlight the difficulties of geological logging with cuttings, while occasionally, apparently clay-rich thin horizons located by the gamma logs have not been identified on the geology log (eg at 25 m depth in borehole Bk 1.21). This borehole also shows two clear examples of fining- downward sequences (ie between 2 m and 7 m and between 16 m and 24 m deep). In general the logs confirm the lateral impersistence of most of the horizons across the short (20 m) interborehole distances, there being little clear evidence of continuity of either major units or thin distinct marker horizons. However, the sandstone near the base of both boreholes Bk 1.22 and 1.23 does possess a similar gamma signature and on this basis there is no evidence for faulting between these two boreholes.

### 4.3 Test site 1.3

#### *GPR*

The moderate to high background resistivity at this site allowed depth penetration of 8 m at the 25 Mhz frequency.

#### *VES*

The two soundings indicate strongly contrasting conditions below about 3 m depth (Figure 4 *res*): a moderately resistive unit (100 ohm.m, sandy shale?) underlies station 80 on BGS Line 0, (bearing 215°) compared with a much more resistive unit (up to 700 ohm.m, arkosic sandstone?) at station 125. This increase in resistivity west of the projected fault at this Test Site is endorsed by the GPR section (not shown) which shows the characteristic fault response at 96.

### 4.4 Test site 1.4

#### *GPR*

An exceptionally well defined anomaly characteristic of faulting is shown at 45 m on Line 30 S (Figures 9 and 7 *gpr*). The quiet nature of the radar section west of approximately 50 m reflects the presence of a thick (3.5 m) and shallow highly conductive clay layer, proved in borehole BK1.43. The GPR section shows some excellent correlations with the shallow layering as defined in the borehole logs (in particular with borehole BK1.44 - Figure 10).

#### *RESCAN*

The half-Schlumberger array data from a single grid of electrodes centred on Line 30 S (Figure 30 *rsc*) extending between 35 W and 54 W is shown in Figure 8 *rsc*. The monotonous pattern of intermediate apparent resistivities (170 ohm.m to 300 ohm.m) observed at the shallowest depth of investigation (AB=3 m) suggests the presence of fairly thick, dry overburden. With increased penetration (AB=13 m) a well defined resistivity contrast is indicated at about 45 W (on Line 30 S), approximately coincident with a GPR response characteristic of a faulted contact (Figure 7 *gpr*). Both the GPR and ground conductivity traverses (Figure 7 *em*) indicate a lithological contact near this station, while borehole evidence proves shallow sandstone (resistive) only to the north-east. This is an example of the indirect detection of faulting by RESCAN.

The resistivity/depth sections of Line 30 S (Figure 8 *rsc*) confirm the thickness of about 2 m of resistive overburden and also the presence of a faulted contact at about 45 W with a resistive lithology (the sandstone proved in Borehole BK 1.44?) extending towards the north-east.

#### *Ground conductivity*

The two conductivity traverses made here both reflect the thickening of conductive near surface clay (revealed by boreholes BK1.43 and BK1.44) as the stream is approached, but neither show any clear indication of faulting. Coincident with the strong GPR feature on Line 30S at 45m, near the projected position of the fault, there are 'steps' in the responses of both dipoles (Figure 7 *em*) but similar (and better defined) features occur along the entire length of this traverse and probably reflect the variable overburden conditions.



## SEISMIC

### *Seismic tomography*

The velocity/depth distribution (Figure 1 *sei*) indicates a fairly uniform gradient consistent with reduced weathering and increased compaction with depth. The minor departure at about 19 m depth may reflect the faulting discussed immediately below.

BK1.43/1.44 : an abrupt lateral velocity contrast at a depth of about 19 m may reflect the position of projected Fault III. The tomogram suggests that relatively low velocities occur at depth in borehole BK1.43. This observation is supported by neither the geological- nor natural gamma logs (Figures 10 and 2 *gam*). Approximately equal distributions of sandstone are revealed in both boreholes on the lithological logs while the gamma logs imply fairly uniform conditions to a depth of about 20 m. Thus it is possible that the low velocities recorded in the sandstone at the bottom of Bk 1.43 reflect fracturing and enhanced porosity.

### *Natural Gamma borehole logging*

The gamma logs from the two vertical boreholes logged at Test Site 1.4 (BK 1.43 and BK 1.44) are shown in Figure 2 *gam*. Fairly uniform lithologies are indicated in both boreholes to a depth of about 20 m.

## 4.5 Test site 1.5

### *GPR*

The GPR technique was effective in locating uncharted faults at both this site and Test Site 1.6, as proved by subsequent trenching. However, penetration was limited (to between 3 m and 4 m) owing to the widespread occurrence of shales, sandy clays and, in particular, a very conductive 0.2 m thick layer of green clay of average depth 2 m.

Typical radar sections from this Test Site are shown in Figures 8 *gpr* and 9 *gpr* (Line 10 S, respectively 25 Mhz and 50 Mhz) while the corresponding trench sections are shown in Figure 12. Two features readily identified on the 25 MHz section (at about 90 m and 126 m) reflect fault edges identified in Trenches 2 and 3 respectively. The 50 MHz section has resolved these two anomalies in addition to numerous other features that may or may not be significant. For instance, the shape of the 50 Mhz anomaly centred at 126 m appears to outline the trench profile at its deeper west end and may thus be responding additionally to rock hardness.

The contact between lithological units 1 and 2 (identified in the trenches) is seen in the GPR sections where the reflection from this interface has combined with the ground wave arrival to form the discontinuous reflection event (the second "black" band). The third reflected event represents the green clay horizon, underlain by unit 3, the shale. Thus GPR has defined fine lithological detail in addition to yielding direct evidence of dislocation/faulting.

The GPR signature of a buried electrical cable and infill material proved in Trench 1 (Figure 12) is seen in Figure 10 *gpr*. The reflection from the green clay horizon has suffered some distortion and, if viewed in isolation, this could be mis-interpreted as evidence for faulting.

An excellent 25 Mhz GPR response at 120 m on Line 0 (Figure 11 *gpr*) identifies the fault proved in Trench 4 (Figure 13) and, considered in plan, confirms the north north east trend of the hitherto unmapped fault defined at Line 10 S. The juxtaposed grey/green shale and brown shale (units 5 and 3 identified in the trench) presumably possess similar electrical properties and are thus not readily distinguished by GPR. However, the more conductive dark red clay layer (unit 2) has been clearly resolved by GPR and its abrupt termination identifies the fault position. The 50 MHz antennae were not used on this line.

#### VES

Two VES (see Figure 5 *res*) were made at this Test Site, on either side of projected Fault IV. VES 1 was located 15 m north of a roadside cutting that revealed 2 m of clay containing angular sandstone blocks overlying a homogenous clay/shale. The VES interpretation suggests the respective resistivities of these lithologies are 80 ohm.m and 40 ohm.m. The geo-electrical structure indicated by VES2 is different; here two shallow, high resistivity units (200 ohm.m and 100 ohm.m) are suggested within the top 15 m. Thus the VESs may lend some support to the presence of an intervening fault.

#### Seismic refraction

*Line 0*: the undulations on the upper refracting surface at this Test Site are even less pronounced than at Test Site 1.2 and again there is no evidence of faulting affecting this unit.

### 4.6 Test Site 1.6

#### GPR

In the following account of possible correlations between features observed on GPR sections and the lithology/structure proved in adjacent trenches, it should be noted that Trenches 5 and 6 lie midway between GPR traverse lines 0 and 20 S (ie some 10 m from these).

There is close correlation between both 25 Mhz and, in particular, the 50 Mhz GPR sections and the disposition of the four lithological units adjacent to the fault plane centred at about 124 on Line 0 as recognised in Trench 6 (see Figures 12 *gpr*, 13 *gpr* and 14). A more confused fault response at 25 Mhz is seen in the GPR section for Line 20 S centred at about 120 (Figure 14 *gpr*).

The fault zone revealed in Trench 5 between 81 m and 85 m on Line 10 S (Figure 14) is apparent in the 25 MHz GPR section of Line 20 S as a disturbed reflector between 75 and 95 (Figure 14 *gpr*) but is not easily recognised in the section for Line 0. It is probable that the two shale units (1 and 2) recognised in the trench lack sufficient contrast in electrical properties for their definition. However, the laterally persistent band of very conductive grey/green clay interbedded between these two shales forms an excellent GPR target and has enhanced the delineation of the shale lithologies.

The disturbance of this thin clay horizon in the vicinity of the fault zone allows the GPR recognition of faulting here. The sewage pipe at 77 m would normally generate a GPR anomaly with relatively low amplitude and high frequency but here it has been obscured by the large

amplitude/low frequency response of the grey/green clay.

The moderate to high conductivities (especially of the grey/green clay) coupled with the highest level of RF interference experienced during the entire fieldwork programme, has resulted in limited GPR penetration (typically 2 m but on rare occasions as much as 6 m) at both Test Sites 1.5 and 1.6. In addition, the rapid lateral change of lithological type or facies as proved in the exploratory trenches and indicated by the GPR sections has occasionally created difficulties when attempting to correlate GPR features between adjacent lines. This is well illustrated in Figure 15 *gpr* which shows the 25 MHz GPR sections for Line 40 S and 20 N at Test Sites 1.6 and 1.5 respectively. These two GPR sections are separated by only 15 m yet they depict quite contrasting detail and penetration. A comparison of Figures 15 *gpr* and 16 *gpr* (50 Mhz sections of Lines 40 S and 20 N at respectively Test Site 1.6 and 1.5) illustrates the value of combined 25 and 50 MHz surveying in complex situations. The 50 MHz sections show a confused fault signature whereas the 25 MHz sections highlight only the significant conductivity variations associated with the fault.

Again, as at Test Site 1.5, the GPR technique has defined detail within lithological units in addition to the disruption diagnostic of faulting.

#### *Seismic refraction*

*Line 20 S:* again only minor undulations are observed on the refractor surface with little of significance in terms of faulting.

#### *Azimuthal seismic*

*Line 20 S at 83 W:* the polar diagram of travel time to the 50 m radius revealed a strong north north west striking "slowness" while a similar trend (also in accord with the local trend of faulting) was displayed by the polar diagram of the time difference between the 20 m and 50 m radii. This latter diagram should largely exclude from total travel times the delays due to variable overburden thickness at both source and receiver.

### **4.7 Test Site 2.1**

#### *GPR*

The Hahnwiese Fault, as proved (somewhat further west than anticipated) in Trenches 1, 1A and 2 (Figures 15, 16 and 17) is clearly defined in the 50 Mhz GPR sections of Lines 16 S, 0, and 30 N (Figures 17 *gpr*, 18 *gpr* and 19 *gpr*). The proven trace of this feature is shown in Figures 15 and 16.

GPR penetration of some 6 m was achieved over the highly resistive shallow sandstone occurring on Line 16 S; this is twice the depth investigated (using the same 50 Mhz frequency) in the more conductive shale environment of Lines 0 and 30 N. (Borehole logs for Test Site 2.1 are shown in Figure 18). Only part of the characteristic fault response is visible at the western limit of Figure 17 *gpr*; this section also appears to outline the zone of made ground extending to 48. To the east of 44 GPR appears to have identified discrete blocks of the crumbly sandstone proved in Trench 1 as numerous diffraction patterns. An enhanced resolution of this

blocky terrain GPR character was achieved using the 100 MHz antennae (section not shown).

A displaced gate at the site of the demolished house adjacent to Weisbacher Strasse has been assumed to indicate the position of a fault. The GPR section of the road adjacent to this gate is shown in Figure 20 *gpr*; this shows the characteristic fault response centred at about 32, some 10 m east of the gate.

### VES

Uncontrolled interpretations of the three VES made at Test Site 2.1 are given in Figure 6 *res*. The shallow sandstone unit subsequently proved in borehole B1 is shown to have an in situ resistivity in excess of about 500 ohm.m; the effect of underlying conductive shales is apparent on the sounding curve (VES 2). VES 3 indicates a thin less resistive layer at greater depth; this is in accord with the section of Trench 1A which proved hard (unrippable) rock at greater depth than in Trench 1 while the reduced resistivity at this site may reflect the increased "fines" content of the sandstone. VES1 reflects the thick shallow conductive red shale proved in borehole B2.

### Resistivity mapping

Schlumberger array resistivity mapping at both electrode separations (AB 40 m and 20 m) outlined a highly resistive (sandstone/arkosic) block in the south east corner of the Test Site, contained largely between the base line and the projected trace of the Hahnwiese Fault (see for example Figure 7 *res*). The abrupt termination at the south west edge of this unit indicates the position of the Hahnwiese Fault. A further high resistivity zone occurring in the north west corner of the grid probably reflects another sandstone unit.

Figure 8 *res* is the apparent resistivity image derived from gradient array traversing in the zone immediately north of the major resistive sandstone, astride the position of the projected Hahnwiese Fault. The resistive zone at the southern margin extends further north than that observed with the Schlumberger array (Figure 7 *res*), possibly reflecting greater penetration of the AB 60 m gradient array. The narrow north east trending resistive belt at about 25 N may correlate with the thin sandstone unit seen in the Wiesbach 1 borehole at about 865 m depth, some 11 m above the thicker sandstone referred to above.

Figure 9 *res* shows resistivity profiles plotted on a logarithmic scale (to accommodate the large range of values observed) measured by gradient array traversing over the revised Hahnwiese Fault location (ie following the initial surface geophysics but prior to trenching and GPR traversing). The zone of highest resistivity clearly outlines the hard sandstone. The trace of the subsequently proved Hahnwiese Fault grazes the north west corner of the grid; it does partly coincide with reduced resistivity values but there is no consistent line to line signature of the fault. The apparent resistivity values below 100 ohm.m on Lines 5 S and 10 S reflect a mound of dumped soil about 1 m high; it is disturbing to note the strong influence that this superficial feature has on the resistivity observations. The results of two further gradient array traverses, made after trenching operations had proved the fault position, are shown in Figure 10 *res*. At both 16 N and 3.5 S the fault coincides with the shoulder of a local resistive feature and again there does not appear to be a significant fault signature.



### RESCAN

All four styles of the half-Schlumberger array were recorded over a single electrode grid centred on Line 10 S (Figure 31 *rsc*) and extending between 46 W and 65 W; for styles 'a' and 'b' the electrodes were aligned perpendicular to the fault plane while for styles 'c' and 'd' they were parallel to this. The resulting observed apparent resistivity distributions shown in Figure 3 *rsc* are broadly compatible with the mapping yielded by other electrical techniques (eg Figure 7 *res*).

The strong resistivity contrast across the grid reflects the juxtaposition about the Hahnwiese Fault of a resistive arkosic sandstone and a conductive shale (the geological section proved by trenching is shown in Figure 1 *rsc*). All the RESCAN electrode styles exhibit a clear response to the faulted contact but there are significant differences in detail. The position of the contact indicated by styles 'c' and 'd' is both coincident and in close agreement with the proved location of the fault, while the plateau of intermediate (c. 100 ohm.m) apparent resistivity defined at the smallest AB value with these styles may reflect the en echelon downthrow of the arkosic sandstone as observed in Trench T1. However, the location of the contact as defined by styles 'a' and 'b' is not mutually consistent. This suggests that variable current gathering effects exist with this electrode orientation and that the position of the current source, relative to the fault, has significant control on the measured apparent resistivity distribution. Conventionally with half-Schlumberger (pole-dipole) arrays, the actual location of an anomaly is determined by combining the two data sets (ie for current electrode leading and current electrode trailing). In the present case (ie styles 'a' and 'b') this would result in a loss of resolution due to 'smearing' of the contact response and would effectively result in the discarding of significant data.

Figure 4 *rsc* demonstrates the variability of the apparent resistivity distribution with depth (proportional to AB); this highlights the 3-D nature of the geology at this site and the requirement for 3-D data sets and modelling routines. The result of a 3-D inversion is shown in Figure 5 *rsc*. The cut-away block diagram indicates the presence of resistive sandstone towards the south-east corner while its dip to the north north west (consistent with the mapped geology) is revealed by the progressive appearance with depth of the resistive unit as seen in the depth 'slices' shown above the block diagram.

Focussed array measurements were made on several lines of the RESCAN grid and indicated the west-east apparent resistivity gradient observed with other electrical surveys. Figure 20 *rsc* shows typical focussed and pole-pole profiles (at Line 11 S), indicating the more pronounced contact response (between stations 56 W and 60 W) of the focussed measurements. The corresponding focussed west-east balance factors exhibit the largest variation (Figure 21 *rsc*) confirming that the principal variation in electrical properties occurs in this direction. The most notable features are the decreased E value at array position 3 m and the increased W value at 6 m. The normalised W-E balance factors (Figure 22 *rsc*) indicate that the anomaly is symmetrical and centred at 4.5 m (station 58.5 W). This suggests that, moving from left to right, the E factor drops as resistive material is encountered (which the sensing current tends to avoid), whilst the W factor rises once the array is centred over the resistive zone (since the sensing current must be prevented from flowing preferentially back into the conductive zone).

Numerical modelling was undertaken to test these assumptions. The model parameters are shown in Figure 23 *rsc*. Figure 24 *rsc* confirms the excursions of the E and W balance factors as described above while the normalised balance factors exhibit a crossover displaced some 0.3 m towards the resistive material (Figure 25 *rsc*). By extension of these modelled results, the inferred surface trace of the faulted contact is indicated in Figure 26 *rsc*. While this displays a similar trend to the proven fault trace it lies some 4 m to the south west of this.

#### *VLF*

The results of VLF-R profiling by our collaborators at this Test Site yielded an encouraging initial coincidence of the Hahnwiese Fault with various types of resistivity anomaly (either a shoulder- or minima type). However, when this apparent coincidence is examined in the context of the full resistivity profiles (plotted using both linear and logarithmic scales) a line to line fault signature is not clear (see Figure 20 *vlf*).

#### *Ground conductivity*

EM31 observations, particularly those made with the relatively shallow penetrating vertical coil orientation, largely complement the apparent resistivity observations described above. Figure 8 *em*, for example, clearly defines the two main resistive units outlined by the Schlumberger array surveys as zones of low conductivity. The sinuous conductive feature towards the east side of the grid, north of the base line, largely corresponds to a zone of damp/marshy soils. The high conductivities recorded at the south east edge of the grid reflect the presence of wire fences. It is noteworthy that the EM31 is a single operator device offering continuous reading (ie measurements can proceed at walking pace) and hence conductivity mapping in this instance is clearly a more efficient technique than galvanic resistivity.

#### *Magnetometry*

The total field profiles in the north west corner of Test Area 2.1 reveal a well defined positive feature (16 nT) generally conforming to local strike (Figure 1 *mag*). The profile of Line 85 W was modelled (Figure 2 *mag*) and suggests a north west dipping (at c. 25°) horizon of susceptibility  $1.8 \times 10^{-3}$  SI units and thickness some 8 m, subcropping between approximately 30 N and 50 N. This may correspond to the dark red shale proved in borehole B3. Figure 1 *mag* shows the proved Hahnwiese Fault immediately south of the magnetic anomaly on Line 55 W; unfortunately it was not possible to extend the magnetic survey to the east of Line 50 W (due to the presence of various cultural features) to determine if the magnetic unit is terminated by faulting.

#### *Natural gamma surface mapping*

A zone of relatively high natural gamma activity outlined in the south west corner of the grid is thought to reflect clay/shale horizons (Figure 3 *gam*). The abrupt linear nature of the eastern edge of this zone is suggestive of faulting (with clay/shale abutting low activity clean sandstone) and close coincidence with the subsequently proved Hahnwiese Fault trace is demonstrated. It should be observed, however, that made ground was also proved by Trench 1 in this zone and if sufficiently areally extensive, such imported soils may also be responsible for the high natural gamma activity.

#### 4.8 Test Site 2.3

##### *GPR*

The variable penetration and resolution afforded by the 25, 50, and 100 MHz frequencies are clearly shown in Figure 21 *gpr*. Bearing in mind the variable depth scales used in these sections, a strong reflector (indicated as sandstone underlying shale) has been identified at a depth of 7 m with the 25 MHz frequency whereas the deepest penetration achieved with 100 MHz is some 3.5 m. The location of the projected Hahnwiese Fault on line 0 is 146m and all three frequencies display a well defined anomaly in this vicinity. As has been shown at other Test Areas, the 50 MHz frequency gives the best overall definition, and images a fault zone here dipping towards the southwest.

The character of the reflections at the three frequencies also show a distinct change about this point, reflecting the contrasting lithologies juxtaposed by the faulting, as proved by boreholes BK2.31 and BK2.32 (Figure 20). This is discussed further in the VLF section below. Figure 22 *gpr* illustrates the 50 MHz response on all three surveyed lines at this Test Site; the Hahnwiese Fault is again clearly defined on Line 20 S but less well so on Line 10 S. The contrasting reflector patterns to the north east of the fault plane occurring over a distance of just 20 m attest to complex layering and an apparent transposition of lithologies adjacent to the fault.

##### *VES*

The interpretations of VES made on either side of the Hahnwiese Fault on Line 0 (see Figure 11 *res*) largely reflect the lithological arrangement shown in Figure 20 and suggested by the GPR sections. Thus at 177 the shallow highly resistive ( $> 500$  ohm.m) unit correlates with the red conglomeratic sandstone while lower resistivity values ( $< 300$  ohm.m) at 110 suggest a thinner, less resistive sandstone. Both sites are underlain by shale (c 70 ohm.m) at about 6 m depth.

##### *RESCAN*

A single electrode grid was established here, centred on Line 0, (Figure 32 *res*) and half-Schlumberger array coverage was obtained between stations 135 W and 154 W. Figure 6 *res* shows the mapped apparent resistivity distributions for two AB spacings (3 m and 9 m). The rather monotonous pattern of intermediate apparent resistivities (150 ohm.m to 300 ohm.m) measured at the smaller AB spacing indicates the presence of a uniform thickness (c 1 m) of moderately resistive overburden. With increased AB separation (to 9 m, providing penetration in a homogeneous case of approximately 3 m) a well defined north-east trending conductive feature about 3 m wide is clearly defined. This feature, believed to represent the Hahnwiese Fault, traverses Line 0 between stations 143 W and 146 W and is thus in fairly close agreement with both the GPR- and VLF-R interpretations (see Figure 19). The zone of high apparent resistivity (with values in excess of 440 ohm.m) immediately south west of the fault represents the shallow, partly conglomeratic sandstone indicated by VES 2 (Figure 11 *res*) and subsequently proved by drilling (Figure 20). The apparent resistivity *distribution* along Line 0 is also in close agreement with that interpreted from VLF-R data (Figure 21 *vlf*) although the absolute observed values differ between the two techniques.



### VLF

Occam inversion was applied to three short profiles of VLF-R and VLF-Z measurements from Test Site 2.3. The VLF measurements consist of 11 VLF-R and VLF-Z measurements obtained at 5 m separation along each profile. The data were obtained using the Rugby transmitter (303<sup>0</sup>) operating at 16 kHz.

The low magnitude of the VLF-Z field (consistently less than 7%) together with the observed VLF-R data characteristics led Beamish (1994) to conclude that the VLF observations were consistent with a TM mode response. The VLF-R data along each profile were then inverted to provide the smooth (Occam) resistivity cross-sections shown in Figure 21 *vlf*.

The level of fit that can be achieved by automatic inversion is shown in Figure 22 *vlf* for Line 10 S. The diagram shows the observations (as symbols) and model results for two levels of misfit. The dashed line was obtained at an r.m.s. misfit of 1.0% and the continuous line at an r.m.s. misfit of 0.25%. All three cross-sections shown in Figure 21 *vlf* were obtained at an r.m.s. misfit of 0.25%.

The cross-sections contain some high wavenumber features which, particularly in the upper 10 m of the section, are likely to be "noise". Using the synthetic model results as control, a subsurface conductive zone, assumed to be fault-related, occurs on all three model sections. In the case of Line 20 S, the same (assumed) feature appears to lie too close to the edge of the profile to allow the same degree of resolution.

From the behaviour observed on all three sections, the upper surface of the conductive zone (<25 ohm.m) appears to lie in the depth range 2 m to 3 m. The dip of the zone (inferred from resistivity gradients) is estimated to lie between 45° (Line 0) and 60° (Line 10 S). There is evidence (Lines 10 S and 20 S) that the conductive feature extends to a considerable depth (at least 20 m to 30 m). The models also indicate that the at- and near-surface resistivities which abut the fault-zone are transposed between Lines 0 and 10 S. This implies that the strike of the fault is not linear and there are significant lateral variations in the configuration of the rock units mainly across the 10 m separating Lines 0 and 10 S.

### *Comparison of VLF-R, GPR and other geophysical results.*

Beamish et al. (1994) report a comparison of the above VLF-R results and coincident (GPR) sections. The coincident GPR (50 Mhz) sections along the three profiles are shown in Figure 22 *gpr*. The conversion from time to depth in the radar sections is based on a velocity of 0.07 m/ns. The projected location of the Hahnwiese Fault on Line 0 is 139 and the GPR section displays a strongly anomalous feature in this vicinity. The GPR section suggests a low angle (c 35°) fault plane dipping towards the south west at this location. The character of the reflections also show a distinct change about this point; to the south west the layering appears to dip and is rather complex whereas conditions to the north east seem far more uniform and possibly more conductive (as suggested by the more rapid signal attenuation). The location of the probable fault is clearly defined on Line 20 S (at about 152 m) and less well on Line 10 S. It is also clear that the indications of more complex layering (and resistive conditions) on the two southerly lines occurs to the north east of the fault. This is entirely in accord with the VLF-R results



shown previously.

It is clear that both VLF-R and GPR have detected an anomalous dipping zone in the vicinity of the projected fault plane. The geophysical indications are almost laterally coincident on Lines 0 and 10 S but appear to diverge along 20 S; this, however, may reflect the poorer resolution of the VLF-R inversion towards the end of the traverse. Both techniques reveal the presence of contrasting lithologies about the fault plane and the apparent transposition of the units over the 10 m separating Lines 0 and 10 S. On Line 0, VES interpretations suggest the presence of shallow resistive strata ( $> 500 \text{ ohm.m}$ ) to the south west and intermediate resistivities ( $< 300 \text{ ohm.m}$ ) to the north east. The VES, VLF-R and GPR results, together with observations at adjacent Test Sites suggest that on Line 0 a low porosity, coarse grained to conglomeratic sandstone/arkose is present to the south west of the fault and a fissile, finer grained sandstone occurs to the north east.

The apparent transposition of these units between Lines 0 and 10 S is not easy to explain given that the expected horizontal displacement of shallow dipping layers by a 60 m downthrow (as measured underground) is some 130 m. One possible explanation is that the fault we have detected does not suffer such a large throw at this site.

#### *Comparison of geophysical and drilling results (Line 0)*

Guided by the geophysical results two inclined boreholes BK2.31 and BK2.32 were drilled and cored at the locations on Line 0 shown in the survey map of Figure 19. The geological section inferred from the inclined drilling is summarised in Figure 20.

The two cored boreholes prove the presence of a fault zone, largely comprising "fat" clays, subcropping between 143 m and 146 m. A coarse grained (partly conglomeratic) sandstone was proved to the south west and a medium to fine grained sandstone with shaley intercalations to the north east, thus confirming the geophysical predictions. In Figure 20, an inferred fault zone indicated by the dashed lines is shown dipping to the south west at  $60^\circ$ .

Figure 23 *vlf* attempts to summarise the geophysical and borehole information obtained across Line 0. It should be noted that the inclined boreholes were not drilled in the plane of the geophysical sections and so a degree of geometrical skew is inevitable. The upper plot of Figure 21 *vlf* shows the GPR section (with vertical exaggeration of 2.3) and the position of the upper portion of the boreholes. The section extends to an estimated depth of 10 m. The lower plot shows the model resistivity section as an equal-area contoured image to emphasise the central low resistivity of  $13 \text{ ohm.m}$  to  $27 \text{ ohm.m}$ . This plot is true scale and extends to 25 m in depth. The plot shows the two inclined boreholes with bars denoting significant, along borehole (inclined depth) markers obtained from Figure 20.

For borehole BK2.31 the marker at 2.5 m denotes the base of the upper red sandstone. The second marker at 6.7 m denotes the termination of the red clay/shale sequence. For borehole BK2.32 the first marker at 8 m denotes the end of the upper red sandstone. The middle marker at 14.5 m denotes the boundary between a dark red shale and a deeper green/red shale. The middle marker also denotes the upper surface of the suggested fault trace in Figure 19. The

third marker is at 21 m and is used for referencing the deeper lithologies shown in the geological cross-section.

The information discussed above points to the overall complexity of the near surface rocks associated with the Hahnwiese Fault zone. The cores provide a great amount of detail particularly when compared with the "simple" images obtained from the surface geophysics. The surface geophysics responds to the first-order changes in material properties (dielectric in the case of GPR and resistivity in the case of VLF) and any second-order features are unlikely to be resolved. The geophysical images appear to represent a "useful summary" of the primary changes in rock properties associated with the faulting.

#### *Magnetometry*

Figures 3 *mag* and 4 *mag* show respectively the magnetic profiles and colour filled contours at this site. As at Test Site 2.1 there occurs a well defined generally south west trending positive anomaly of amplitude about 10 nT. In Figures 3 *mag* and 4 *mag* this feature is seen to be generally associated with the proved trace. In addition there occurs a general rise in magnetic field strength to the north of Line 20 S, this is highlighted in the contour presentation of Figure 4 *mag*. This strike-parallel (north east trending) belt of higher field strength can be modelled by a similar body to that described above (at Test Site 2.1), and at the present site it may correspond to the shallow horizon of dark red shale identified by borehole BK 2.32 (Figure 20). Within this belt the positive closure and continuation of minor positive features to the south is coincident with the fault trace and may represent some alteration/emplacement within the fracture-zone. However, it is not clear why the magnetic unit has apparently not suffered any significant lateral displacement about the presumed fault.

### **4.9 Hahnwald Traverse**

#### *GPR*

The GPR section for the Hahnwald track (Figure 23 *gpr*) provides an example of the distorting effect that trees (both their trunks and leaf canopy) can have on GPR data by re-reflecting upward transmitted EM energy from the unshielded antennae. It is possible that the roots of the trees also contribute to this effect. These distortions are evidenced as reflections in the GPR section but they have limited lateral extent (between 1 m and 3 m) and occur with a distinct, broken and slightly curved pattern and may thus be differentiated from lithological signal. Thus feature F1 is the typical characteristic fault response. The tight parabolic nature of feature F2 is indicative of diffraction above a point source and here it corresponds with a buried duct. Reflections of lateral extent greater than about 5 m seen in the GPR section below 100 nS may well represent the occurrence of interbedded shales (and the absence of the shallow resistive sandstone) (as suggested by VES) in the western part of the section.

#### *VES*

The VES at 100 indicates a high value of resistivity ( $> 1000 \text{ ohm.m}$ ) for the shallow hard sandstone exposed in the nearby disused quarry (Figures 12 *res* and 21). The VES at 30, to the west of the fault, shows no evidence of this highly resistive unit; the intermediate resistivities

proved here probably reflect a less compact/pure sandstone.

#### 4.10 Test Site 2.5

##### *GPR*

Three GPR traverses made here failed to detect signs of faulting. A GPR anomaly on Line 10 N tentatively ascribed to faulting in our Periodic Report (PRJ-D92, Figure 25) is now, in the light of increased GPR experience, believed to indicate a pipeline or infilled trench because of its hyperbolic shape. Overall, the initial suspicion remains that much of the area has been disturbed by man. Figure 24 *gpr* shows an example of the disruptive effect of a 2 m high wire mesh fence adjacent to the antennae; interference in the form of radio wave propagation is evident on all the traces from 2 onwards.

#### 4.11 Test Site 3.1

##### *GPR*

The clearest fault response is seen on Line 80W at 36 (Figure 25 *gpr*); similar responses are seen in the other GPR sections and when mapped in plan they correlate very closely with the projected fault trace (Figure 22). The average penetration here is 3 m; the strata appear to dip northwards.

In Figure 22 features B to H may indicate the en echelon disturbances commonly evidenced in Target Areas 1 and 2.

##### *VES*

The interpretation of the four electrical soundings completed at this site are shown in Figure 14 *res*. These confirm the presence of thin resistive cover towards the northern end of Lines 60 W and 80 W and the absence of this cover at 80 S on Line 80 W (as indicated by the dipole dipole data discussed below and shown in Figure 13 *res*). The apparent resistivity of the lithology subcropping in the northern part of Line 80 W exceeds 1000 ohm.m which is comparable to the value yielded by the outcropping violet sandstone/arkose at Test Site 2.1. The 60 Ohm.m layer included in the sounding interpretations is assumed to reflect the northward dipping low resistivity layer shown in the dipole-dipole models.

##### *Resistivity mapping*

The modelled dipole-dipole pseudo-sections for Line 80W are shown in Figure 13 *res*; this depicts a shallow conductive layer (20-60 Ohm.m) near the southern end of the traverse dipping at a low angle towards the north, beneath a thickening resistive zone; numerous high angle fractures in the resistive cover are suggested near stations 50 S, 46 S, 38 S and 22 S. The projected fault trace occurs at approximately station 36 S and could hence be coincident with the fracture suggested at station 38 S.

##### *RESCAN*

A single electrode grid was established, centred on Line 80 W, and half-Schlumberger array coverage was obtained between stations 34 S and 53 S (Figure 11 *rsc*). The apparent resistivity

distributions measured at three AB separations (3 m, 7 m and 11 m) are shown in Figure 12 *rsc*. These indicate the presence of a resistive unit largely parallel to the survey line (north-south) and lying immediately west of this. Such a feature was not observed with the other electrical surveys conducted at this site and we cannot explain this discrepancy at present. There is no anomaly associated with the projected fault location.

#### *Spontaneous potential*

There is no characteristic SP signature associated with the projected fault plane. It is noteworthy, however, that values in the south east quadrant of the grid are markedly more positive (with respect to the fixed reference point) than elsewhere and this may reflect a contrast in electrical properties of the subsurface material. Alternatively it may be due to a streaming potential phenomenon since the south east sector of the grid has the lowest elevation and substantial rainfall occurred throughout several days prior to the measurements.

#### *VLF*

VLF-R and VLF-Z data were obtained here using two transmitters: Rugby (16 kHz) with a transmitted E-field at N123E and Cutler-Maine (24 kHz) with a transmitted E-field at N85E. The azimuth separation of only  $38^\circ$  is not ideal. The data were acquired along 7 lines 20 m separate at a station interval of 5 m. The projected fault trace traverses the site in an east-west sense, approximately perpendicular to the VLF survey line positions. The VLF data obtained prove to be complex and difficult to interpret and require detailed assessments as described below.

Errors in recording VLF measurements are usually discussed in the manual associated with each instrument. Of prime concern is the strength of the received horizontal magnetic field (H) from a particular VLF transmitter. Both VLF-R and VLF-Z measurements are "normalised" by the H vector which is, in addition, recorded alongside the VLF parameters. When H falls below a certain threshold, the signal is regarded as "weak" and the measurement is abandoned as unreliable. For the VLF receiver used here the threshold H is of the order of 3 to 5 units. In both Test Sites 3.1 and 3.2, the H field amplitudes received were consistently above 20 units using the Rugby transmitter at 16 kHz and were consistently 5 to 7 units using the weaker Cutler-Maine transmitter at 24 kHz. Although "above threshold", the low signal amplitude of the 24 kHz data should be taken into account in the interpretation.

The data obtained at 16 kHz are assembled as contour maps in Figure 24 *vlf*. The upper two diagrams display the VLF-R data and the lower two diagrams display the VLF-Z data. Allowing for the line orientation of  $10^\circ$ , the 16 kHz E-field vector is orientated at  $103^\circ$  to each line; any east west structure should therefore respond in a TE mode (and thus provide a significant VLF-Z response).

The main anomaly observed in the VLF-R data is a resistive feature with a north north east trend which traverses the whole survey area. Assuming the lower resistivity values (50 to 100 ohm.m) represent background, the anomaly exceeds background by factors of 2 to 3. The same feature is observed to a far lesser extent in the phase data which show a slight perturbation to the lowest values ( $50^\circ$ ) above the feature. The main phase movement (to limiting phase values



of  $90^\circ$ ) is provided by an undefined feature occurring in the north east corner of the survey. This feature exerts an influence on all the survey parameters, and although only partially resolved, is likely to be cultural.

Allowing for the 5 m x 20 m data sampling of the contour maps, the resistive feature observed in the VLF-R data can be considered linear and a possible cultural origin may be considered. The resistive anomaly is responding in an approximate TM mode sense and is largely galvanic judging by the lack of phase perturbation. The resistivity anomaly responsible must be electromagnetically compact and near-surface.

The same feature is not observed in the VLF-Z data shown in the lower two frames of Figure 24 *vlf*. This again confirms a likely TM mode response for the VLF-R data. The VLF-Z data indicate east west resistivity structure responding in an approximate TE mode. The "zero-crossing" of the VLF-Z data is always important in delineating resistivity boundaries. This type of feature is observed in the real component but is absent in the imaginary component. The real component identifies a zone of low positive values in the south (a conductive feature dipping to the south?) with a zone of much stronger negative gradients to the north of the zero-crossing.

The corresponding data obtained at 24 kHz are shown in Figure 25 *vlf*. Allowing for the line orientation of  $10^\circ$ , the 24 kHz E-field vector is orientated at  $75^\circ$  to each line; again any east west structure will respond largely in a TE mode sense. In these data the cultural feature in the north east is more pronounced. The VLF-R data identify the same north north east trending linear resistive anomaly as previously.

The VLF-Z data of Figure 25 *vlf* show a modification from the previous case indicating a dependence on E-field azimuth. The broad pattern of negative real component and positive imaginary component is consistent with the previous case. Zero-crossing behaviour in the 24 kHz data is less consistent. It may be that small values of the Z/H ratio using the weaker 24 kHz H vector are more prone to error than the 16 kHz data.

In order to provide an example of invariant mapping applied to field VLF-R data, two invariant maps for the Test Site are shown in Figure 26 *vlf*. The upper two frames show the  $Z_{av}$  invariant average obtained using the 16 kHz and 24 kHz data while the lower two frames show the  $Z_{det}$  invariant. Clearly the two invariants provide equivalent results. The results in both apparent resistivity and phase confirm the previous identification of the main north north east trending anomaly and the undefined (cultural?) feature in the north east.

The VLF-R data appear dominated by the TM mode response discussed above. In this situation it appears that the VLF-Z data provide the most diagnostic information with regard to geological structure with a main east west component of strike. The maps of the VLF-Z data presented in Figures 24 *vlf* and 25 *vlf* summarise the complete range of values in order that the behaviour of the zero-crossing can be mapped. For spatially-compact anomalies which are completely traversed by a survey this method of presentation may be adequate. In cases of extensive structure, the regions in which field gradients change most rapidly may be useful in

mapping the most significant subsurface resistivity gradients.

Maps of the VLF-Z data at 16 kHz and 24 kHz are contoured in Figure 27 *vlf* using a banded contour scale. This method of presentation emphasises the main changes in spatial gradient in the mapped parameters. By reducing the mapping of the limiting values of each parameter the same zone of "most-intense" gradients can be seen to be mapped by all four parameters. This mutual consistency across components is clearly important to a successful geological interpretation. The band of gradients identified in Figure 27 *vlf* is considered to be an expression of an east trending, fault-related feature traversing the Test Site. Additional complexity (cultural effects) occurs towards the north east corner and may mask the correct geological trend towards this zone.

#### 4.12 Test Area 3.2

##### *GPR*

The increased average depth of penetration (6 m) both here and in the Extension area to the south east, probably result from the extensive cover of near surface resistive sandstone, particularly to the south of the main fault. There are no multiple reflectors at this site which may imply the lack of clay cover (which could generate "ringing") or alternatively could indicate that the sandstone is at a greater depth here. However, the presence of numerous well developed diffraction patterns suggest that the sandstone may be fractured into blocks varying in size from 0.5 m to 10 m within a zone averaging 50 m width. Figure 23 indicates the lateral extent of this zone of characteristic diffractions within which feature A represents the characteristic fault response. The major change in character of the GPR response associated with the mapped fault is well illustrated in the section of Line 100 E (Figure 26 *gpr*) where the fault, evidenced at 4 S, is apparently associated with downthrow of the sandstone to the north. The fault at this site differs from all other faults investigated during this programme by virtue of its association with the very prominent shear zone which terminates abruptly to the north (Feature B of Figure 23). The GPR responses comprising feature C are not readily correlated between adjacent traverses because, although indicative of local fracturing, they exhibit different dips of displacement.

In the GPR sections for the south-east quadrant of the Test Site, multiple, parallel, reflectors are seen and are ascribed to facies changes within the sandstone which here occurs at shallower depth than elsewhere across the grid. Alternatively such multiple reflectors may indicate the presence of a clay rich layer overlying the sandstone; this reflects and re-reflects energy from a single horizon within the sandstone to create the pattern of multiples, a process referred to as "ringing".

##### *VES*

The four soundings made on Line 0 largely confirm the resistivity distribution suggested by the modelled dipole-dipole response discussed below (Figure 16 *res*). At stations 30 N and 38 S the conductive (60 ohm.m) layer is overlain by about 3 m of moderately resistive (150 ohm.m to 380 ohm.m) lithologies while at 4 S there occurs a much more resistive (> 600 ohm.m) and significantly thicker (>5 m) lithology.

### *Resistivity mapping*

Observed and modelled dipole dipole resistivity distributions for Line 0 are shown in Figure 15 *res*. The modelled data indicates a central resistive ( $>500$  ohm.m) belt some 50 m broad flanked both north and south by more conductive lithologies (25 ohm.m to 40 ohm.m). The transition from high to low resistivity is abrupt and suggestive of faulted contacts. The pseudo-section also reveals a narrow steeply dipping low resistivity feature near 20 S that may be indicative of additional faulting. The models suggest that the high resistivity feature has limited depth extent.

### *RESCAN*

Three overlapping grids were established here, centred on Line 0 and providing half-Schlumberger type B coverage between 6 N and 33 S (Figure 13 *rsc*); the measured apparent resistivity distribution for an AB spacing of 3 m is shown in Figure 14 *rsc*. This indicates (in plan view) a similar resistivity structure to that observed with the dipole-dipole array (Figure 15 *res*). Faulting is suggested by the east trending conductive zones centred at approximately 15 S and 32 S where the dipole-dipole section indicates abrupt thinning of the cover of the resistive lithology (arkosic sandstone).

### *VLF*

The same two transmitters were employed as at Test Site 3.1. The data were obtained along 9 lines 25 m separate at a 5 m sampling interval. Again the projected fault trace traverses the area in an approximately east-west sense, approximately perpendicular to the VLF survey line positions. The data obtained at 16 kHz is assembled in Figure 28 *vlf*. Allowing for the line orientation of  $30^\circ$ , the 16 kHz E-field vector is orientated at  $93^\circ$  to each line. Clearly any east west structure should respond in a "true" TE mode in this case.

The apparent resistivity map is difficult to interpret since it displays very little in the way of spatially consistent trends. This is in direct contrast to the phase information which provides values  $<45^\circ$  to the north and values  $>45^\circ$  to the south. The anomaly responsible is, however, clearly not uniform in consistency of response across the entire survey area. The high "spot" phase value at 35 m on Line 75 W is interpreted as a measurement error.

The small magnitudes of both components of the VLF-Z data shown in Figure 28 *vlf* should be noted. The small Z/H magnitudes imply small resistivity contrasts. Despite their small magnitude both components show trends and perturbations which appear spatially consistent with the VLF-R phase information. The highly localised zone of negative values in the imaginary component (grid position 25 m) is particularly noteworthy.

The corresponding data obtained at 24 kHz are shown in Figure 29 *vlf*. Allowing for the line orientation of  $30^\circ$ , the 24 kHz data E-field vector is orientated at  $55^\circ$  to each line. Again the apparent resistivity map is difficult to interpret due to lack of clear trends while the phase information maps essentially the same anomaly pattern as the 16 kHz data. One way of reconciling the VLF-R features observed at both 16 kHz and 24 kHz is to assume Test Site 3.2 is a region of reduced fault-related resistivity contrasts. The apparent resistivity maps may be dominated by small-scale galvanic perturbations which have no significant effect on the phase



data. Whatever the cause, the apparent resistivity maps cannot be used for simple geological interpretation in this area.

Slightly larger magnitudes are observed in the VLF-Z fields at 24 kHz. In this case the perturbation pattern is more complex but similar features which are spatially consistent with the 16 kHz VLF-Z data and with both sets of mapped phase values can be observed. The east west feature at grid position 25 m is again emphasised in the data. It should also be noted that the E-field vector of  $55^\circ$  to the line position is less favourable to the mapping of east west components of structure across the area.

In the light of the above discussion, the most reliable indicators of resistivity gradients associated with east west fault-related features across the area are the phase of the VLF-R data together with the VLF-Z data obtained at 16 kHz which provides an "ideal" TE mode. This information is reassembled in Figure 30 *vlf*. The upper two frames of phase data (at 16 kHz and 24 kHz) have had spot errors removed and the individual real and imaginary components of the 16 kHz VLF-Z data, previously shown in Figure 28 *vlf*, have been converted to the magnitude and phase of the Z/H ratio. If  $Z_r$  represents the real component and  $Z_i$  represents the imaginary component then the magnitude ( $Z$ ) and phase ( $\Phi$ ) are determined from  $Z = (Z_r.Z_r + Z_i.Z_i)^{1/2}$  and  $\tan\Phi = Z_i/Z_r$ .

The anomaly patterns that are revealed in Figure 30 *vlf* are clearly not associated with simple and laterally continuous geological structure. The most continuous feature is identified in the VLF-Z phase map as an east west compact zone of maximum negative phase values. The western side of this zone (Lines 100 W to 25 E) is also associated with a significant east west trend in the phase maps. These combined features appear to map the "simplest" trend of resistivity gradients that may be fault-related. To the east of Line 25 E, the zone becomes more diffuse in both the phase maps and in VLF-Z magnitude implying a "break in continuity" of the subsurface resistivity distribution.

#### 4.13 Test Site 3.2 (EXT)

##### *GPR*

All the GPR sections exhibit the pattern of multiple, parallel reflectors seen in Figure 27 *gpr* (cf part of Test Site 3.1) and it is believed that the sandstone here is shallower than 2 m. It is relatively straightforward to correlate characteristic features between adjacent lines. The mapped (subsidiary) fault, evidenced by feature AX in Figure 23, is accompanied by the familiar en-echelon faults shown as features BX, CX, and DX.

#### 4.14 Magnetic susceptibility testing of typical rock types

A wide variety of sandstones were tested, comprising fine to coarse-grained and clean (well sorted) to dirty. Susceptibilities were always low, ranging between  $0.00 \times 10^{-3}$  SI units and  $0.10 \times 10^{-3}$  SI units, with the lowest values associated with the purest, coarse-grained stone. Brown and green shales yielded increased values (in the range  $0.20 \times 10^{-3}$  SI units to  $0.30 \times 10^{-3}$  SI units). The highest values were displayed by siderite-bearing shales (typically  $0.40 \times 10^{-3}$  SI



units but occasionally as high as  $2.3 \times 10^{-3}$  SI units).

## 5 CONCLUSIONS

### *GPR*

The GPR technique has been outstandingly successful in all three Target Areas. It has consistently located the projected fault zones and it is the only geophysical technique applied that has been able to map disturbances (that may be indicative of faulting) in an otherwise uniform lithology due to contrasting electrical properties resulting from variations of either moisture content and/or minor facies changes.

The most significant limiting factor for GPR penetration is the thickness of conductive clay present. At Test Sites 1.5 and 1.6 a shallow and thin (0.2 m) grey/green clay horizon limited penetration to about 3 m but characteristic signatures diagnostic of faulting were still observed beneath the clay within this limit. However, at Test Site 1.4, a 3.5 m thick, shallow layer of clay precluded any penetration thus masking the underlying sandstone.

The GPR frequency also affects penetration; typically penetration depths of 6 m were achieved using 50 MHz while the maximum depth achieved using 25 MHz was some 8 m. At several Test Sites the 25 MHz antennae gave only marginally increased penetration however and this benefit was more than countered by the reduced resolution at this frequency. However, the work at Test Sites 1.5 and 1.6 has shown the advantage of operating the 25 MHz antennae in a reconnaissance mode, yielding complementary data where the results from the 50 MHz/1000V transmitter combination alone have been inconclusive.

Transmitter power proved less significant regarding penetration. The difference in penetration using 400 V and 1000 V transmitters was found to be small, lying in the range 10% to 15%. Overall, the best results have been achieved with the combination of 50 MHz antennae and 1000 V transmitter.

Use of the 100 MHz antennae was limited to the early field work at Target Area 2 where this frequency was found inappropriate for the objectives of this study (mainly because of the reduced penetration depth). However, the enhanced resolution of reflectors afforded with the 100 MHz antennae can be helpful whereby diffractions due to shallow material broken into small fragments - eg a crumbly sandstone; a coarse gravel; cobbles and boulders of assorted dimensions - are defined in the GPR section as a series of characteristic parabolic reflectors, thus aiding the identification of these units.

The Hahnwald and Stangewald traverses show that trees (including their trunks, leaf canopy and roots) can give strong GPR reflections and caution is required when interpreting affected GPR sections. This disruptive effect may often be recognised by a symmetrical "cross-hatch" pattern of short length reflectors. Metallic fences also generate reflections that may be confused with lithological responses. Considerable radio frequency (RF) interference was experienced at many Test Sites. While the precise nature of this interference was not identified, it can probably be ascribed to transmissions from the numerous aerial masts that surround the Target

## Areas.

Trench and borehole control shows that the (average) velocity of 0.07 m/nS determined by numerous CMP measurements and used for the conversion of the two-way travel time to depth is realistic. The vertical velocity values derived from these CMP stacks do not reflect the true velocity of electromagnetic propagation through any individual layer in the ground. This stacked or root mean square (RMS) velocity is an integrated or effective velocity encompassing all of the velocities of the strata within the depth penetrated.

It has not been practicable to produce synthetic radar sections over modelled faults. This is due to the lack of sufficient information required to construct a series of models. In particular, values of dielectric constant and attenuation constant are required for each successive geological layer that comprises the model. In addition, the selection of appropriate velocities is not easy given the problems associated with CMP velocity analysis. Hence, in common with the majority of GPR surveys, the current interpretations have been restricted to the recognition of both discrete reflections (eg the fault signature) or characteristic patterns of reflectors that can be associated with specific lithologies.

The importance of close coupling between the antennae and the ground is apparent from the present work. However, the wet, muddy conditions experienced at Test Site 2.1 and Test Site 3.2 did not cause the anticipated marked reduction in penetration. Dry ground conditions are preferred but where tall grass or crops are encountered in these drier times they will need to be cut down to ensure close contact between the antennae and the surface. The surface condition presented by minor roads with a thin cover of tarmac (eg Weisbacher Strasse, Test Site 2.1) yielded excellent GPR sections.

### *Galvanic resistivity*

VES have provided valuable control data for the GPR technique, indicating likely depths of strong resistivity contrasts while also guiding the identification of discrete lithologies recognised on radar sections. VES have also located faults indirectly by identifying shallow along-strike resistivity contrasts (reflecting the juxtaposition of, for instance, sandstone and shale about the fault plane) but this technique is not appropriate for routine fault detection.

Resistivity traversing using a wide variety of electrode arrays has successfully located fault zones by mapping abrupt dislocations of resistive horizons (sandstones). The gradient array proved most efficient since a grid of observations can be achieved with a fixed pair of current electrodes (ie only two moving electrodes are required). It is noteworthy, however, that the much more rapid non-contacting ground conductivity measurements provided essentially the same information. We found no clear indications of a direct fault response (arising from conductive fault gouge etc). The implication is that where conductive shales occur on either side of the fault plane there exists insufficient resistivity contrast; where sandstone and shales are juxtaposed, any such fault response is dwarfed by the contact anomaly.

Dipole-dipole data, although very slow to acquire, can be inverted to yield a resistivity/depth distribution. In the present work we have identified dipping horizons that correlate quite

closely with GPR sections. We have also noted narrow steeply dipping conductive features within an otherwise resistive lithology (sandstone) and these may well be direct indications of faulting.

### *RESCAN*

High resolution RESCAN surveying at selected sites has mapped 3-D resistivity contrasts that reflect faulting; these contrasts have been imaged with a resolution of 1 m, even at those sites overlain by thick overburden (<3 m).

Typically the faults have been detected indirectly, by mapping the contact between strongly contrasting resistivities reflecting the juxtaposition of sandstone and shale about the fault plane. Occasionally faults have been detected directly, as narrow, linear conductive features spatially coincident with fault anomalies detected with complementary techniques (principally GPR); examples are Test Sites 1.2 and 3.2.

3-D inversion of the resistivity data has shown that the four half-Schlumberger styles (equivalent to pole-dipole arrays) can be integrated to provide a more generalised surveying method. The 3-electrode array data should be treated independently and not summed (as is the convention) since this process 'averages out' any anomalous response.

We have collected a large volume of data defining in great detail the resistivity structure of faults; further modelling (incorporating the available ground truth) is required to fully elucidate the geological nature of these faults.

The focussed surface array appears to provide enhanced penetration and lateral resolution compared with a non-focussed array. Normalised balance current measurements have yielded an additional parameter which has been shown to be characteristic of faulting.

The focussed surface array appears to give optimum results where the resistivity contrast is shallow (as at Test Site 2.1). In such cases, analysis of variation in synthetic focussing balance factors allows accurate location of sub-surface lateral discontinuities, thus enhancing the detection and delineation of faults.

Focussed apparent resistivity traverses do not always correspond directly to the resistivity variations of the underlying earth. In addition, the coverage possible with this technique (for any one electrode grid) is more limited than with the half-Schlumberger style. For these reasons the technique should not be used as an independent survey method but rather to provide extra constraints on more conventional RESCAN data sets.

To date RESCAN has been of particular value at the post reconnaissance stage, following the approximate location of faulting with other techniques. However, since the completion of the fieldwork reported here, further development of the RESCAN system has led to the use of larger electrode grids controlled by robust and compact portable instrumentation and hence the system can now also be used in the reconnaissance mode. Advantages of the RESCAN system include the ability to survey with a variety of electrode arrays and styles, the availability of

both focussed and un-focussed measurements, and the opportunity for rapid processing and evaluation of the resulting data using modelling and inversion processes.

#### *Spontaneous potential*

We observed no fault response with this technique.

#### *VLF*

Extensive numerical modelling studies conducted as part of this Project indicate that conductive bodies that are not optimally aligned with respect to the VLF transmitter will still yield measurable and interpretable anomalies. However, complete resolution of the resistivity structure requires that measurements are made using two frequencies with the azimuthal separation of their transmitters ideally approaching  $90^{\circ}$ . Such "invariant mapping" simplifies interpretation and can yield correct strike and body extent information. It is also suggested that both VLF-R and VLF-Z data are always collected.

VLF-R and VLF-Z data was acquired in Target Area 3, employing two transmitters with azimuthal separation of only  $38^{\circ}$ . At Test Site 3.1 the R data, in particular the apparent resistivity, at both frequencies outlined a resistive north north east trending feature identified by all the electrical techniques applied here. On the basis of the VLF data this is assumed to have a possible cultural origin. However the in-phase Z-field data (in particular at 16 kHz which had optimal TE mode orientation) mapped an east west gradient traversing the grid, generally corresponding to the trend of the projected fault. The use of a banded coloured contour scale enhanced this response. The interpretation at Test Site 3.2 is more confused and here the most reliable indicators of resistivity gradients associated with fault related features are the phase of the VLF-R data together with the VLF-Z data at 16 kHz (whose azimuth again provides an ideal TE mode). These combined features appear to map the simplest trend of resistivity gradients that may be fault related.

Occam inversion of a limited profile of VLF-R measurements yielded a resistivity cross section of minimum structure. This imaged a dipping conductive feature that correlated closely with a coincident GPR section and was subsequently proved by inclined drilling to accurately reflect a fault zone.

Karous-Hjelt filtering of in-phase VLF-Z data over a cultural conductor indicated its shallow location and high electrical conductivity.

VLF equipment is highly portable and its use is cost effective. It is possible for two operators to cover several kilometres of traverse in one day, taking measurements at 5 m intervals of both R and Z from two transmitters. The depth of investigation is largely governed by the ground resistivity, and ranges between about 17 m (10 ohm.m) to 54 m (100 ohm.m). In the present study VLF has been shown to be effective in mapping faults and general geology; it is also largely complementary to the GPR technique.



*Ground conductivity (EM31):*

Sandstone and shale were readily differentiated by characteristic apparent conductivity values observed with both horizontal and vertical coil orientations. The deeper penetrating horizontal coil mode has usually yielded the most definitive profile, suggesting that the observed anomalies do not reflect merely superficial features.

Where both galvanic resistivity and ground conductivity measurements have been made the two resulting data sets are largely complementary. Thus faults have also been located indirectly by ground conductivity observations, which technique is logistically far superior.

Conductivity profiles at Test Site 1.2 reveal a series of abrupt steps, largely consistent from line to line. The inferred lithological contacts have been correlated with both GPR and RESCAN data while a hypothetical geological section involving repetitive faulting of a sandstone/shale sequence has been presented.

The conductivity data has also been of value in identifying lithologies observed in GPR sections. Predictably this technique was least successful in areas of thick (> 4 m) conductive overburden.

*Seismic methods*

Conventional seismic refraction proved the presence of a shallow undulating refracting layer of intermediate velocity but gave no indication of faulting.

Limited azimuthal seismic experiments gave weak indications of fracture trends consistent with those anticipated at two test sites.

The tomograms indicate a fairly uniform increase of velocity with depth, consistent with reduced weathering and increased compaction. At Test Site 1.2 the lateral impersistence of lithologies shown by the geological logs (and suggested by the natural gamma logs) of adjacent boreholes is largely confirmed by the tomograms. Unequivocal direct evidence for faulting was seldom seen. Only one of the three tomograms at Test Site 1.2 exhibited a marked low velocity zone that could reflect faulting.

The seismic techniques are labour intensive (at both the data acquisition and interpretation stages) while seismic tomography is also invasive. In view of this, and in the light of the disappointing results obtained, the seismic techniques are not thought appropriate for routine fault detection.

*Magnetometry*

Several weakly magnetic horizons were identified. Susceptibility measurements on local borehole cores suggest that these may be siderite bearing shales. We were not able to map an abrupt termination of any magnetic horizon due largely to cultural clutter. At one Test Site we found limited evidence of epithermal magnetic mineralisation within a fault zone. Since magnetometry is such a rapid technique its application to fault location should be investigated further.

*Natural gamma logging and mapping*

Natural gamma logs were run to identify geophysical units with which to constrain the seismic tomography inversions. Sandstones and shales are clearly distinguished on the natural gamma logs, with the shale yielding some 50% extra counts. Gamma logging of four boreholes separated by about only 20 m proved the lateral variability of the facies at Test Site 1.2. Fining-downward sequences have been identified, as have clay-rich thin horizons which are not recorded in the geological log.

A novel application of natural gamma logging to observe surface profiles has yielded data largely complementary to both galvanic resistivity and ground conductivity mapping (ie we have identified the abrupt termination of a shale (high counts) against a sandstone (low counts) and hence indirectly detected a fault). It is clearly important that the soils and weathered material are in situ ie. they are derived from the underlying parent rock. Since gamma radiation is shielded by about a 1 m thickness of clay, the technique will have very limited application. There was no indication of increased counts over the fault zone reflecting the upward migration of radon gas.

**ACKNOWLEDGEMENTS**

We acknowledge the continuous support (both technical and logistical) provided by Saarberg and in particular by Dr Dietmar Clasen, the overall Project Leader. At BGS, Mr A C Cripps digitised the natural gamma data and the geological logs of Saarberg's boreholes, and Mr G E Rippin participated in the initial fieldwork during May 1992. We are grateful to the European Coal and Steel Community who, through the Commission of the European Communities, has provided generous funding for this Project.

## 7 REFERENCES

- Apparao A. and Roy A. (1971) Resistivity model experiments, 2. *Geoexploration* 9(4), 195205.
- Apparao A., Roy A. and Mallick K. (1969) Resistivity model experiments. *Geoexploration* 7(1), 4554.
- Arcone, S.A. 1979. Resolution studies in airborne resistivity surveying with VLF. *Geophysics*, 44, 937-946.
- Barker, R.D., 1992. A simple algorithm for electrical imaging of the sub-surface. *First Break*, vol 12, no. 2, 53-62.
- Beamish, D. 1994. Two-dimensional regularised inversion of VLF data. *J. Appl. Geophysics.*, 32, 357-374.
- Berdichevsky, M.N. and Dmitriev, V.I., 1976. Basic principles of interpretation of magnetotelluric curves. In : Adam (Editor), *Geoelectric and Geothermal Studies*. Akad. Kaido, Budapest, KAPG Geophys. Monogr., pp. 165-221.
- Beres, M. and Haeni, F. P., 1991. Application of Ground Penetrating Radar methods in hydrogeological studies. *Ground Water*, v. 29, (3) pp. 375-386.
- Busby, J. P., 1995. Calibration and Interpretation of Ground Penetrating Radar from around Sellafield. Technical Report no. WN/95/28C, British Geological Survey
- Constable, S.C., Parker, R.L. and Constable, C.G., 1987. Occam's inversion : a practical algorithm for generating smooth models from EM sounding data. *Geophysics*, 92: 289-300.
- Davis, J. L. and Annan, A. P., 1989. Ground Penetrating Radar for high-resolution mapping of soil and rock stratigraphy. *Geophysical Prospecting*, v. 37, pp. 531-551.
- deGroot-Hedlin, C.M. and Constable, S.C., 1990. Occam's inversion to generate smooth, two-dimensional models from magnetotelluric data. *Geophysics*, 55: 1613-1624.
- Doll, H.G., 1951. The Laterolog: A new resistivity logging method with electrodes using automatic focussing system. *Transactions American Inst. Mining & Metall. Engineers*, vol. 198, 17-32.

- Ellis D. V. (1987) Well Logging for Earth Scientists. Elsevier, New York.
- Fischer, G., Le Quang, B.V. and Muller, I., 1983. VLF ground surveys, a powerful tool for the study of shallow two-dimensional structures. *Geophys. Prosp.*, 31: 977-991.
- Gianzero S. (1981) The mathematics of resistivity and induction logging. *The Technical Review* 29(1), 432.
- Guerin, R., Tabbagh, A., Bendritter, Y. and Andrieux, P., 1994. Invariants for correcting field polarisation effect in MT-VLF resistivity mapping. *J. Appl. Geophys.*, 32, 375-383.
- Jackson, P.D., 1981. Focussed electrical resistivity arrays: some theoretical and practical experiments. *Geophysical Prospecting*, Vol. 29, pp. 601-626.
- Jackson P.D., Hallam, J.R., Raines M.G., Rainsbury M.G., Greenwood P.G., & Busby J.P. 1991. Reconnaissance geophysics to locate major faults in clays. CEC Nuclear Science and Technology, Directorate-General Science, Research and Development, Topical Report EUR 13203, ECSC-EEC-EAEC, Brussels, Luxembourg, 1991.
- Jackson P.D., Lovell M. A., Harvey P.K., Ball J.K., Williams C., Ashu P., Flint R., Meldrum P.I., Reece G., Zheng G. 1992. Electrical Resistivity Core Imaging:- theoretical and practical experiments as an aid to reservoir characterisation. SPWLA 33rd Annual Logging Symposium, June 14-17, Oklahoma USA., Vol II, Paper VV
- Jackson P.D., Gunn D.A., Meldrum P.I., and Flint R.C., 1994. 3D data processing and tomographic presentation. British Geological Survey, Technical report WN/94/20
- Jackson P.D., Ogilvy R.D., Meldrum P.I., Hallam J.R., and Szymanski J.E. 1995. A borehole resistivity array for single hole and cross hole tomographic imaging. Paper D038. 57th EAGE Conference and Technical Exhibition, Glasgow, Scotland, 29 May - 2 June 1995.
- Jackson P. D. (1976) Comments on "New results in resistivity well logging". *Geophysical Prospecting* 24.
- Jackson P. D., Meldrum P. I. and Williams G. M. (1989) Principles of a computer controlled multi-electrode resistivity system for automatic data acquisition. Technical Report WE/89/32, British Geological Survey, Keyworth, Nottingham.



- Karous, M and Hjelt, S E. 1983 Linear filtering of VLF dip-angle measurements. *Geophysical Prospecting* Vol 31, pp782-794
- Mackie, R.L., Madden, T.R. and Wannamaker, P.E., 1993. Three-dimensional magnetotelluric modeling using difference equations - theory and comparisons to integral equation solutions. *Geophysics*, 58, 215-226.
- McNeill, J.D. and Labson, V.F., 1991. Geological mapping using VLF radio fields. In : M.N. Nabighian (Editor), *Electromagnetic Methods in Applied Geophysics*. Soc. Explor. Geophys., 2(B), pp. 521-640.
- Meldrum P. I., Jackson P. D., Williams C. G., Gunn D. A. and Flint R. C. (1994) Automatic data acquisition for 3D resistivity surveys. Technical Report WN/94/19, British Geological Survey, Keyworth, Nottingham.
- Moran J. H. and Chemali R. (1985) Focused resistivity logs. In *Developments in Geophysical Exploration Methods* (ed. A. A. Fitch), pp. 225-260. Applied Science Publishers Ltd., London.
- Ogilvy, R D and Lee, A C. 1991 Interpretation of VLF-EM in-phase data using current density pseudosections. *Geophysical Prospecting*, Vol 39, pp567-580
- Parra J. O. and Owen T. E. (1990) Synthetically focused resistivity for detecting deep targets. In *Geotechnical and Environmental Geophysics* (ed. S. H. Ward), pp. 3750. Society of Exploration Geophysicists, Tulsa, OK.
- Pedley, R C 1992 VLFCDI-user manual. A programme for current density imaging of VLF-EM survey data. British Geological Survey publication.
- Ramirez, A. L., Dailey, W. D., Owen, E. W., 1991. High frequency electromagnetic and Electrical Resistance tomography of the Savannah River Integrated Demonstration Project, UCRL-LR-105199, p. 6, Lawrence Livermore Lab. (1991).
- Roy A. (1982) Focused resistivity logs. In *Developments in Geophysical Exploration Methods*3 (ed. A. A. Fitch), Chapter 3. Applied Science Publishers Ltd., London.
- Sasaki, Y., 1992. Resolution of resistivity tomography inferred from numerical simulation. *Geophysical Prospecting*, 40, 453-463
- Sasaki, Y., 1994. 3-D resistivity inversion using the finite element method.. *Geophysics*, 59, No. 11, 453-463
- Sasaki, Y., 1994. 3-D resistivity inversion using the finite element method.. *Geophysics*, 59, No. 11, 453-463

Spies, B.R., 1989. Depth of investigation in electromagnetic sounding methods. *Geophysics*, 54, 872-888.

Williams, C.G. (1996) Assessment of electrical resistivity properties through development of three-dimensional numerical models. Ph.D. thesis, University of Leicester

## APPENDIX A

### Listing of Project Reports and other publications

#### Periodic Reports:

Peart, R J, Raines, M G and Rippin, G E. **1992 Project Periodic Report (January to June 1992)**. British Geological Survey Project Note PN 92/20.

Greenwood, P G and Peart, R J. **1993 Project Periodic Report (July to December 1992)**. British Geological Survey Technical Report WN/93/02C.

Greenwood, P G, Jackson, P D, Meldrum, P I, Peart, R J and Raines, M G. **1994 Project Periodic Report (July to December 1993)**. British Geological Survey Technical Report WN/94/02.

Greenwood, P G, Peart R J and Raines, M G. **1994 Project Periodic Report (January to June 1994)**. British Geological Survey Technical Report WN/94/13.

Greenwood, P G, Peart R J and Meldrum, P I. **1995 Project Periodic Report (July to December 1994)**. British Geological Survey Technical Report WN/95/7.

Flint, R, Greenwood, P G, Jackson, P D and Peart, R J. **1995 Project Periodic Report (January to June 1995)**. British Geological Survey Technical Report WN/95/22.

#### Other internal reports:

Beamish, D. 1993 **Two-dimensional inversion of VLF-EM data**. British Geological Survey Technical Report WN/93/30.

Beamish, D, Flint, R C, Greenwood, P G, Jackson P D, Meldrum, P I, Peart, R J, Raines, M G and Williams, C. **1995 Methods for the recognition of geological weakness zones and other surface discontinuities caused by underground mining in Carboniferous terrain. Final Report**. British Geological Survey Technical Report WN/95/37

Greenwood, P G. **1994 Comments on the Ground Probing Radar surveys completed by DFA (Chemnitz) and BGS during 1993**. British Geological Survey Project Note 94/13.

Meldrum, P I and Williams, C. **1994 Report on field work in the Saarland, Germany (15 September to 24 September 1994)**. British Geological Survey Project Note 94/XX.

Pear, R J. 1994      **Notes on the Project Technical Meeting held in Germany, February 22-24, 1994.** BGS internal paper.

**External publications:**

Beamish, D. 1994      **Two-dimensional, regularised inversion of VLF data.** Journal of Applied Geophysics, Vol 32 p 357-374

Beamish, D, Clasen, D, Greenwood, P G and Pear, R J. 1994 **Novel regularised inversion of VLF (R) data and coincident radar sections over a probable fault affecting Carboniferous sedimentary rocks in the Saar Region, Germany.** Paper presented at the 30th Annual Conference of the Engineering Group of the Geological Society, Liege, Belgium, 1994 (Modern Geophysics in Engineering Geology) and published in Conference Preprints, p 185-194.



## APPENDIX B

### RESCAN focussed surface array

#### *Background*

A novel resistivity technique involving a 'dual laterolog' focussed surface array proposed by Jackson (1981) was implemented and tested in the field. The focused field measurement is based on a numerical algorithm which is described briefly below and in more detail by Williams (1996). This algorithm is also used by a numerical model developed to simulate the measurement and is based on the work of Doll (1951).

The resistivity observations used to create focussed measurements were made with the BGS RESCAN resistivity equipment. This is a computer-controlled multi-electrode resistivity measurement system (Meldrum et al., 1994; Jackson et al., 1989). In view of its lack of mobility and large number of measurements required, it was envisaged that RESCAN would provide relatively high-resolution characterisation of the electrical properties at a specific location of interest rather than being used as a prospecting tool. It was hoped that this would aid the other electrical methods employed routinely by providing a more detailed picture of the electrical properties of a fault zone, thus giving an insight into the electrical characteristics associated with the faulting (or perhaps due to other associated processes such as alteration, weathering or fluid-flow).

RESCAN is capable of making four-electrode measurements, where one electrode introduces an artificially generated current into the earth, one electrode provides a current return, and the remaining pair of electrodes measure a potential difference. Electrodes in a grid may be addressed independently allowing a variety of different arrays to be employed. The work described here is concerned specifically with the development and testing of the focussed surface array resistivity measurement.

The focussed surface array forms part of the suite of different survey styles carried out by the RESCAN measurement system. It is essentially a pole-pole type measurement in which a single electrode injects current (measuring) thereby creating a voltage field which is measured using a single potential electrode; both the current return and the potential reference electrodes are located some distance away from the survey area, effectively at infinity. The focussed array proposed by Jackson (1981) requires four independently controlled focussing currents in addition to the measurement current; these are used to constrain the volume of earth through which the measurement current flows. The RESCAN system cannot simultaneously emit multiple currents but the focussed measurement may be reconstructed from a set of conventional pole-pole measurements. This is the principal difference between the focussed measurement and the other survey styles used by RESCAN.

The principles used in making focussed downhole logging measurements may be developed for surface measurements. Figure 15 *rsc* illustrates the operation of a typical focussed surface array schematically. The central electrode is the sensing electrode, the current from which is used to make resistivity measurements; this is surrounded by focussing electrodes which emit current

with the intention of constraining the region of earth through which the measurement (sensing) current flows.

At the surface of the earth, the maximum focussing effect would be achieved by using a ring-shaped electrode surrounding the measurement electrode, as is the case with the microlaterolog. However, Jackson (1981) showed that four orthogonal electrodes in a cross shape around the measurement electrode can still achieve a significant focussing effect. Such an arrangement has an additional benefit since the focussing currents may be adjusted independently of each other, allowing compensation for lateral inhomogeneities in the electrical properties of the earth (as illustrated in the lower part of Figure 15 *rsc*). An implementation of a focussed surface array proposed by Jackson (1981), similar in principle to that of the Laterolog 7 borehole tool (Doll, 1951), but using four focussing electrodes, is illustrated in Figure 16 *rsc*. In this arrangement, P is the measurement current electrode, while N, S, E and W are the focussing current electrodes. The current electrodes simultaneously inject current into the ground (which returns to a common electrode located effectively at infinity), and the magnitudes of the focussing currents are adjusted automatically to achieve focussing. Active focussing of the array is achieved by monitoring the measurements across four pairs of potential electrodes N1 and N2, S1 and S2, E1 and E2 and W1 and W2.

The focussing conditions for the array shown in Figure 16 *rsc* are:

$$V_{N1} = V_{N2}, V_{S1} = V_{S2}, V_{E1} = V_{E2} \text{ and } V_{W1} = V_{W2}.$$

Focussed electric borehole tools operate by continually adjusting the magnitude of the focussing currents using electronic feedback loops to ensure that the tool remains correctly focussed. These principles have been applied to downhole arrays (Apparao et al., 1969; Apparao and Roy, 1971) but are not used extensively in surface geophysics.

The RESCAN system can only supply current to one electrode at any one time. In order to produce a focussed measurement, a hybrid approach using physical measurements in conjunction with numerical processing techniques is taken, using ideas originally developed for numerical simulations of focussed borehole tools. In such models, focussing current magnitudes are determined theoretically rather than by simulating the electronic balancing process, which is less expensive in terms of time.

The principles involved in simulating focussed electric borehole tools have been described in detail by Gianzero (1981) and Moran and Chemali (1985). Jackson (1981) investigates the response of various focussed surface arrays, including a combination of two surface laterologs at 90° to each other which is equivalent to the focussed surface array being described in the present work. Parra and Owen (1990) develop a methodology to create focussed surface measurements from readings taken with a single line of current electrodes. Theoretical approaches involve the combination of electric potentials, computed for individual current electrodes, in a weighted sum to derive the potential that would exist if all current electrodes were simultaneously emitting current. The relative weighting of the contributions from individual electrodes are calculated so that focussing conditions are satisfied.

### *Focussed measurement technique*

A synthetically focussed measurement may be 'reconstructed' from sets of independent RESCAN measurements, made for the measurement electrode and the four focussing electrodes, by numerically balancing and superimposing the readings. For each of the five current positions, the electric potential is measured at the eight potential electrodes, resulting in 40 measurements which are then combined to produce a focussed measurement.

In summary, a focussed measurement is obtained as follows (see Figure 16 *rsc*):

1. With the current source located at N (and current sink at infinity), measure the electric potential at the eight potential electrodes ( $N_1, N_2, S_1, S_2, E_1, E_2, W_1$ , and  $W_2$ ). Calculate the corresponding transfer impedances  $Z_{NN1}, Z_{NN2}, Z_{NS1}, Z_{NS2}, Z_{NE1}, Z_{NE2}, Z_{NW1}$  and  $Z_{NW2}$ ;
2. Repeat (1) for current sources located at S, E, W and P;
3. Substitute the transfer impedance values obtained into a set of simultaneous equations and solve for  $I_N, I_S, I_E$  and  $I_W$ ;
4. Derive the focussed potential distribution for the eight potential electrodes;
5. Use the focussed electric potentials to give eight focussed apparent resistivity measurements, one for each potential electrode.

### *Measurement objectives*

In common with other electrical measurements, the focussed measurement will respond to changes in resistivity of the earth. In the present work contrasts in the resistivity of shale and sandstone layers could be readily identified, allowing a fault line to be located where these two rock types lie on either side of the fault.

There are two potential advantages of using a focussed measurement, which stem from the fact that the region of measurement is constrained by the focussing:

1. Enhanced depth of investigation in comparison with equivalent unfocussed measurements allowing, for example, penetration of overburden to investigate deeper structures;
2. Accurate lateral placement of conductive/resistive boundaries. Conventional measurements are often distorted by preferential current flow in conductive zones, since standard methods (before inversion) do not take account of such effects when attributing an apparent resistivity measurement to a region of earth. The focussed measurement can reduce distortion effects at the measurement (rather than interpretation) stage, by forcing the measurement region to remain below the measurement electrode, as illustrated in Figure 15 *rsc*.

*Fieldwork and data acquisition*

The focussed array was run in addition to other measurement styles using the standard RESCAN electrode grid. The focussed measurements were made at only five sites due to lack of time; the results from two of these sites (Test Site 1.2 and Test Site 2.1) are outlined in the main body of this report.

Within the standard RESCAN grid of electrodes, a focussing star with a 6 m span was used, allowing a total of 14 measurement positions along the longer axis of the grid and 5 positions in the perpendicular direction (Figure 17 *rsc*).

In the field, surveys were arranged as a series of 14 measurements along the long axis of the electrode array. A series of parallel surveys were conducted, enabling a two-dimensional array of focussed measurements to be built up. Measurements were made on overlapping adjacent grids in the attempt to cover a wider lateral range (Figure 18 *rsc*).

*Measurement data*

The raw data observed with the RESCAN equipment consist of a series of resistance measurements which are then given coordinates using data in a position file. The resistance measurements are converted to focussed apparent resistivities using the technique summarised below. The balance factors required to satisfy the focussing conditions are also output for reference. For comparison, defocussed and conventional pole-pole apparent resistivity values have also been calculated from the same data sets.

The focussed apparent resistivity is calculated using:

$$r_a = (V/I_p) \cdot 2\pi / \{ Bf (1/r_N + 1/r_S + 1/r_E + 1/r_W) + 1/r_P \}$$

where  $V$  is a superimposed electric potential calculated by combining the voltages due to current sources adjusted in magnitude to satisfy the focussing conditions.  $Bf$  is an analytically determined balance factor which is the relative proportion of the focussing currents to the measurement current required to balance the focussed array for a homogeneous half-space. The defocussed apparent resistivity is calculated with the formula:

$$r_a = (V_a/I_p) \cdot 2\pi / \{ Bf (1/r_N + 1/r_S + 1/r_E + 1/r_W) + 1/r_P \}$$

where  $V_a$  is the superimposed electric potential calculated using current sources of fixed magnitude equal to those required for a homogeneous half-space (i.e. focussing conditions will not in general be satisfied, except in the case of a uniform, homogeneous earth). The pole-pole apparent resistivity is calculated using:

$$r_a = (V_p/I_p) \cdot 2\pi r_p$$

where  $V_p$  is the electric potential due to the measurement electrode only (i.e. the focussing electrodes are effectively inactive).



### *Focussed apparent resistivity traverses*

The results of focussed apparent resistivity traverses are presented for Test Sites 1.2 and 2.1. The focussed and pole-pole data are plotted for each line and four apparent resistivity curves (W, E, S, and N) have been superimposed, corresponding to calculations using the potential on electrodes W2, E2, S2 and N2 respectively. The vertical scale (apparent resistivity) is logarithmic. The horizontal scale refers to the relative position of the focussing star in the electrode array (as illustrated in Figure 17 *rsc*).

Also presented are the calculated balance factors required for focussing; a plot of the normalised balance factors for the orthogonal current electrode pairs W-E and N-S is also included to aid analysis of balance variation. The normalised balance factor for the W-electrode,  $Bf'_w$  is calculated using

$$Bf'_w = \log (Bf_w / Bf_h)$$

where  $Bf_w$  is the (non-normalised) W-balance factor and  $Bf_h$  is the analytically calculated balance factor for a homogeneous medium. Similarly for the E, S and N balance factors. The normalised balance factors express the relative increase or decrease of a balance current relative to the homogeneous balance factor,  $Bf_h$ . A normalised balance factor of 2 would correspond to a reduction to 50% or an increase to 200% of  $Bf_h$ .

### *Interpretative methodology*

Interpretation of the electrical properties in the region of the electrode array initially centres on the focussed apparent resistivity traverses; however, important information can also be gained by inspecting the magnitude of the focussing currents, or in the case of the synthetically focussed array, the calculated balance factors required to focus the array.

Numerical models of the response of the focussed array to specific simplified geological models have been used to provide a quantitative guide to the response to key situations. It is noted that as a further step, models may be 'fine-tuned' to simulate specific field situations in order to confirm any inferences made, but the models considered in this work have not been extended beyond a low level of complexity.

### *Apparent resistivity data*

The primary data source is the focussed apparent resistivity traverse. Changes in apparent resistivity can be used to infer changes in the electrical properties of the earth which can be caused by faulting (e.g. where two rock types of differing resistivity lie alongside each other). More detailed information may be derived by analysis of the relationship between the focussed, de-focussed and pole-pole traverses (although in practice the de-focussed measurement was not found to be of much assistance in data interpretation). The focussed measurement is taken to be indicative of the resistivity of a cylindrical region directly below the central, sensing electrode (see above), due to the constraining effect of the balance currents. The focussed current may also penetrate further into the ground than in a conventional unfocussed measurement, giving an indication of electrical resistivity at greater depth.

### *Focussing balance factors*

The variation of the focussing currents (calculated balance factors) is often more sensitive to changes in resistivity than the focussed apparent resistivity measurement itself. When one side of the array is in a conductive medium, current will tend to flow preferentially into that medium, and the focussing current on the conductive side will increase to counteract this effect. Conversely, the focussing current required on the resistive side is reduced since the sensing current already has a tendency to flow away from that region. In this way, lateral inhomogeneities such as faults are expected to disturb the balance currents as was illustrated schematically in Figure 15 *rsc*.

### *Numerical modelling*

This section describes the development of the three-dimensional finite difference model to analyse both apparent resistivity profiles and variations in balance current magnitudes in order to aid and enhance interpretation.

### *Finite difference grid*

The choice of the extent and resolution of a finite difference grid is compromised by requirements for accuracy and speed. In the case of the focussed array, the most crucial region of the model is in the immediate vicinity of the current injection point, since the electric potentials calculated here are used to generate the focussed measurement. Unfortunately, this is also the most difficult area to model accurately because the electric potential varies most rapidly around a current source or sink.

The region to be modelled in the case of a surface measurement is a semi-infinite half-space, since the earth may be considered to extend to infinity laterally and with depth (at the measurement scales considered here), and is bounded above by air which is electrically insulating. In practice, the electric potential approaches zero a finite distance away from the current source, and the model grid need only extend to the region where the voltage and its derivative (the potential gradient) are to all intents and purposes zero. This is checked by inspecting the values of voltage at the boundary. As an additional check, the difference between applying conductive (Dirichlet) or resistive (Neumann) boundaries should be minimal in the region of interest.

By following the guide-lines outlined above, a rectangular mesh was used to represent a 160 m by 80 m by 80 m region of earth, with mesh spacing (and therefore model resolution) down to 0.5 m in the region of the focussed array measurement electrodes (Figure 19 *rsc*). Away from the source region, the grid is expanded since the potential gradient changes much less rapidly between nodes. It was not found to be necessary to place as large a number of nodes at the sink location as at the source.

### *Simulated Focused measurements*

The numerical model works on a similar principle to the method of focussing described above. For a given resistivity model, the electric potential due to a single current source (with the sink located effectively at infinity) is calculated. This process is repeated five times for each of the source locations in the focussing star; the five calculated electric potentials are then combined

in a weighted sum so that the focussing conditions are satisfied. The combined electric potential may then be used to derive a focussed apparent resistivity. The modelled electric potential is used to create data files with an identical format to the measurement file generated by RESCAN in the field. This allows the similarity between real and modelled focussed measurements to be exploited, since the modelled focussed apparent resistivity can be generated using the same program code as that used for the field data processing.

Typical models simulated surveys where the focussed array is moved along an 8 m line. The grid employed allowed steps of 0.5 m to be simulated (compared with 1 m in the field, since this was the fixed electrode spacing used in all the surveys concerned with focussed measurements).

British Geological Survey  
Engineering Geology and Geophysics Group

Technical Report WN/95/37

**Methods for the recognition of geological  
weakness zones and other surface  
discontinuities caused by underground  
mining in Carboniferous terrain**

**Final Report. Part 2: Figures**

D Beamish, R C Flint, P G Greenwood, P D Jackson  
P I Meldrum, R J Peart, M G Raines and C Williams

The **Final Report** comprises the volumes - **Part 1: Text**  
**Part 2: Figures**

*Bibliographic Reference :*

Beamish, D, Flint R C, Greenwood, P G, Jackson, P D  
Meldrum, P I, Peart, R J, Raines, M G, Williams, C  
Methods for the recognition of geological weakness  
zones and other surface discontinuities caused by  
underground mining in Carboniferous terrain.  
*British geological Survey.*  
*Technical Report, WN/95/37*

Research funded in part by the  
Commission of the European  
Communities European Coal and  
Steel Community.  
EC Contract No. 7220/AF/136

British Geological Survey, Keyworth, Nottingham, NG12 5GG

©NERC copyright 1996





This report has been generated from a scanned image of the document with any blank pages removed at the scanning stage.

Please be aware that the pagination and scales of diagrams or maps in the resulting report may not appear as in the original

## List of Figures

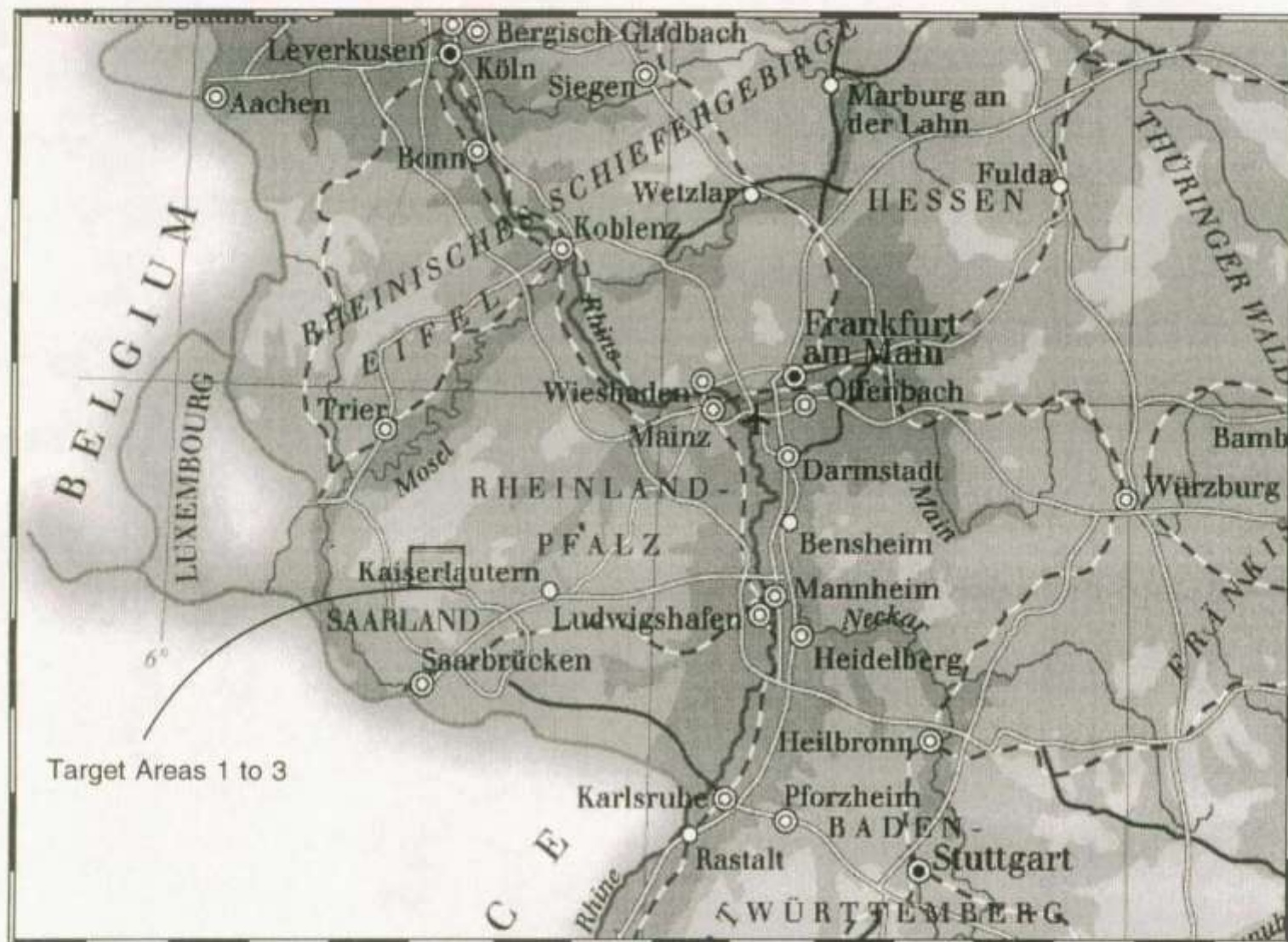
Figure 1a.	Location map for Saarland.
Figure 1b.	Location map for Target Areas 1 to 3.
Figure 2.	Location map for Test Sites 1.1 to 1.6.
Figure 3.	Location map for Test Sites 2.1 to 2.5.
Figure 4.	Location map for Test Sites 3.1 to 3.2 and 3.2 (Ext).
Figure 1 <i>res.</i>	Electrode arrays used for the resistivity surveys.
Figure 2 <i>rsc.</i>	The 2D electrode grid used for RESCAN surveys, and the definition of the 'half Schlumberger' mapping technique.
Figure 1 <i>vlf.</i>	Depth of investigation of VLF EM fields.
Figure 2 <i>vlf.</i>	Azimuths of VLF transmitters relative to Test Areas 1, 2, and 3.
Figure 3 <i>vlf.</i>	Synthetic VLF model for non-dipping target.
Figure 4 <i>vlf.</i>	Synthetic VLF model for dipping target.
Figure 5 <i>vlf.</i>	Principal components of the VLF field.
Figure 6 <i>vlf.</i>	VLF modelling. Model 1: apparent resistivity and phase.
Figure 7 <i>vlf.</i>	VLF modelling. Model 1: Z field ratios.
Figure 8 <i>vlf.</i>	VLF modelling. Model 2: apparent resistivity and phase, $E_y$ polarisation.
Figure 9 <i>vlf.</i>	VLF modelling. Model 2: Z field ratios, $E_y$ polarisation.
Figure 10 <i>vlf.</i>	VLF modelling. Model 2: apparent resistivity and phase, $E_x$ polarisation.
Figure 11 <i>vlf.</i>	VLF modelling. Model 3: Z field ratios, $E_x$ polarisation.
Figure 12 <i>vlf.</i>	VLF modelling. Model 3: apparent resistivity and phase, $E_y$ polarisation.
Figure 13 <i>vlf.</i>	VLF modelling. Model 3: Z field ratios, $E_y$ polarisation.
Figure 14 <i>vlf.</i>	VLF modelling. Model 3: apparent resistivity and phase, $E_x$ polarisation.
Figure 15 <i>vlf.</i>	VLF modelling. Model 3: Z field ratios, $E_x$ polarisation.
Figure 16 <i>vlf.</i>	VLF modelling. Model 1: use of rotational invariants.
Figure 17 <i>vlf.</i>	VLF modelling. Model 2: use of rotational invariants.
Figure 18 <i>vlf.</i>	VLF modelling. Model 3: use of rotational invariants.
Figure 6.	Test Site 1.1. Geological section: boreholes BK1.11, BK1.12, and BK1.13.
Figure 1 <i>gpr.</i>	Test Site 1.1. GPR profiles for line 0. 25 MHz antennae.
Figure 2 <i>gpr.</i>	Test Site 1.1. GPR profiles for line 0. 50 MHz antennae.
Figure 5.	Test Site 1.1. Geophysical grid, borehole locations, and interpretation.
Figure 2 <i>res.</i>	Test Site 1.1. Interpretation of VES 1, 2, and 3.
Figure 9 <i>rsc.</i>	Test Site 1.1. Plan (partial) of site showing location of RESCAN survey grid.
Figure 29 <i>rsc.</i>	Test Site 1.2. Plan (partial) of site showing location of RESCAN grid.
Figure 10 <i>rsc.</i>	Test Site 1.1. Apparent resistivity data, showing projected position of the fault.
Figure 19 <i>vlf.</i>	Test Site 1.1. Line 10S. Karous-Hjelt filtering of VLF M-field response over cultural feature.
Figure 3 <i>gpr.</i>	Test Site 1.2. GPR profiles for line 20S. 25 MHz antennae.
Figure 4 <i>gpr.</i>	Test Site 1.2. GPR profiles for line 20S. 50 MHz antennae.
Figure 7.	Test Site 1.2. Geophysical grid, borehole locations, and interpretation.
Figure 8.	Test Site 1.2. Geological section: boreholes BK1.21, BK1.22, BK1.23 and BK1.24.
Figure 5 <i>gpr.</i>	Test Site 1.2. GPR profiles for line 20N. 25 MHz antennae.
Figure 6 <i>gpr.</i>	Test Site 1.2. GPR profiles for line 20N. 50 MHz antennae.
Figure 3 <i>res.</i>	Test Site 1.2. Interpretation of VES 1, 2, and 3.

Figure 7 <i>rsc.</i>	Test Site 1.2. RESCAN apparent resistivity maps for three overlapping sections.
Figure 27 <i>rsc.</i>	Test Site 1.2. Grids a, b, and c. Apparent resistivity traverse
Figure 28 <i>rsc.</i>	Test Site 1.2. Grids a, b, and c. Focussing balance factors.
Figure 1 <i>em.</i>	Test Site 1.2. Horizontal and vertical dipole conductivity contours.
Figure 2 <i>em.</i>	Test site 1.2. Composite horizontal and vertical dipole conductivity and GPR section for line 0.
Figure 3 <i>em.</i>	Test Site 1.2. Composite horizontal and vertical dipole conductivity and GPR section for line 20S.
Figure 4 <i>em.</i>	Test Site 1.2. Composite horizontal and vertical dipole conductivity and GPR section for line 60S and possible geological section.
Figure 5 <i>em.</i>	Test Site 1.2. Composite horizontal and vertical dipole conductivity and GPR section for line 20N and proven geology.
Figure 6 <i>em.</i>	Test Site 1.2. Composite of conductivity profiles and Rescan images of part of line 20N.
Figure 1 <i>sei.</i>	Test Sites 1.2 and 1.4. Plots of horizontal velocity versus depth.
Figure 2a,b <i>sei.</i>	Test Site 1.2. Setup BK1.24/1.21. Hydrophone data. (a) Raypath coverage. (b) Straight ray, 10% anisotropy correction.
Figure 1 <i>gam.</i>	Test Site 1.2. Natural gamma logs for boreholes BK1.21 to BK1.24.
Figure 4 <i>res.</i>	Test Site 1.3. Interpretation of VES 1, and 2.
Figure 9.	Test Site 1.4. Geophysical grid, borehole locations, and interpretation.
Figure 7 <i>gpr.</i>	Test Site 1.4. GPR profile for line 30S. 50 MHz antennae.
Figure 10.	Test Site 1.4. Geological section: boreholes BK1.43, BK1.44
Figure 30 <i>rsc.</i>	Test Site 1.4. Plan (partial) of site showing location of RESCAN grid.
Figure 31 <i>rsc.</i>	Test Site 2.1. Plan (partial) of site showing location of RESCAN grid.
Figure 8 <i>rsc.</i>	Test Site 1.4. Resistivity imaging using pole-dipole 'half Schlumberger' measurements made under computer control. Pseudo and 1D corrected XZ sections show different responses over a fault identified by GPR.
Figure 7 <i>em.</i>	Test Site 1.4. Composite horizontal and vertical dipole conductivity and GPR section for line 30S.
Figure 2 <i>gam.</i>	Test Site 1.4. Natural gamma logs for boreholes BK1.43 to BK1.44.
Figure 11.	Test Sites 1.5 and 1.6. Geophysical grid, trench locations, and interpretation.
Figure 8 <i>gpr.</i>	Test Site 1.5. GPR profile for line 10S. 25 MHz antennae.
Figure 9 <i>gpr.</i>	Test Site 1.5. GPR profile for line 10S. 50 MHz antennae.
Figure 12.	Test Site 1.5. Trenches 1, 2, and 3, line 10S.
Figure 10 <i>gpr.</i>	Test Site 1.5. GPR profile for line 10S (eastern end). 50 MHz antennae.
Figure 11 <i>gpr.</i>	Test Site 1.5. GPR profile for line 0. 25 MHz antennae.
Figure 13.	Test Site 1.5. Trench 4, line 0.
Figure 5 <i>res.</i>	Test Site 1.5. Interpretation of VES 1, and 2.
Figure 12 <i>gpr.</i>	Test Site 1.6. GPR profile for line 0. 25 MHz antennae.
Figure 13 <i>gpr.</i>	Test Site 1.6. GPR profile for line 0. 50 MHz antennae.
Figure 14.	Test Site 1.6. Trenches 5 and 6, line 10S.
Figure 14 <i>gpr.</i>	Test Site 1.6. GPR profile for line 20S. 25 MHz antennae.
Figure 15 <i>gpr.</i>	Test Site 1.6. GPR profile for line 40S and line 20N (Test Site 1.5). 25 Mhz antennae.
Figure 16 <i>gpr.</i>	Test Site 1.6. GPR profile for line 40S and line 20N (Test Site 1.5). 50 MHz antennae.



- Figure 15. Test Site 2.1. Geophysical grid, trench and borehole locations, and interpretation. May 1992 survey.
- Figure 16. Test Site 2.1. Geophysical grid, trench and borehole locations, and interpretation. December 1992 survey.
- Figure 17. Test Site 2.1. Exploratory trenches T1, T1a, and T2.
- Figure 17 *gpr*. Test Site 2.1. GPR profile for line 16S. 50 MHz antennae.
- Figure 18 *gpr*. Test Site 2.1. GPR profile for line 0. 50 MHz antennae.
- Figure 19 *gpr*. Test Site 2.1. GPR profile for line 30N. 50 MHz antennae.
- Figure 20 *gpr*. Test Site 2.1. GPR profile for line ROAD. 50 MHz antennae.
- Figure 18. Test Site 2.1. Geological section: boreholes B1, B2, B3.
- Figure 6 *res*. Test Site 2.1. Interpretation of VES 1, 2, and 3.
- Figure 7 *res*. Test Site 2.1. Schlumberger array resistivity contours.
- Figure 8 *res*. Test Site 2.1. Gradient array resistivity contours.
- Figure 9 *res*. Test Site 2.1. Gradient array resistivity profiles (logarithmic scale).
- Figure 10 *res*. Test Site 2.1. Gradient array detail over proven fault trace.
- Figure 3 *rsc*. Test Site 2.1. Half Schlumberger apparent resistivity maps for AB=3m.
- Figure 1 *rsc*. Test Site 2.1. Geological sections constrained by boreholes B1 and B2 and Trench T1.
- Figure 4 *rsc*. Test Site 2.1. Variable response from different depths of investigation (proportional to AB).
- Figure 5 *rsc*. Test Site 2.1. Smooth inversion of resistivity data illustrating the 3D nature of the geological structure.
- Figure 20 *rsc*. Apparent resistivity traverses.
- Figure 21 *rsc*. Test Site 2.1. Line 7. Focussed balance factors.
- Figure 22 *rsc*. Test Site 2.1. Line 7. Normalised W-E balance factors.
- Figure 23 *rsc*. Idealised model of a vertical face.
- Figure 24 *rsc*. Vertical interface model results, Focussed balance factors.
- Figure 25 *rsc*. Vertical interface model results, Normalised W-E balance factors.
- Figure 26 *rsc*. Test Site 2.1. Inferred surface location of fault trace.
- Figure 20 *vlf*. Test Site 2.1. VLF R-field (Interuran data) profiles and proved fault trace.
- Figure 8 *em*. Test Site 2.1. Apparent conductivity contours (EM31 horizontal dipole).
- Figure 1 *mag*. Test Site 2.1. Total field magnetic profiles.
- Figure 2 *mag*. Test Site 2.1. Magnetic model line 85W.
- Figure 3 *gam*. Test Site 2.1. Natural gamma surface mapping.
- Figure 21 *gpr*. Test Site 2.3. GPR profile for line 0. Comparison of 25, 50, and 100 MHz antennae frequencies.
- Figure 20. Test Site 2.3. Geological section: boreholes BK2.31 and BK2.32.
- Figure 22 *gpr*. Test Site 2.3. GPR profiles for lines 0, 10S, and 20S. 50 MHz antennae.
- Figure 11 *res*. Test Site 2.3. Interpretation of VES 1, and 2.
- Figure 32 *rsc*. Test Site 2.3. Plan (partial) of site showing location of RESCAN grid.
- Figure 6 *rsc*. Test Site 2.3. Apparent resistivity maps for two depths of investigation.
- Figure 21 *vlf*. Test Site 2.3. Modelled resistivity cross sections for lines 0, 10S, and 20S.
- Figure 22 *vlf*. Test Site 2.3. Occam inversion: levels of fit of models to observed data.
- Figure 19. Test Site 2.3. Geophysical grid, borehole locations, and interpretation.
- Figure 23 *vlf*. Test Site 2.3. Coincident GPR and VLF resistivity cross sections for line 10S.
- Figure 3 *mag*. Test Site 2.3. Total field magnetic profiles.

Figure 4 <i>mag</i> .	Test Site 2.3. Total field magnetic contours.
Figure 21.	Test Site Hahnwald. Hahnwald traverse and interpretation.
Figure 23 <i>gpr</i> .	Test Site Hahnwald. GPR profile for line Hahnwald.
Figure 12 <i>res</i> .	Hahnwald track. Interpretation of VES 1, and 2.
Figure 24 <i>gpr</i> .	Test Site 2.5. GPR profile for line Fence.
Figure 25 <i>gpr</i> .	Test Site 3.1. GPR profile for line 80W. 50 MHz antennae.
Figure 22.	Test Site 3.1. Geophysical grid and interpretation.
Figure 14 <i>res</i> .	Test Site 3.1. Interpretation of VES 1, 2, 3, and 4.
Figure 13 <i>res</i> .	Test Site 3.1. Line 80W. Dipole-dipole resistivity data.
Figure 11 <i>rsc</i> .	Test Site 3.1. Plan (partial) of site showing location of RESCAN survey grid.
Figure 13 <i>rsc</i> .	Test Site 3.2. Plan (partial) of site showing location of RESCAN survey grid.
Figure 12 <i>rsc</i> .	Test Site 3.1. Apparent resistivity data, showing projected position of the fault.
Figure 24 <i>vlf</i> .	Test Site 3.1. VLF-R and VLF-Z field data for 16 kHz transmitter.
Figure 25 <i>vlf</i> .	Test Site 3.1. VLF-R and VLF-Z field data for 24 kHz transmitter.
Figure 26 <i>vlf</i> .	Test Site 3.1. Invariant mapping: 16 kHz and 24 kHz transmitters.
Figure 27 <i>vlf</i> .	Test Site 3.1. VLF-Z field data using banded contour scale.
Figure 23.	Test Sites 3.2 and 3.2 (Ext). Geophysical grid and interpretation.
Figure 26 <i>gpr</i> .	Test Site 3.2. GPR profile for line 100E. 50 MHz antennae.
Figure 16 <i>res</i> .	Test Site 3.2. Interpretation of VES 1, 2, 3, and 4.
Figure 15 <i>res</i> .	Test Site 3.2. Line 0. Dipole-dipole resistivity data.
Figure 14 <i>rsc</i> .	Test Site 3.2. RESCAN apparent resistivity maps for three overlapping sections.
Figure 28 <i>vlf</i> .	Test Site 3.2. VLF-R and VLF-Z field data for 16 kHz transmitter.
Figure 29 <i>vlf</i> .	Test Site 3.2. VLF-R and VLF-Z field data for 24 kHz transmitter.
Figure 30 <i>vlf</i> .	Test Site 3.2. VLF-R (phase) for 16 and 24 kHz transmitters and VLF-Z
Figure 27 <i>gpr</i> .	Test Site 3.2 (Ext). GPR profile for line 50EX. 50 MHz antennae. (converted magnitude and phase) for 16 kHz transmitter.
Figure 15 <i>rsc</i> .	Focussed currents over a conductive/resistive boundary (schematic).
Figure 16 <i>rsc</i> .	Electrode configuration (schematic) for a 'double laterolog' focussed array proposed by Jackson (1981).
Figure 17 <i>rsc</i> .	RESCAN electrode grid and focussed array positions.
Figure 18 <i>rsc</i> .	Adjacent grids.
Figure 19 <i>rsc</i> .	Model grid used in simulations of the focussed array.



After Dorling Kindersley Multimedia (1995)

Figure 1a. Location map for Saarland.



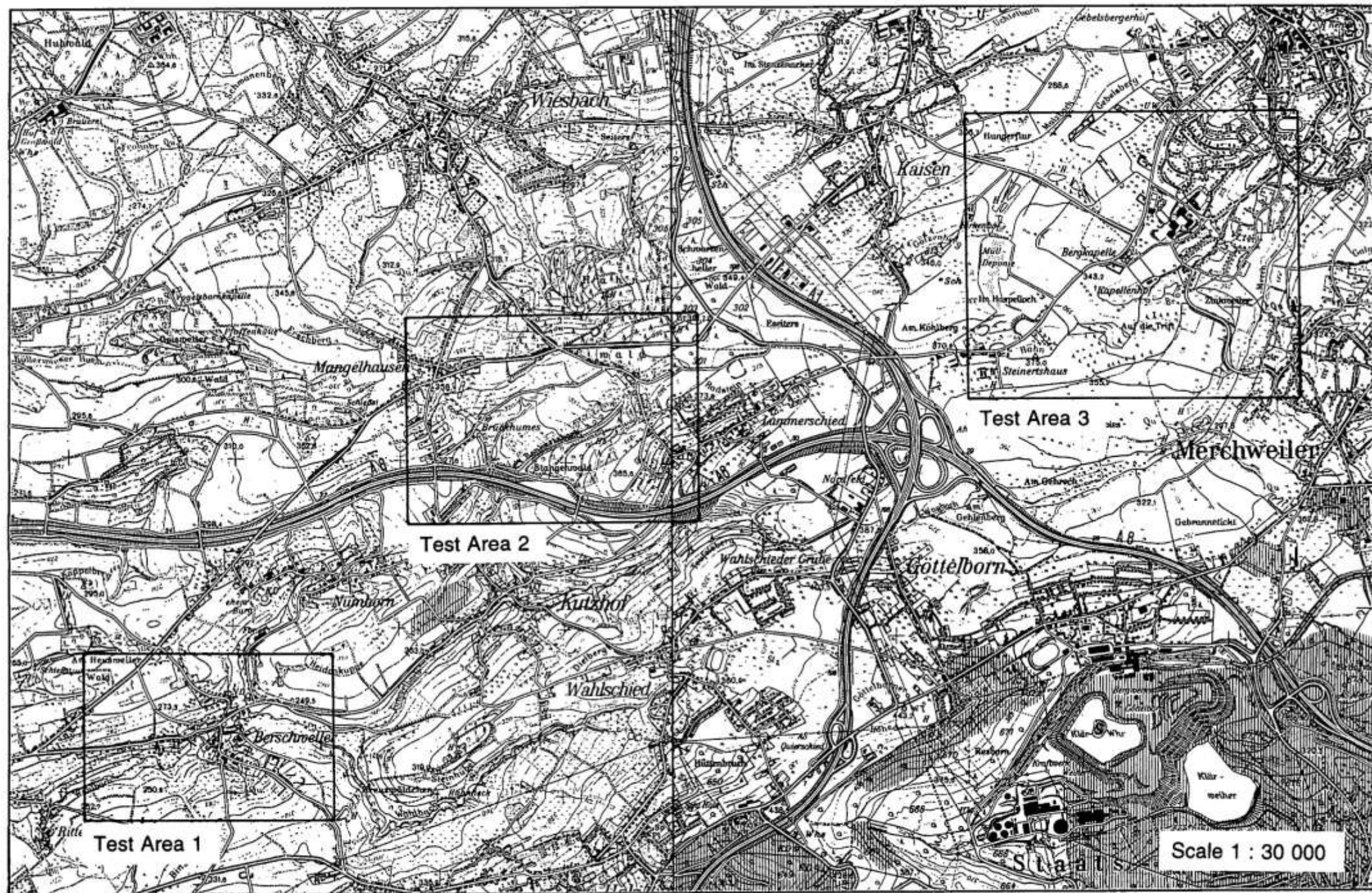


Figure 1b. Location map for Target Areas 1 to 3.



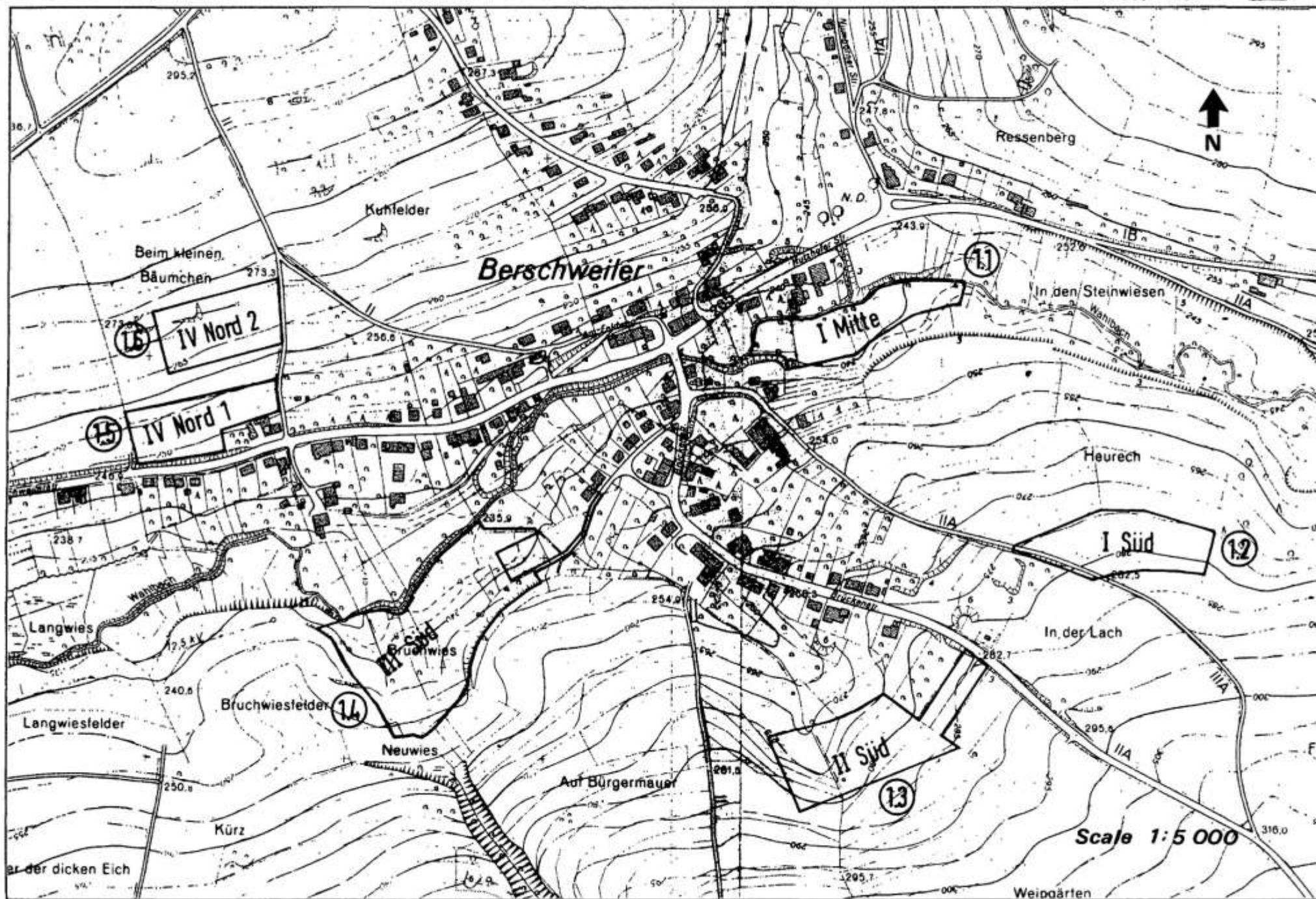


Figure 2. Location map for Test Sites 1.1 to 1.6.

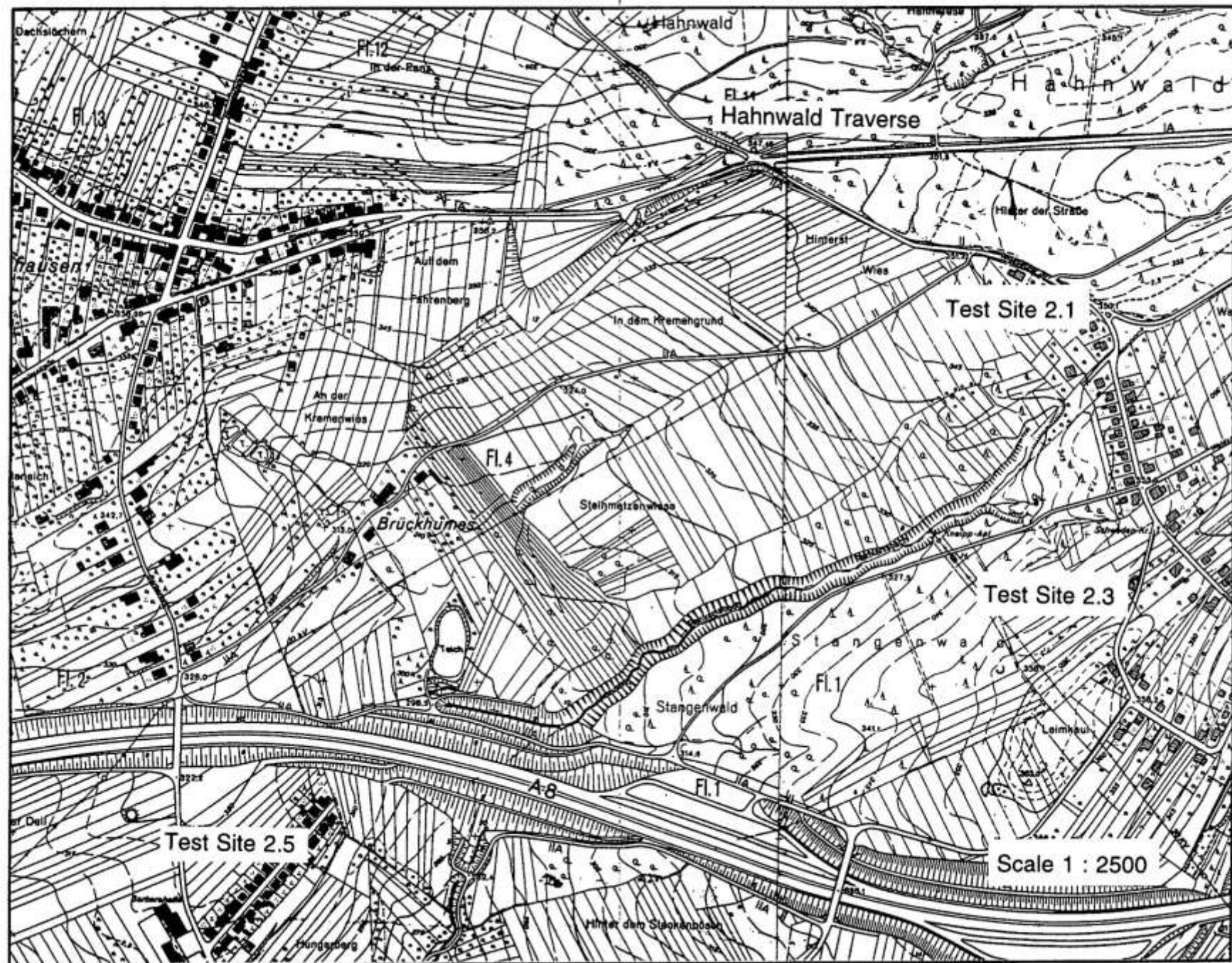


Figure 3. Location map for Test Sites 2.1 to 2.5.



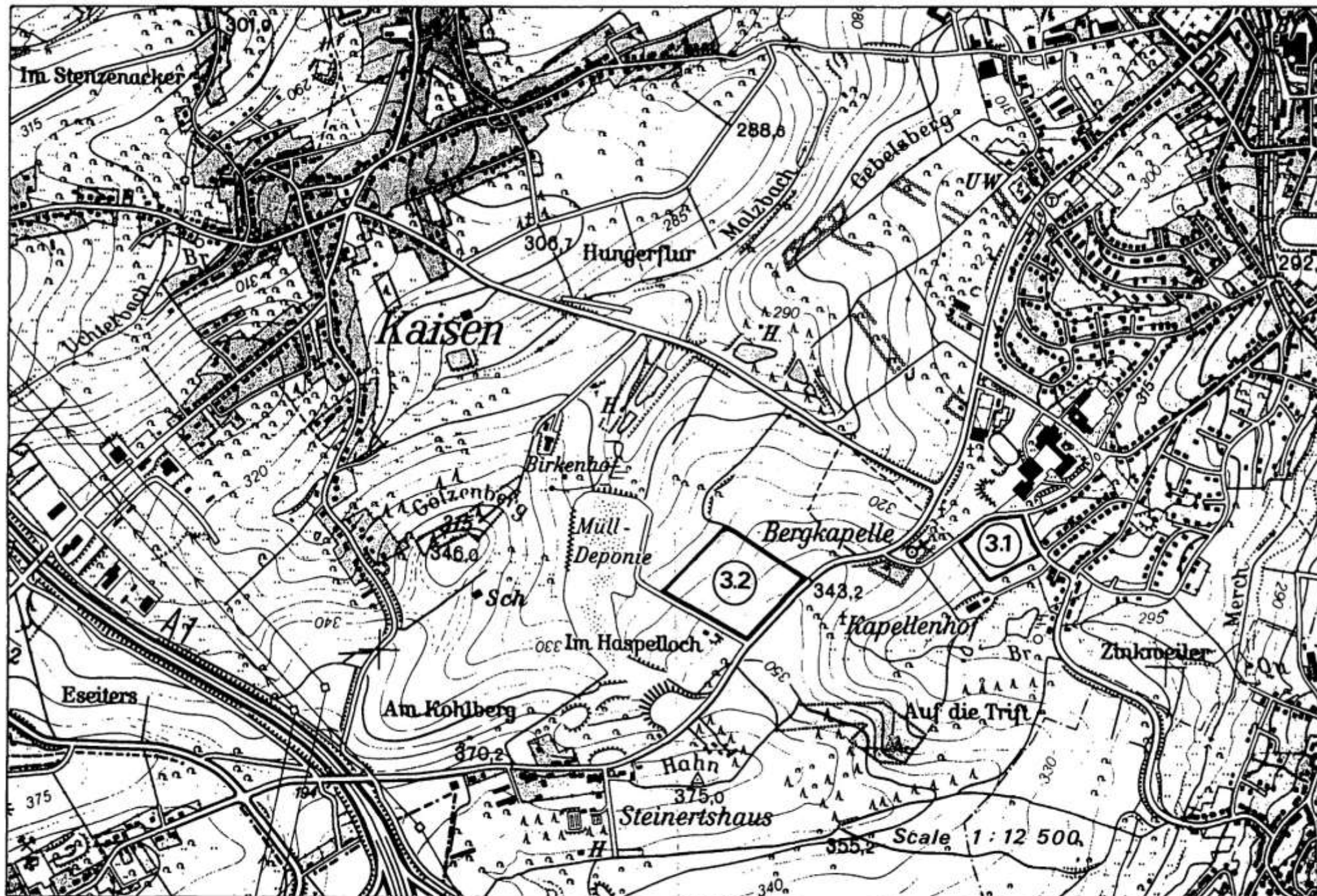
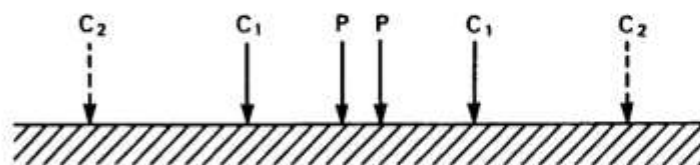


Figure 4. Location map for Test Sites 3.1 to 3.2 and 3.2 (Ext).

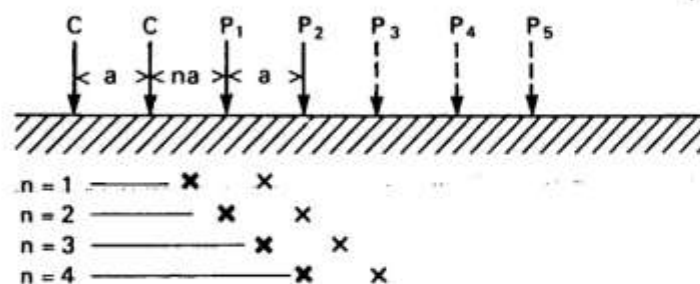
SCHLUMBERGER



GRADIENT



DIPOLE-DIPOLE



POLE - POLE

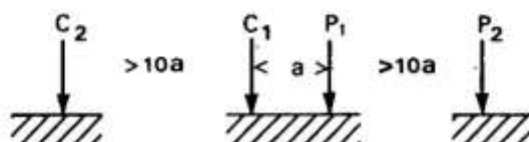
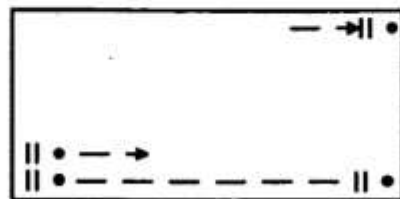


Figure 1 res.

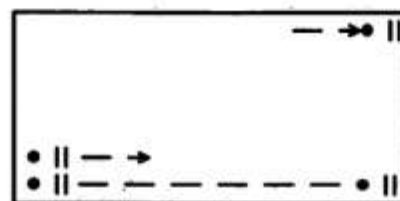
Electrode arrays used for the resistivity surveys.



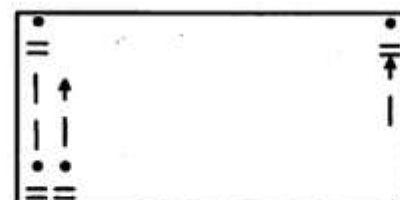
Half Schlumberger is split into four measurement styles  
A,B and C,D.



Style A



Style B



Style C



Style D

= Potential Electrodes  
• Current Electrode

Figure 2 *rsc.* The 2D electrode grid used for RESCAN surveys, and the definition of the 'half Schlumberger' mapping technique.

# Decay of E-field amplitude in homogenous materials

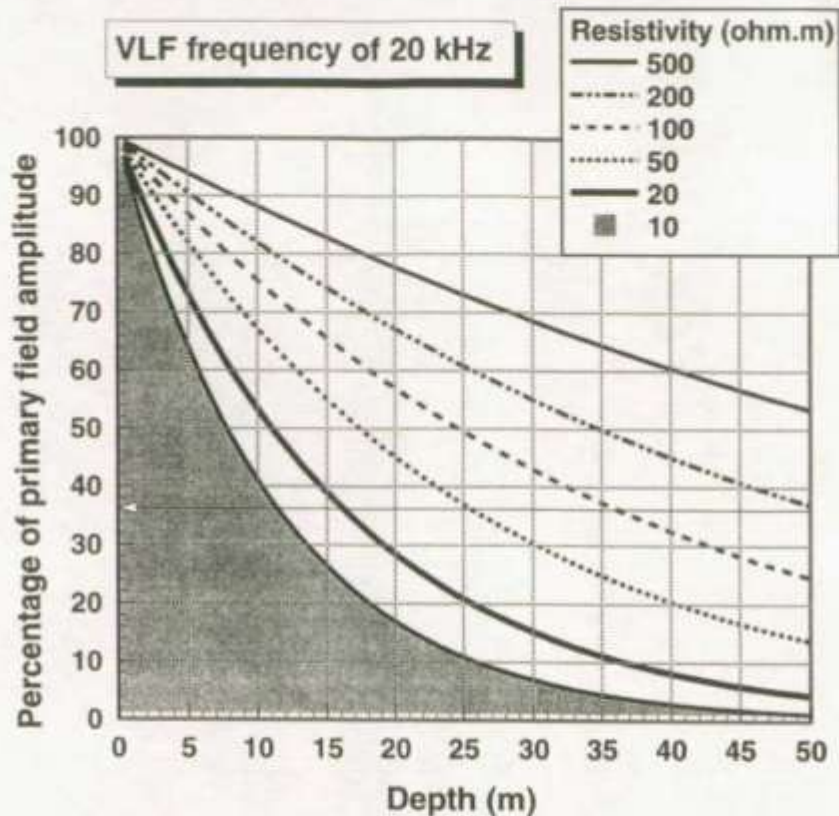


Figure 1 vlf. Depth of investigation of VLF EM fields.

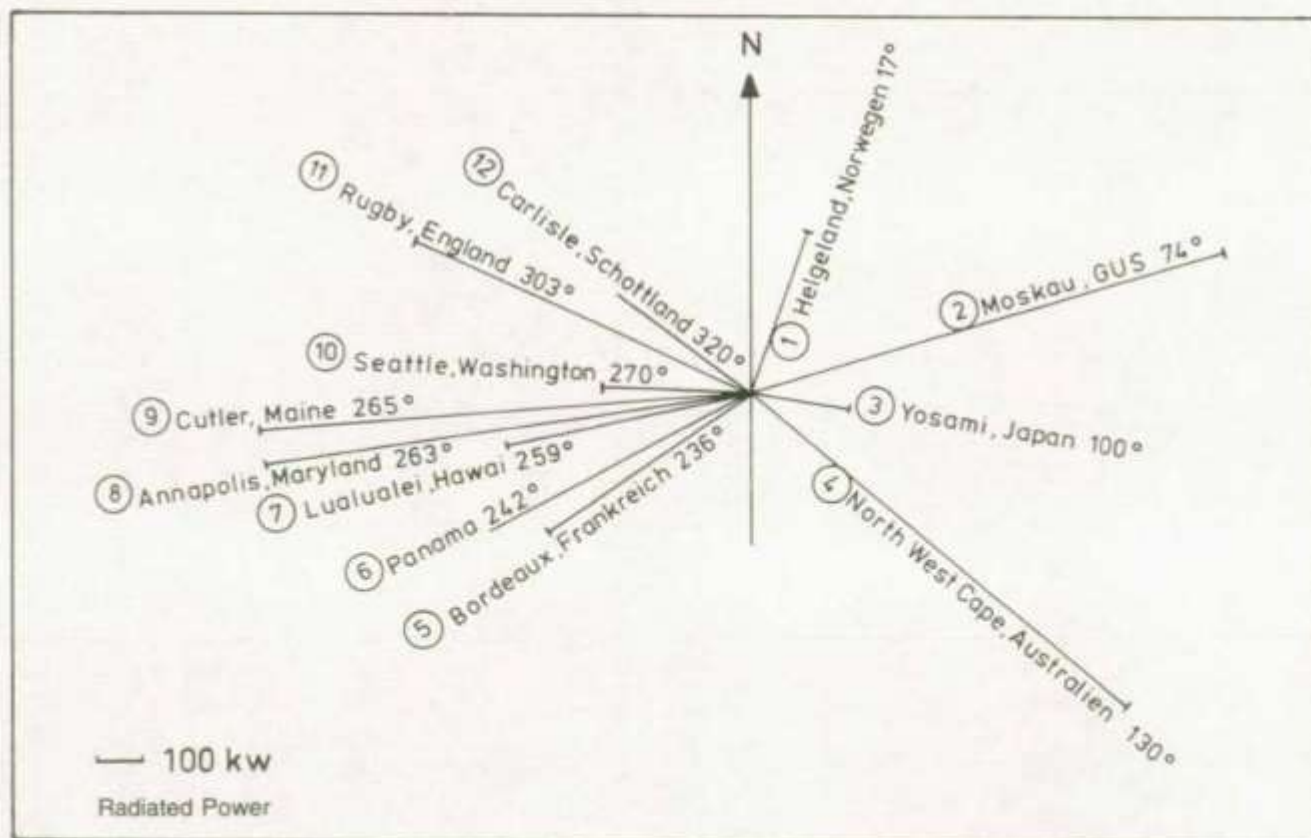
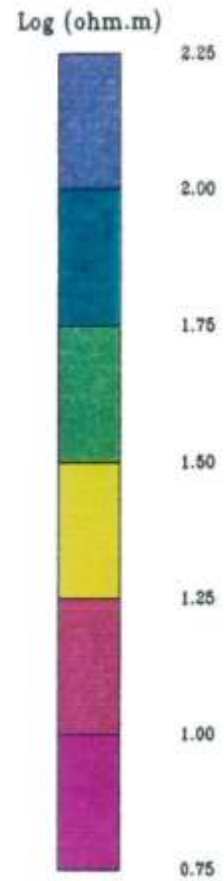
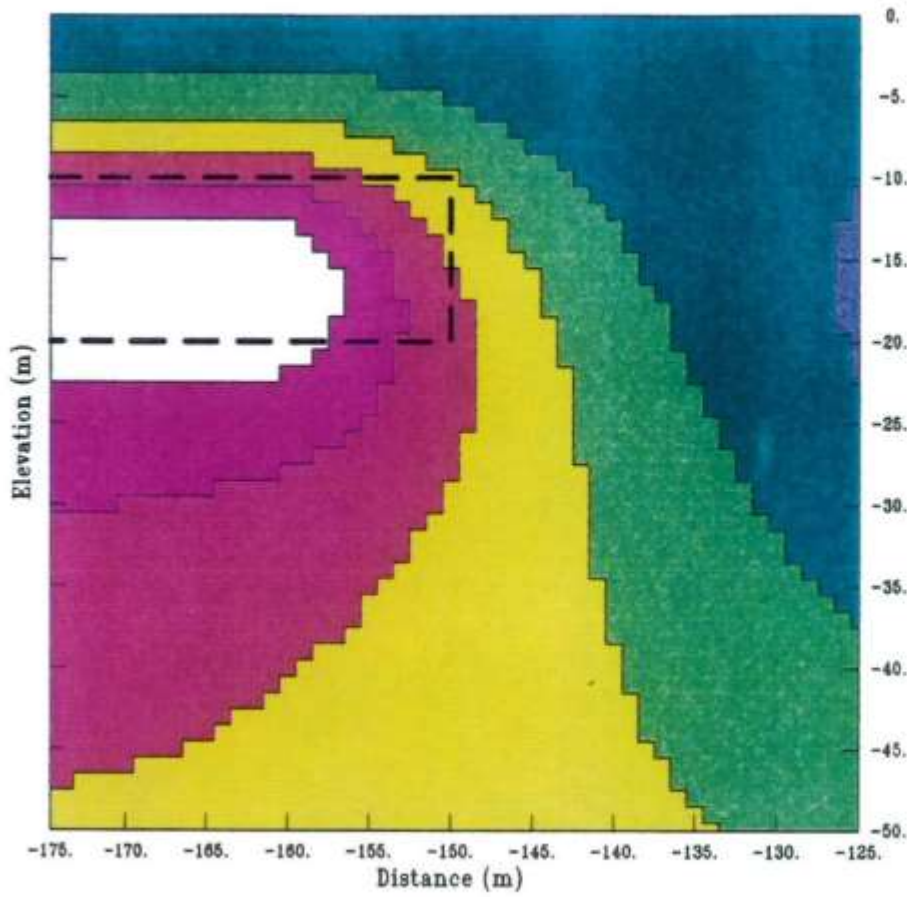


Figure 2 vlf. Azimuths of VLF transmitters relative to Test Areas 1, 2, and 3.

# VLF SYNTHETIC, 2d OCCAM INVERSION (TE,1f)



# VLF SYNTHETIC, 2d OCCAM INVERSION (TE,2f)

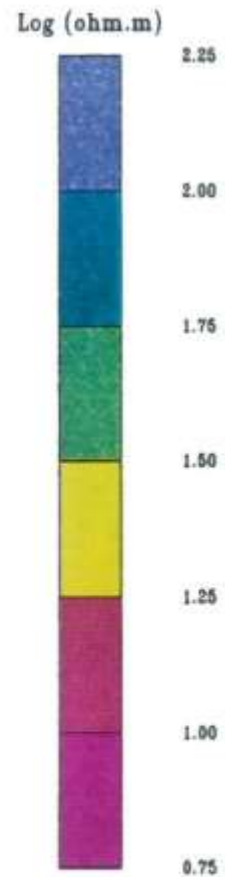
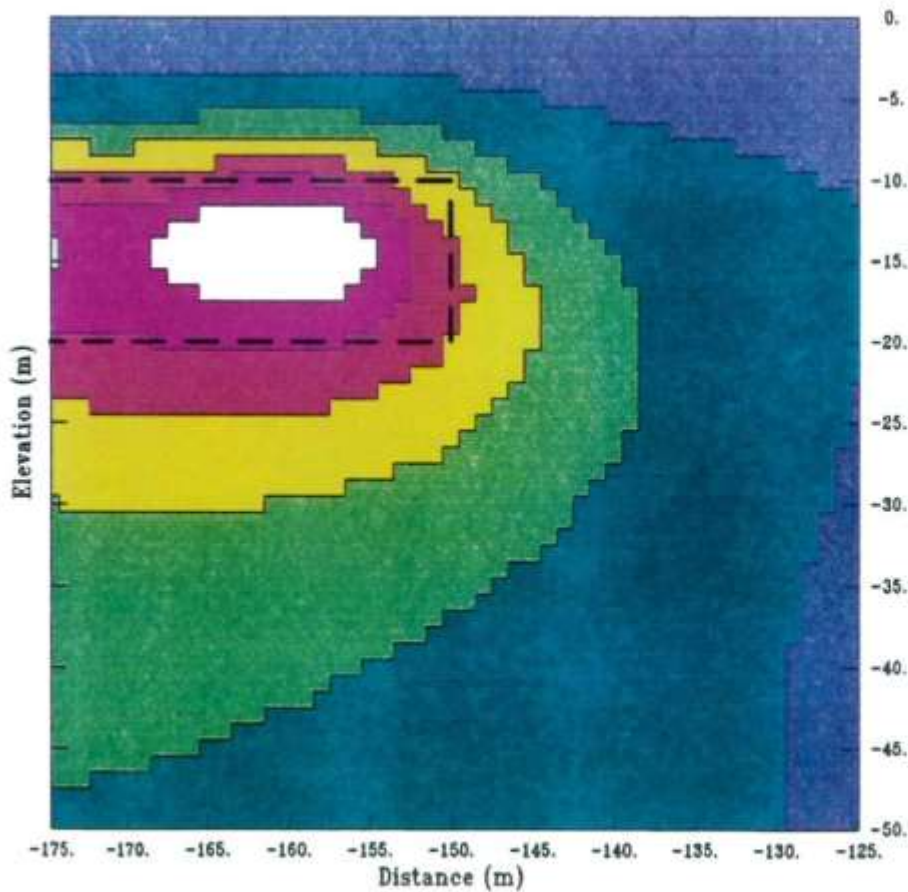
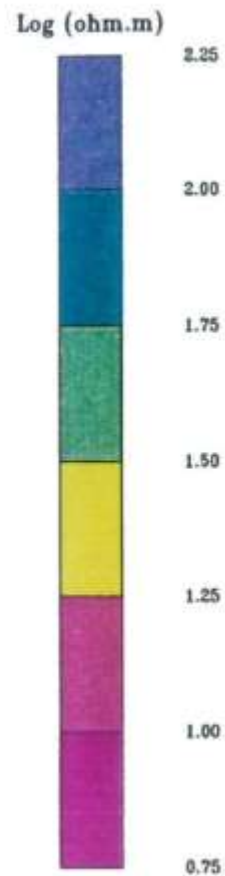
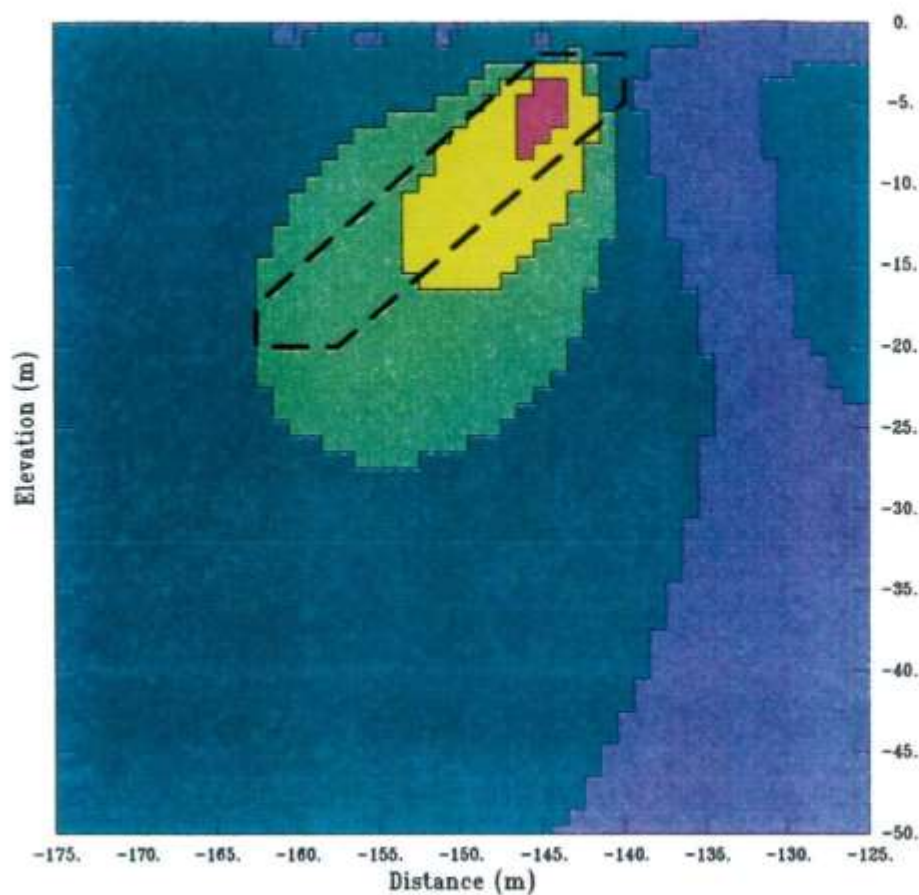


Figure 3 vlf. Synthetic VLF model for non-dipping target.



# VLF SYNTHETIC, 2d OCCAM INVERSION (TM,1f)



# VLF SYNTHETIC, 2d OCCAM INVERSION (TM,2f)

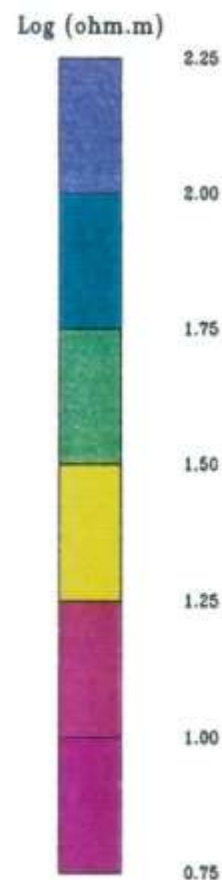
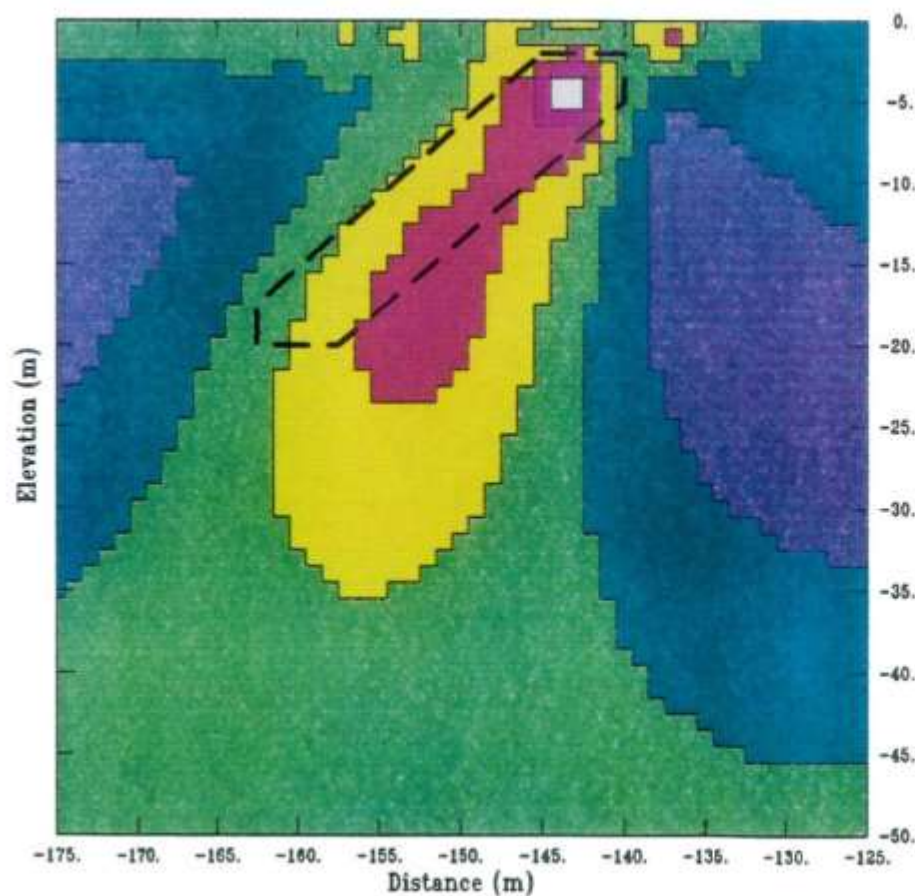
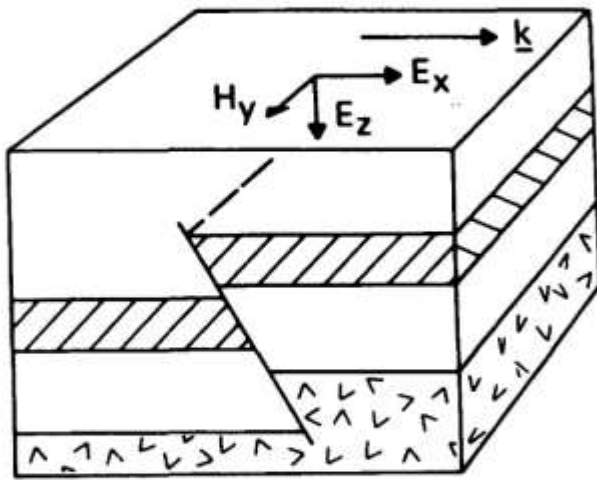


Figure 4 vlf. Synthetic VLF model for dipping target.

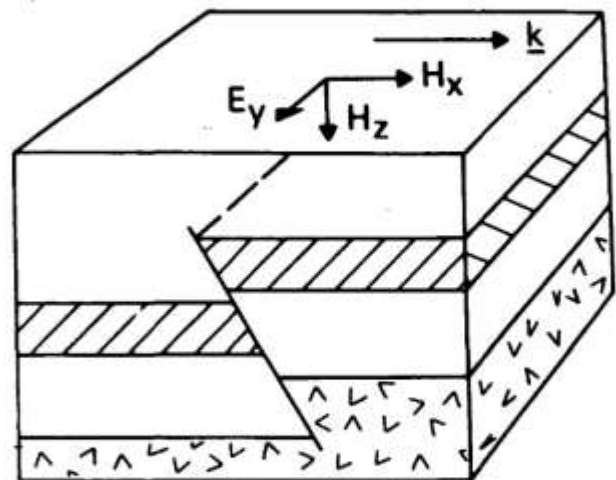


$\underline{k}$  is the direction of propagation of the VLF E field



H polarisation

TM mode. Magnetic field parallel to strike



E polarisation

TE mode. Electric field parallel to strike

Figure 5 *vlf*. Principal components of the VLF field.

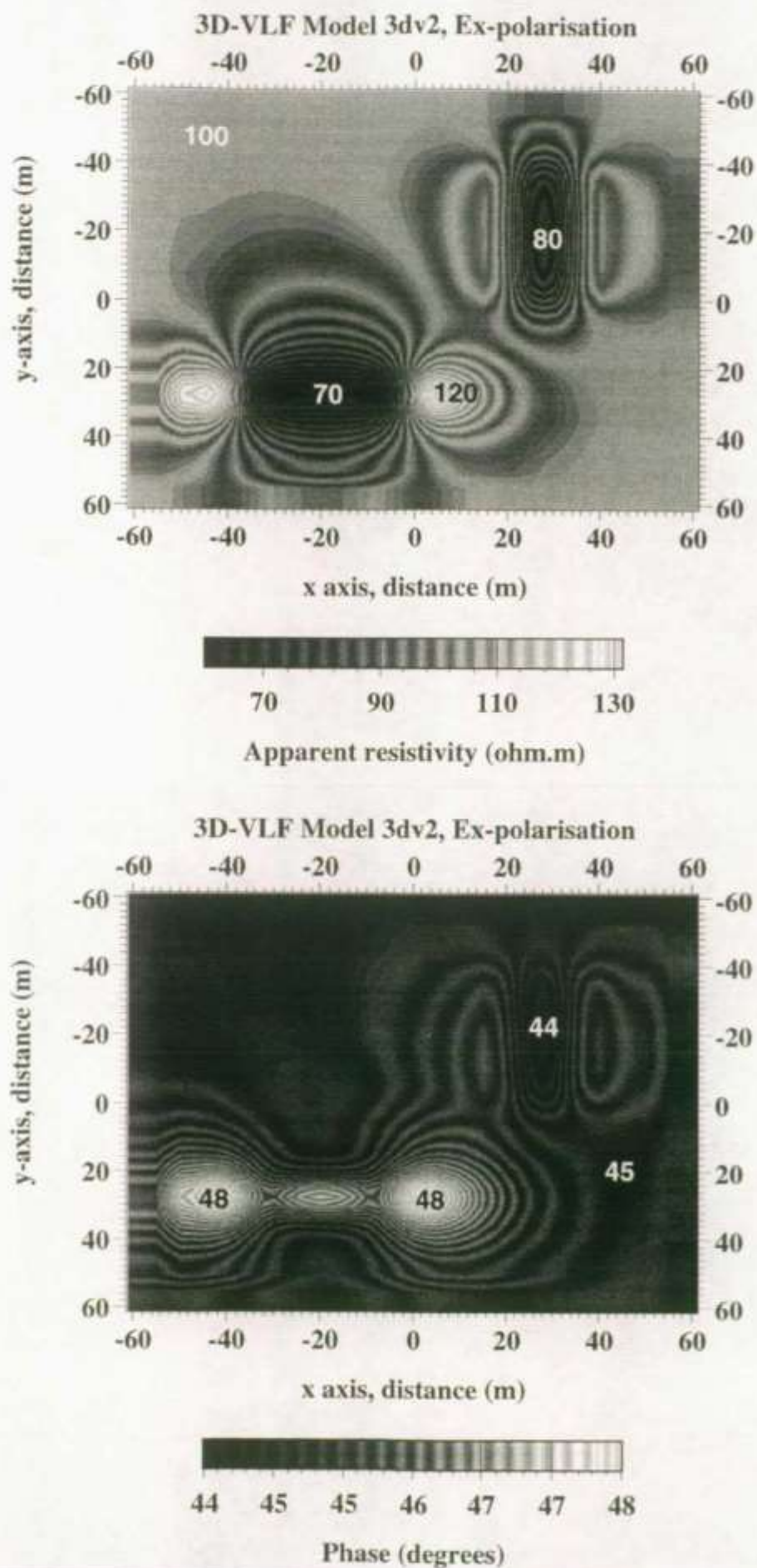
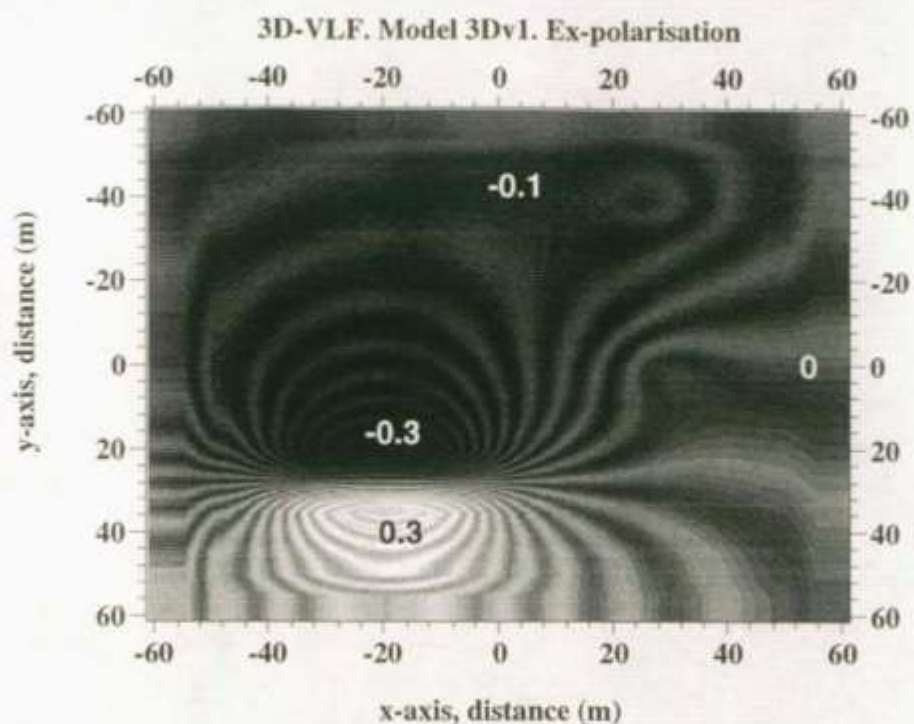
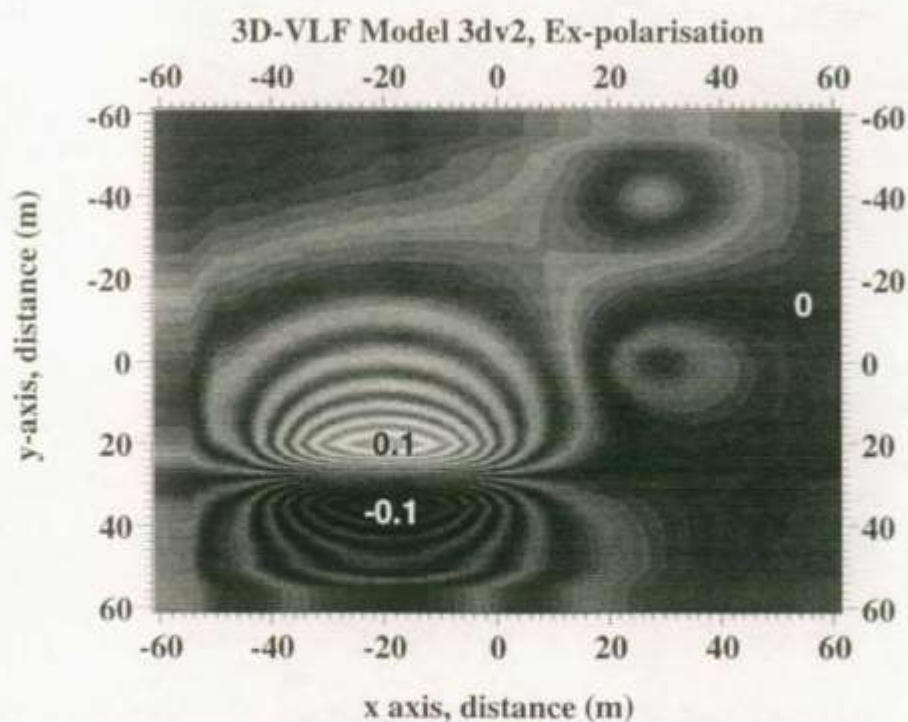


Figure 6 vlf. VLF modelling. Model 1: apparent resistivity and phase.



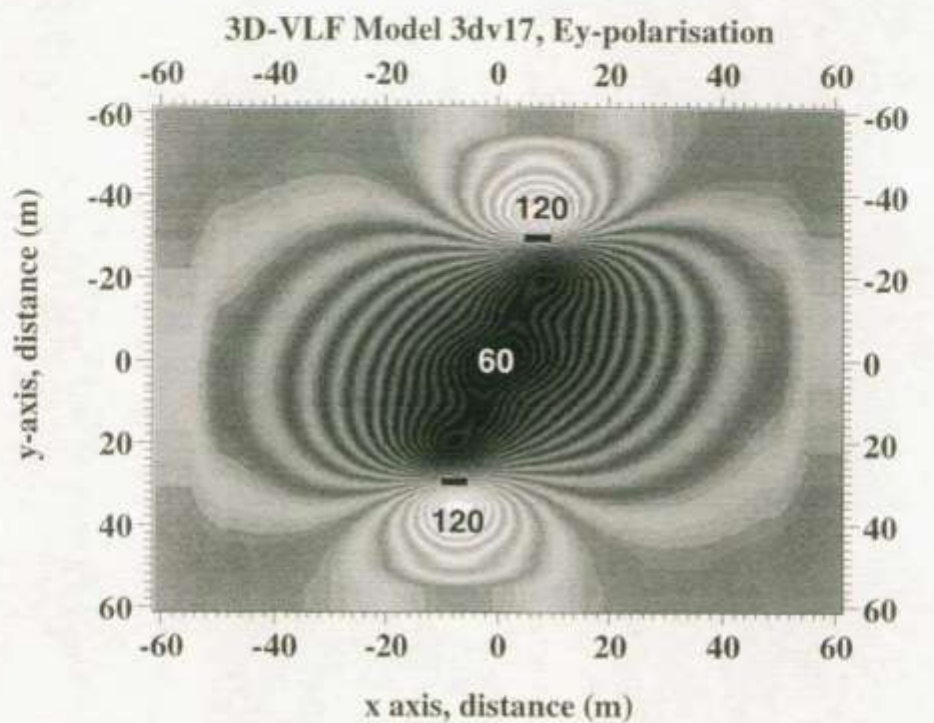
Real (Z/H) %



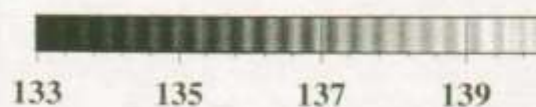
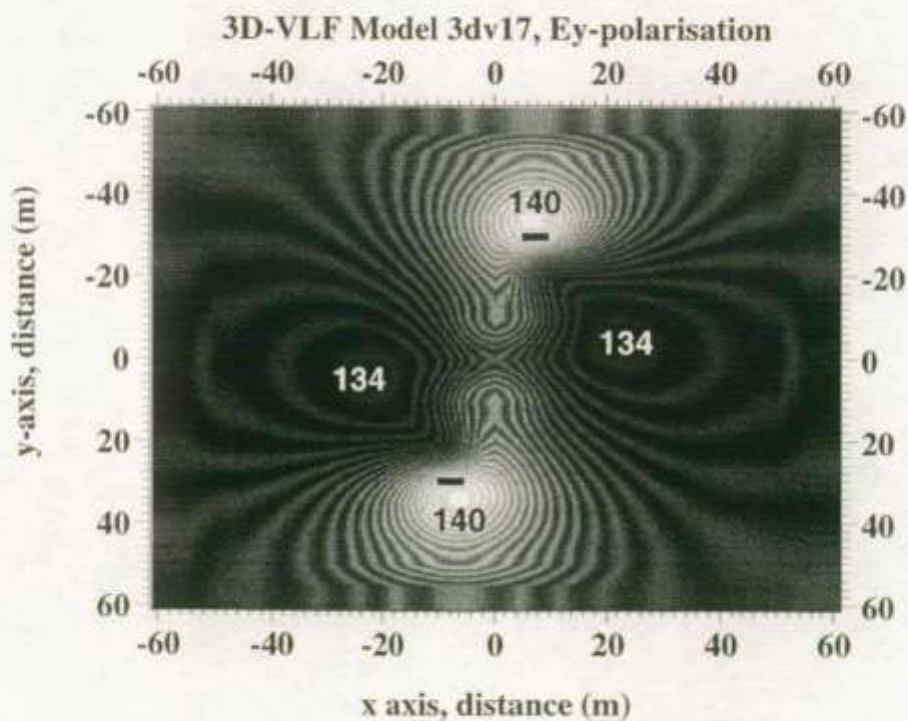
Imag (Z/H) %

Figure 7 *vlf*. VLF modelling. Model 1: Z field ratios.





Apparent resistivity (ohm.m)



Phase (degrees)

Figure 8 *vlf*. VLF modelling. Model 2: apparent resistivity and phase,  $E_y$  polarisation.



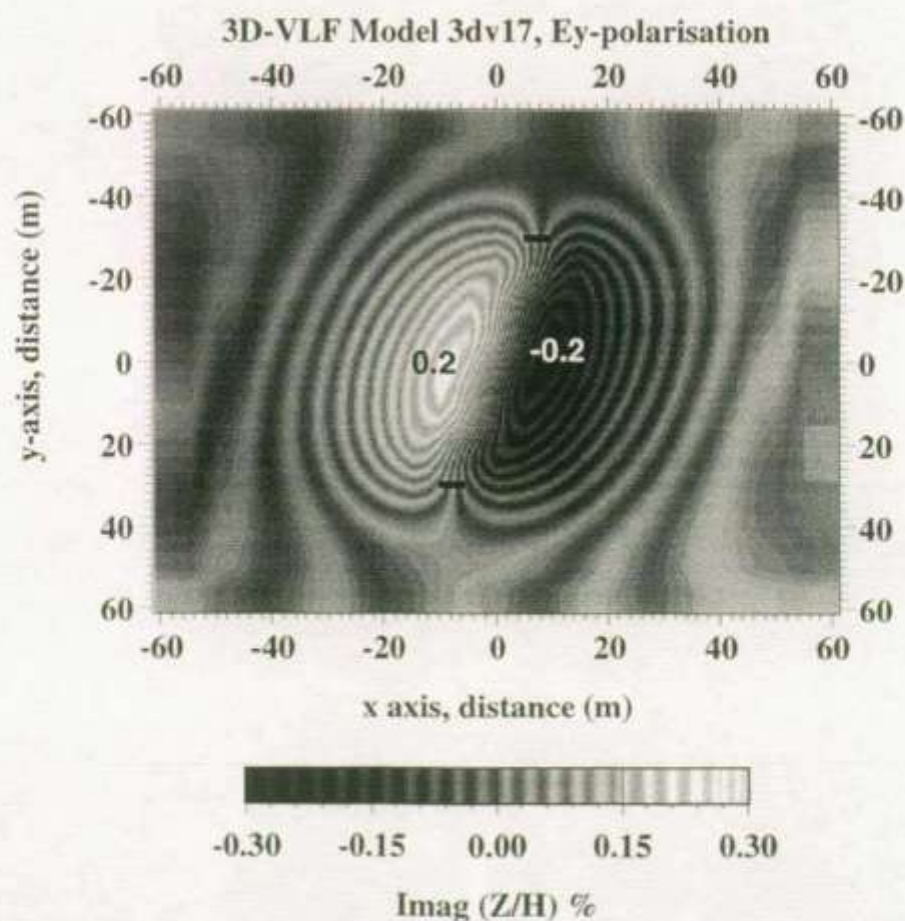
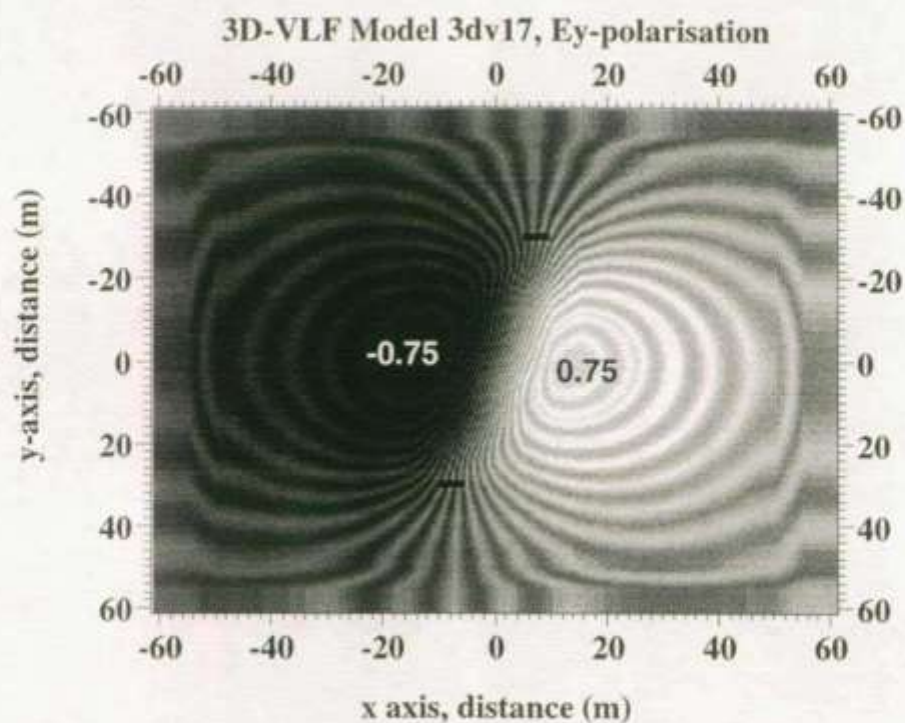


Figure 9 *vlf*. VLF modelling. Model 2: Z field ratios,  $E_y$  polarisation.

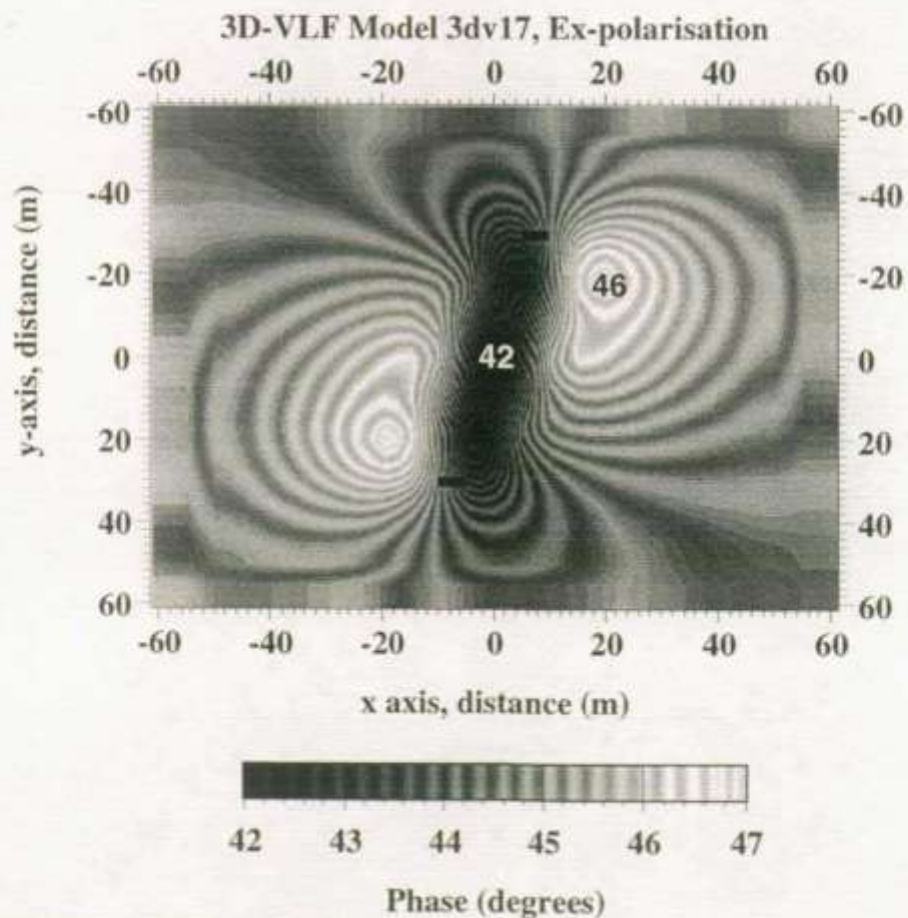
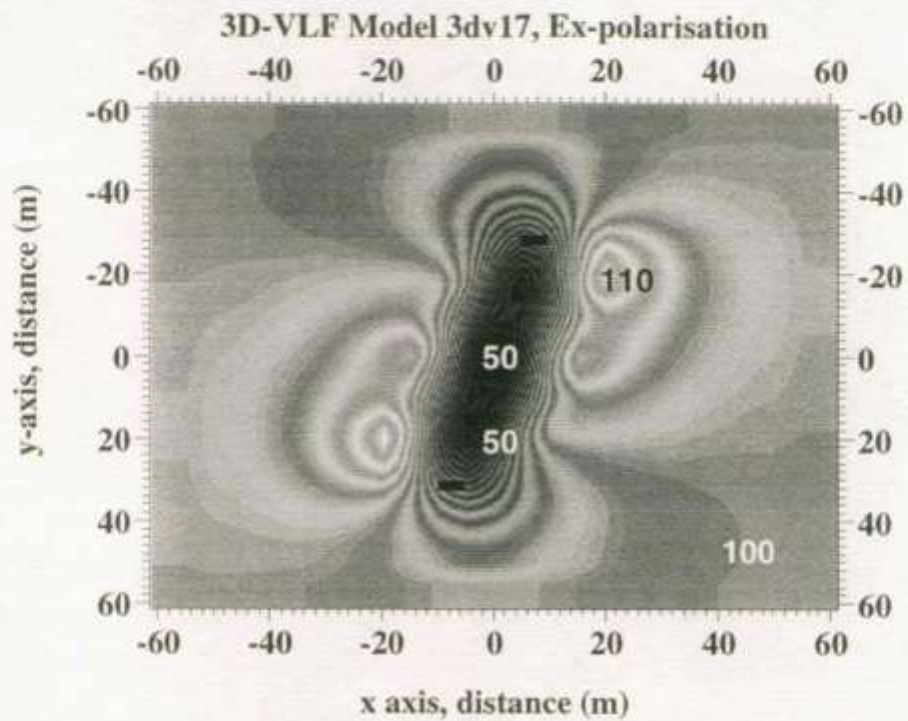


Figure 10 vlf. VLF modelling. Model 2: apparent resistivity and phase,  $E_x$  polarisation.



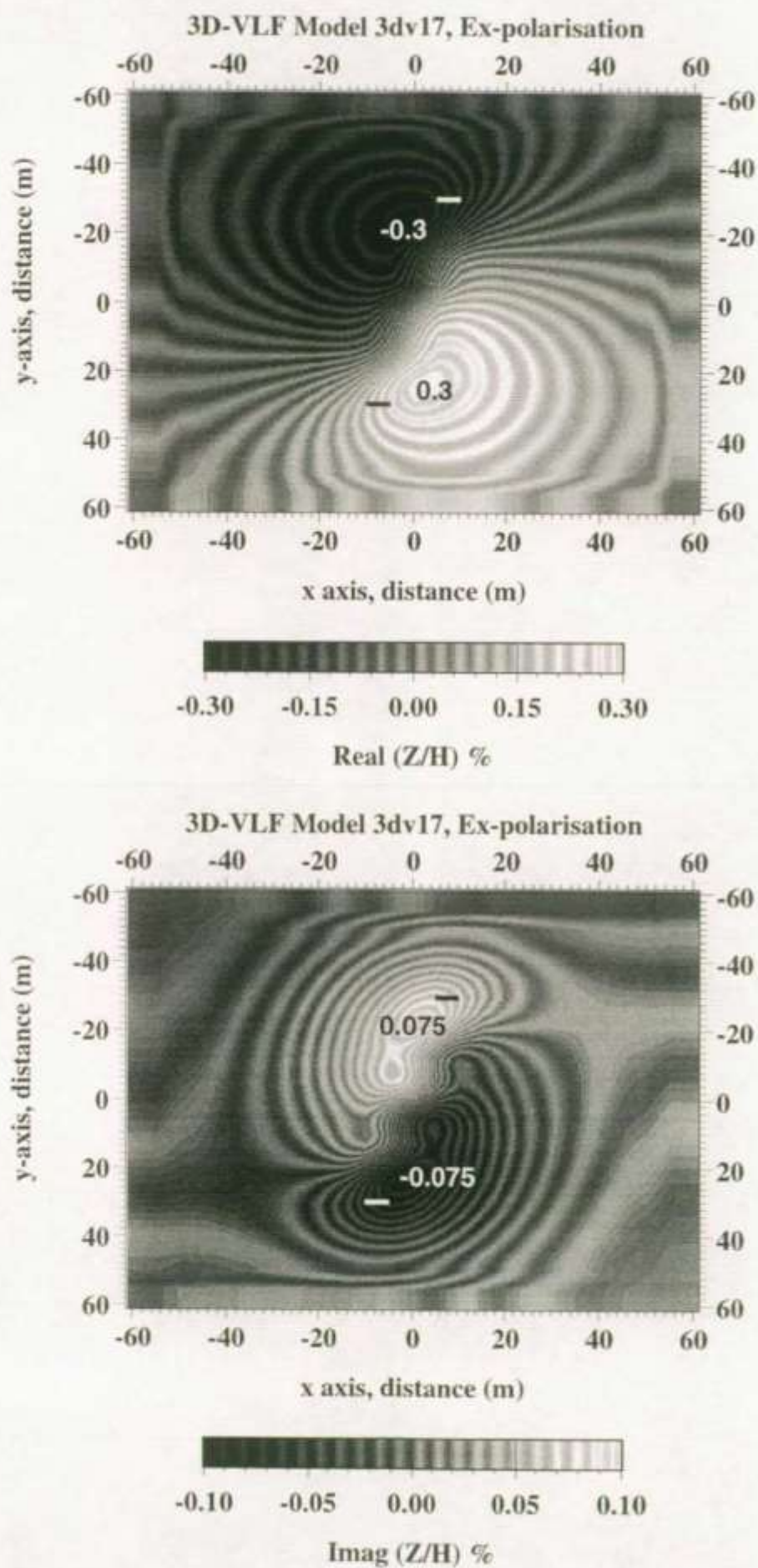


Figure 11 *vlf*. VLF modelling. Model 3: Z field ratios,  $E_x$  polarisation.

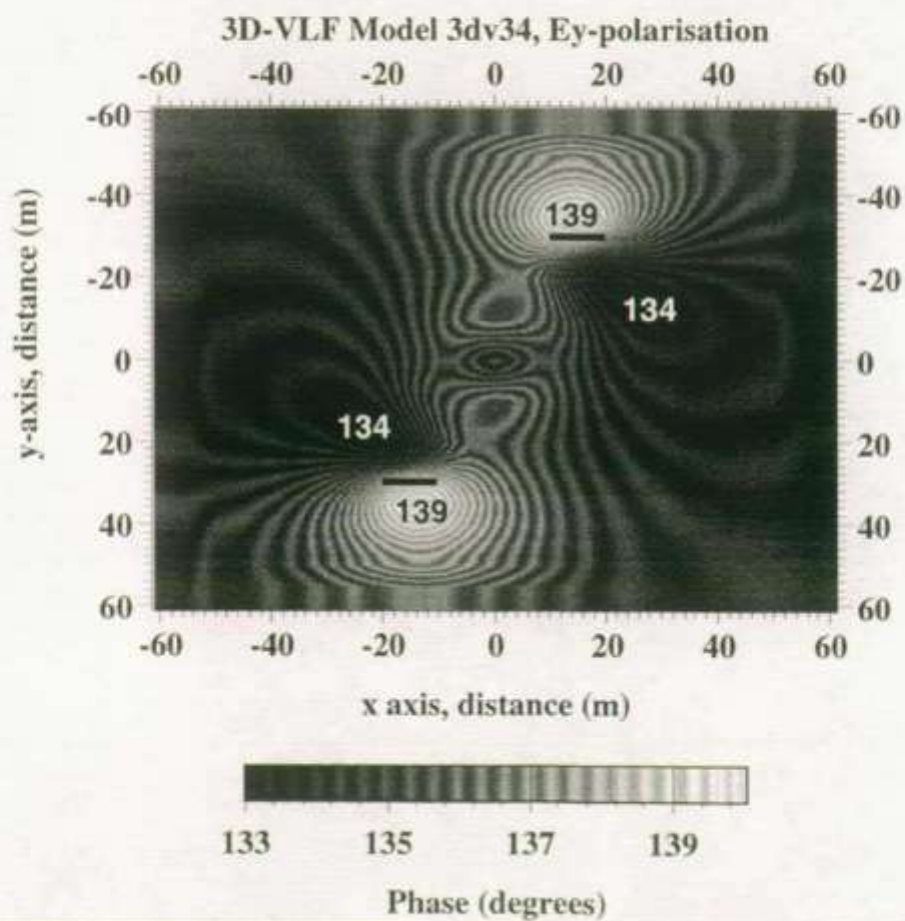
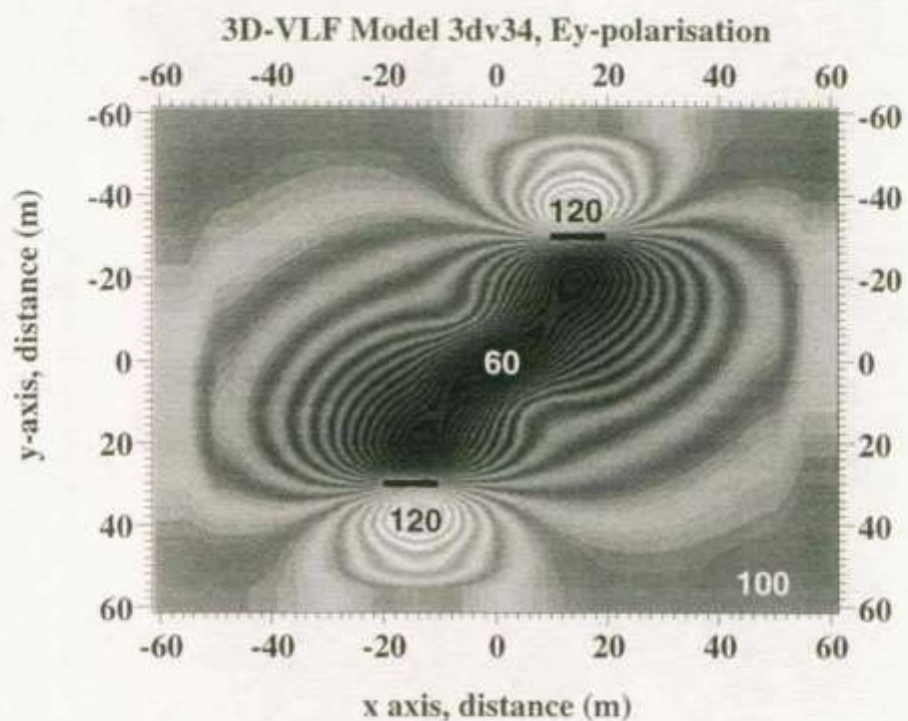


Figure 12 *vlf*. VLF modelling. Model 3: apparent resistivity and phase,  $E_y$  polarisation.



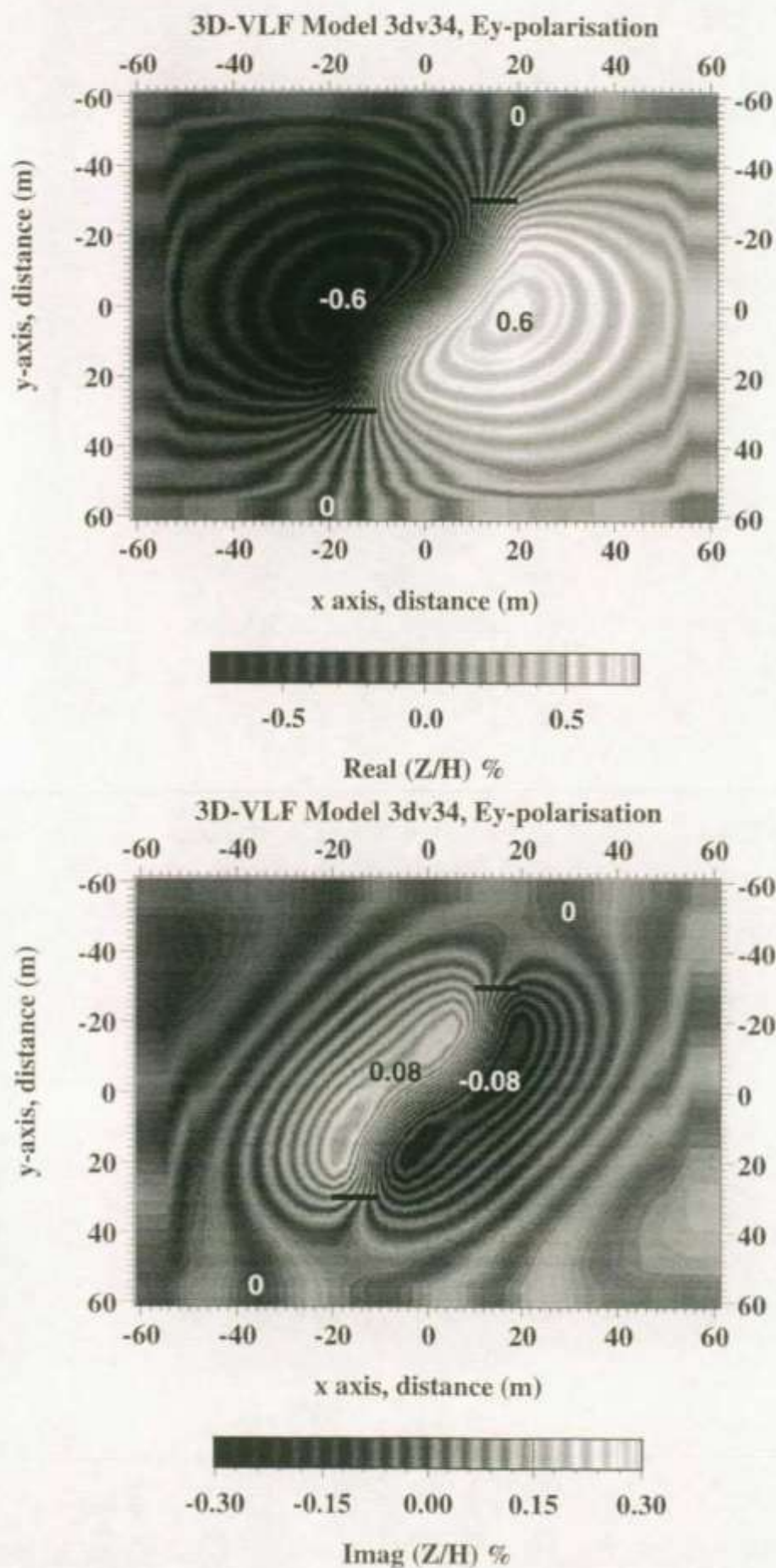


Figure 13 vlf. VLF modelling. Model 3: Z field ratios,  $E_y$  polarisation.

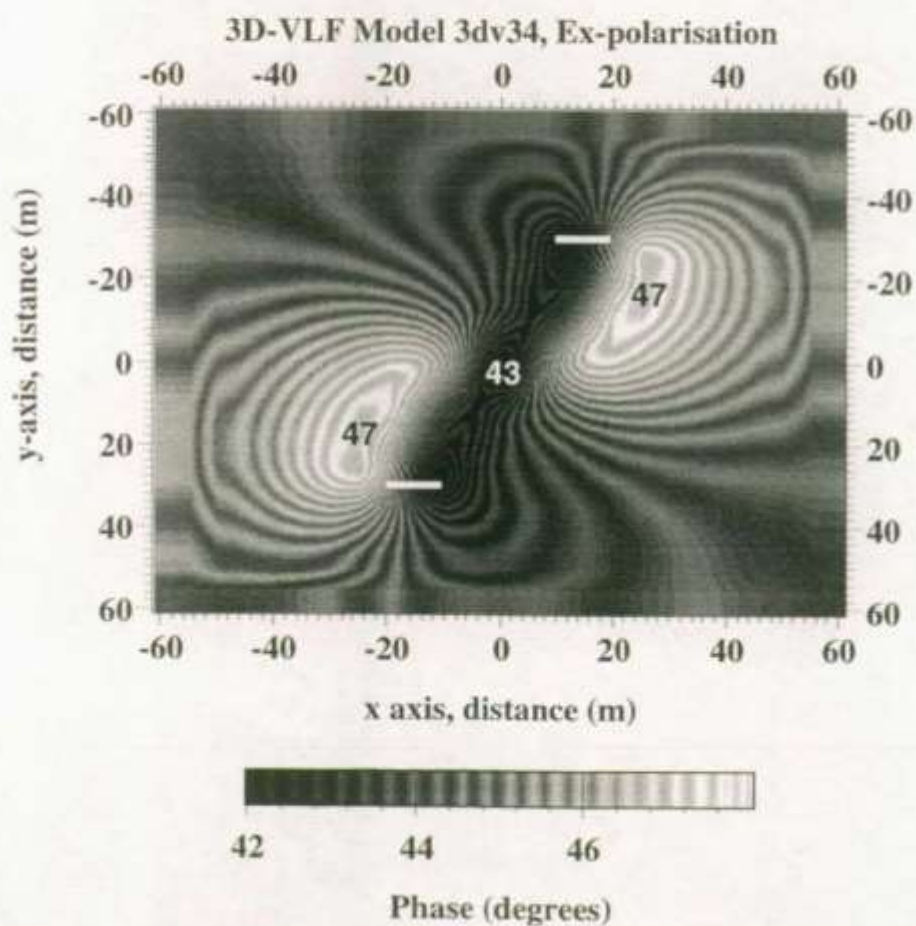
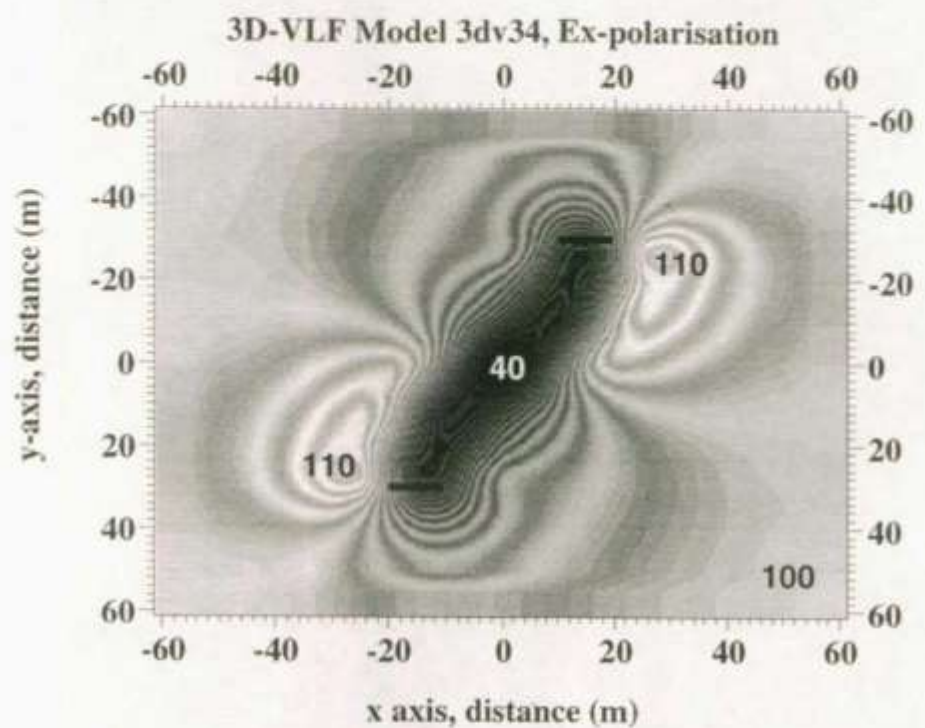


Figure 14 *vlf*. VLF modelling. Model 3: apparent resistivity and phase,  $E_x$  polarisation.



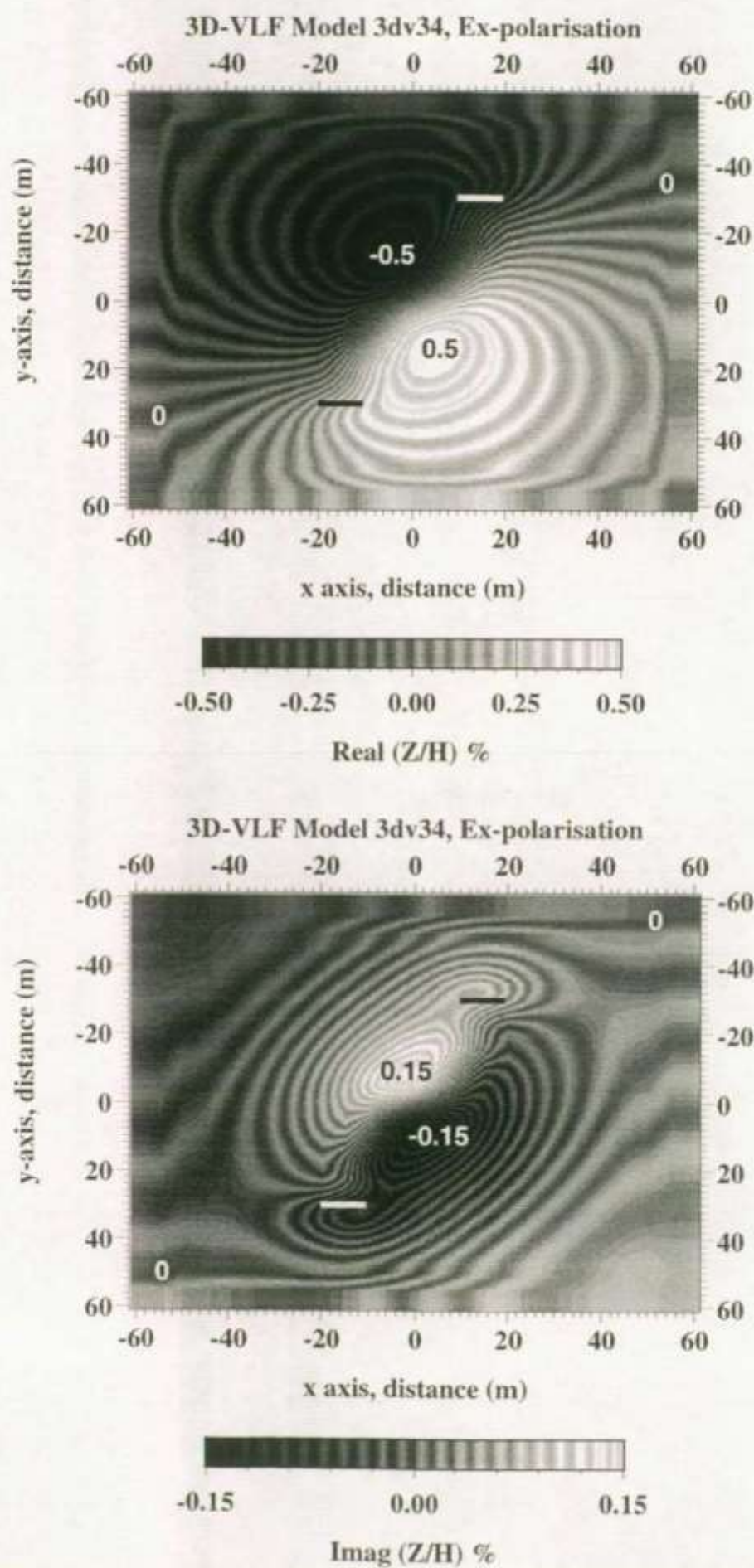


Figure 15 v/f. VLF modelling. Model 3: Z field ratios, E, polarisation.

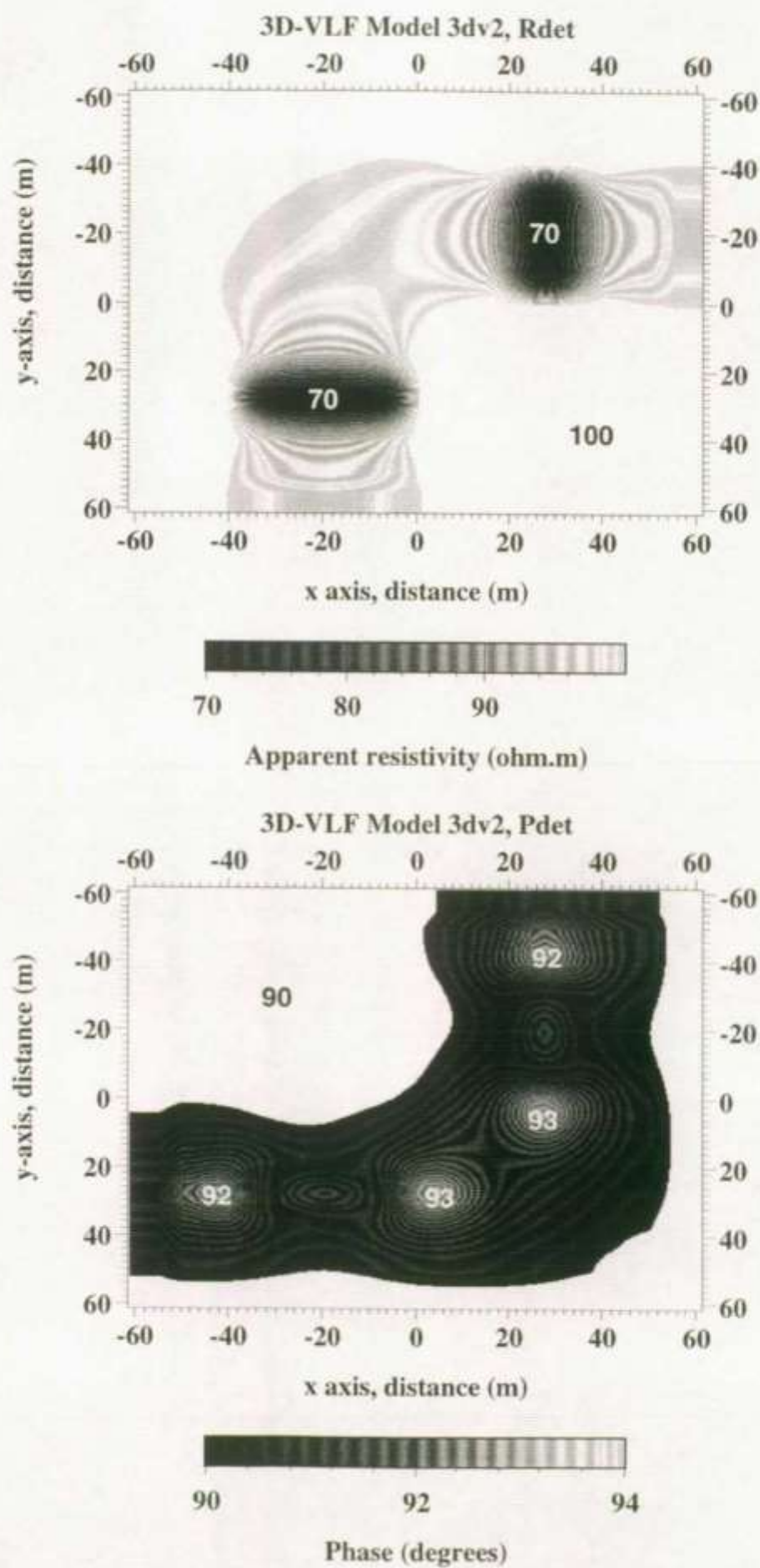


Figure 16 *vlf*. VLF modelling. Model 1: use of rotational invariants.



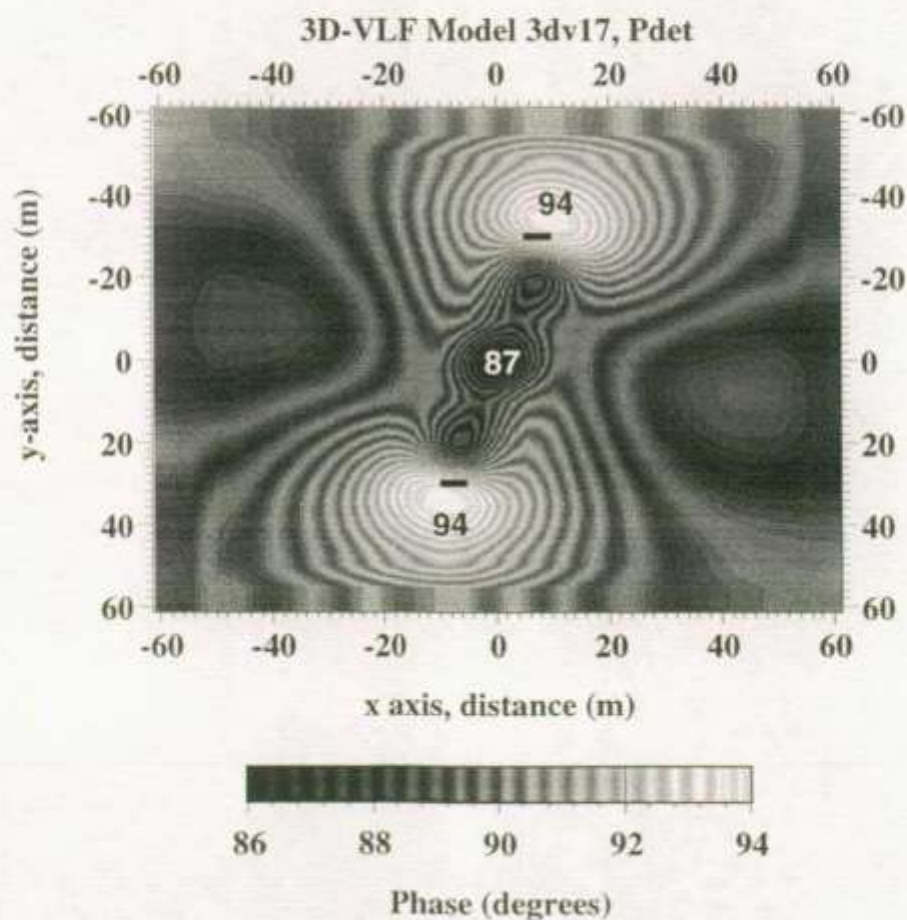
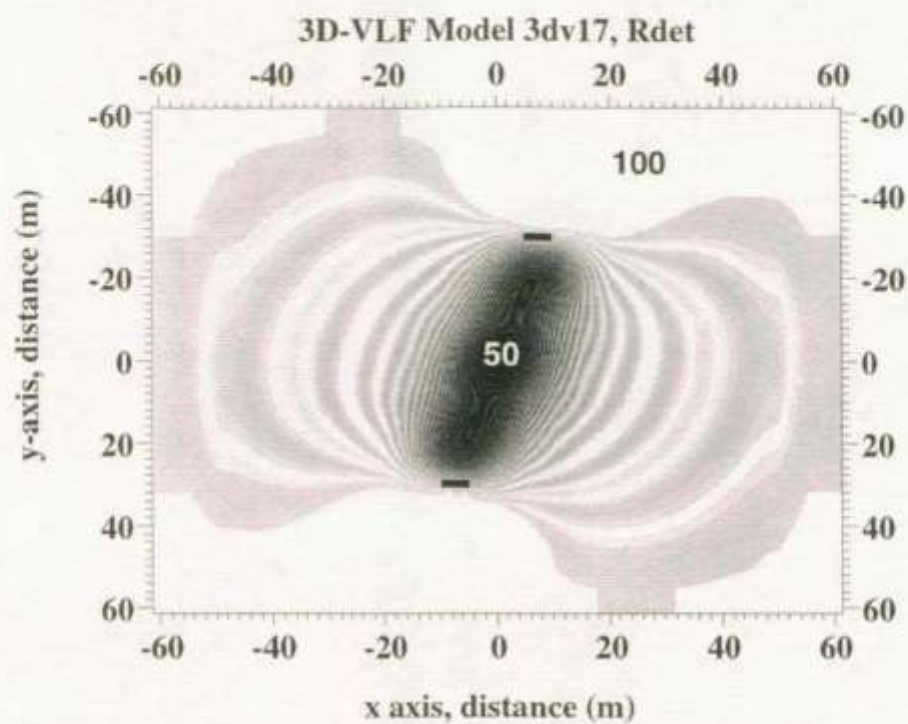


Figure 17 *vlf*. VLF modelling. Model 2: use of rotational invariants.

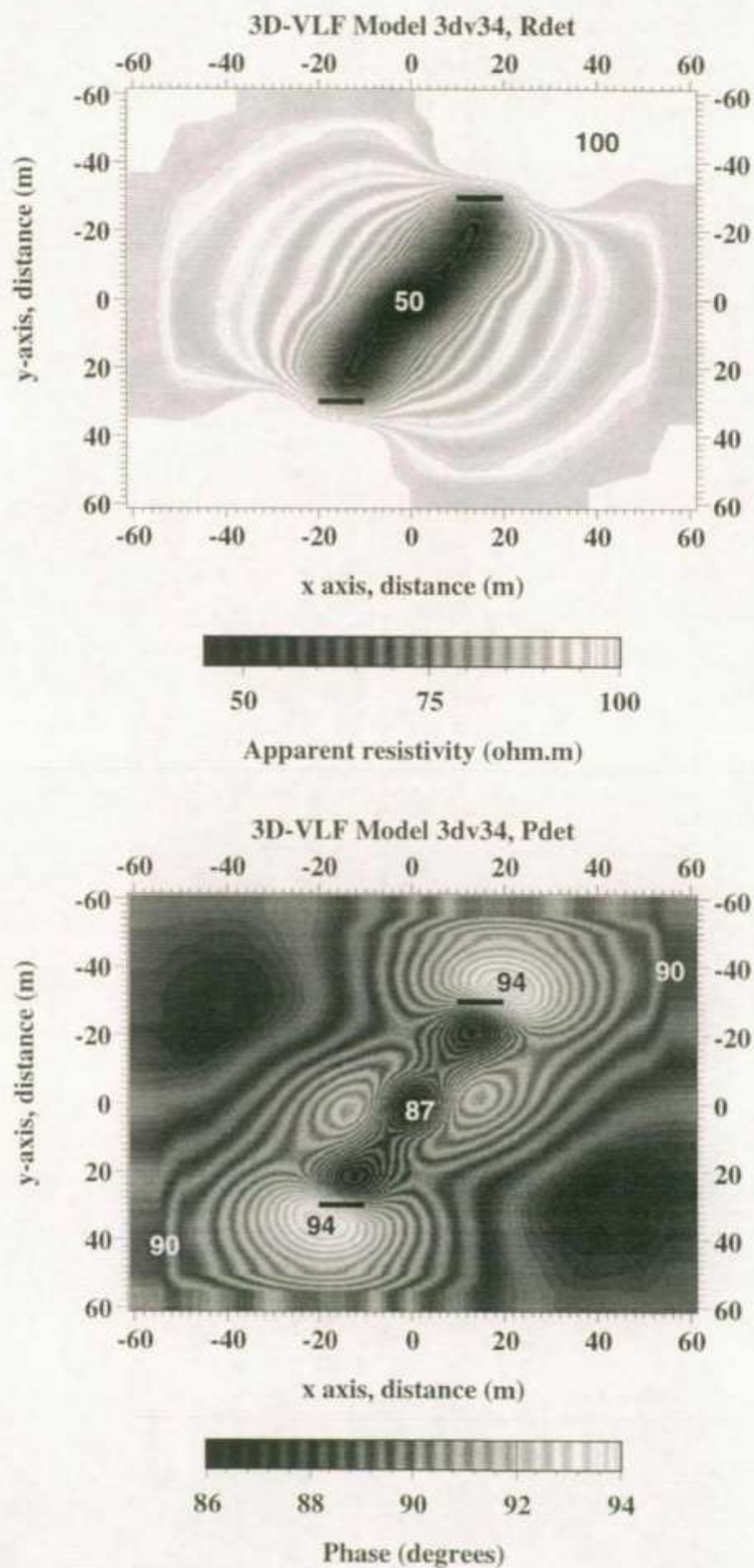
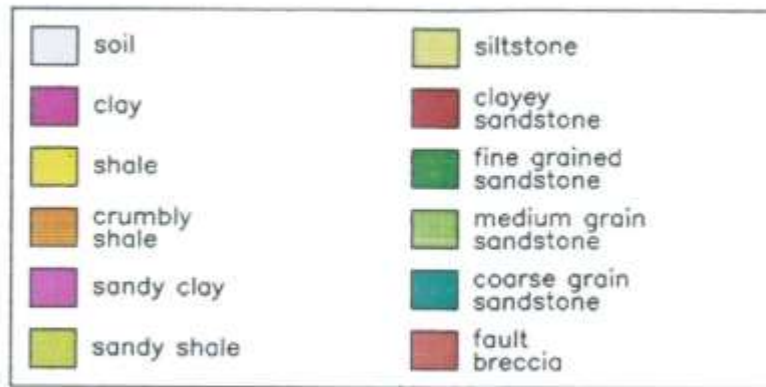
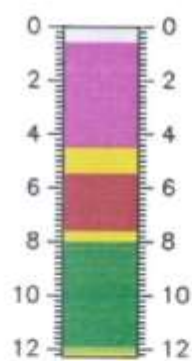


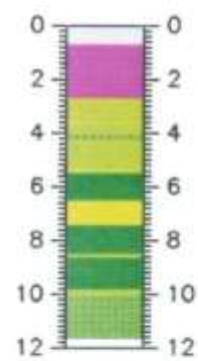
Figure 18 *vlf*. VLF modelling. Model 3: use of rotational invariants.



BK 1.12



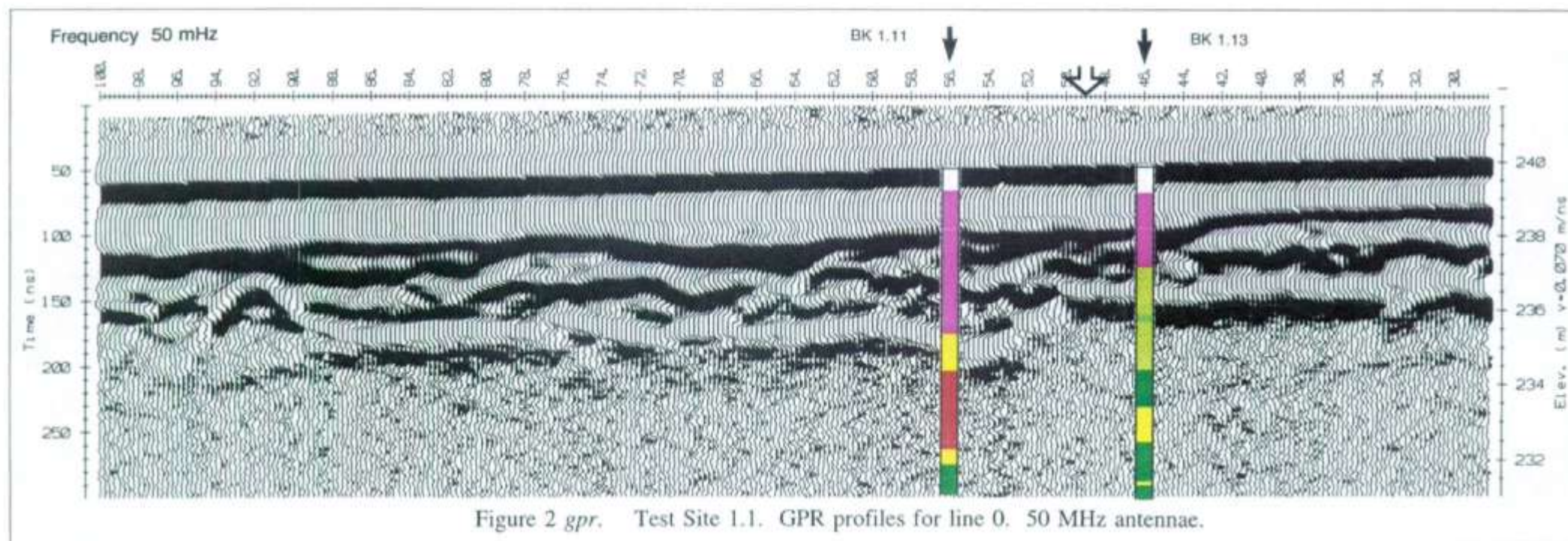
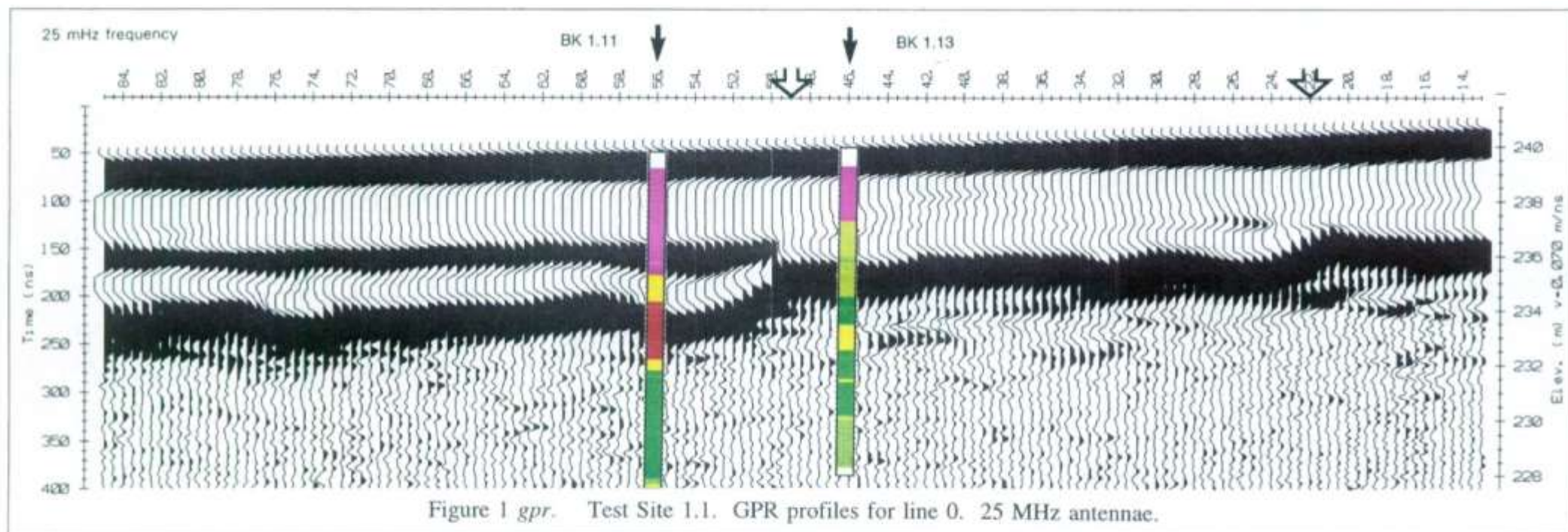
BK 1.11



BK 1.13

Figure 6. Test Site 1.1. Geological section: boreholes BK1.11, BK1.12, and BK1.13.







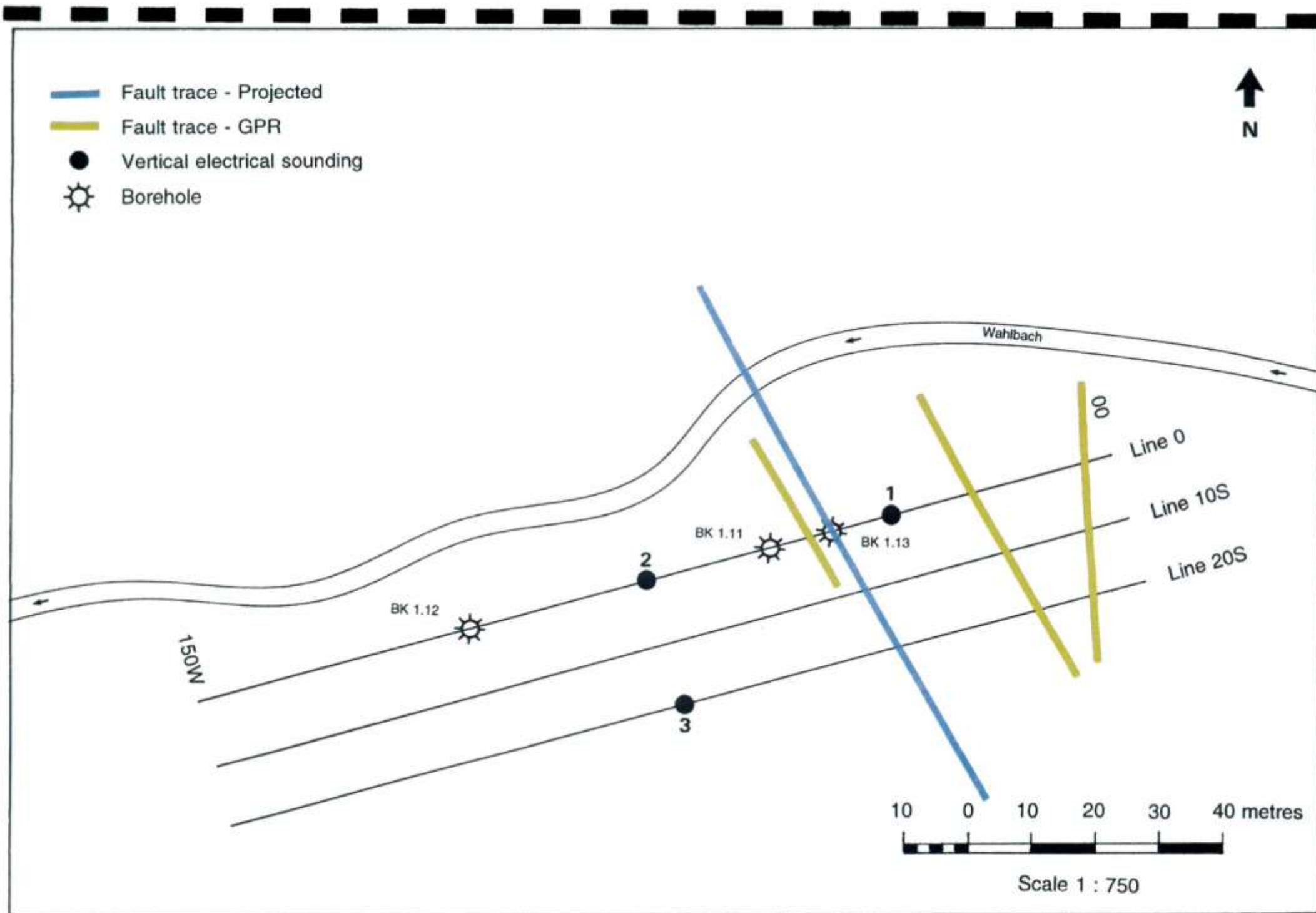


Figure 5. Test Site 1.1. Geophysical grid, borehole locations, and interpretation.

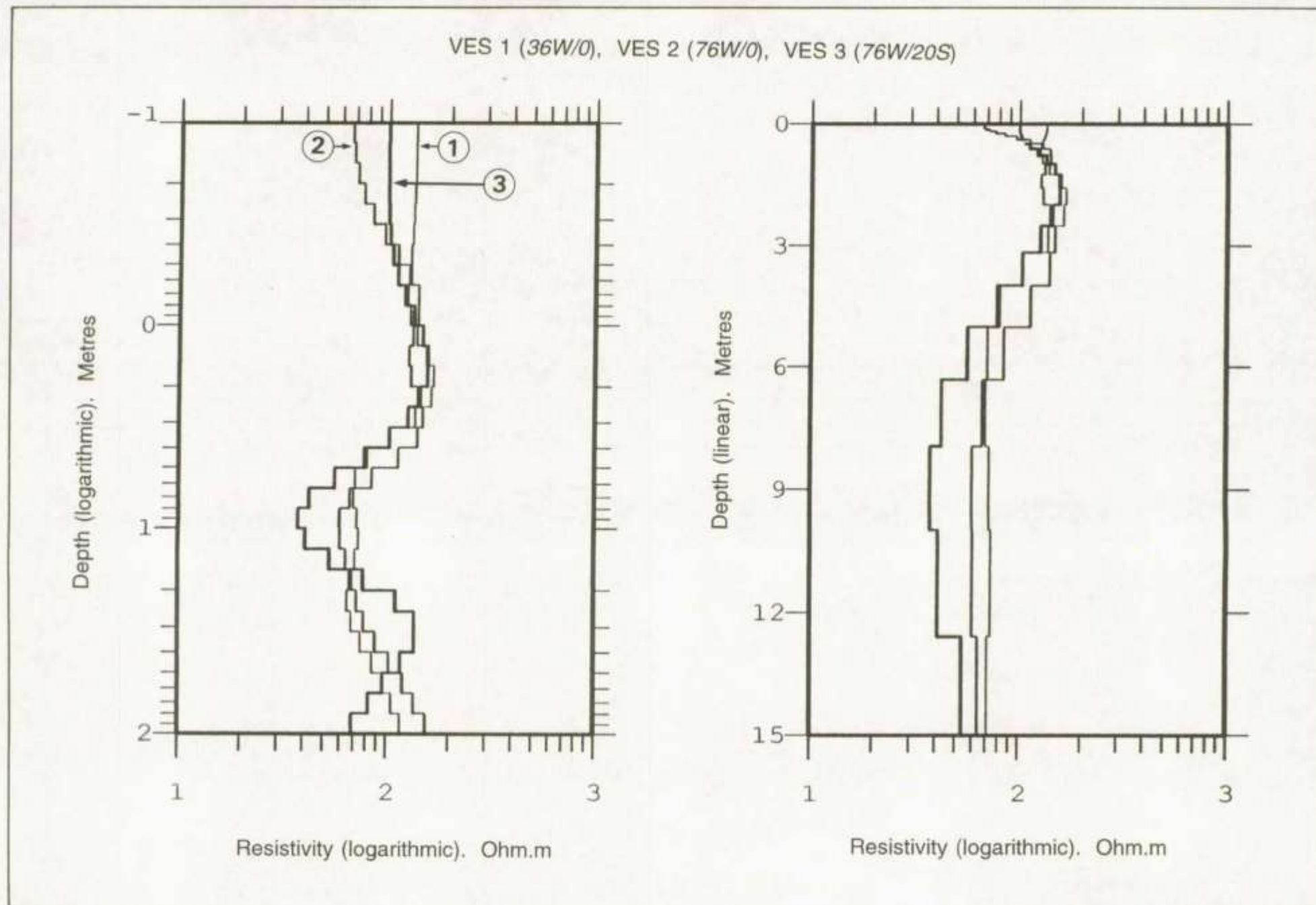
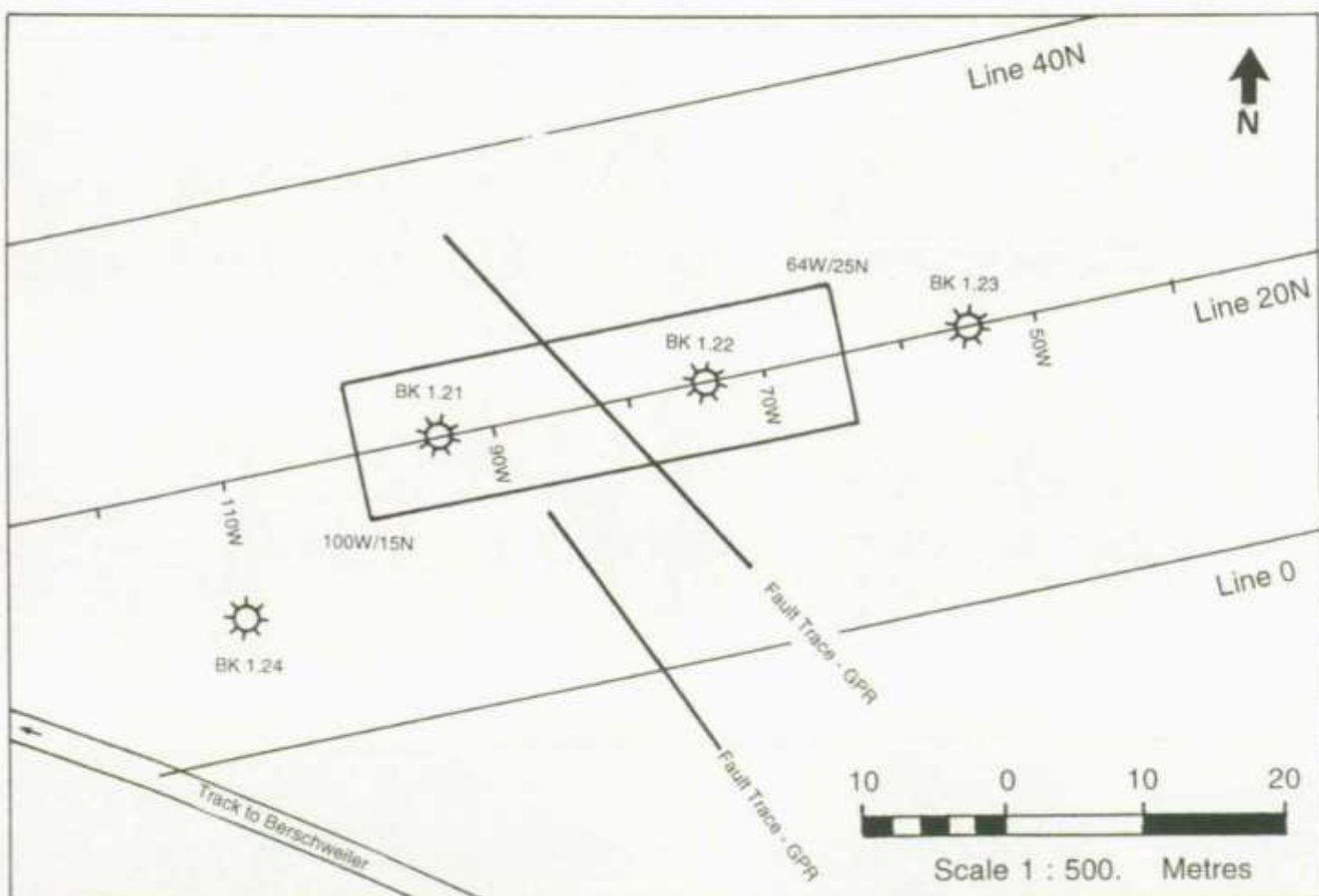
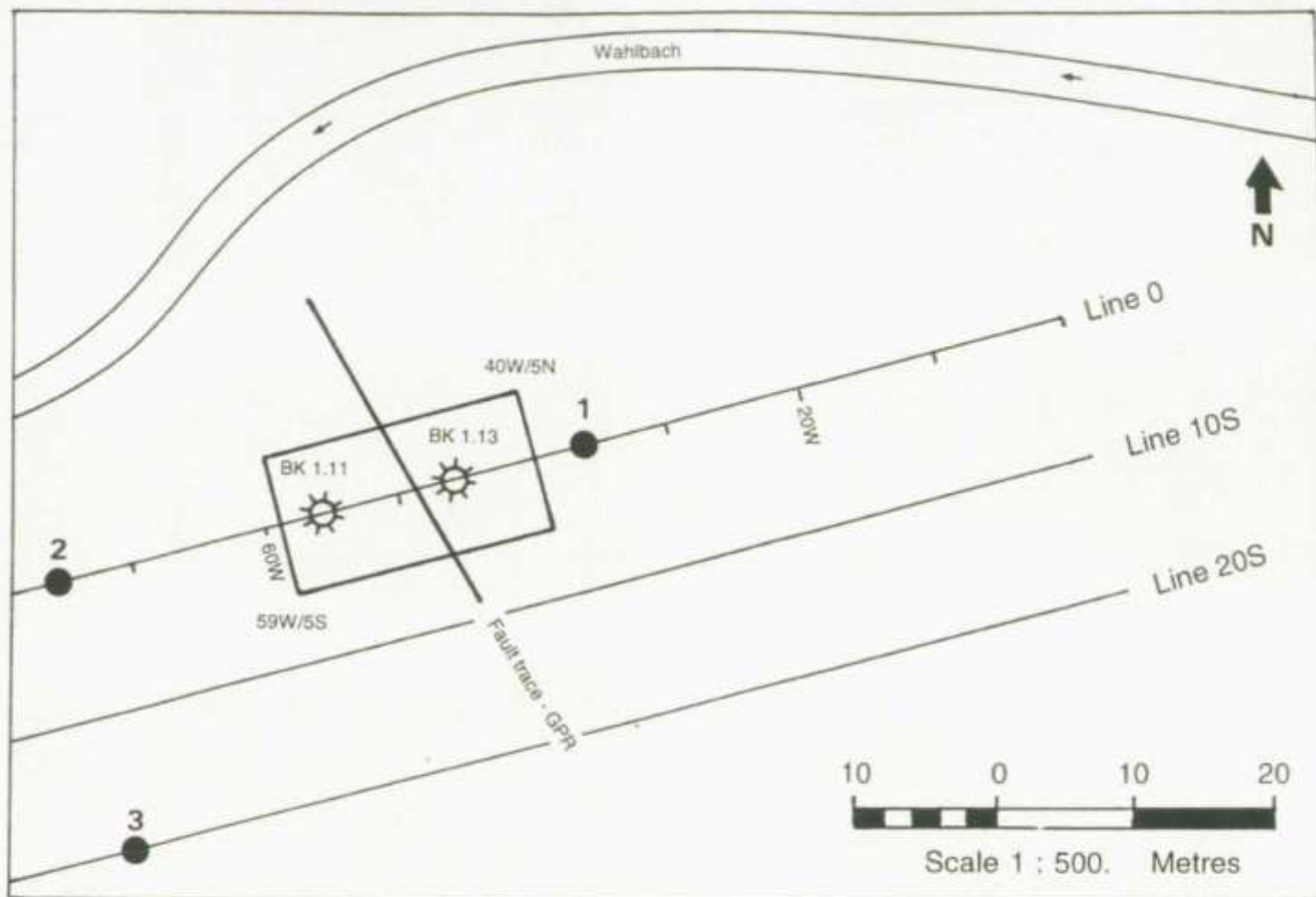


Figure 2 *res.*

Test Site 1.1. Interpretation of VES 1, 2, and 3.



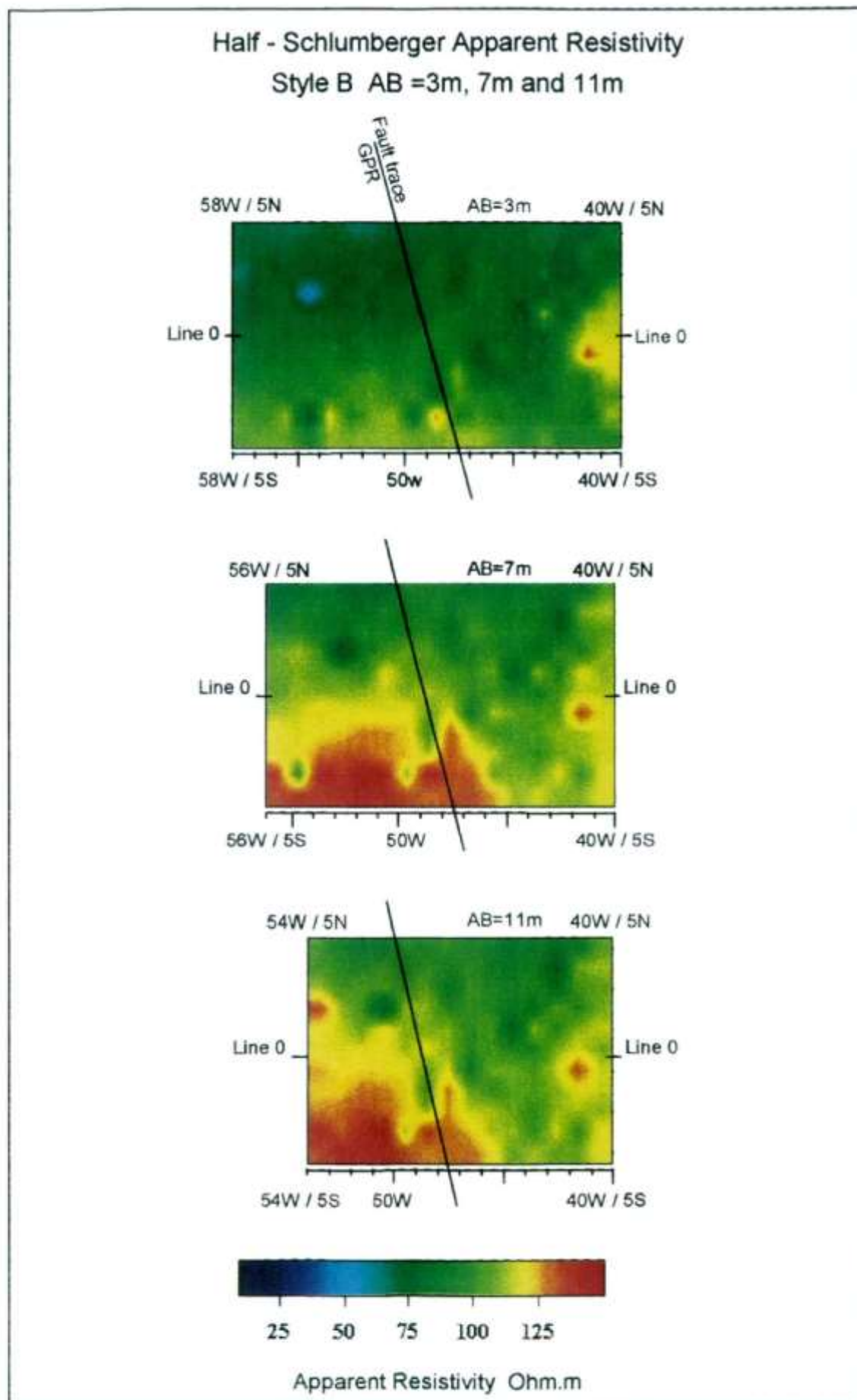


Figure 10 *rsc.* Test Site 1.1. Apparent resistivity data, showing projected position of the fault.



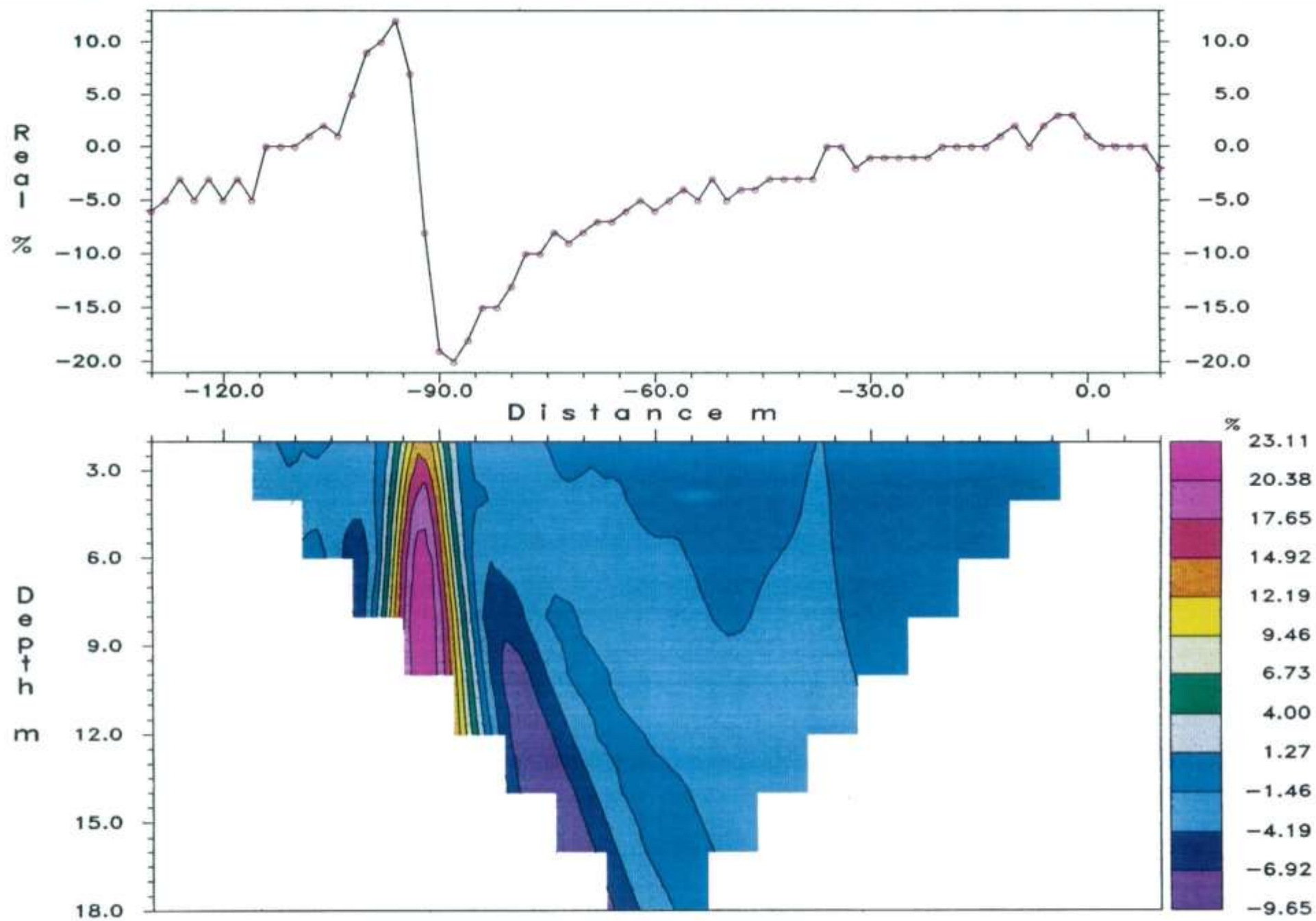


Figure 19 *vlf*. Test Site 1.1. Line 10S. Karous-Hjelt filtering of VLF M-field response over cultural feature.



25 MHz frequency

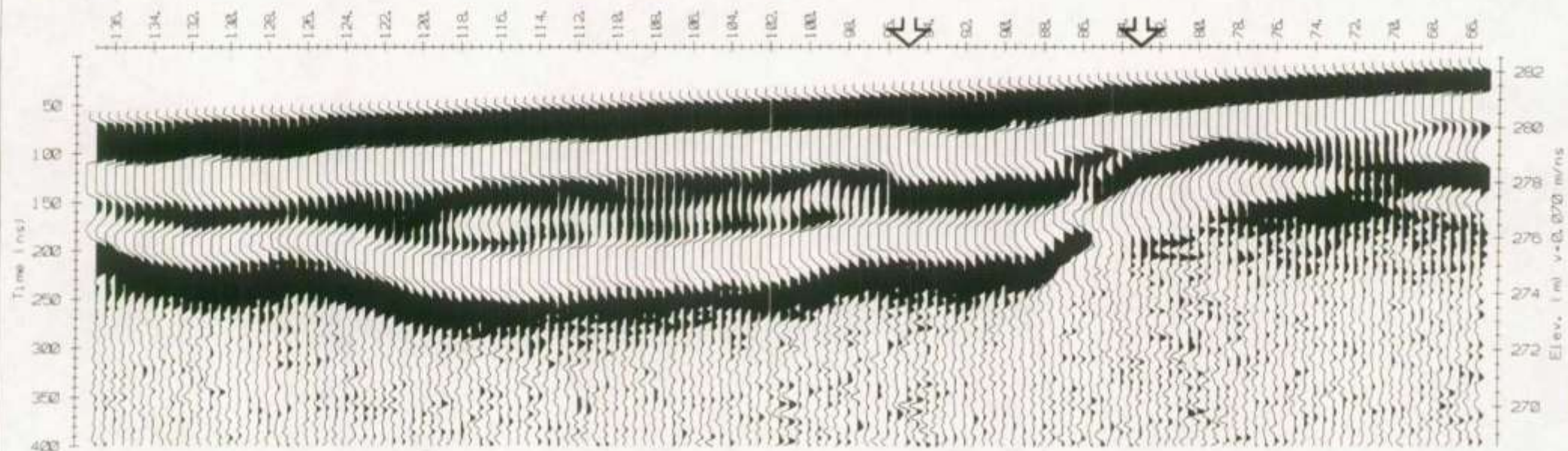


Figure 3 *gpr.* Test Site 1.2. GPR profiles for line 20S. 25 MHz antennae.

Frequency 50 MHz

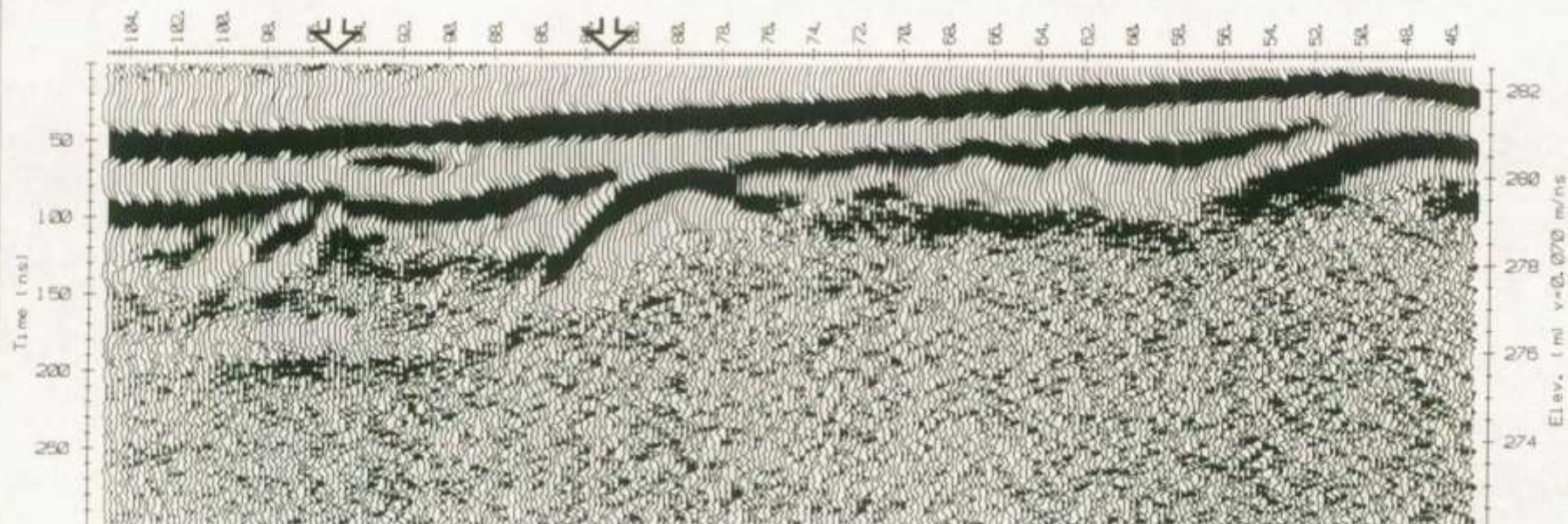


Figure 4 *gpr.* Test Site 1.2. GPR profiles for line 20S. 50 MHz antennae.



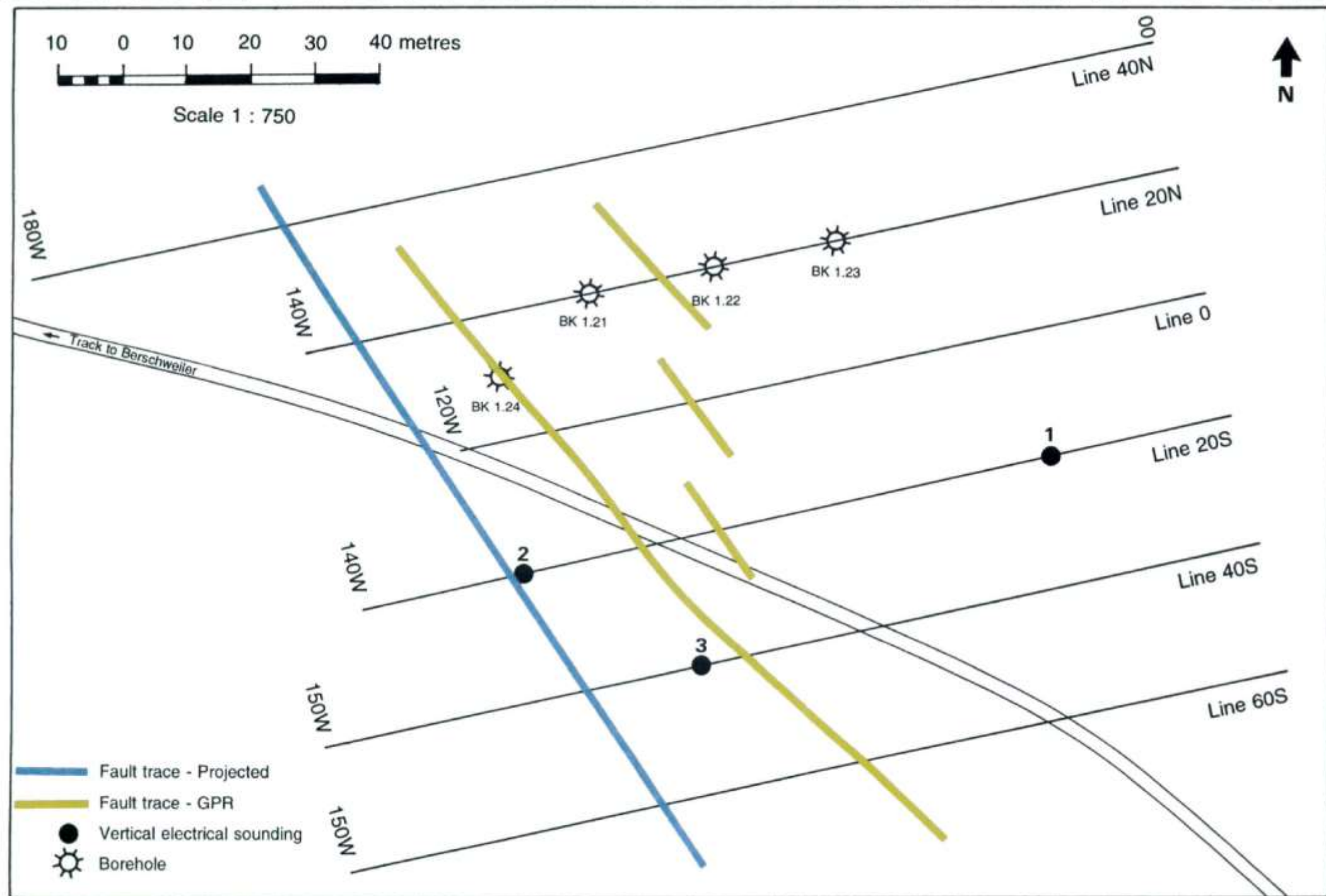


Figure 7. Test Site 1.2. Geophysical grid, borehole locations, and interpretation.

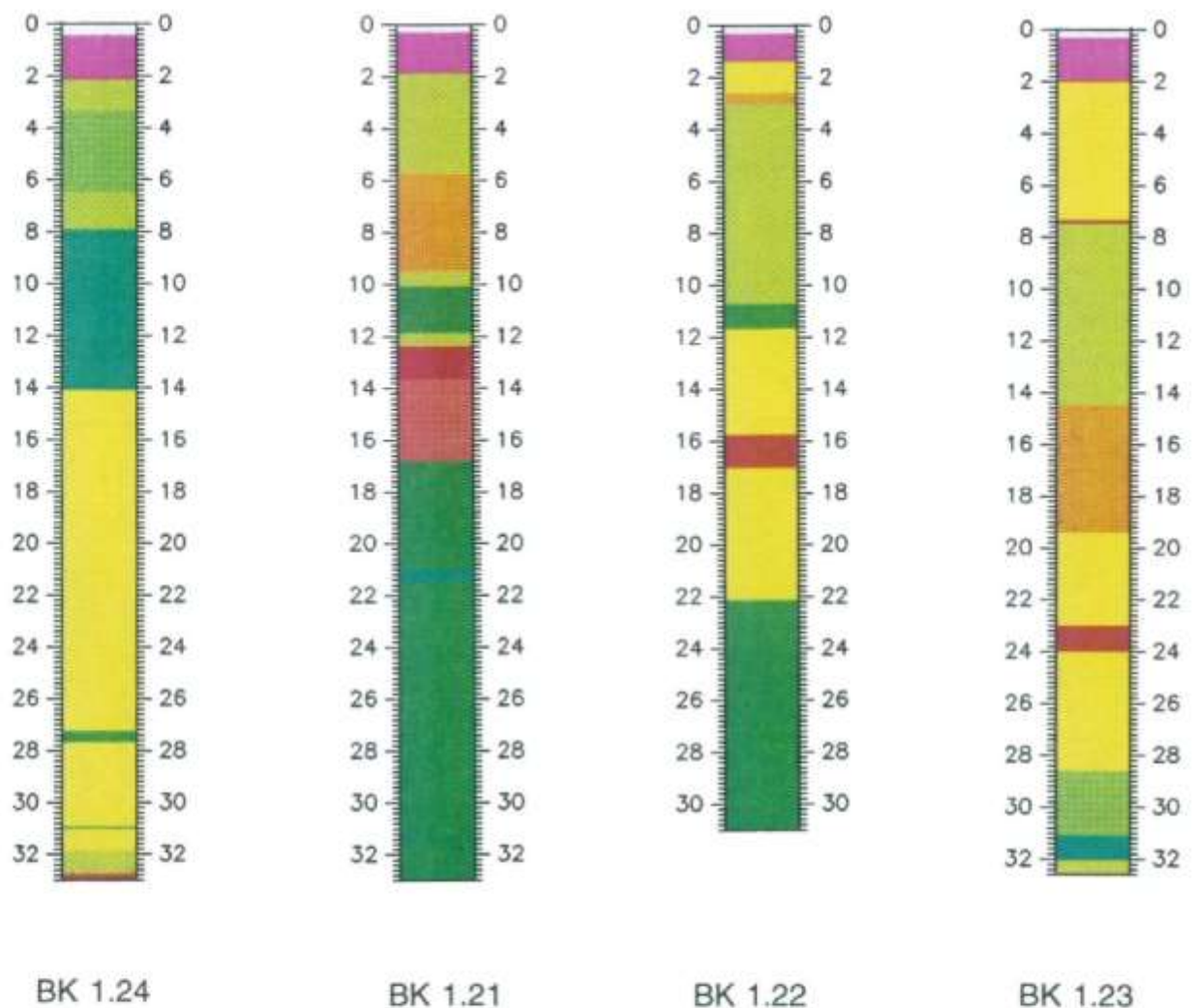
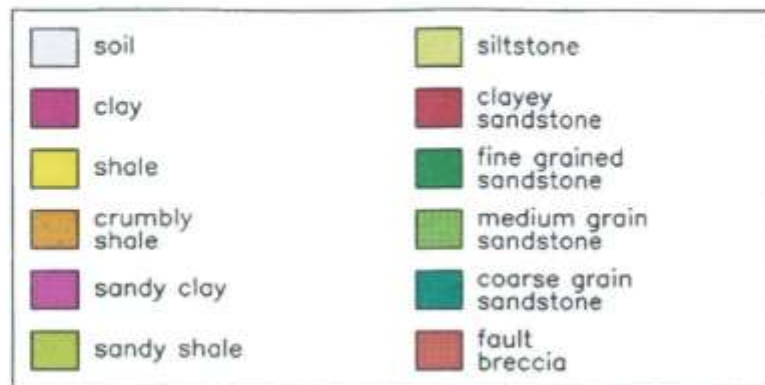


Figure 8. Test Site 1.2. Geological section: boreholes BK1.21, BK1.22, BK1.23 and BK1.24.



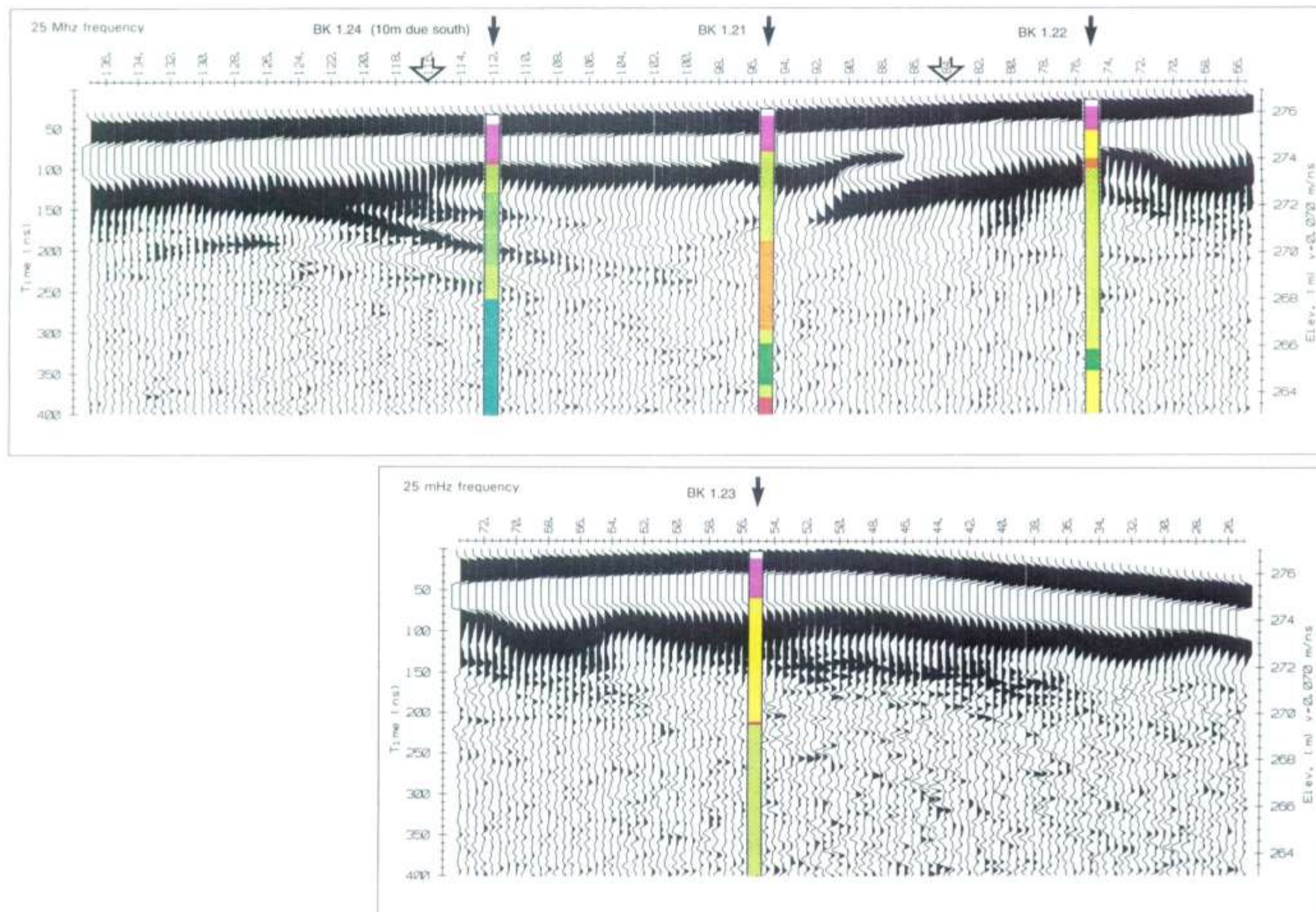


Figure 5 *gpr*. Test Site 1.2. GPR profiles for line 20N. 25 MHz antennae.



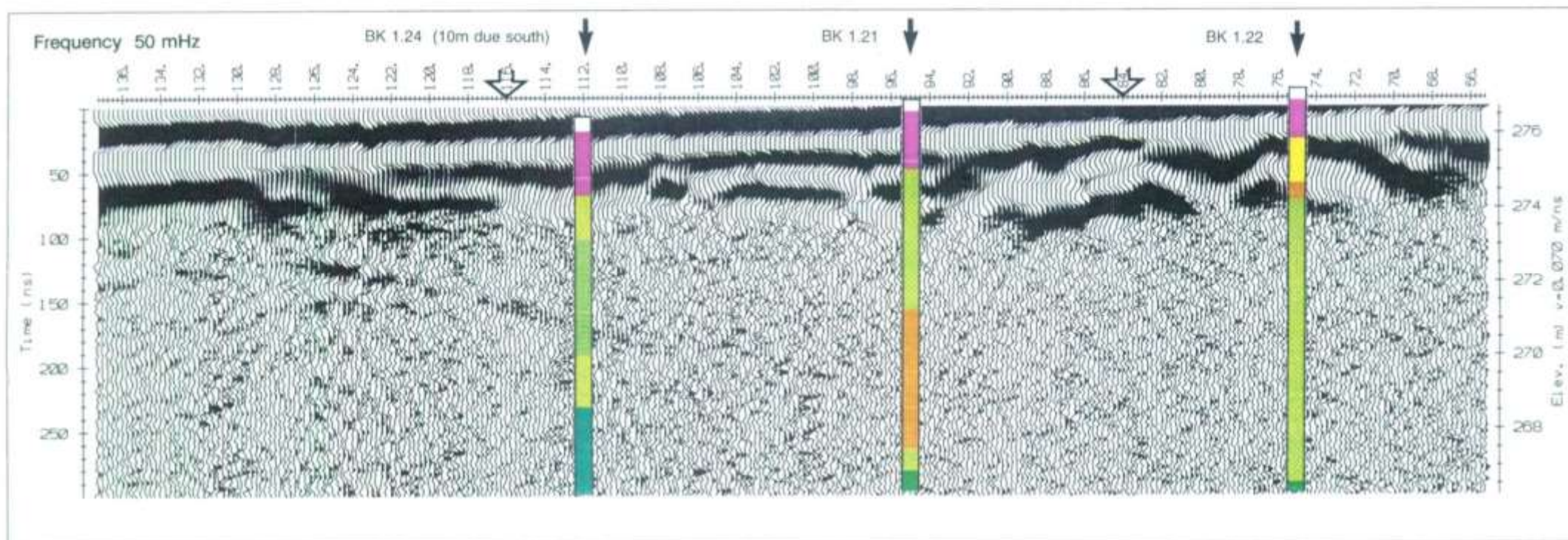


Figure 6 *gpr*. Test Site 1.2. GPR profiles for line 20N. 50 MHz antennae.

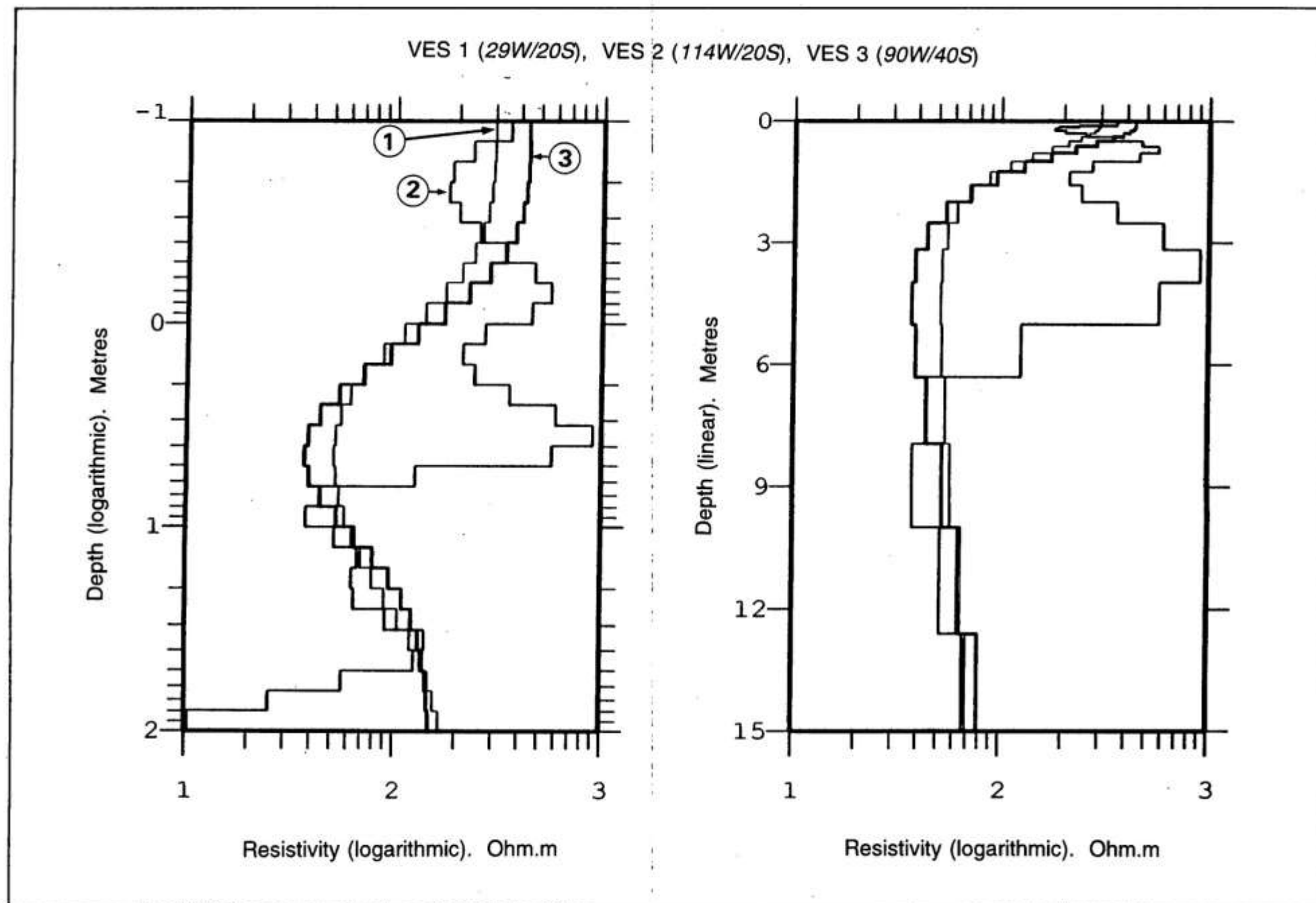


Figure 3 res.

Test Site 1.2. Interpretation of VES 1, 2, and 3.

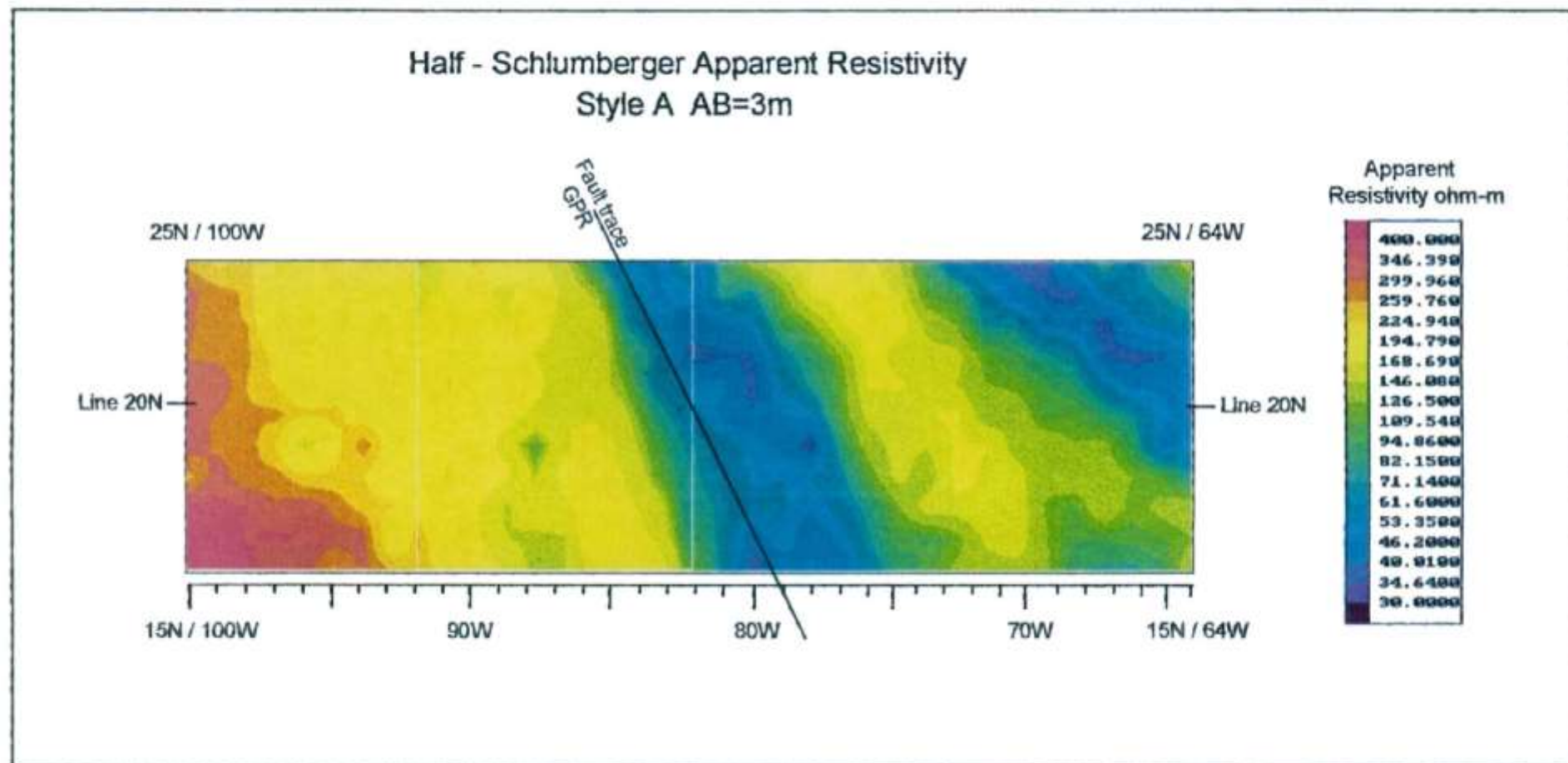


Figure 7 *rsc.* Test Site 1.2. RESCAN apparent resistivity maps for three overlapping sections.



# Site 1.2 a, b & c: Averaged overlaps

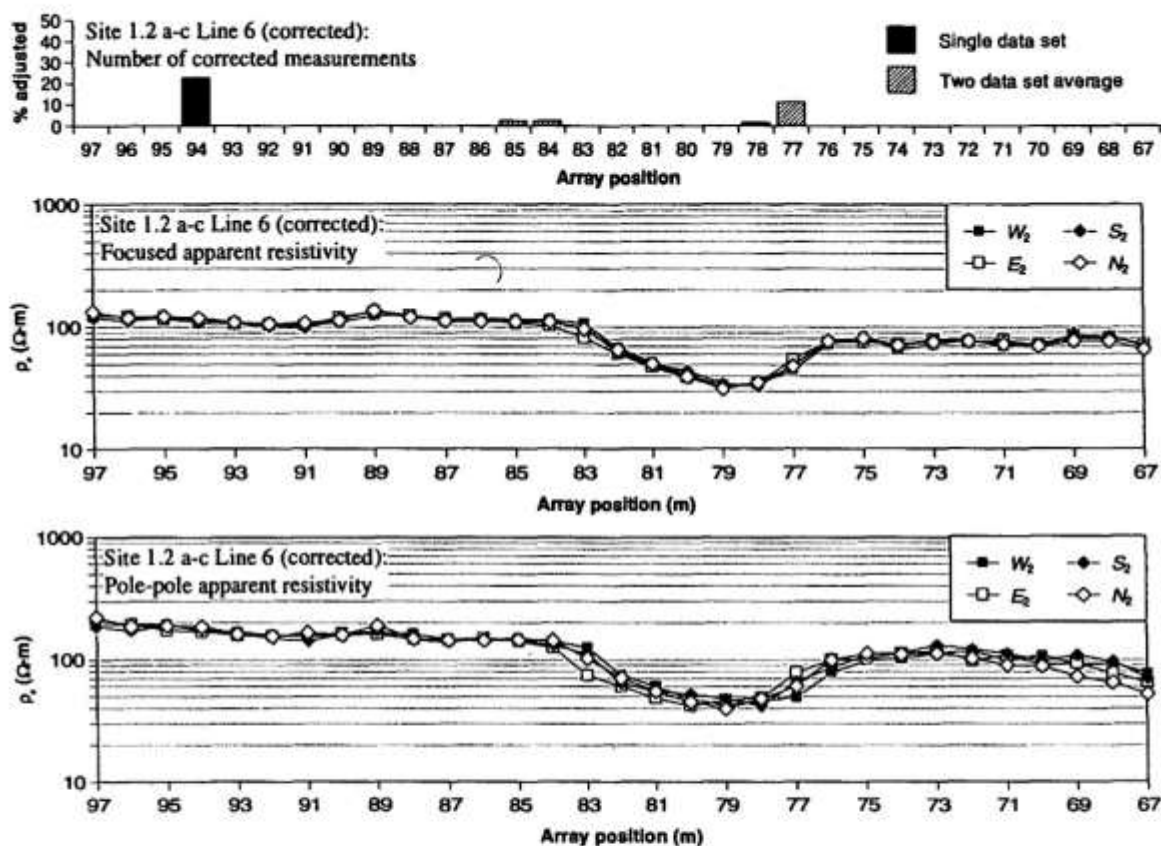


Figure 27 *rsc.* Test Site 1.2. Grids a, b, and c. Apparent resistivity traverse.

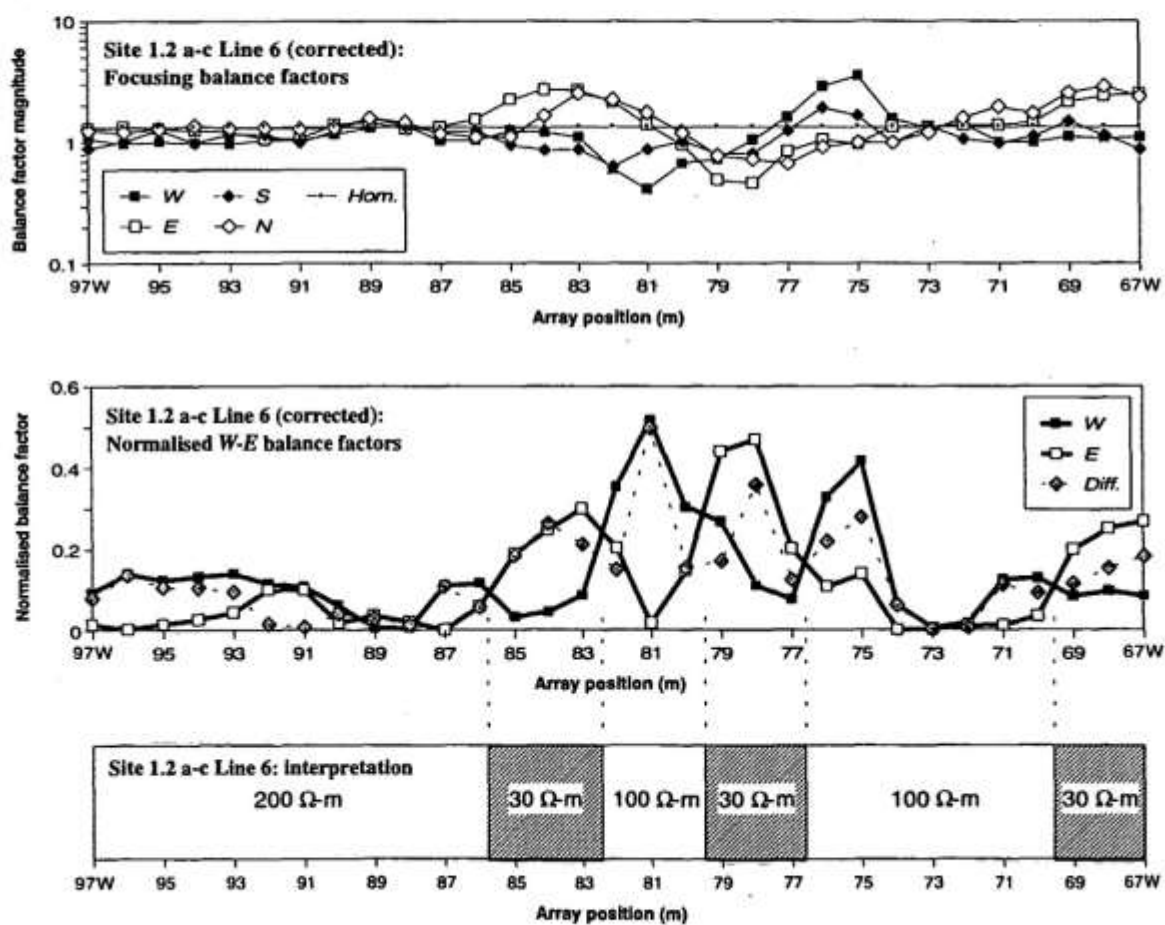


Figure 28 *rsc.* Test Site 1.2. Grids a, b, and c. Focussing balance factors.

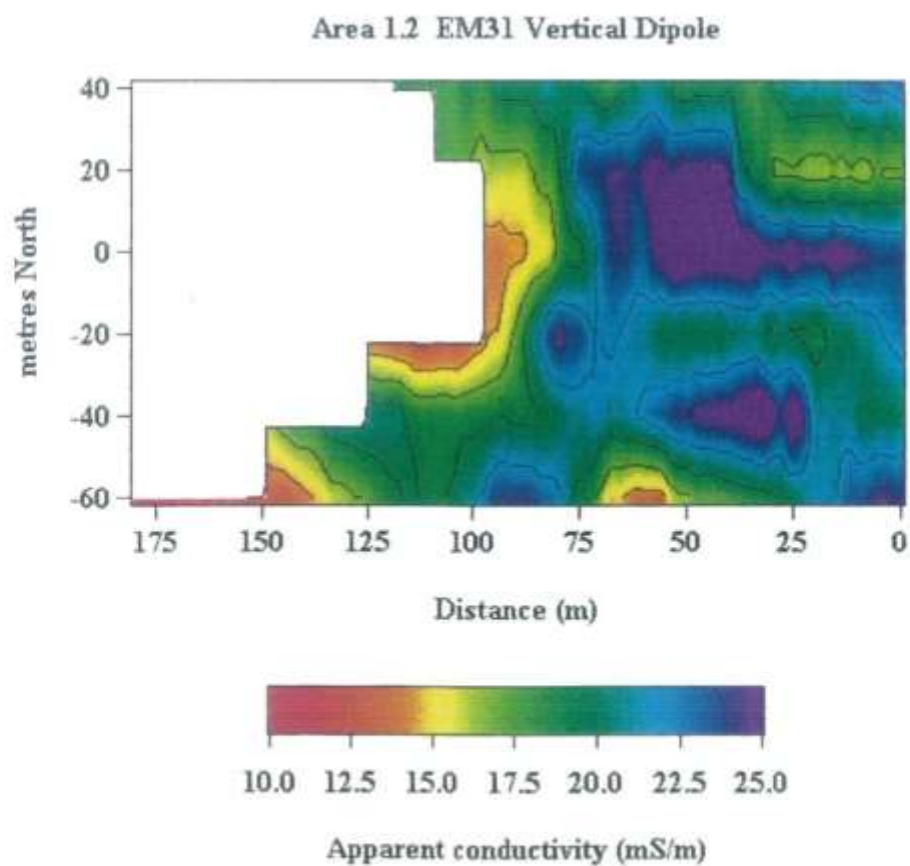
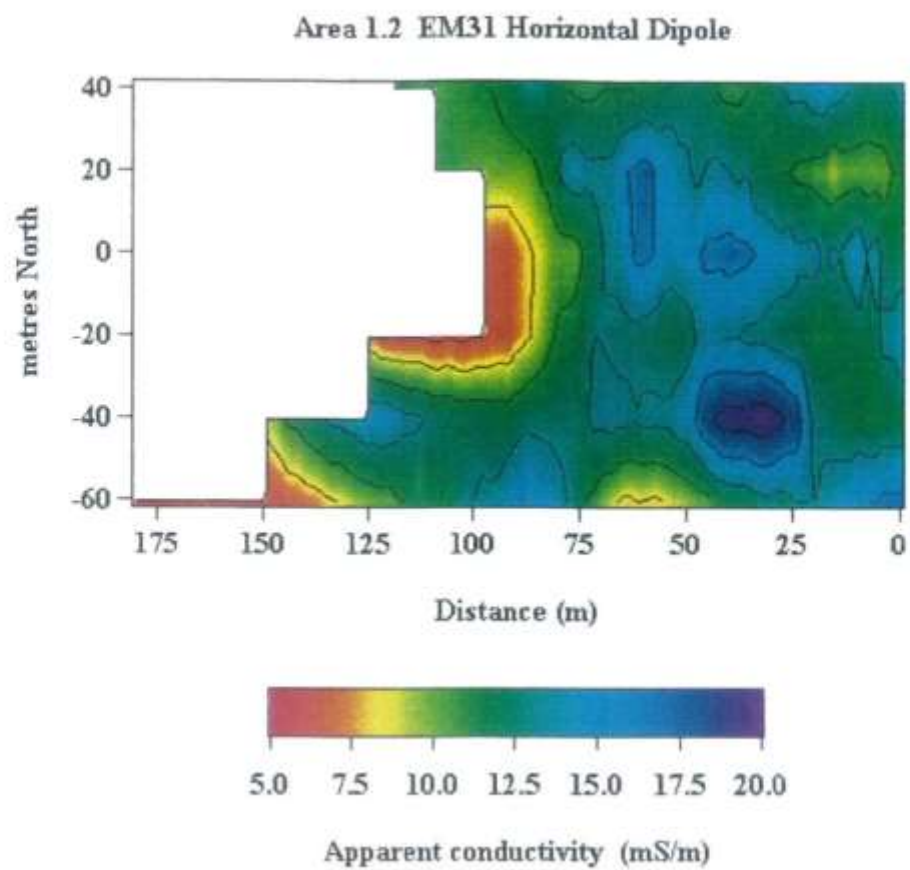


Figure 1 *em.* Test Site 1.2. Horizontal and vertical dipole conductivity contours.

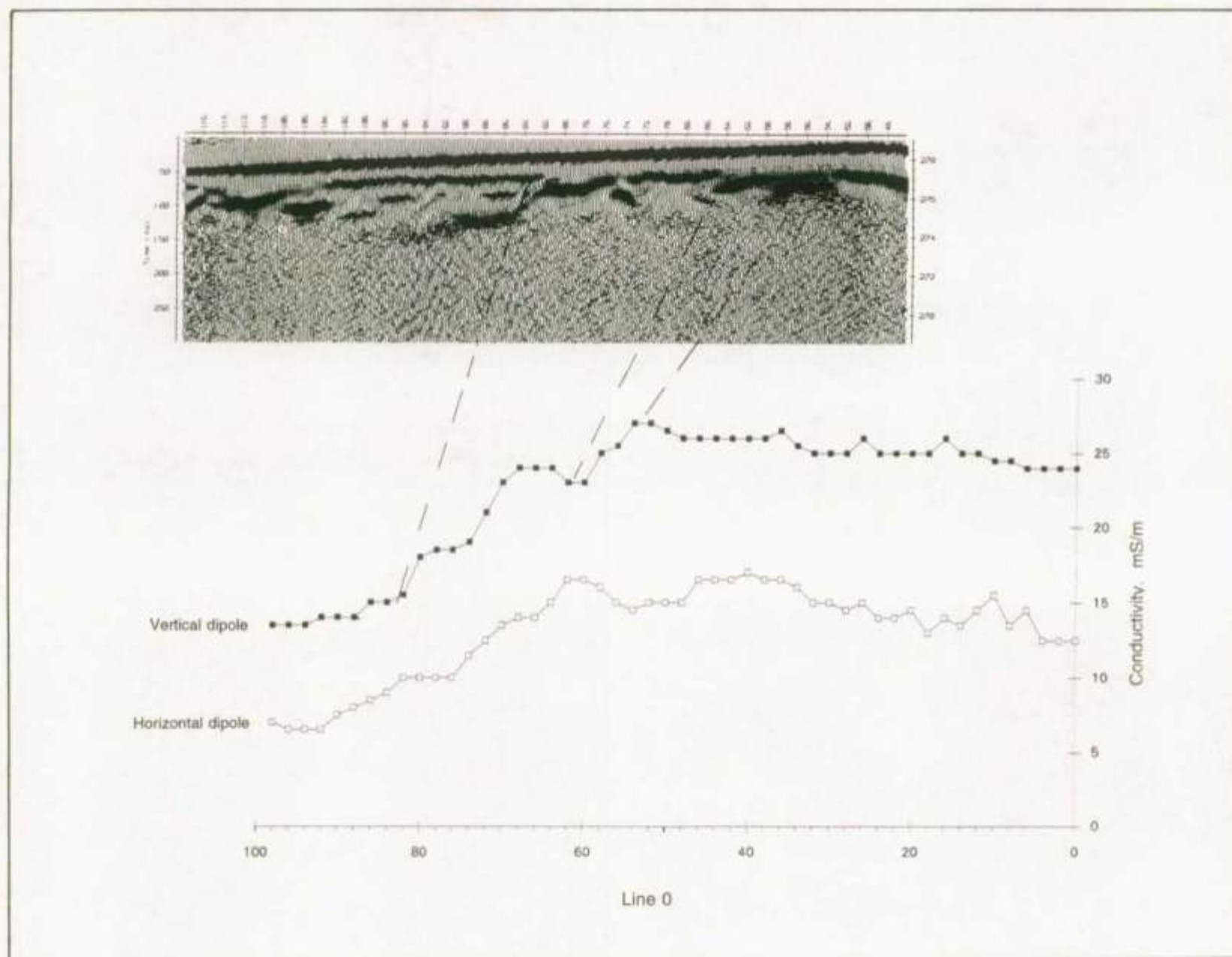


Figure 2 *em*. Test site 1.2. Composite horizontal and vertical dipole conductivity and GPR section for line 0.



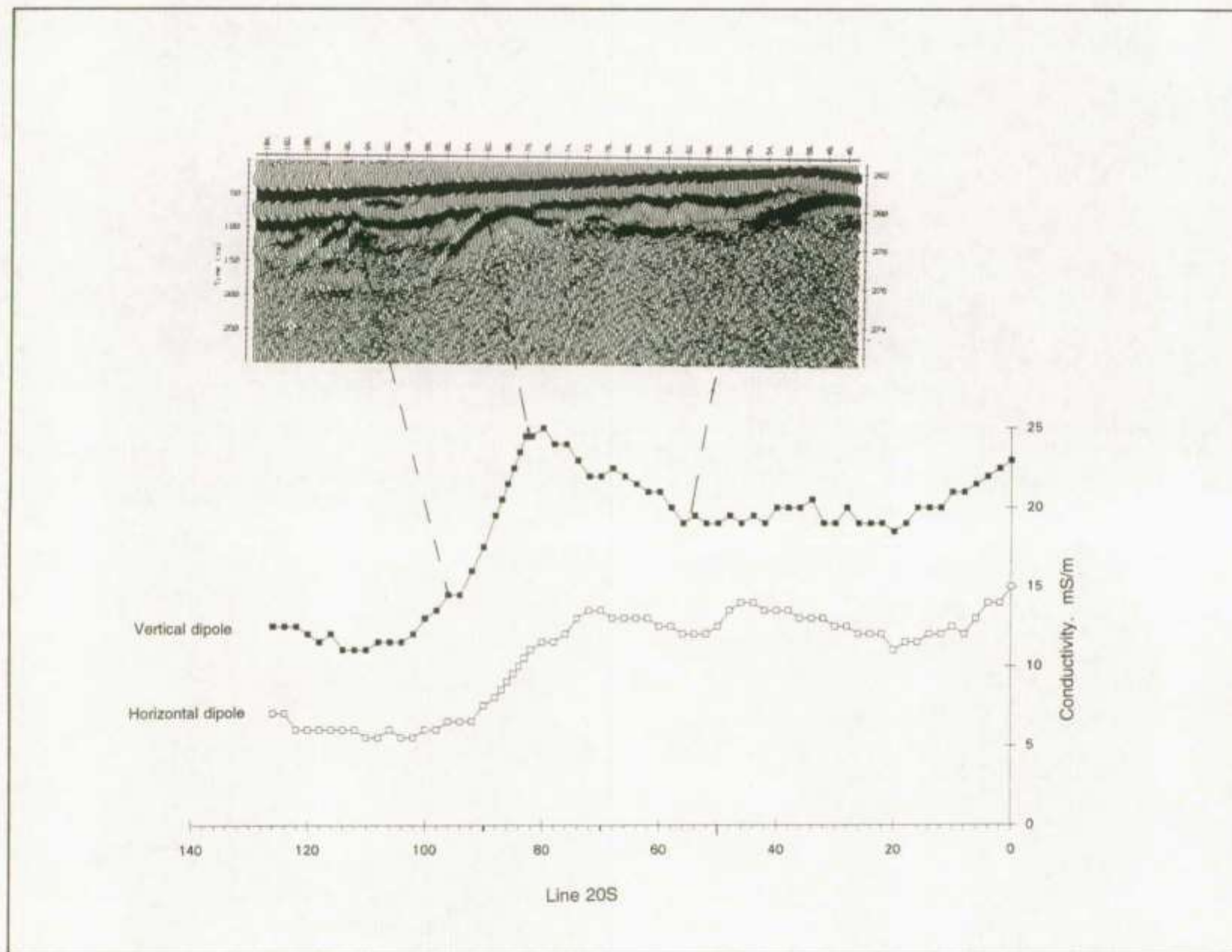


Figure 3 em. Test Site 1.2. Composite horizontal and vertical dipole conductivity and GPR section for line 20S.

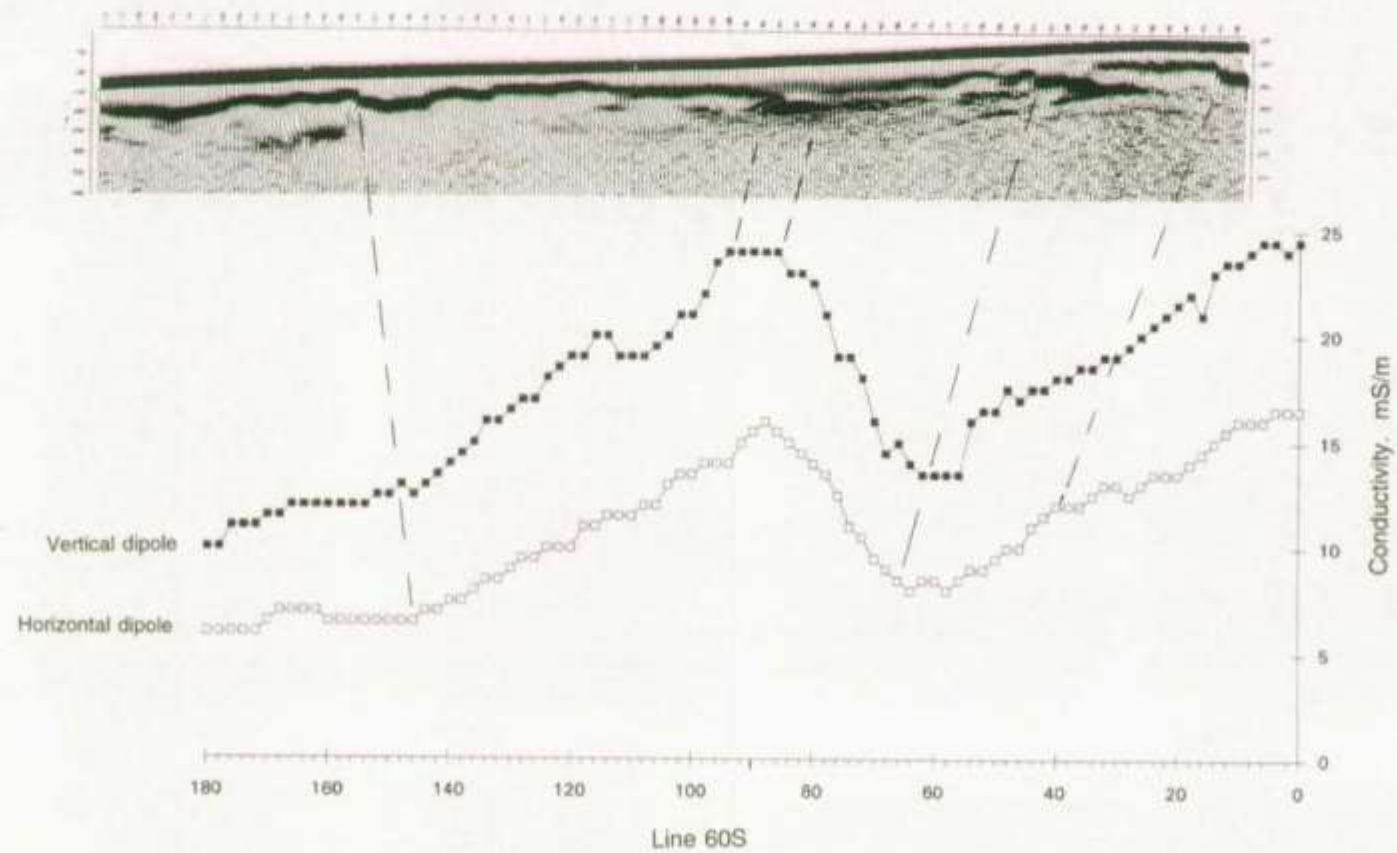


Figure 4 *em*. Test Site 1.2. Composite horizontal and vertical dipole conductivity and GPR section for line 60S and possible geological section.

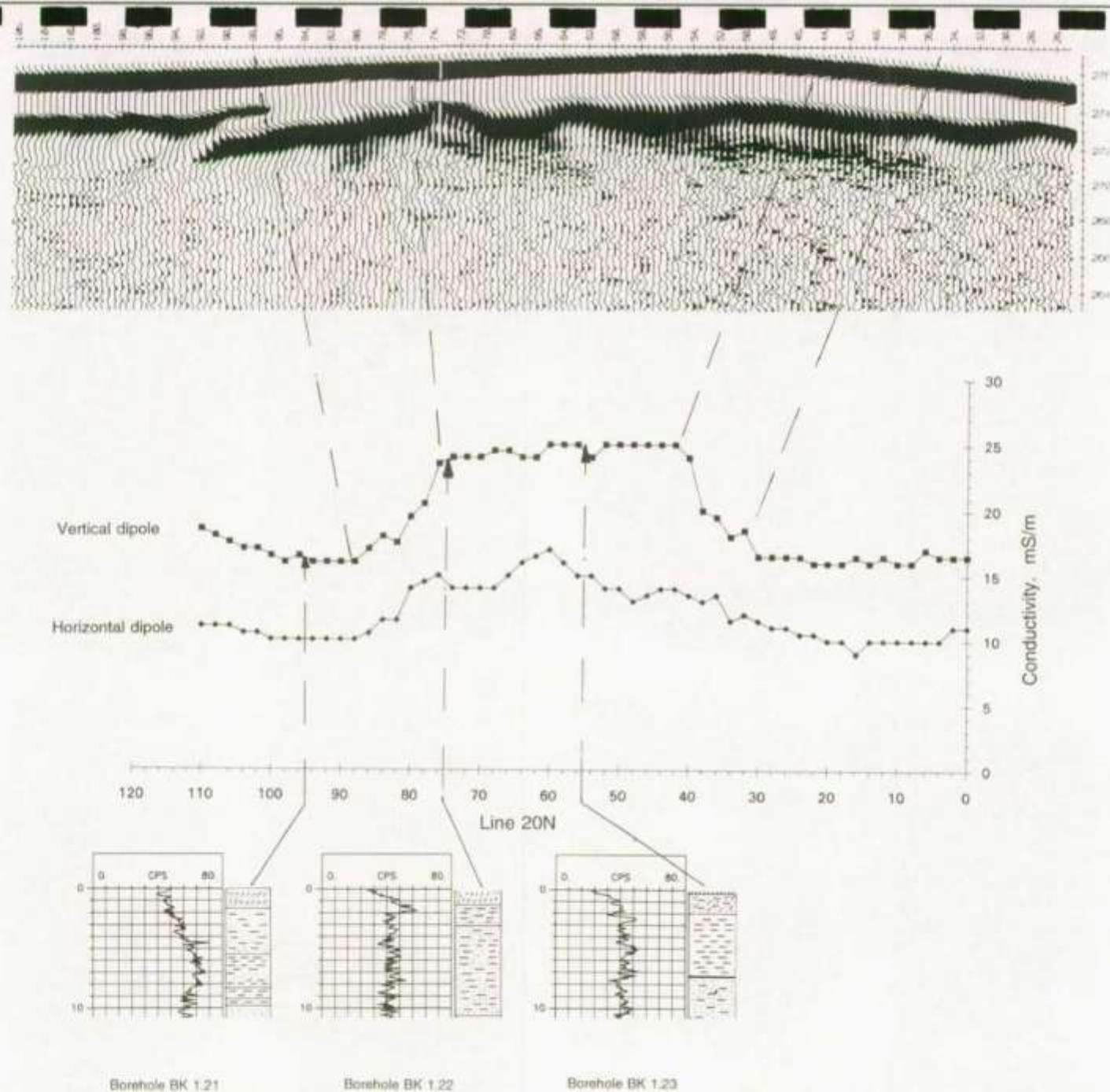


Figure 5 *em*. Test Site 1.2. Composite horizontal and vertical dipole conductivity and GPR section for line 20N and proven geology.



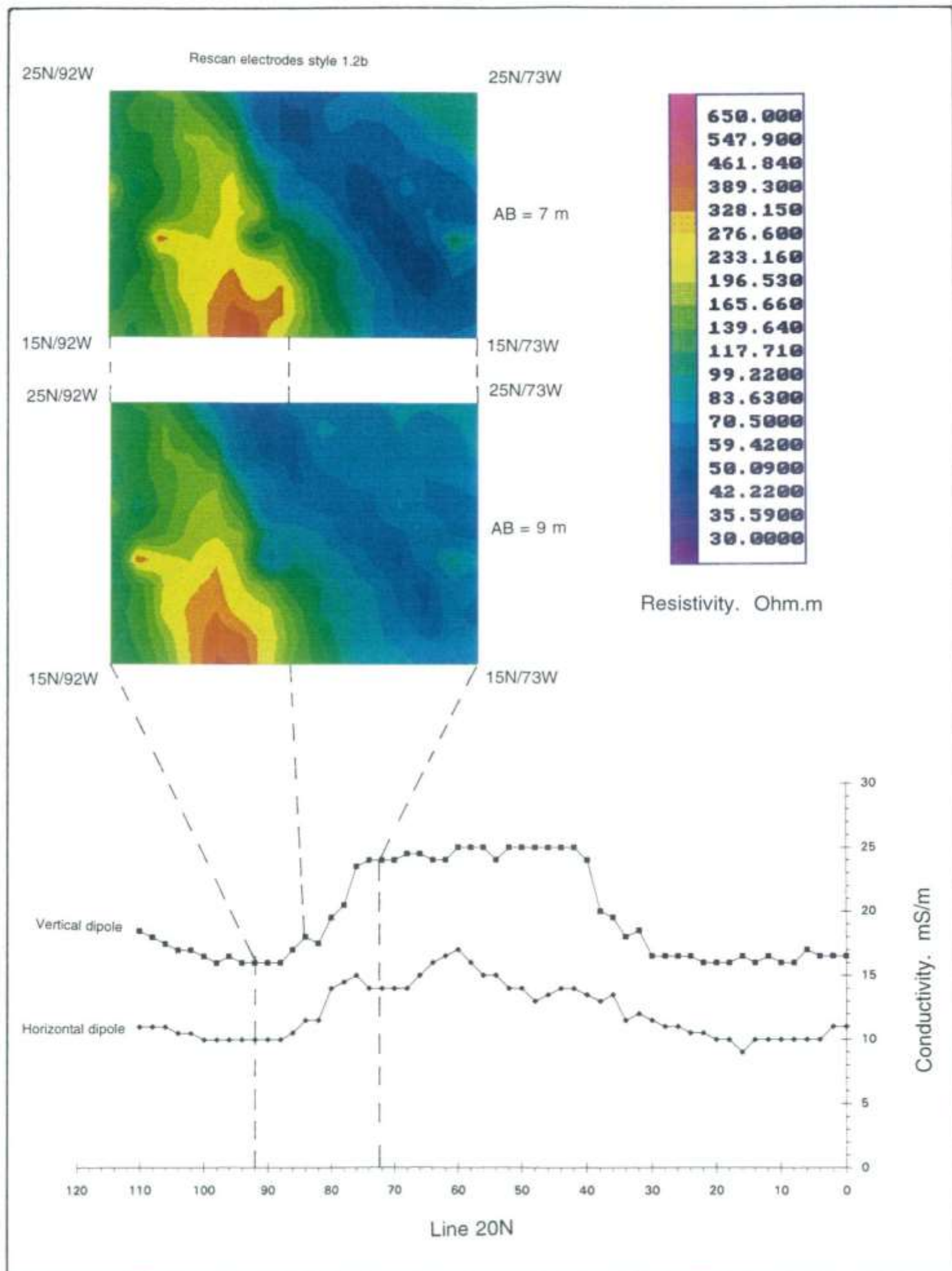
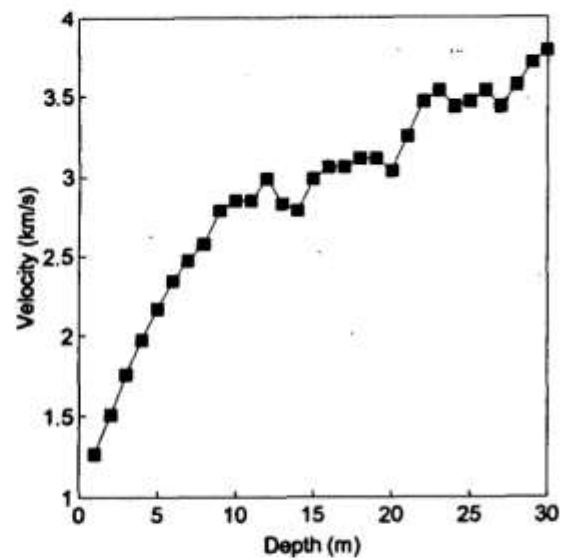
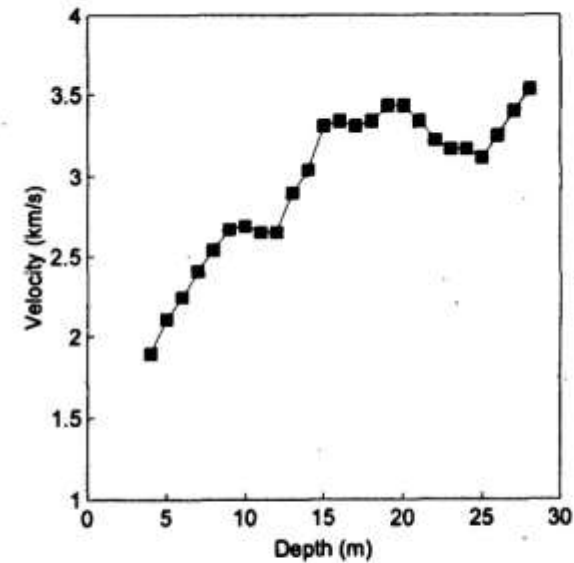


Figure 6 em. Test Site 1.2. Composite of conductivity profiles and Rescan images of part of line 20N.

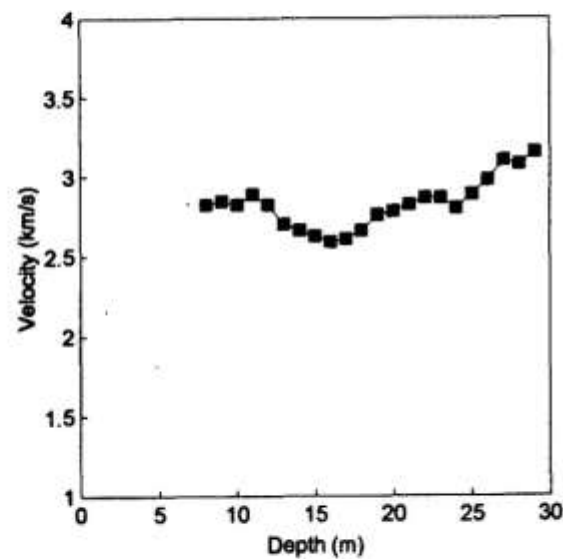




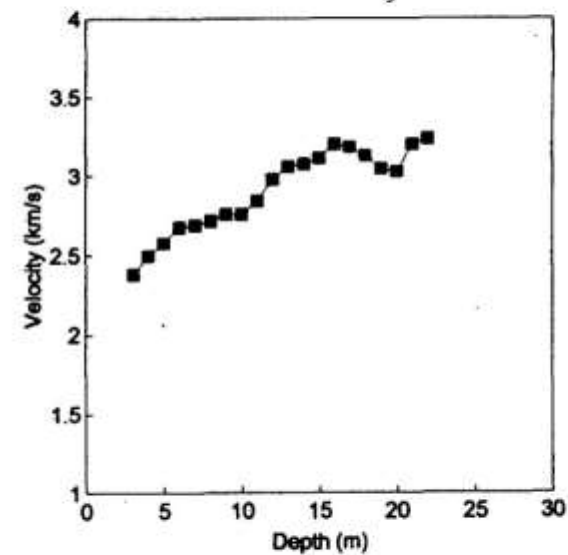
Test Site 1.2. Setup BK1.22/BK1.23



Test Site 1.2. Setup BK1.21/BK1.22



Test Site 1.2. Setup BK1.24/BK1.21



Test Site 1.4. Setup BK1.43/BK1.44

Figure 1 *sei*.

Test Sites 1.2 and 1.4. Plots of horizontal velocity versus depth.

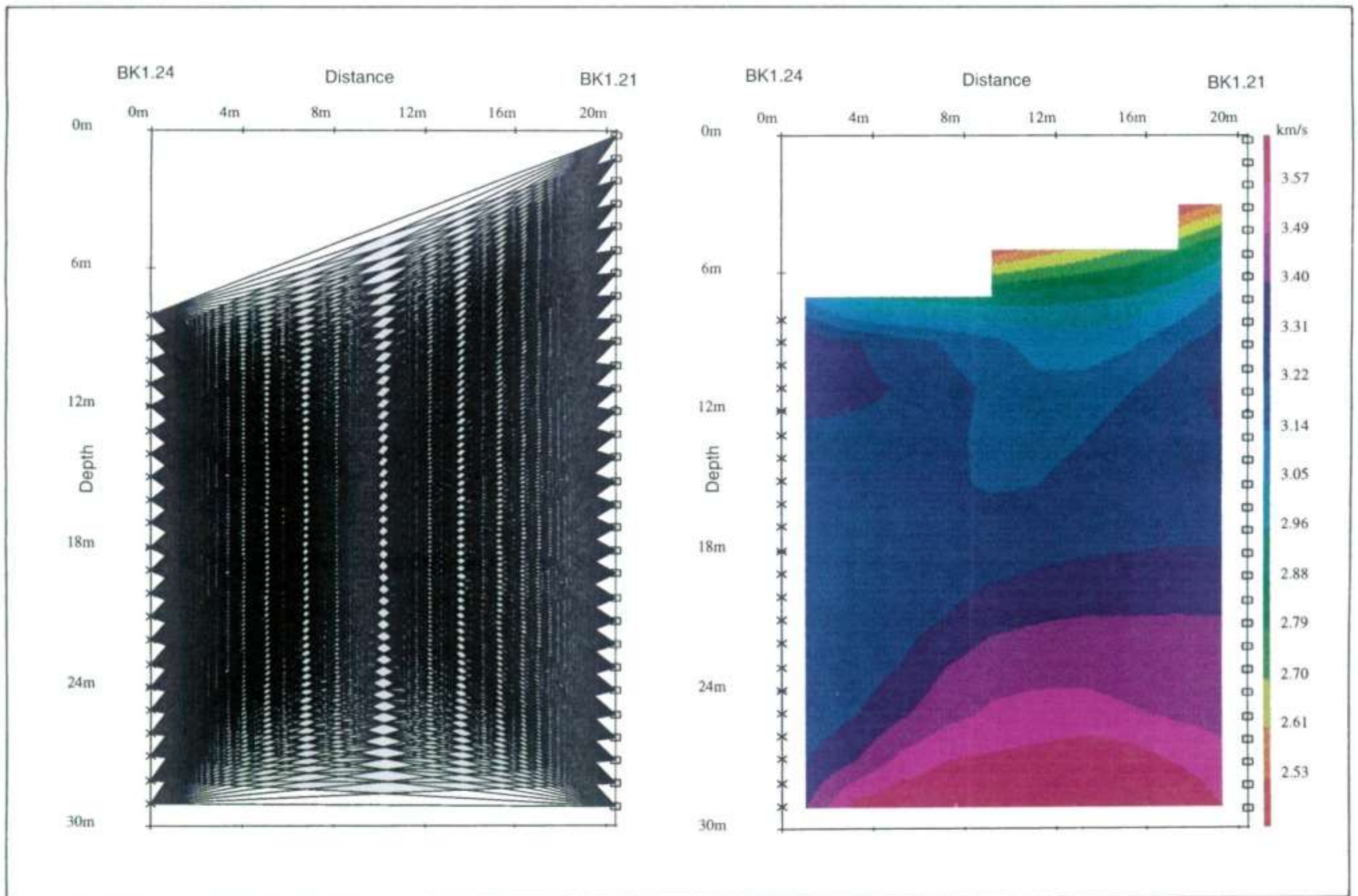


Figure 2a, 2b *sei*. Test Site 1.2. Setup BK1.24/1.21. Hydrophone data. (a) Raypath coverage. (b) Straight ray, 10% anisotropy correction.

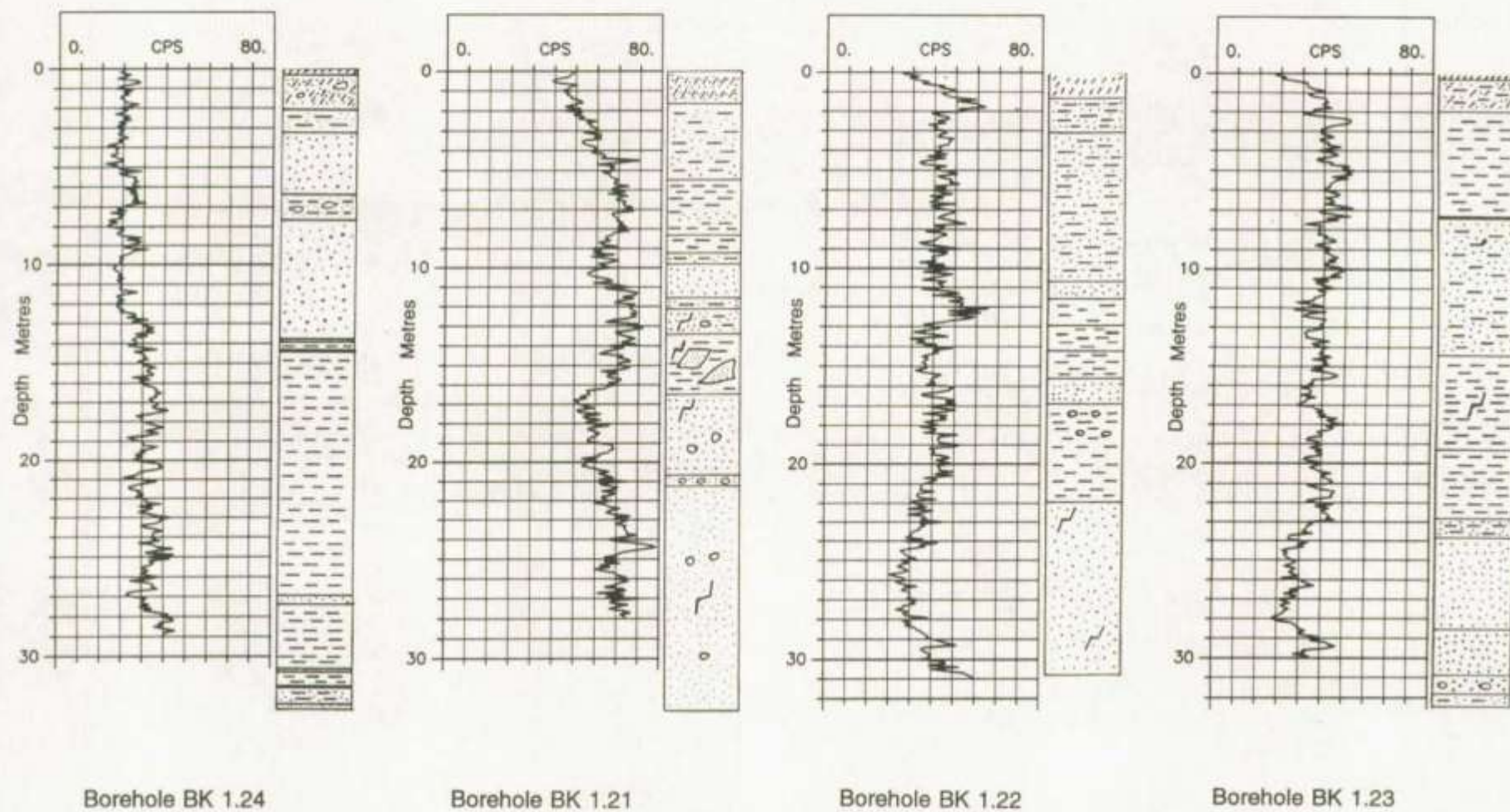


Figure 1 gam.

Test Site 1.2. Natural gamma logs for boreholes BK1.21 to BK1.24.



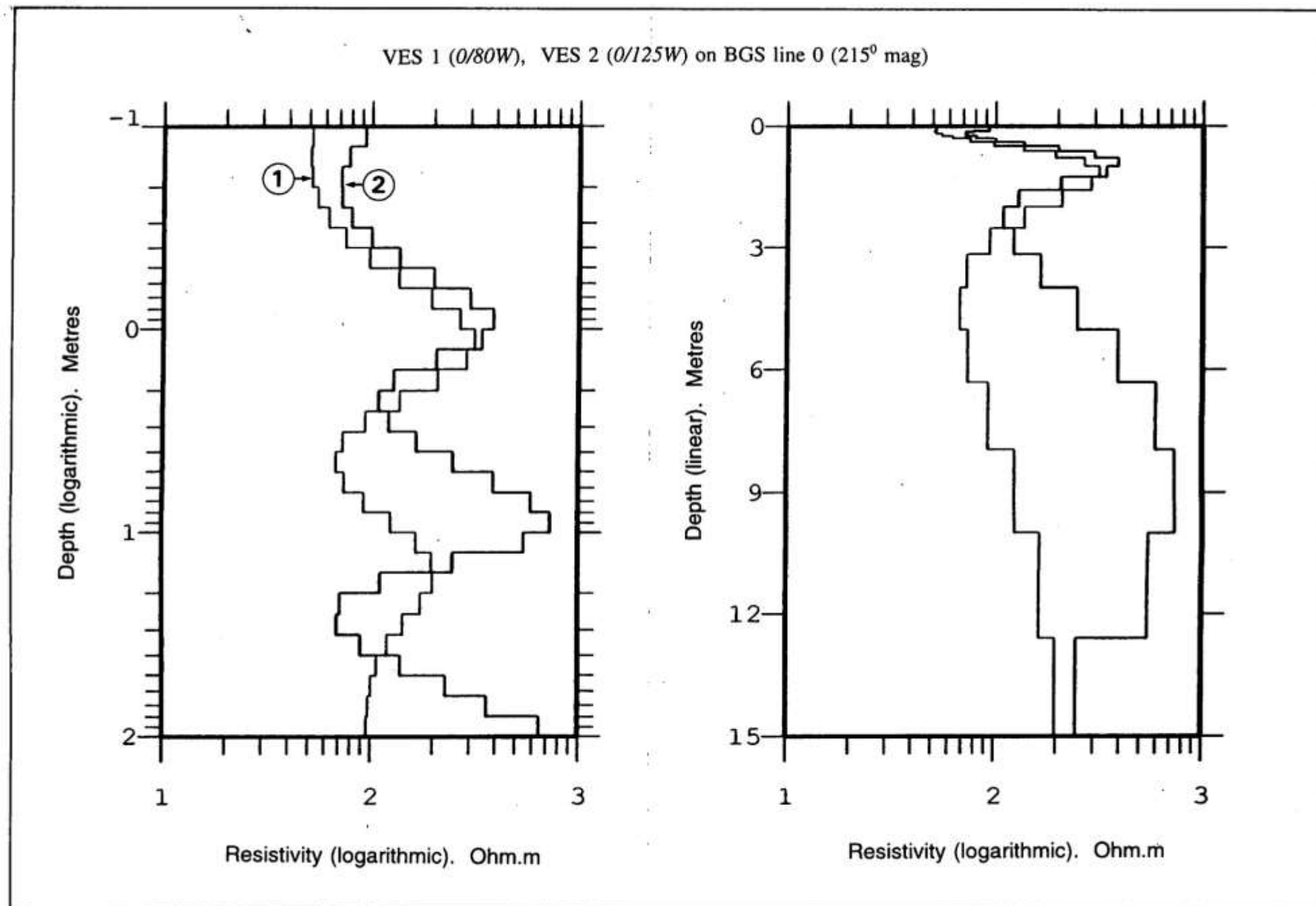


Figure 4 *res.*

Test Site 1.3. Interpretation of VES 1, and 2.

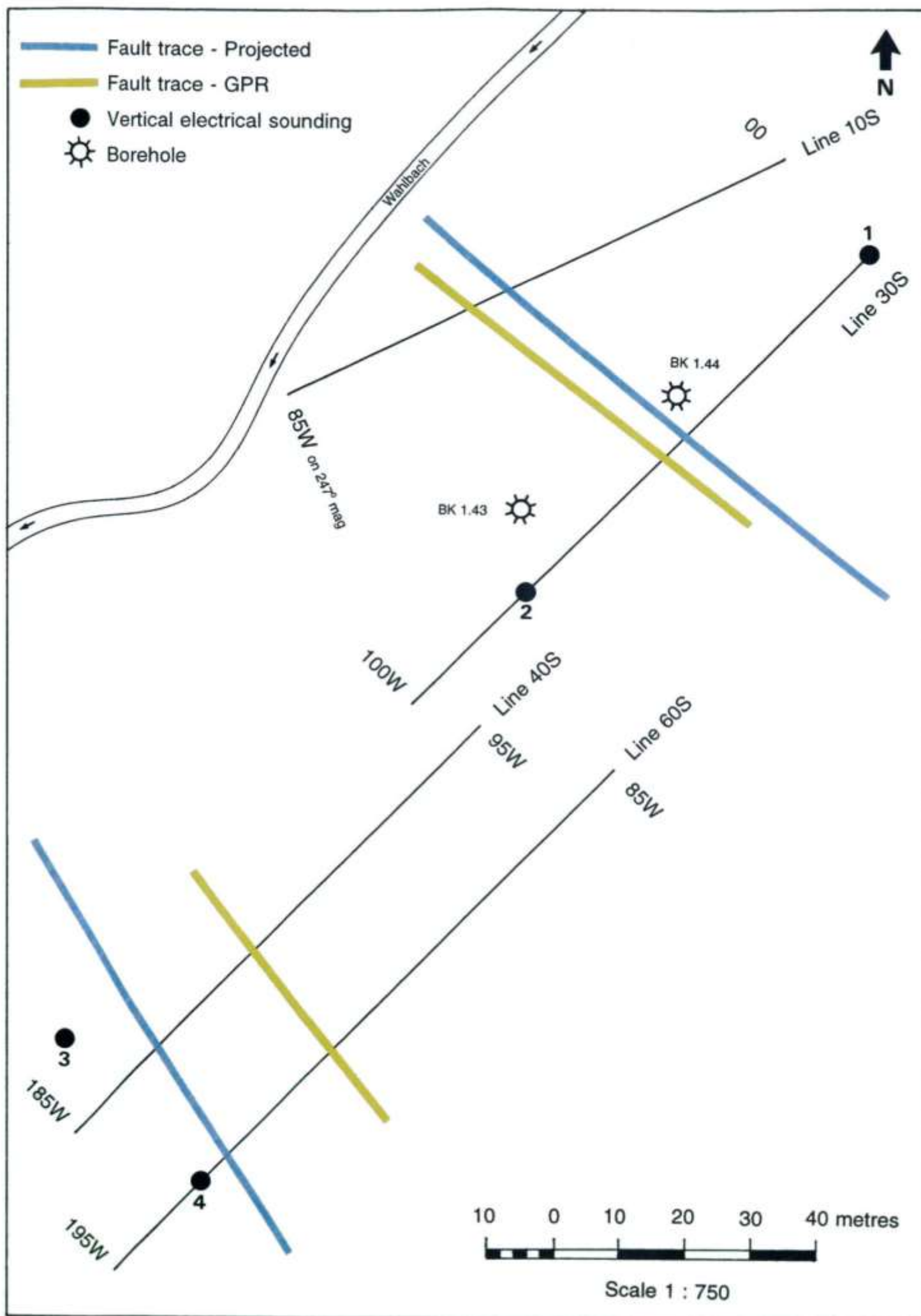


Figure 9. Test Site 1.4. Geophysical grid, borehole locations, and interpretation.

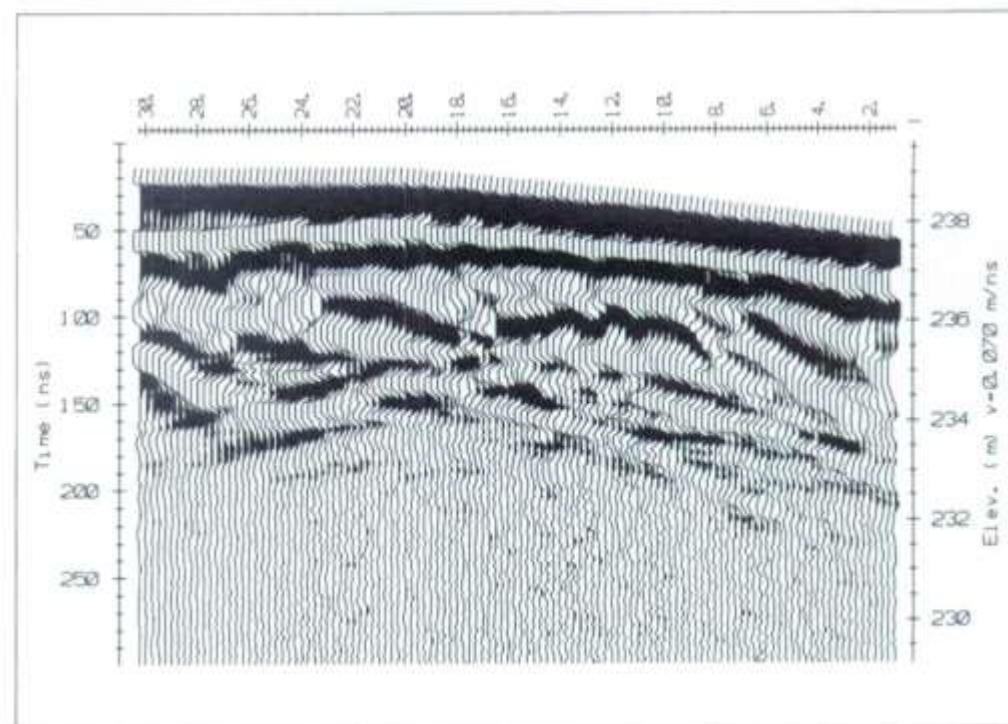
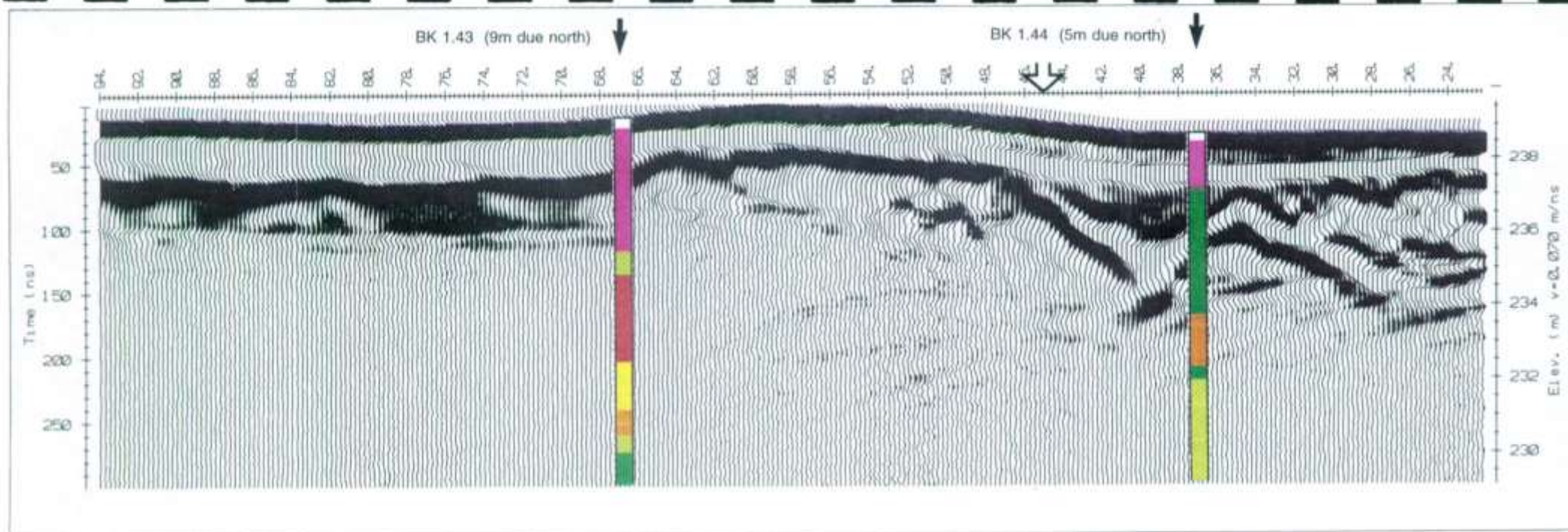
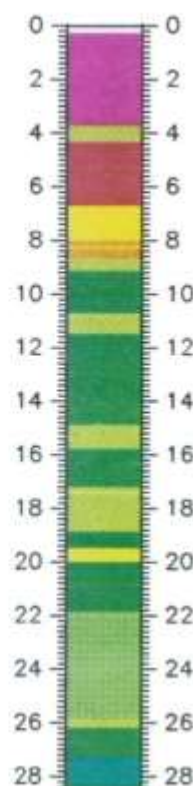
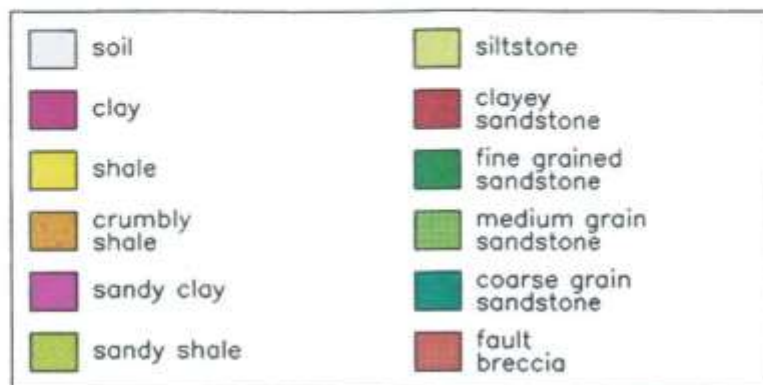
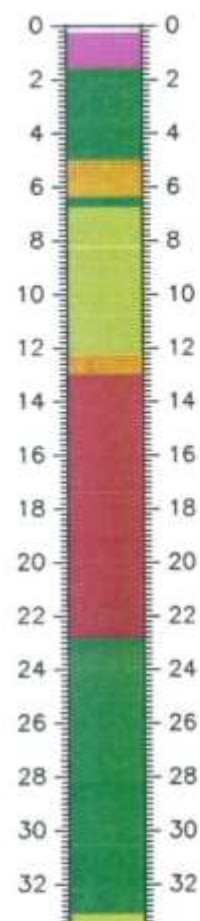


Figure 7 *gpr*. Test Site 1.4. GPR profile for line 30S. 50 MHz antennae.





BK 1.43



BK 1.44

Figure 10. Test Site 1.4. Geological section: boreholes BK1.43, BK1.44

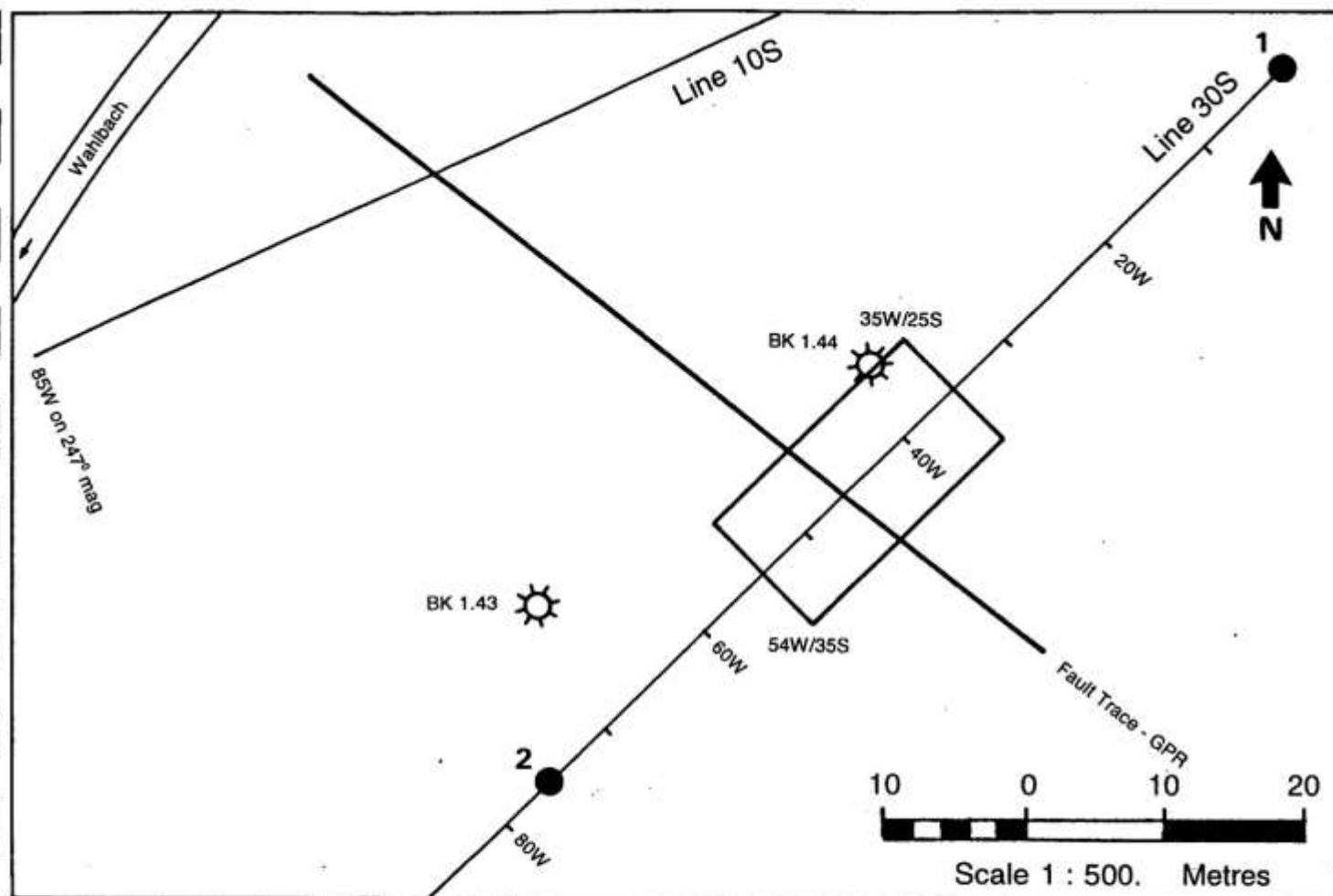


Figure 30 *rsc.* Test Site 1.4. Plan (partial) of site showing location of RESCAN grid.

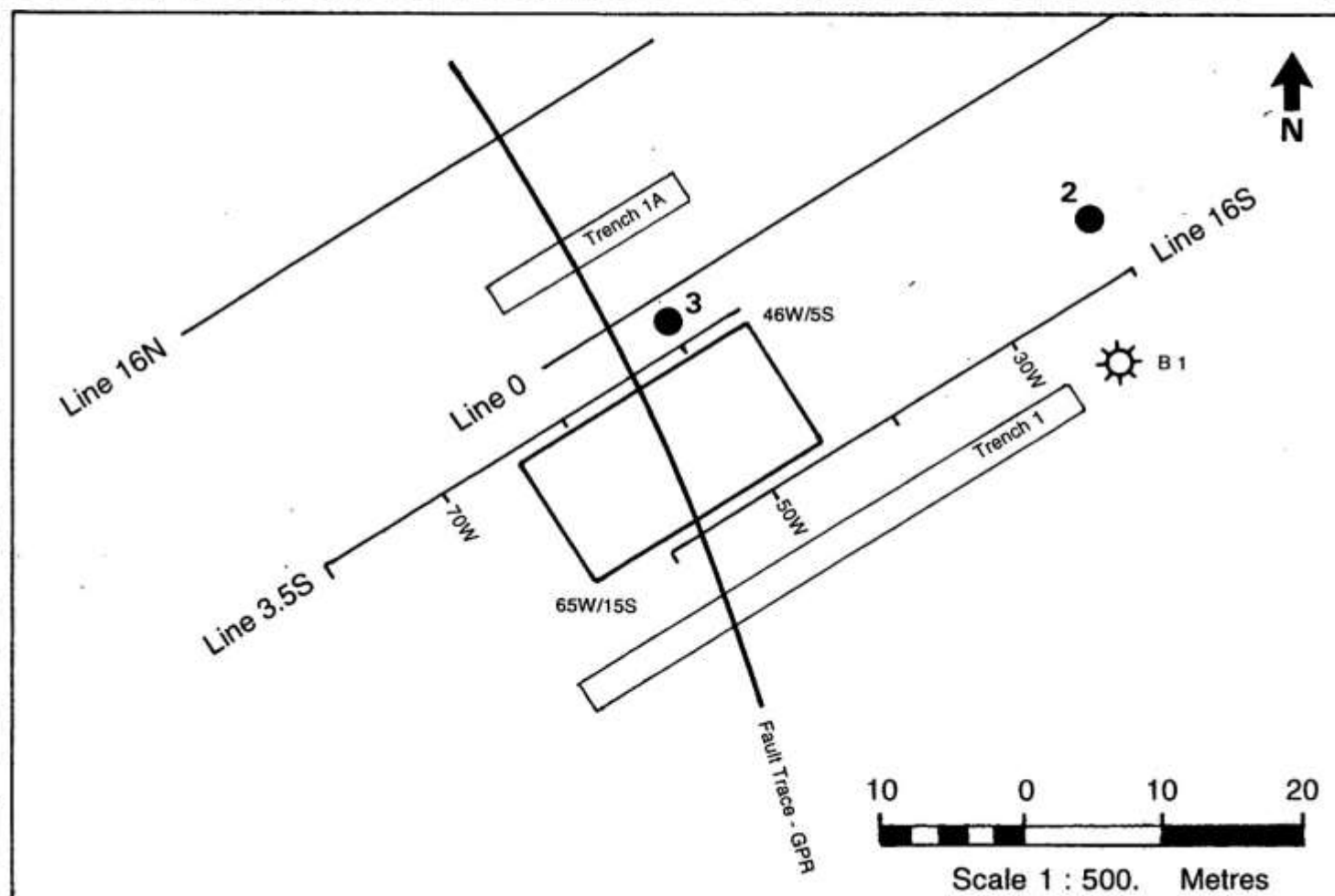


Figure 31 *rsc.* Test Site 2.1. Plan (partial) of site showing location of RESCAN grid.

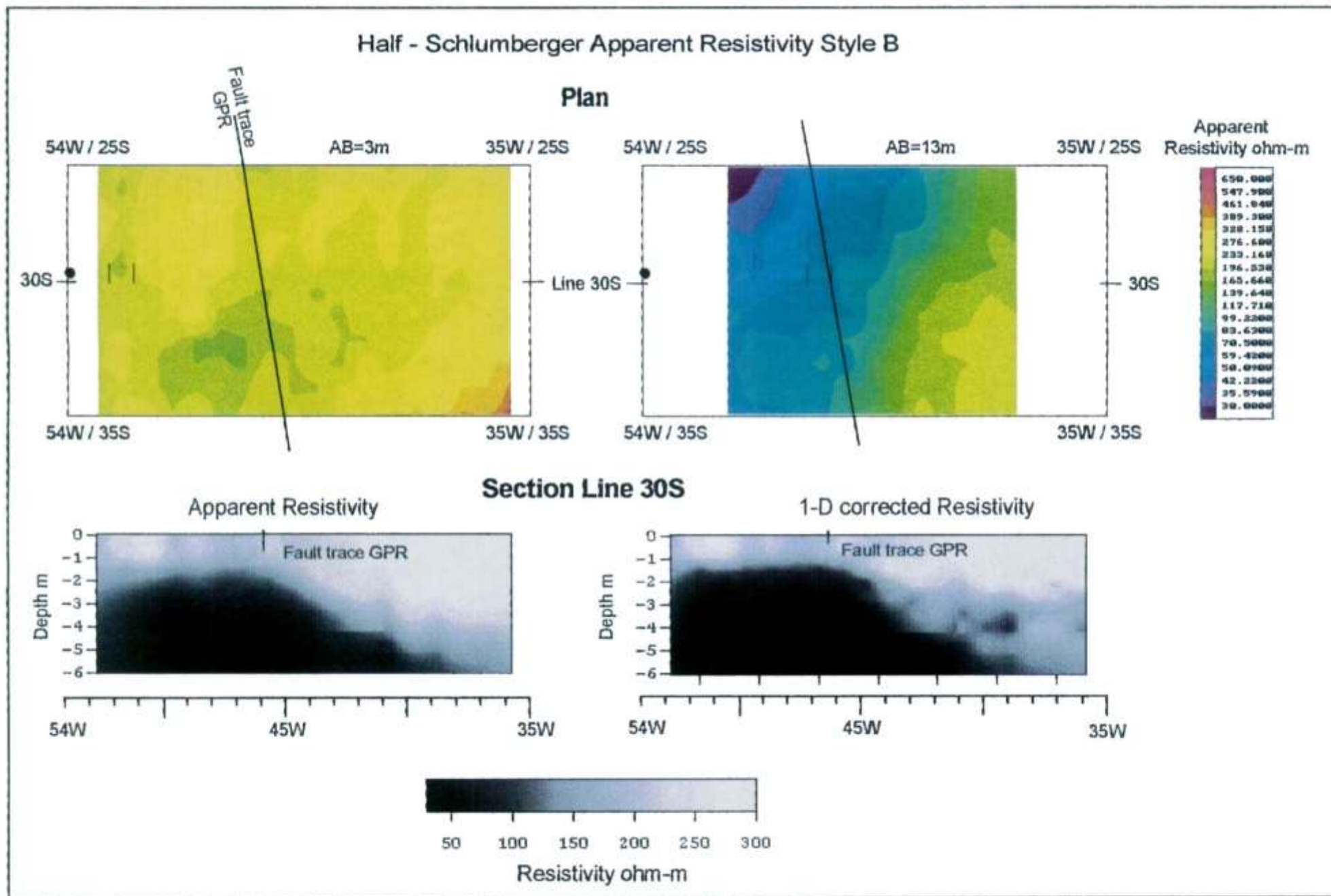


Figure 8 *rsc.* Test Site 1.4. Resistivity imaging using pole-dipole 'half Schlumberger' measurements made under computer control. Pseudo and 1D corrected XZ sections show different responses over a fault identified by GPR.



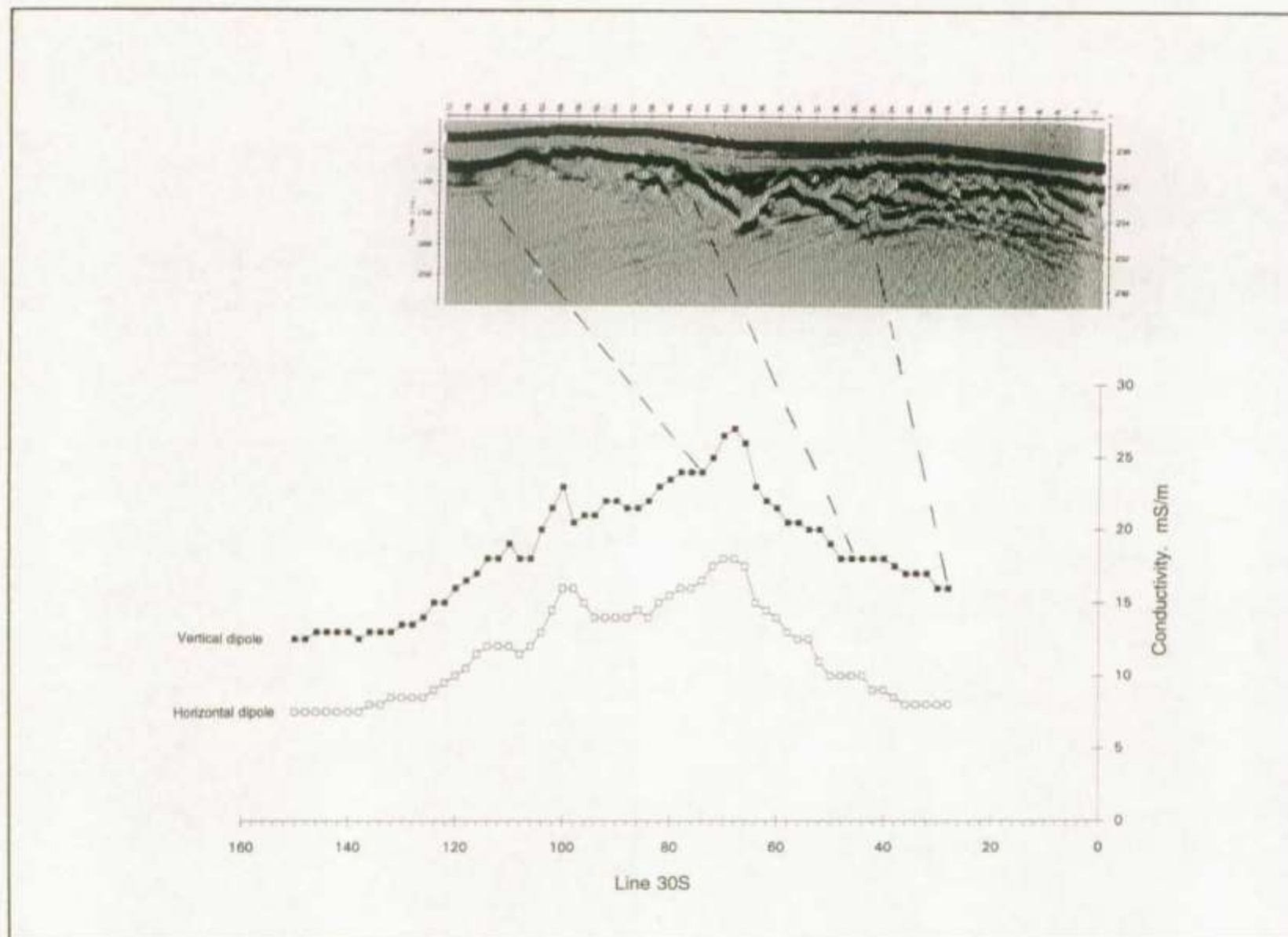
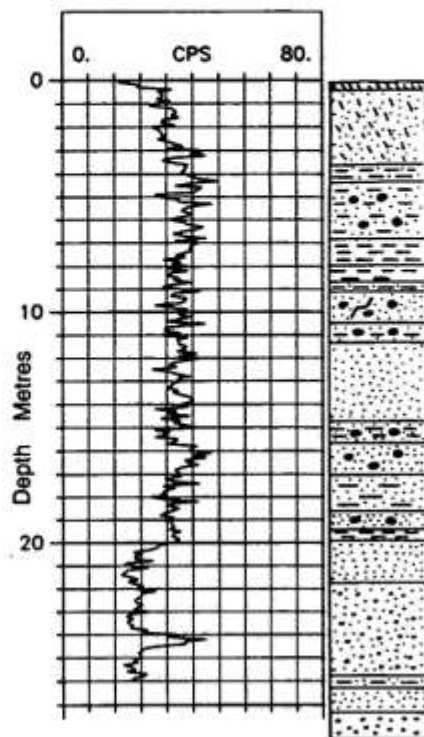
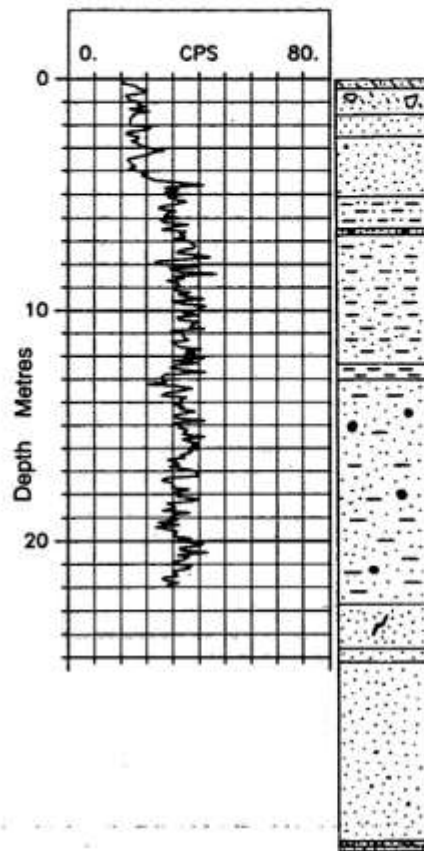


Figure 7 em. Test Site 1.4. Composite horizontal and vertical dipole conductivity and GPR section for line 30S.



Borehole BK 1.43



Borehole BK 1.44

Figure 2 *gam.*

Test Site 1.4. Natural gamma logs for boreholes BK1.43 to BK1.44.

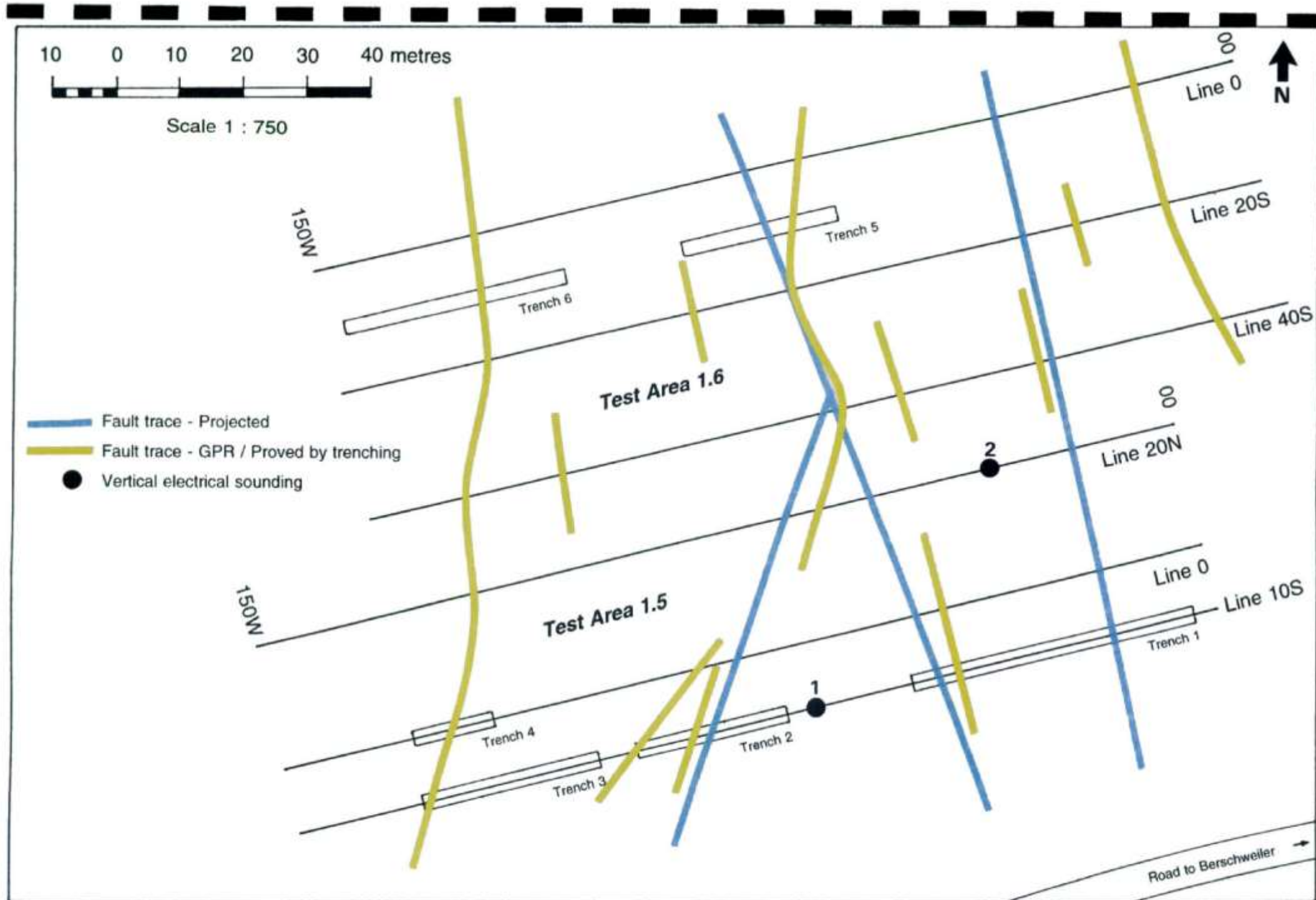
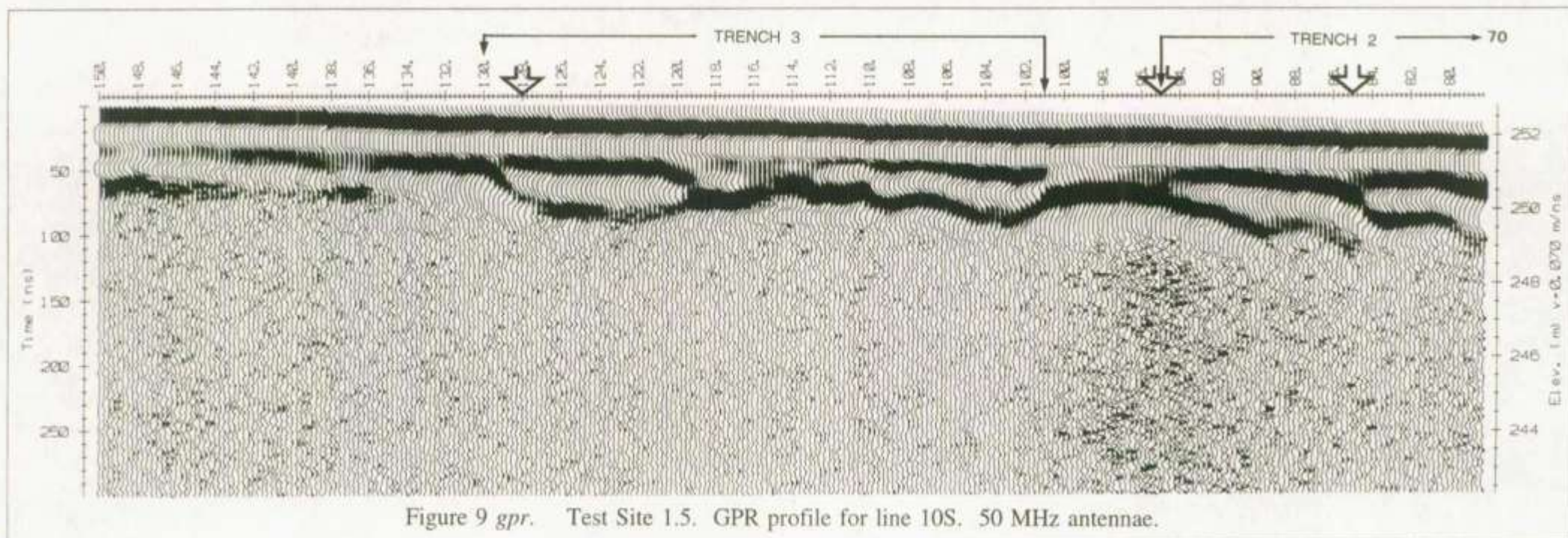
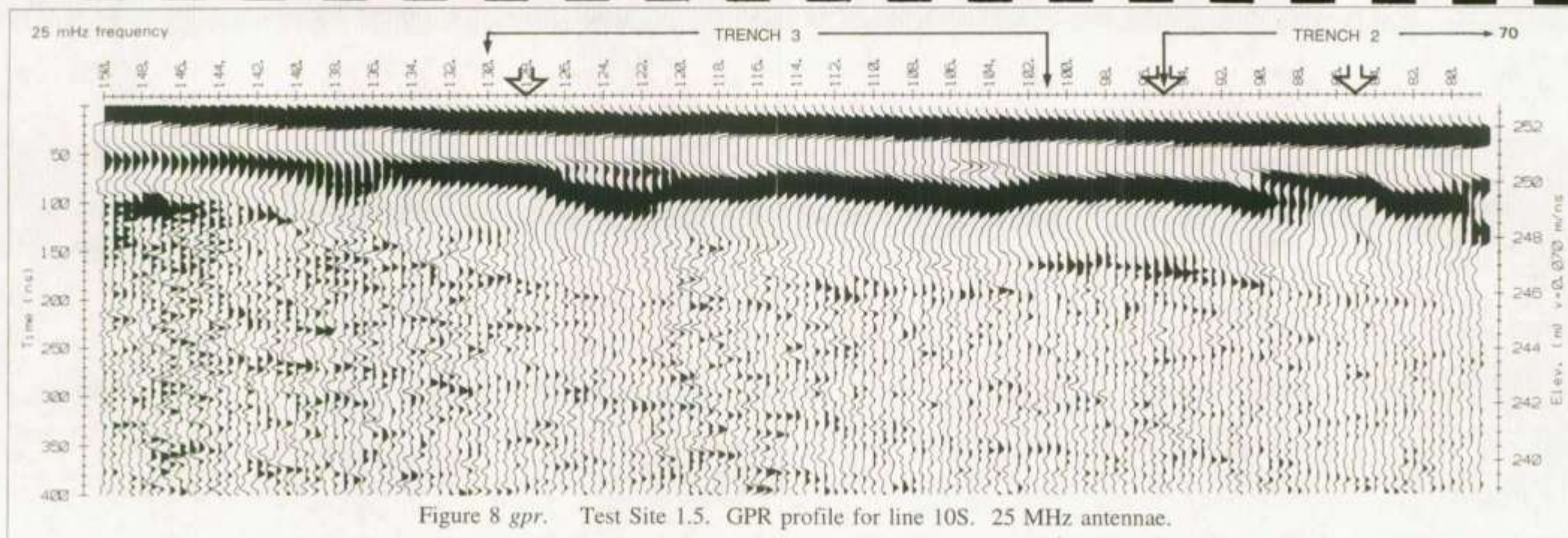
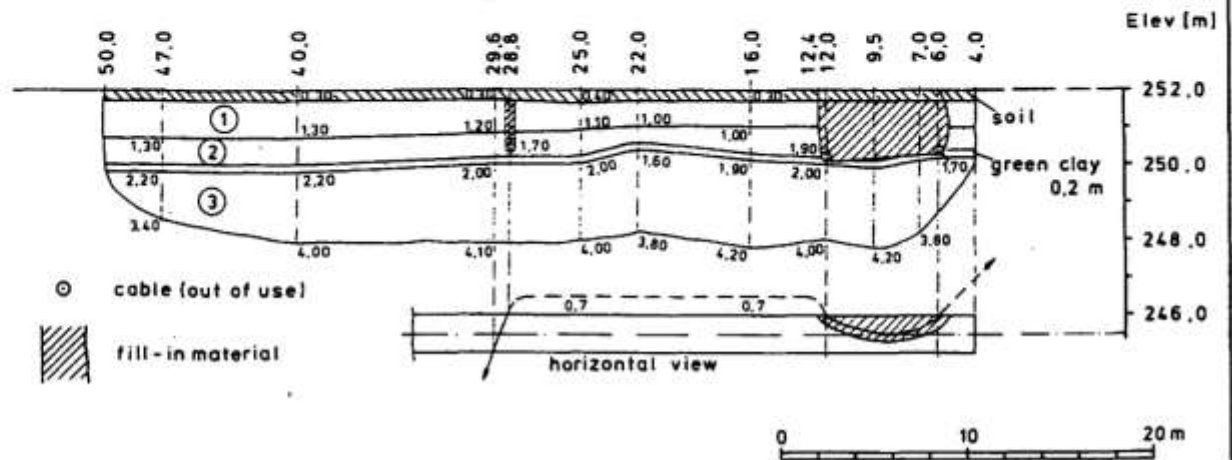


Figure 11. Test Sites 1.5 and 1.6. Geophysical grid, trench locations, and interpretation.

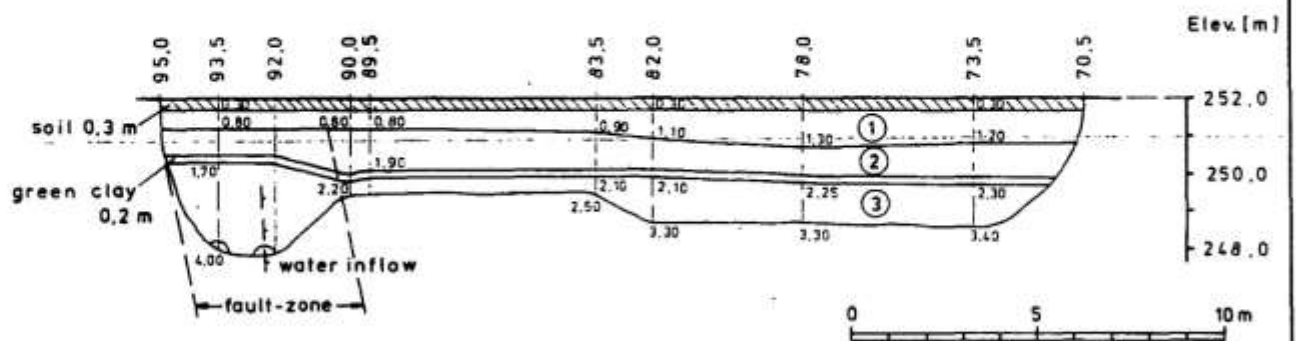




### Test Area 1.5, Line 10 S, Trench 1



### Test Area 1.5, Line 10 S, Trench 2



### Test Area 1.5, Line 10 S, Trench 3

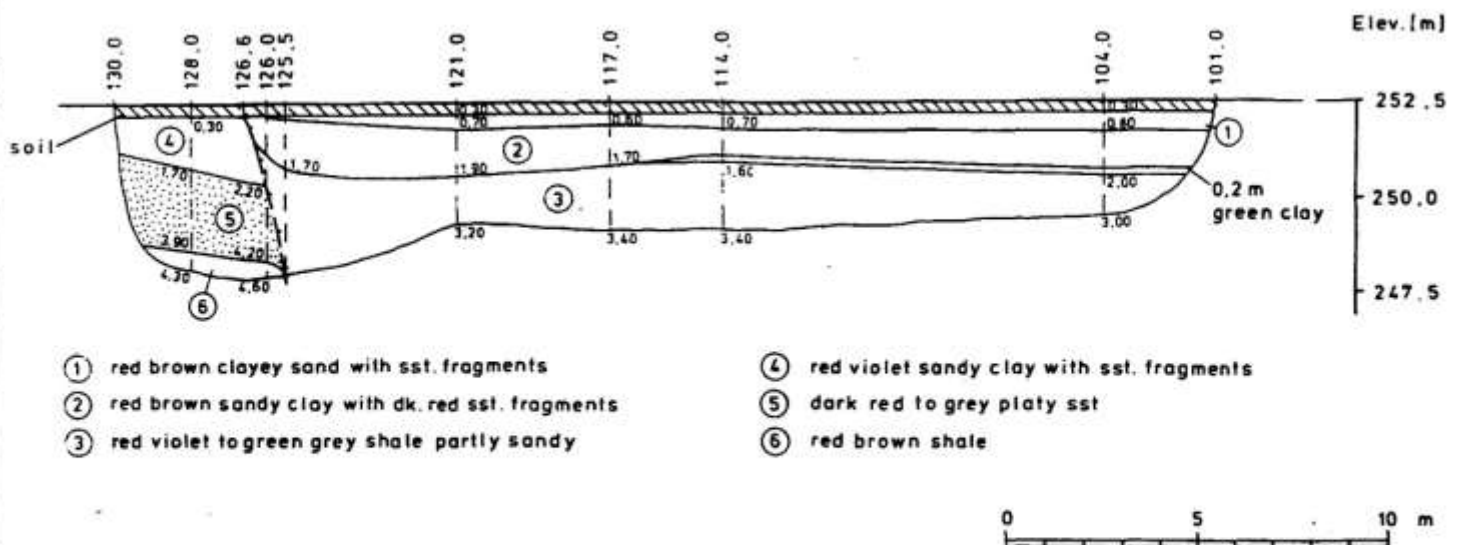


Figure 12. Test Site 1.5. Trenches 1, 2, and 3, line 10S.



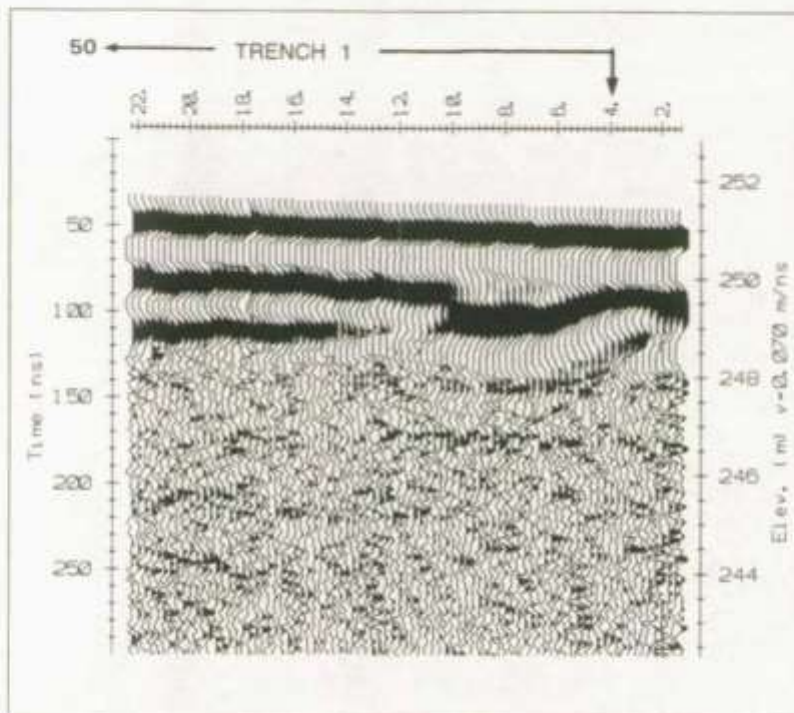


Figure 10 *gpr*. Test Site 1.5. GPR profile for line 10S (eastern end).  
50 MHz antennae.



# Test Area 1.5, Line 0N, Trench 4

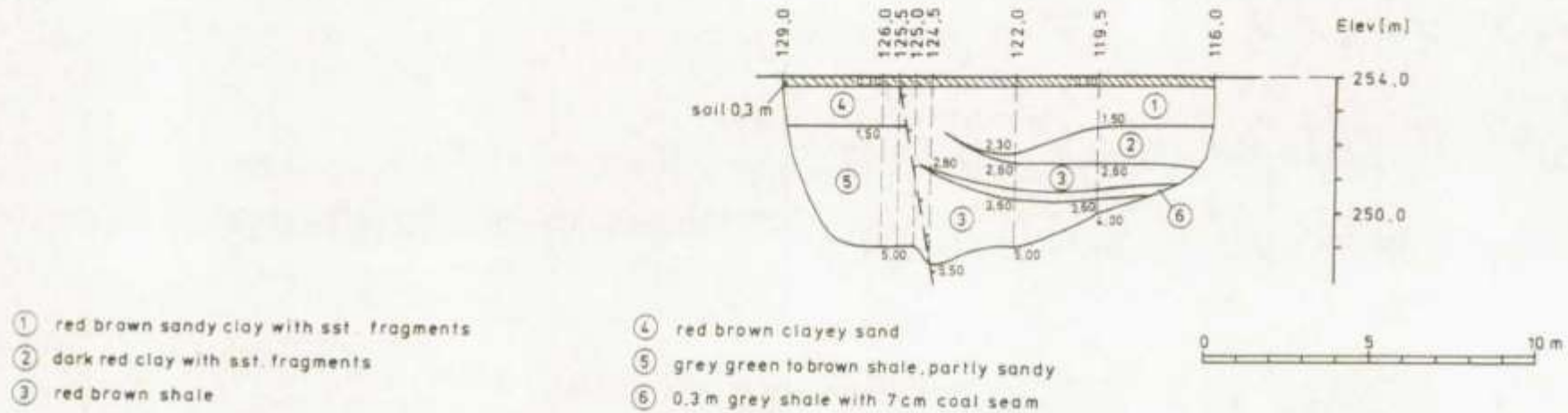
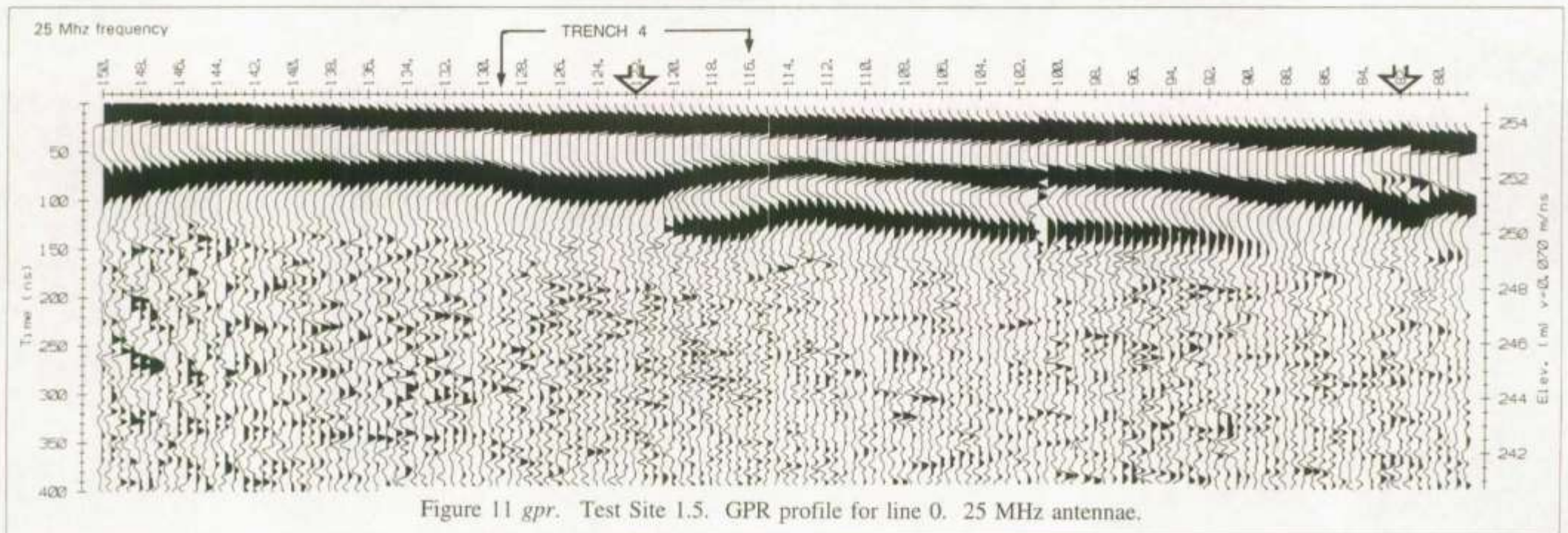


Figure 13. Test Site 1.5. Trench 4, line 0.



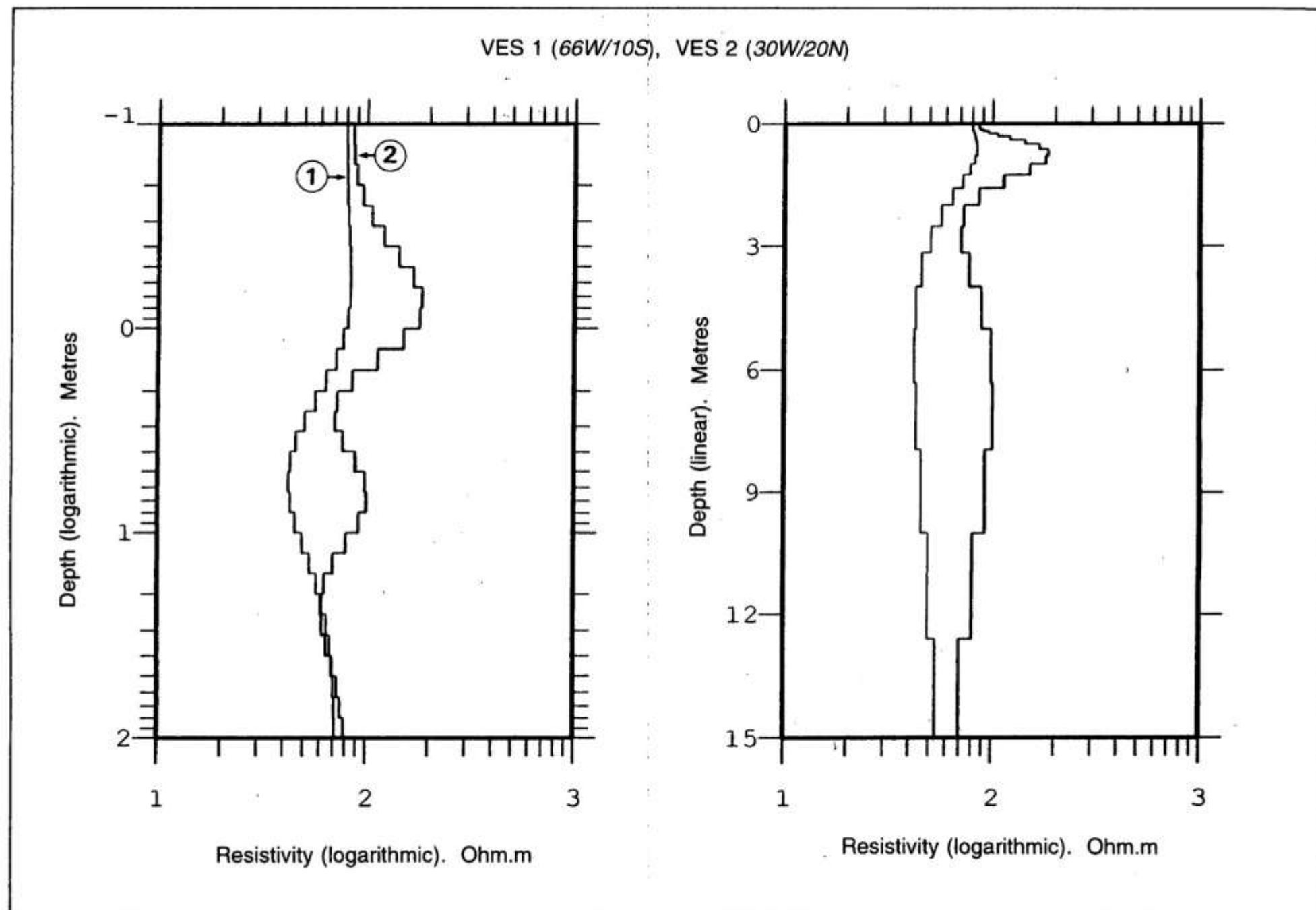
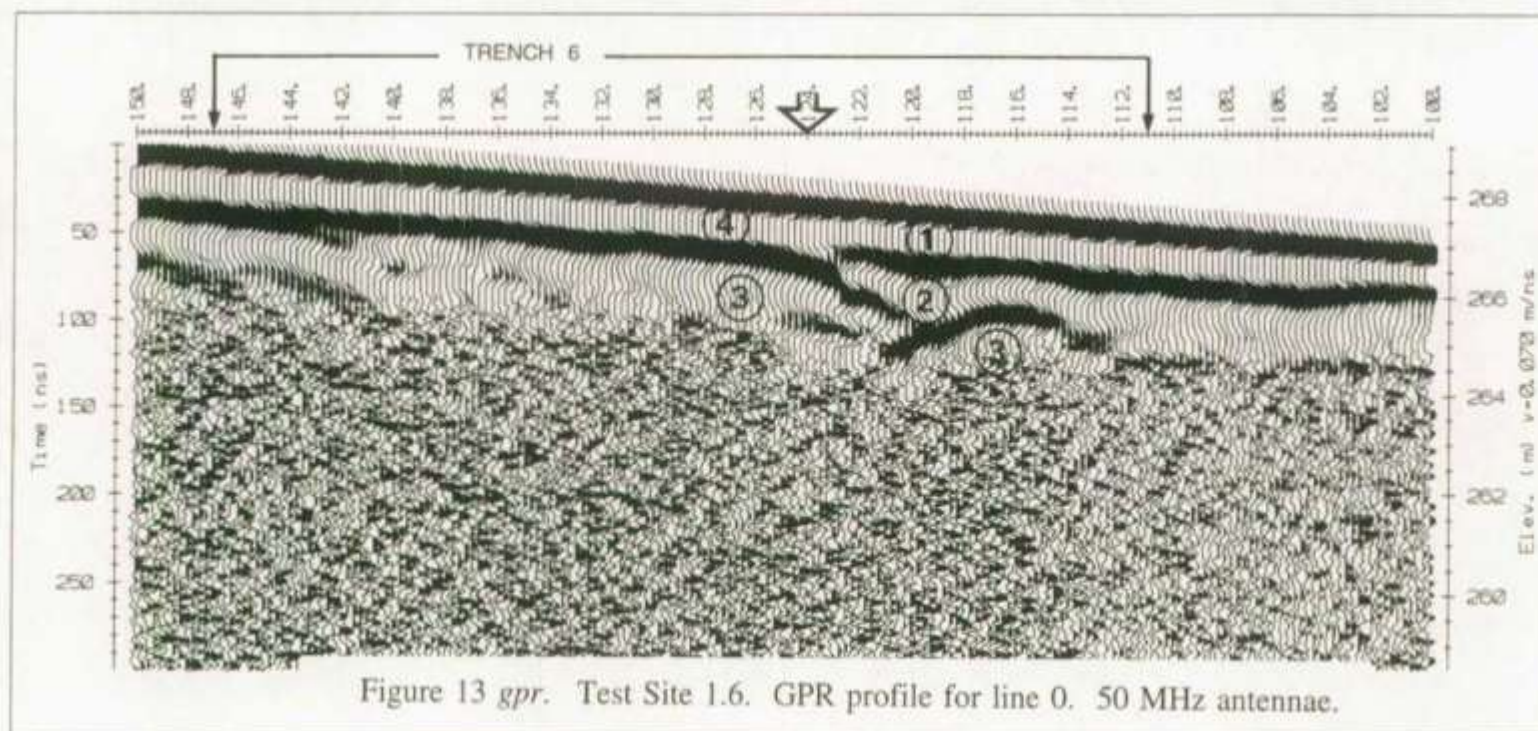
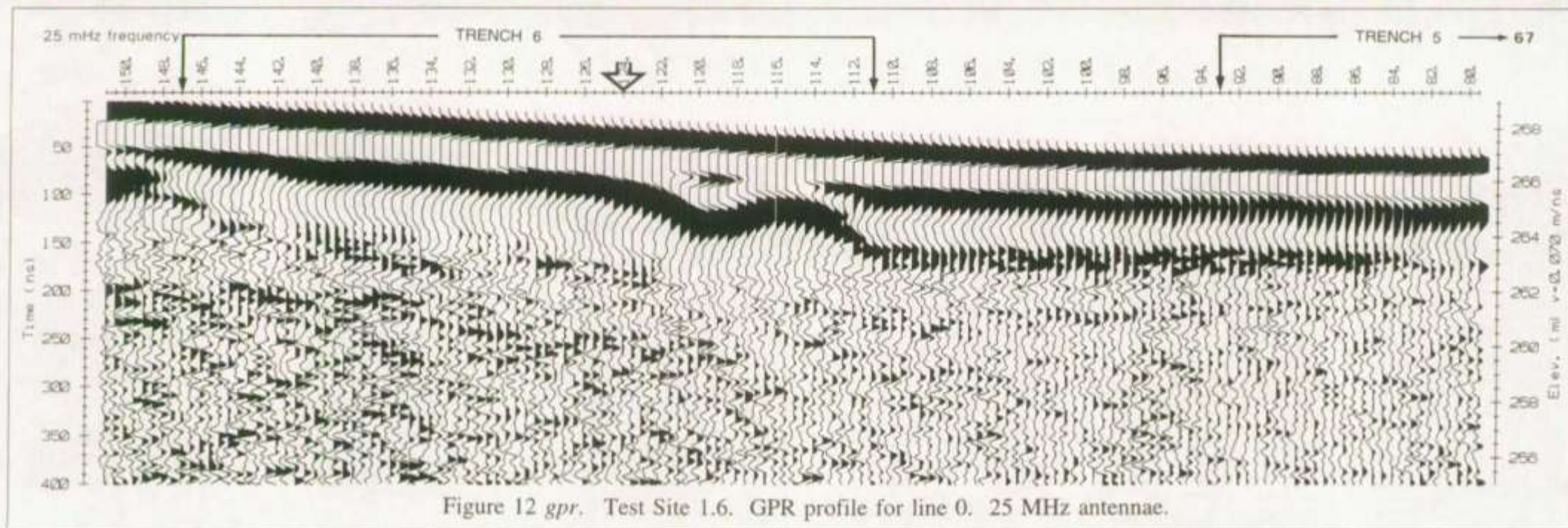


Figure 5 *res.*

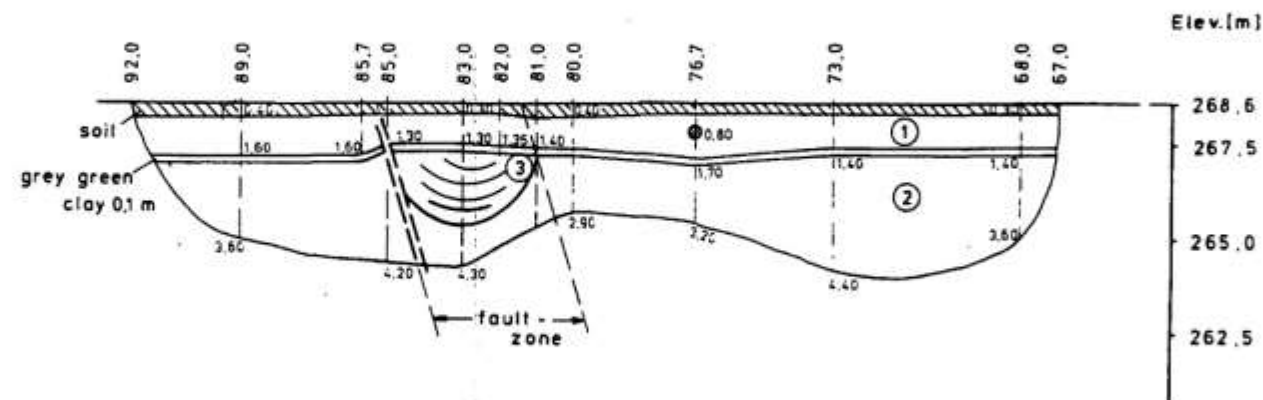
Test Site 1.5. Interpretation of VES 1, and 2.





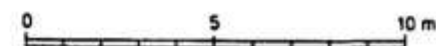


# Test Area 1.6, Line 10 S, Trench 5

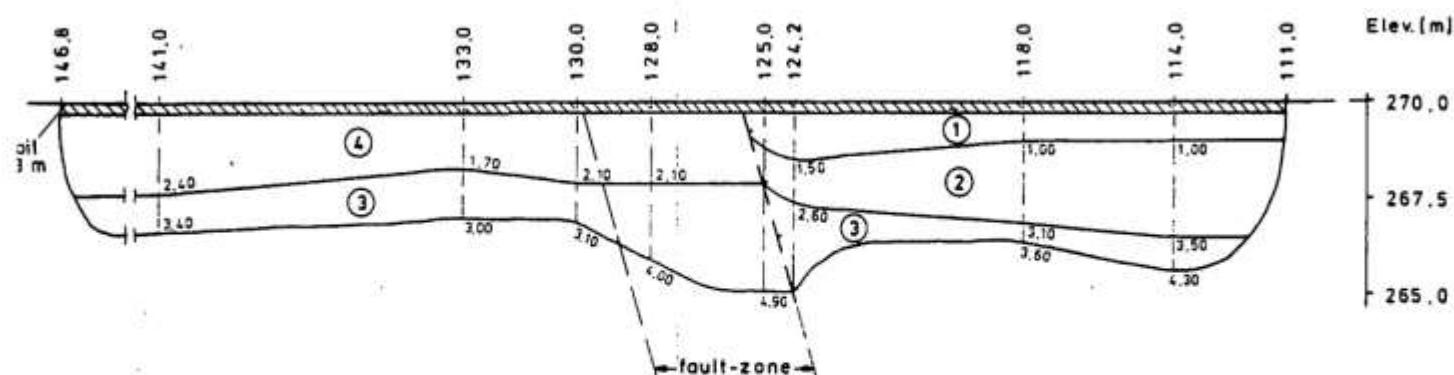


- ① red brown shale partly crumbly
- ② red violet shale partly sandy

- ③ slickenside dipping to the south
- sewage pipe (concrete 20 cm Ø)



# Test Area 1.6, Line 10 S, Trench 6



- ① light brown sandy clay with sst. fragments
- ② grey green to red violet shale, partly sandy and compact, partly brittle

- ③ red violet shale
- ④ red brown clayey sand with sst. fragments

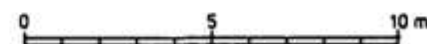
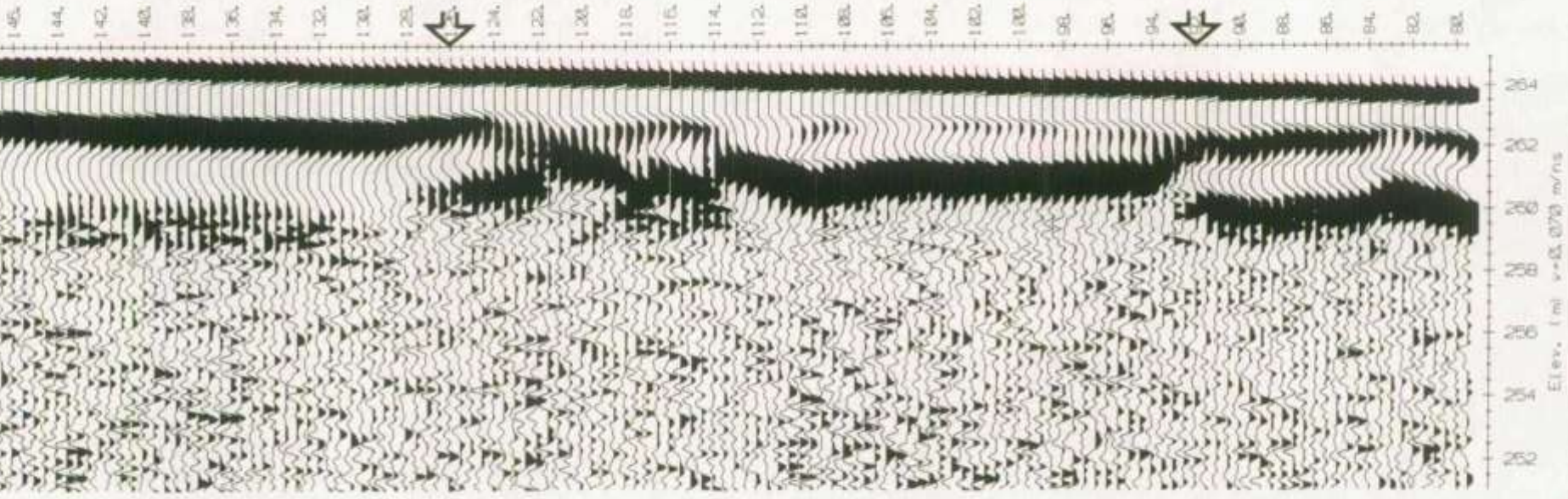
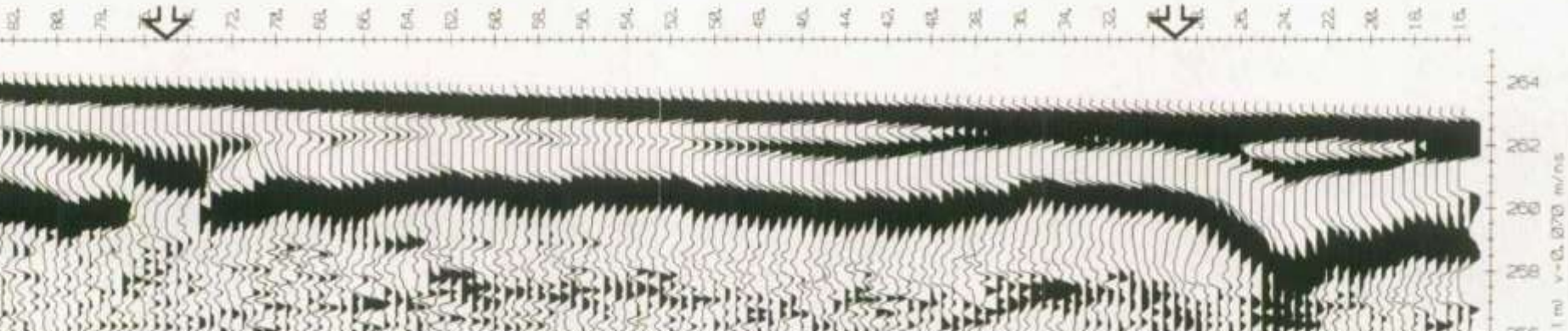
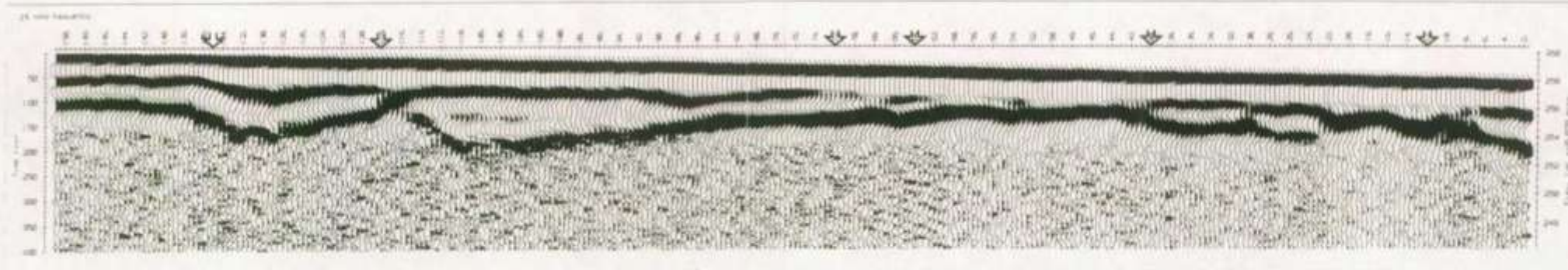


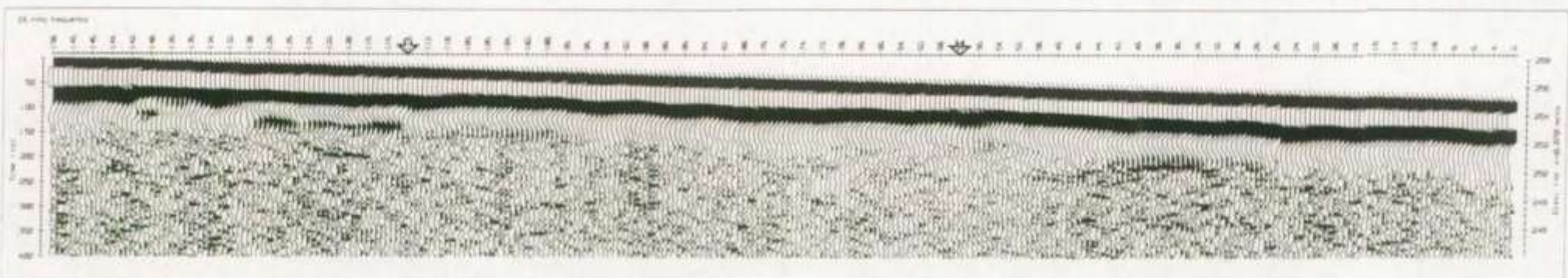
Figure 14. Test Site 1.6. Trenches 5 and 6, line 10S.







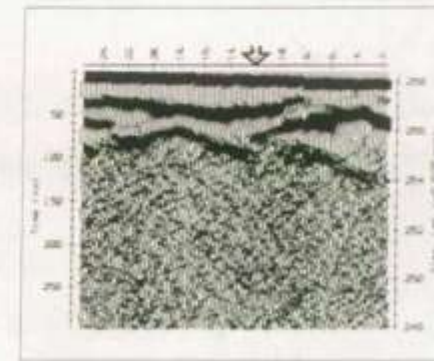
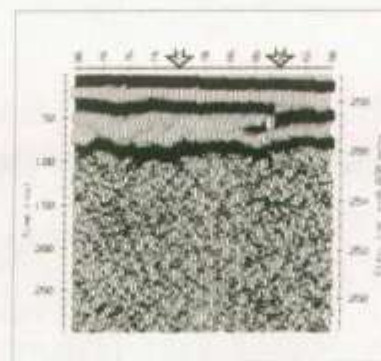
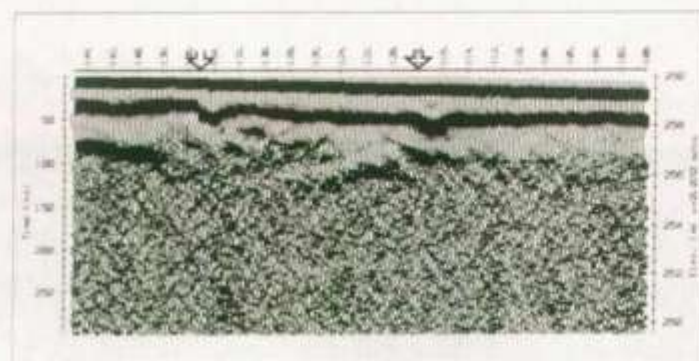
Line 40S (Test Site 1.6)



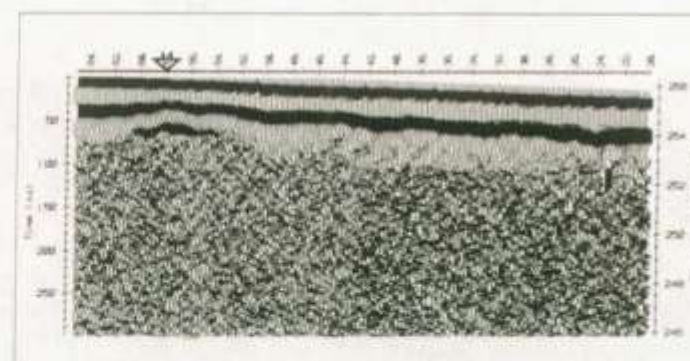
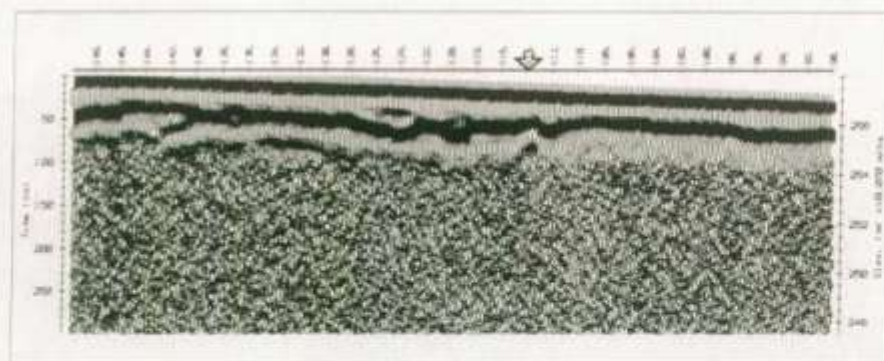
Line 20N (Test Site 1.5)

Figure 15 *gpr*. Test Site 1.6. GPR profile for line 40S and line 20N (Test Site 1.5). 25 MHZ antennae.





Line 40S (Test Site 1.6)



Line 20N (Test Site 1.5)

Figure 16 *gpr*. Test Site 1.6. GPR profile for line 40S and line 20N (Test Site 1.5). 50 MHz antennae.



Figure 15. Test Site 2.1. Geophysical grid, trench and borehole locations, and interpretation. May 1992 survey.



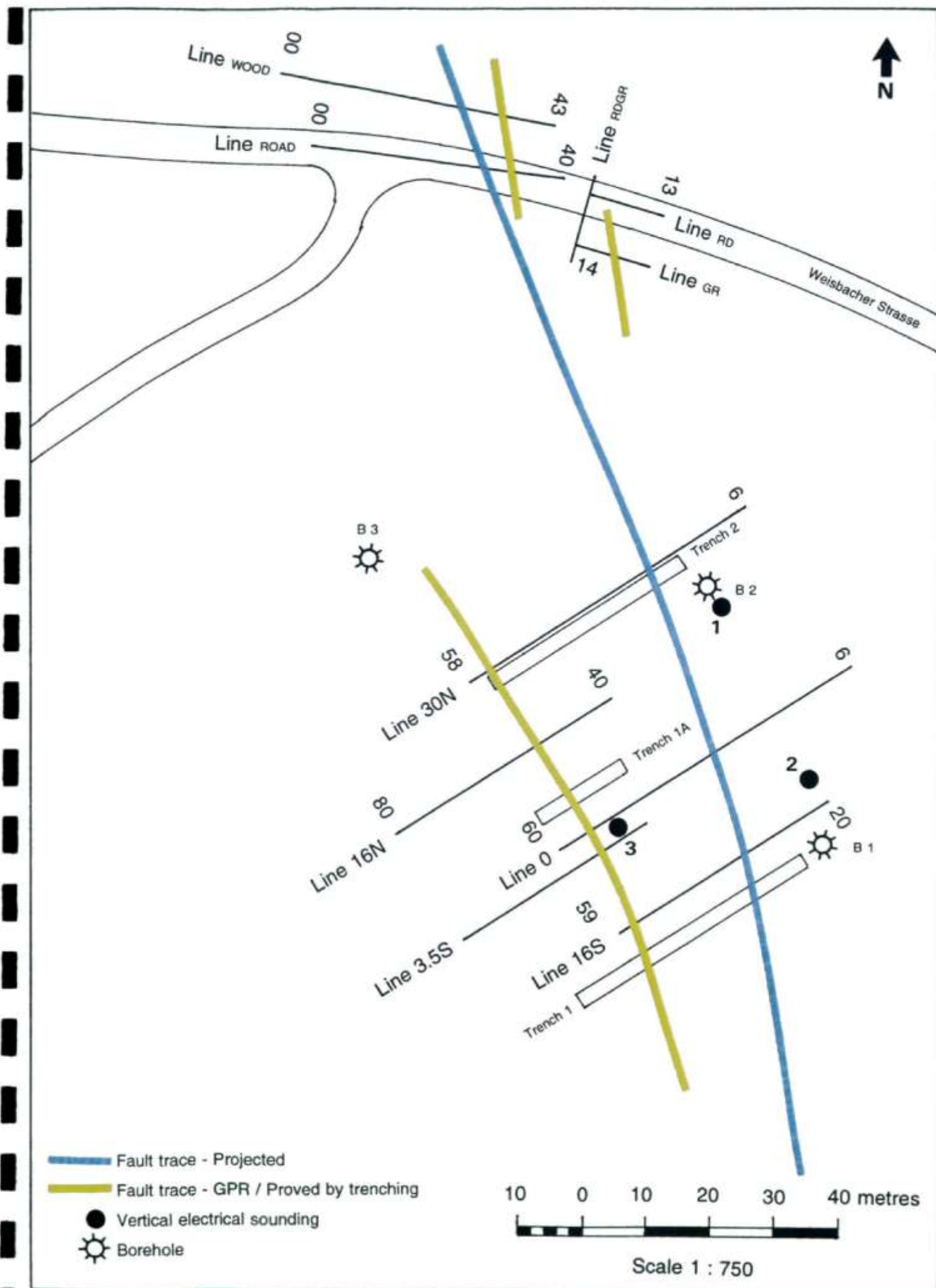


Figure 16. Test Site 2.1. Geophysical grid, trench and borehole locations, and interpretation. December 1992 survey.



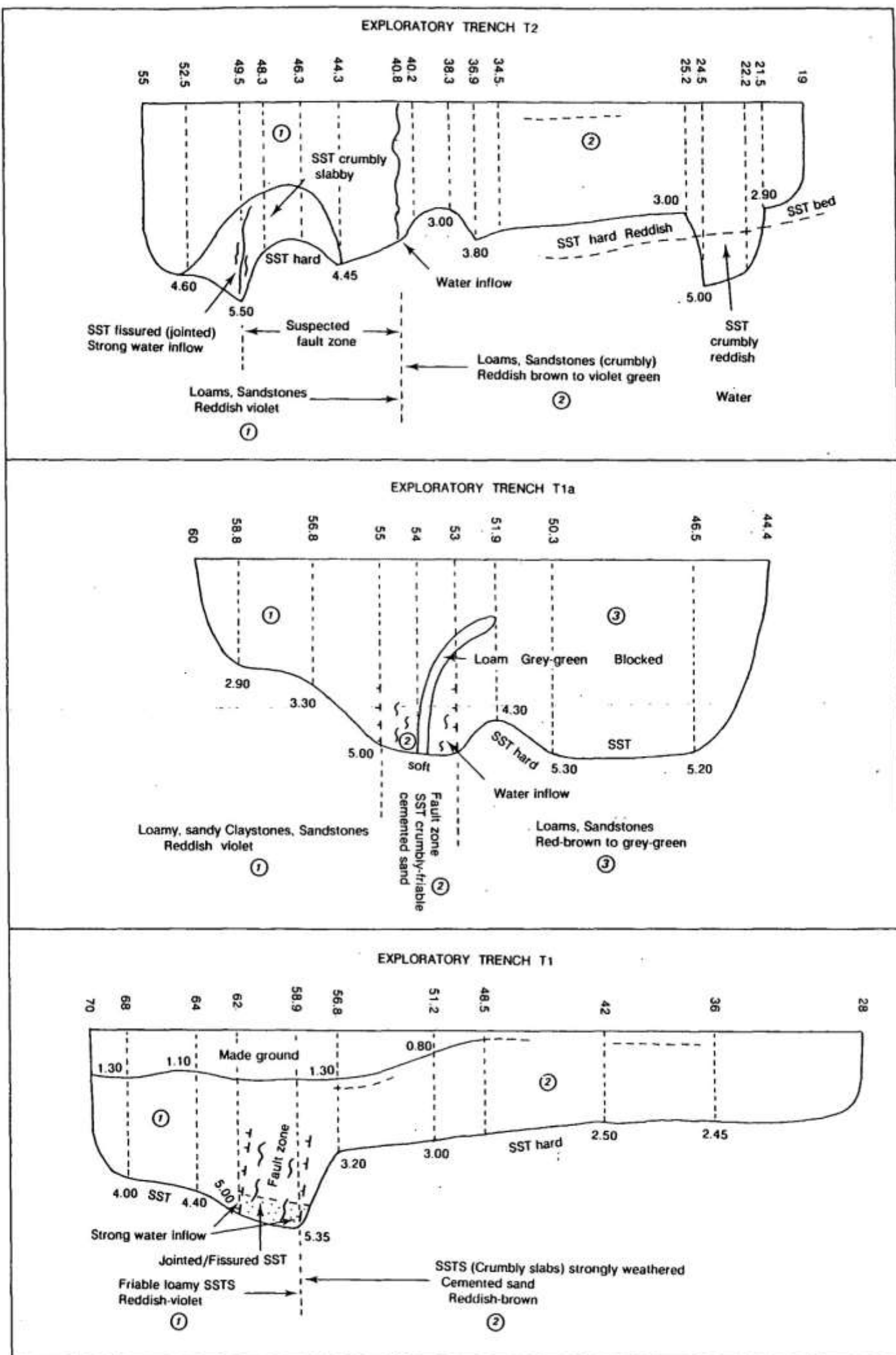
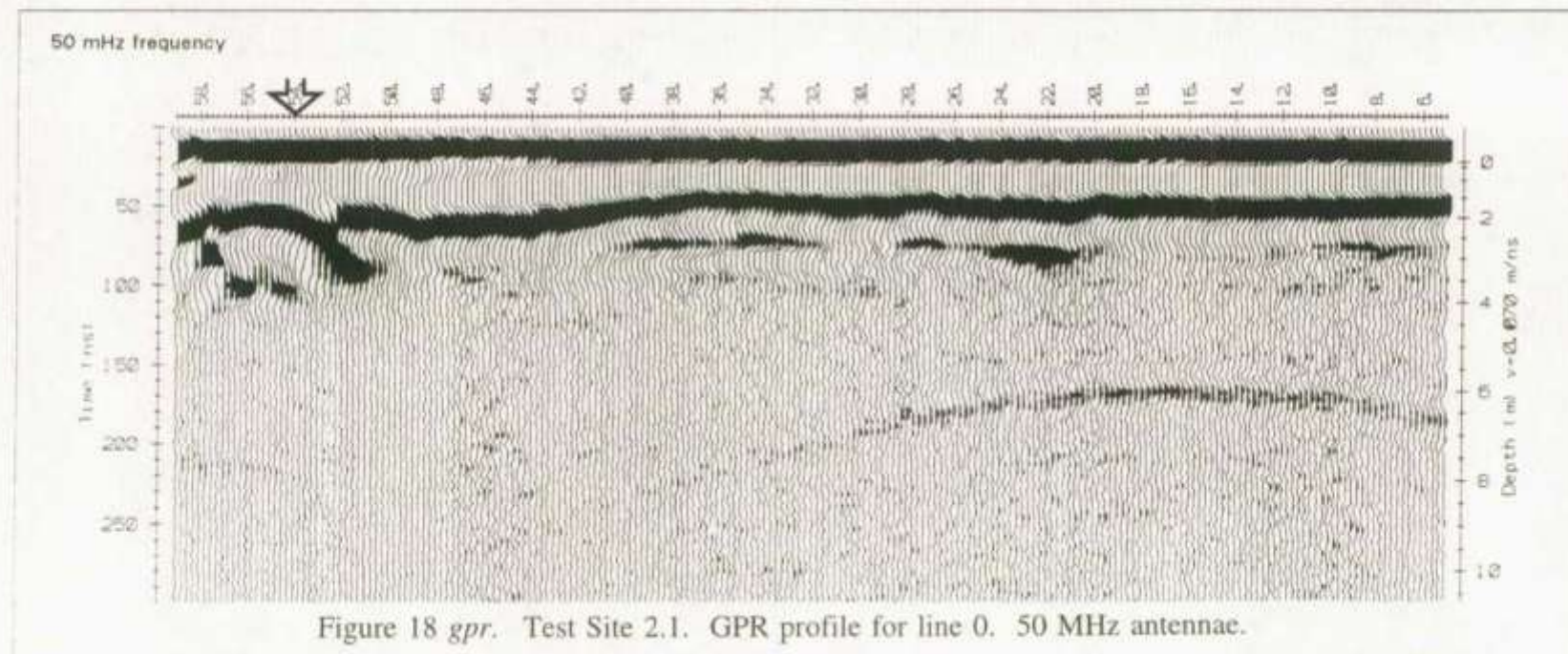
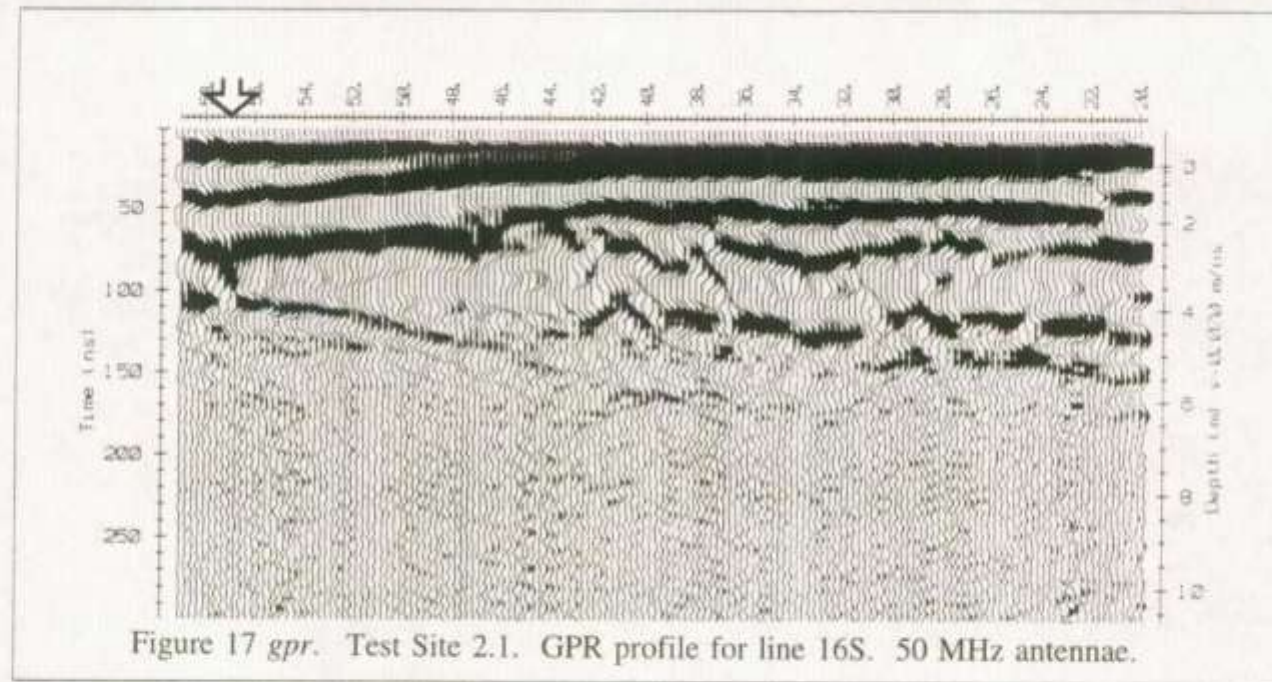


Figure 17. Test Site 2.1. Exploratory trenches T1, T1a, and T2.





50 MHz frequency

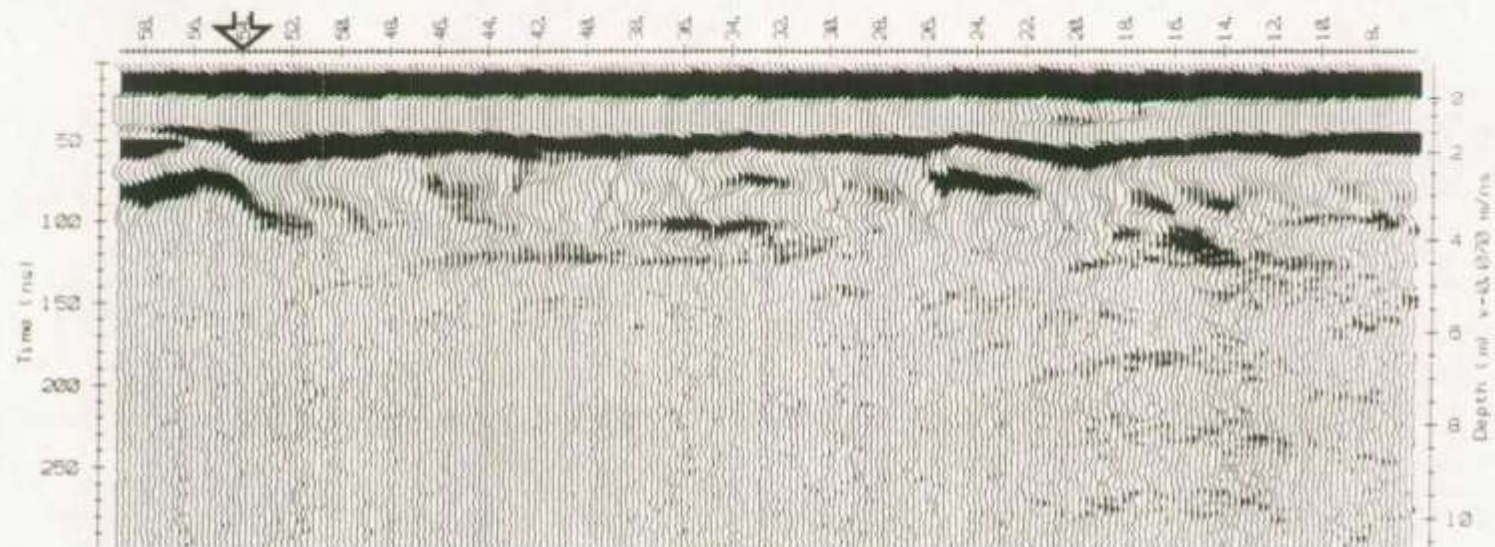


Figure 19 *gpr*. Test Site 2.1. GPR profile for line 30N. 50 MHz antennae.

50 MHz frequency

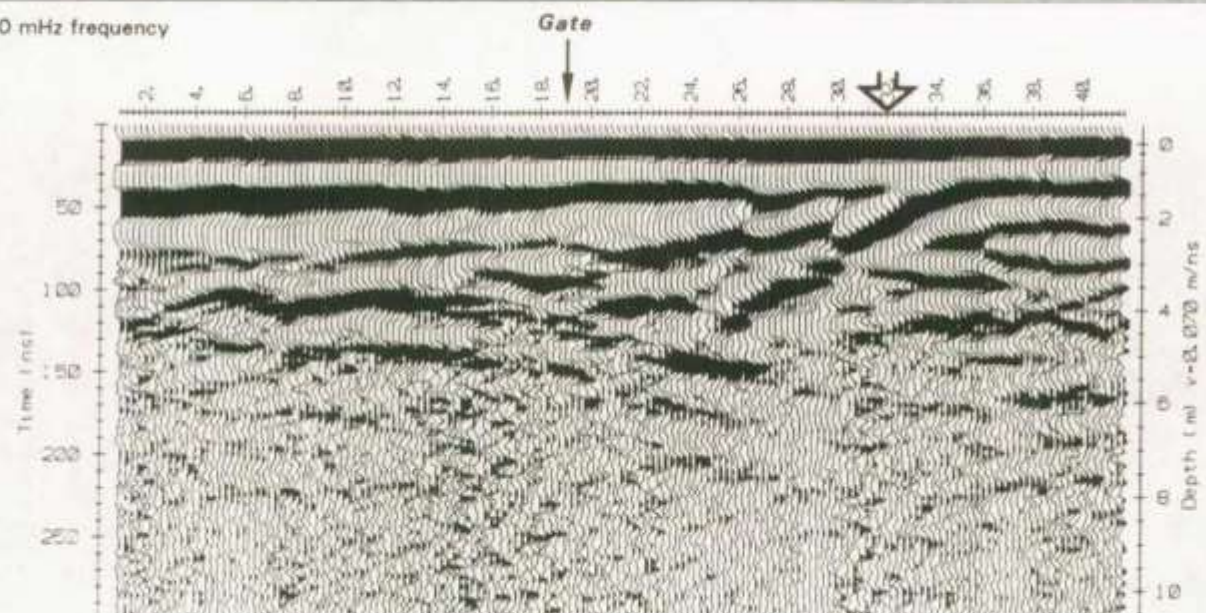


Figure 20 *gpr*. Test Site 2.1. GPR profile for line ROAD. 50 MHz antennae.



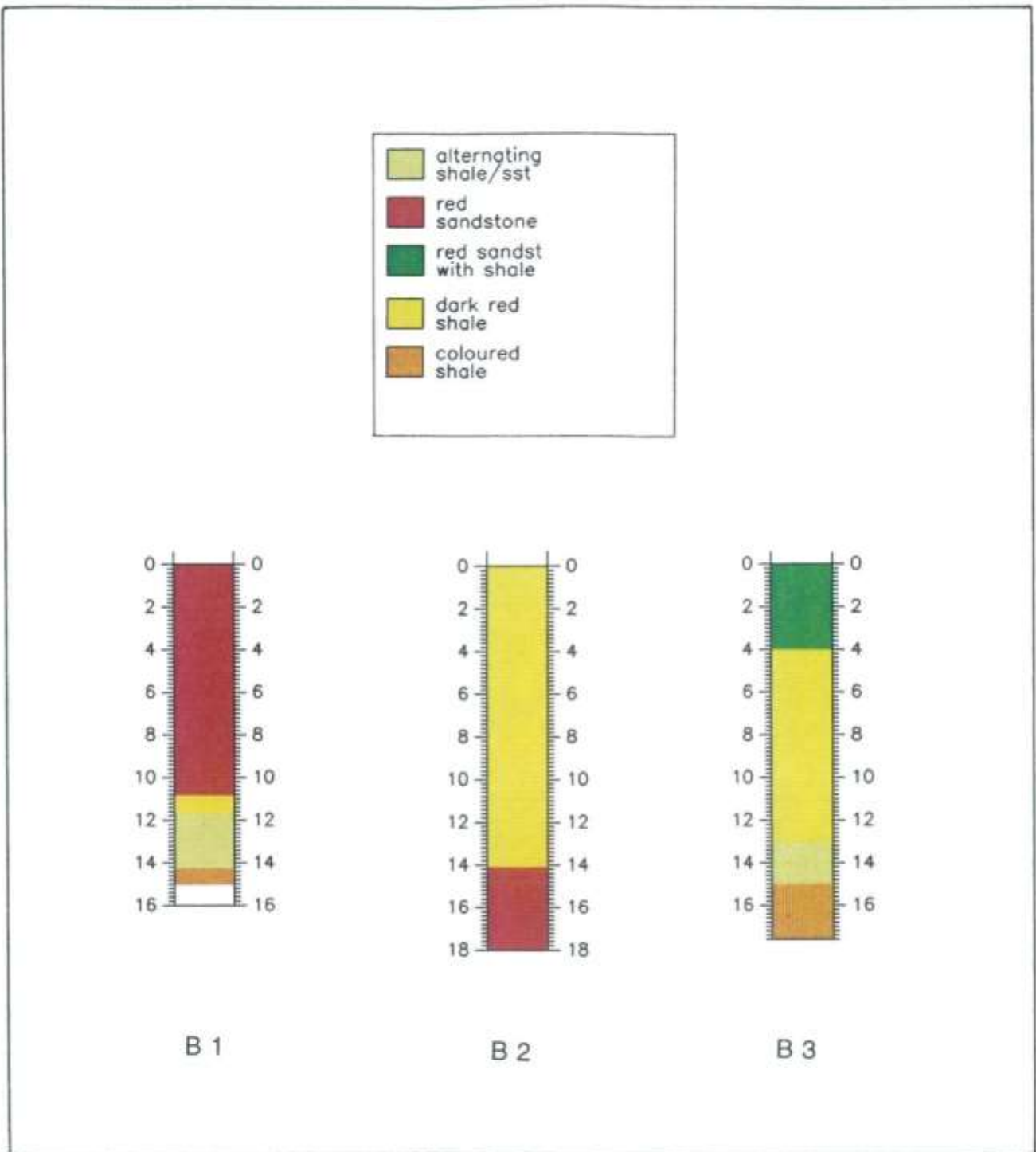


Figure 18. Test Site 2.1. Geological section: boreholes B1, B2, B3.

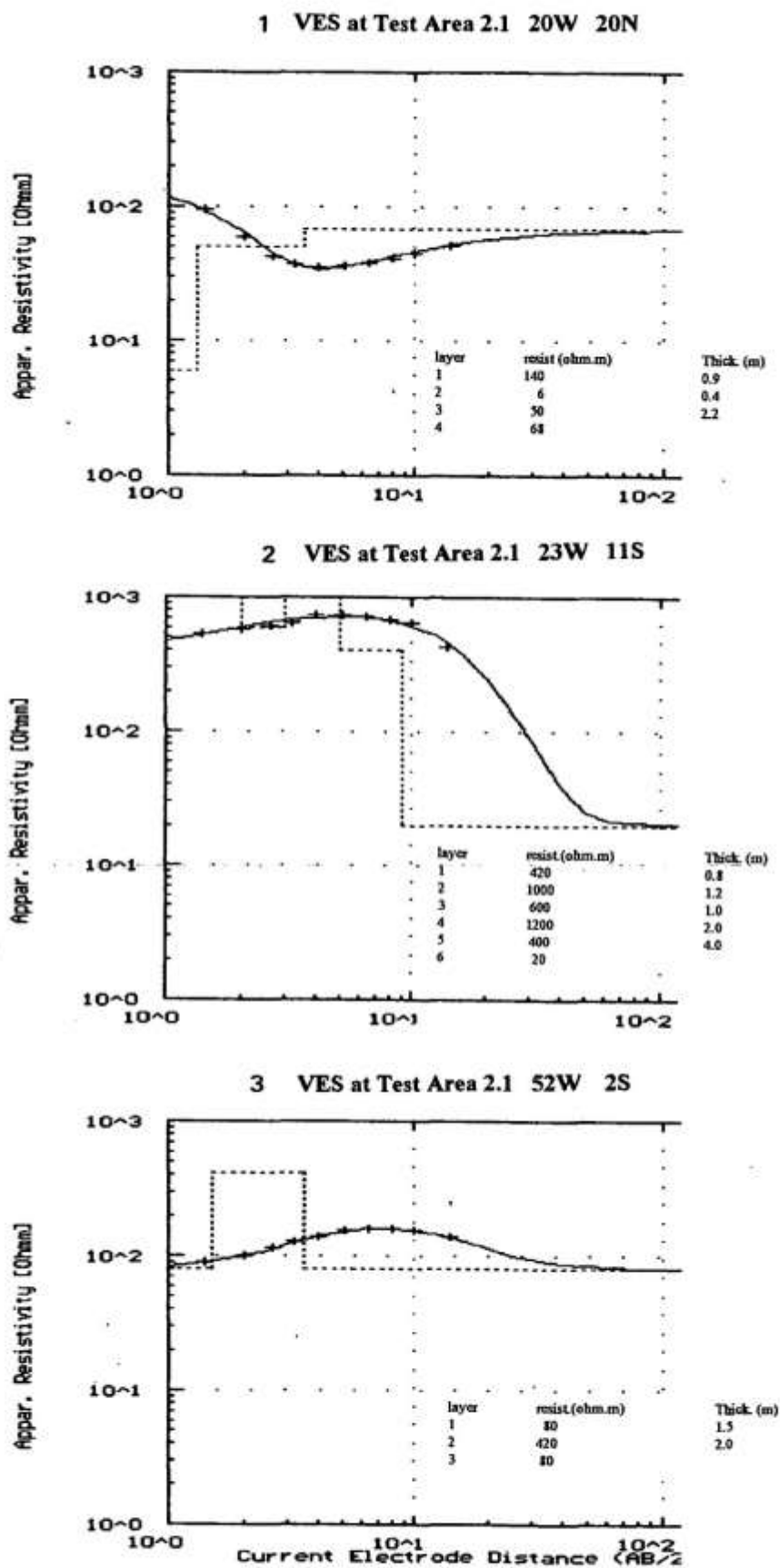


Figure 6 res.

Test Site 2.1. Interpretation of VES 1, 2, and 3.

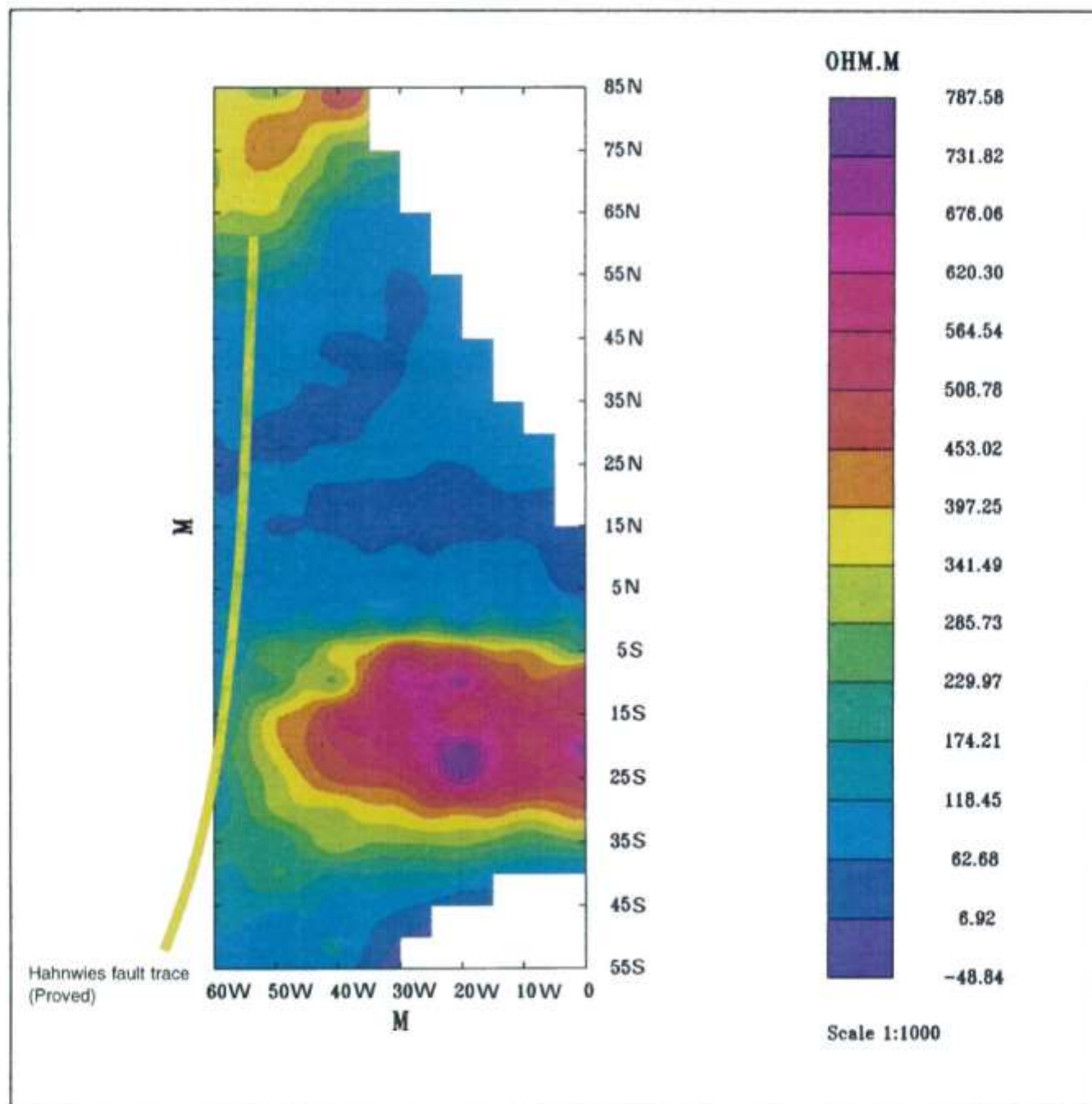


Figure 7 res.

Test Site 2.1. Schlumberger array resistivity contours.



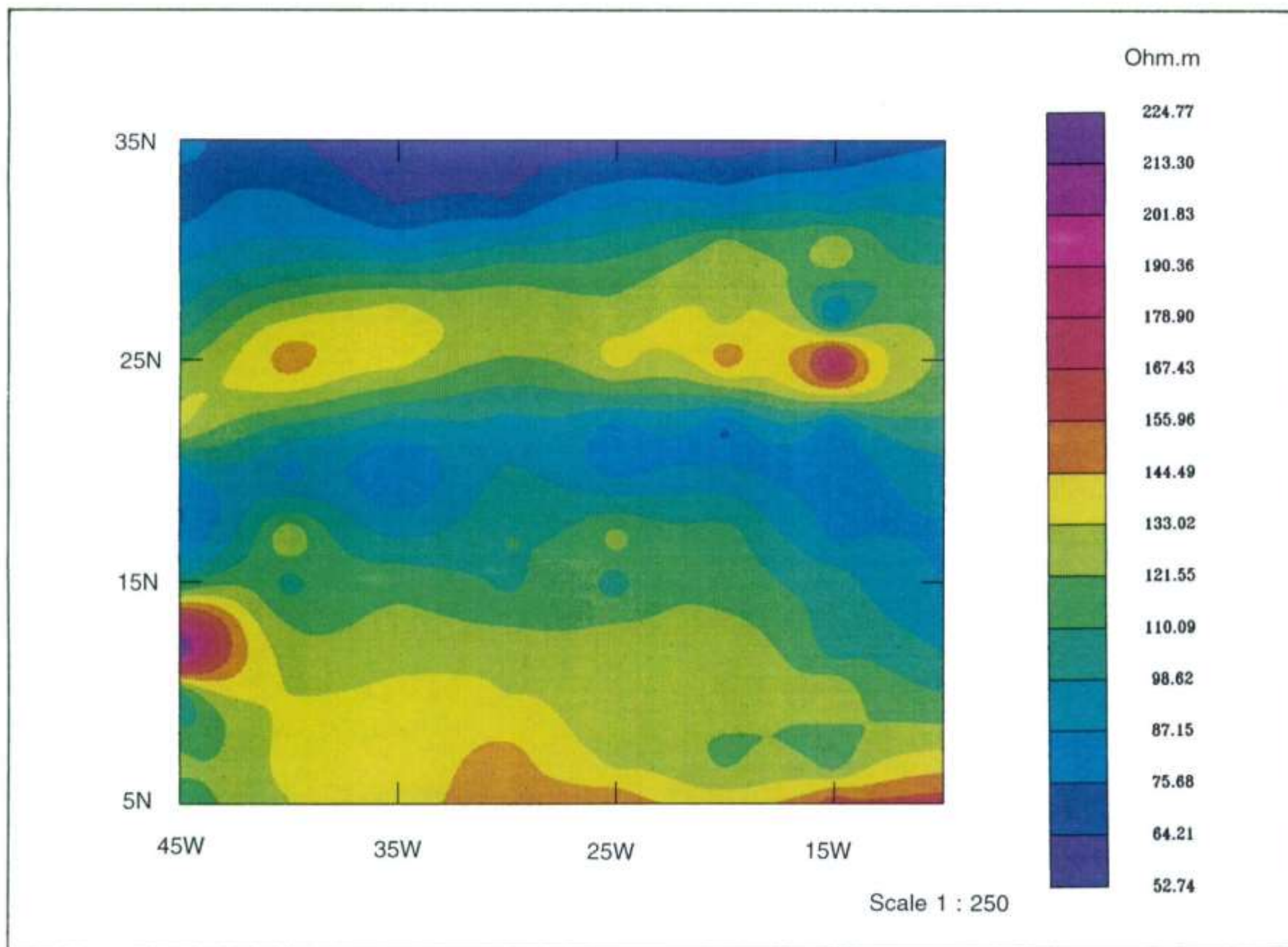


Figure 8 *res.*

Test Site 2.1. Gradient array resistivity contours.

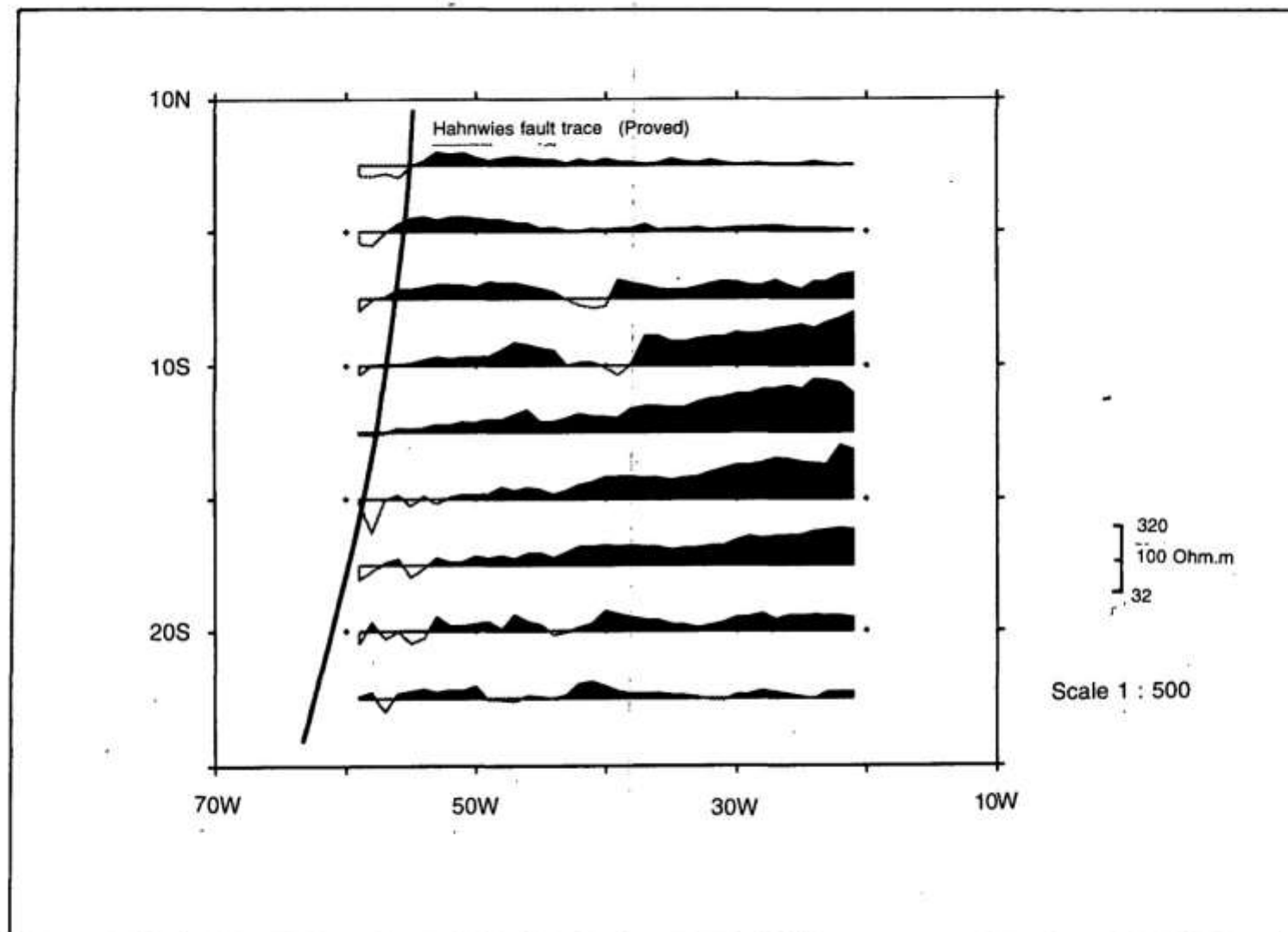


Figure 9 res.

Test Site 2.1. Gradient array resistivity profiles (logarithmic scale).

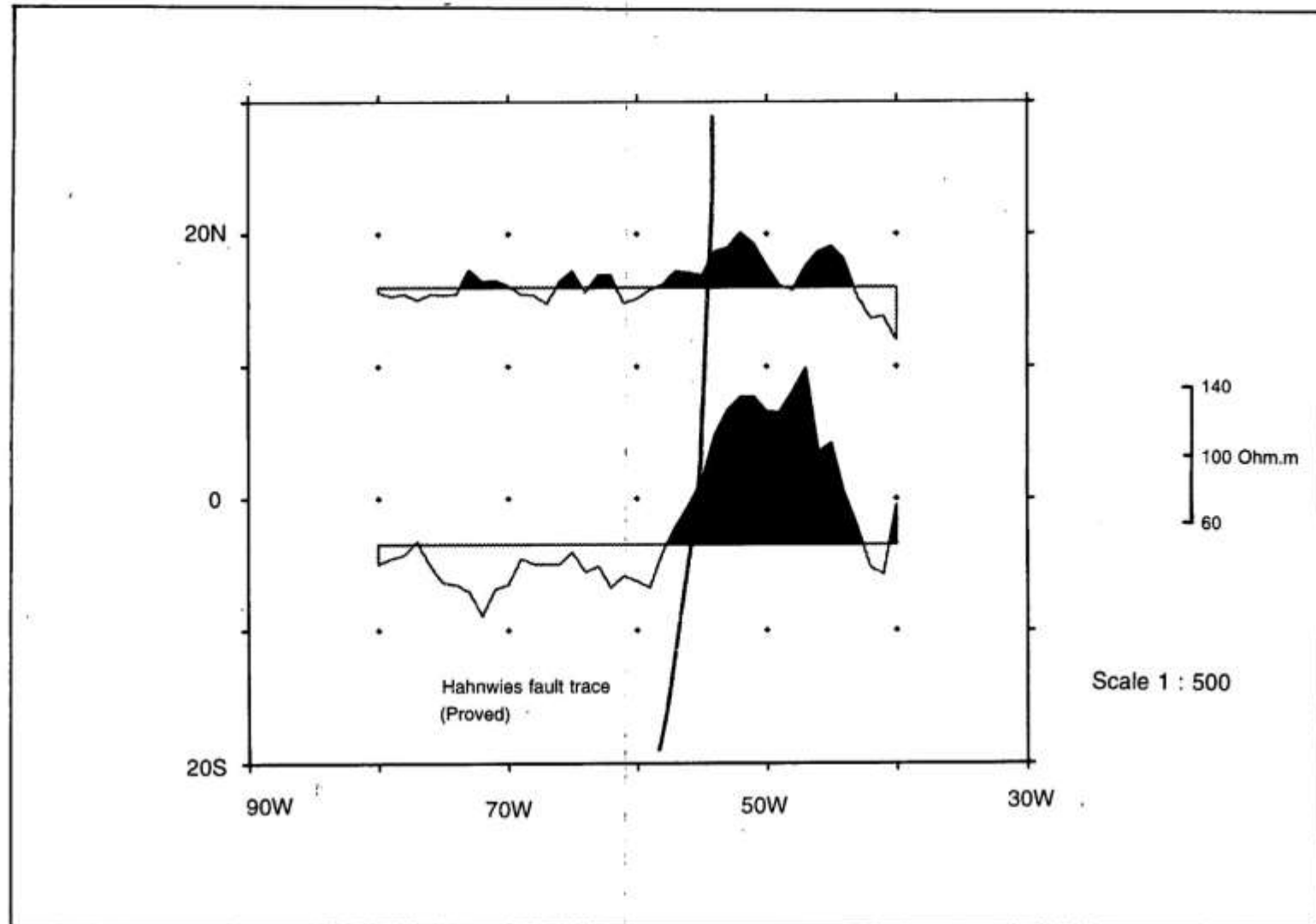


Figure 10 *res.* Test Site 2.1. Gradient array detail over proven fault trace.



# Half - Schlumberger Apparent Resistivity AB = 3 m

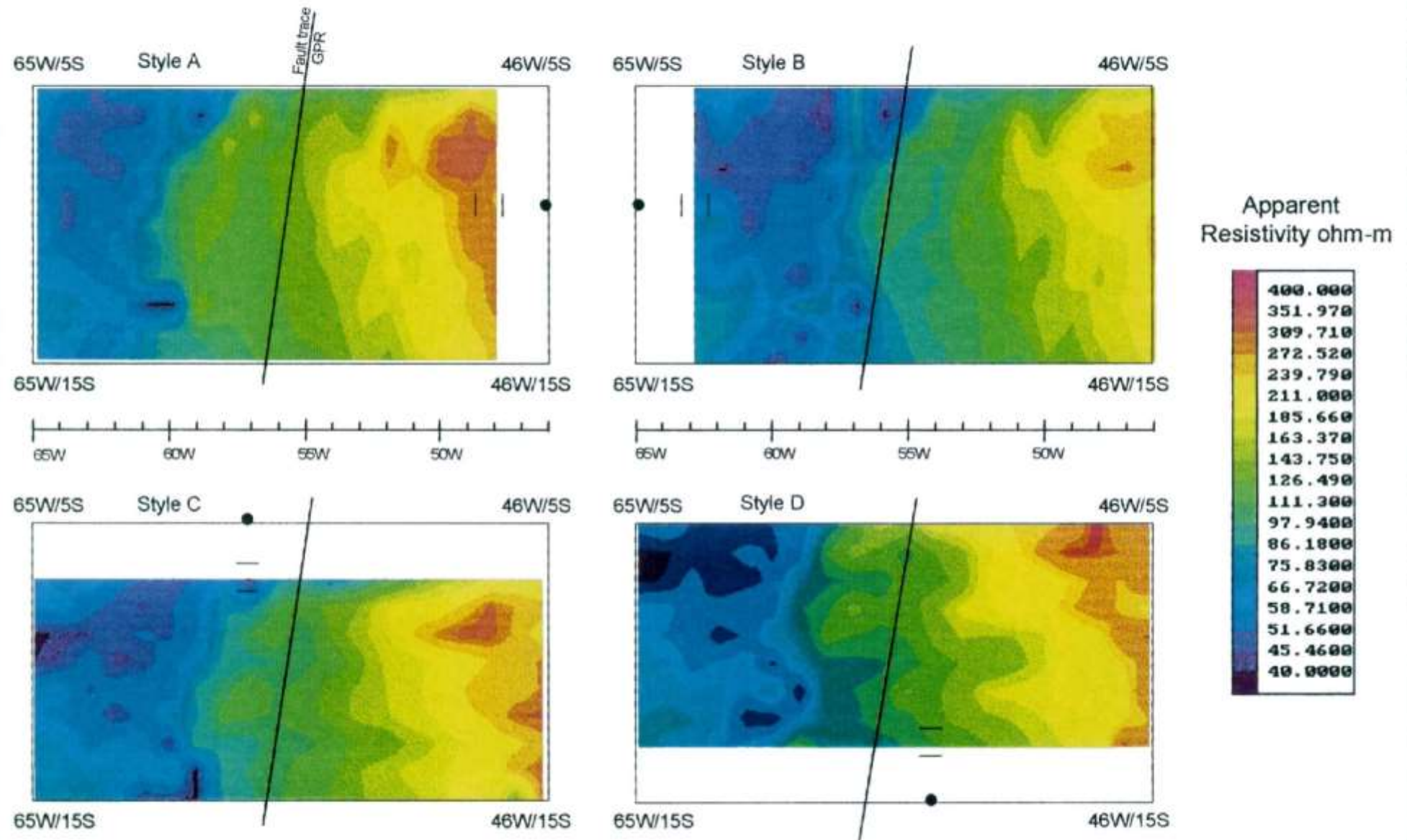


Figure 3 *rsc*. Test Site 2.1. Half Schlumberger apparent resistivity maps for AB=3m.

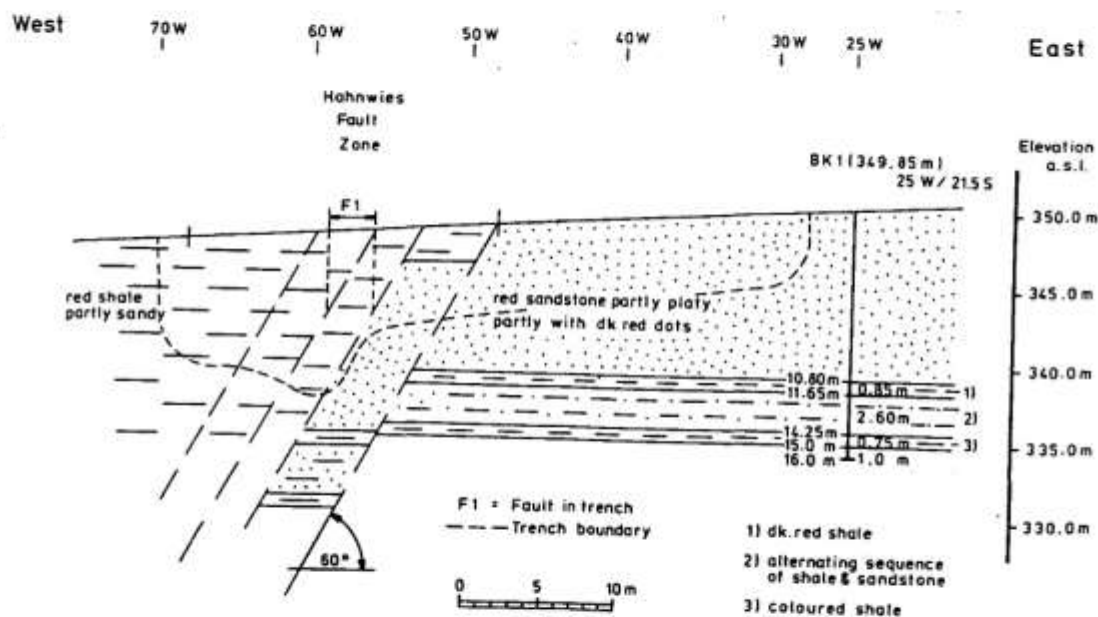
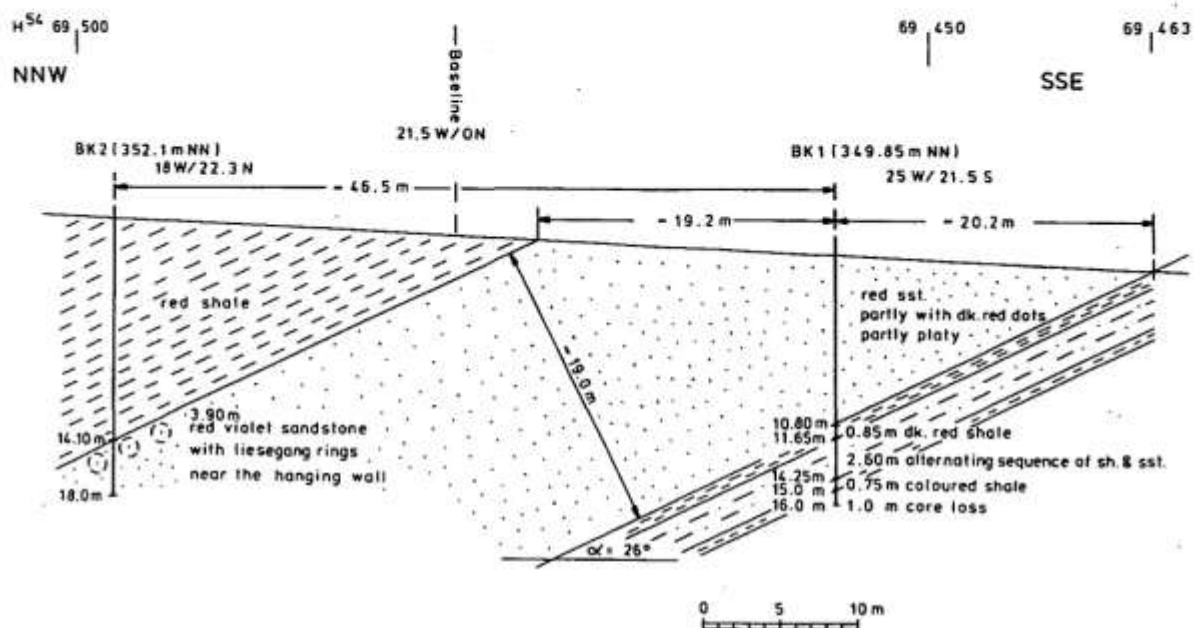


Figure 1 rsc. Test Site 2.1. Geological sections constrained by boreholes B1 and B2 and Trench T1.

## Half - Schlumberger Apparent Resistivity

Style B AB =3 and 9 m

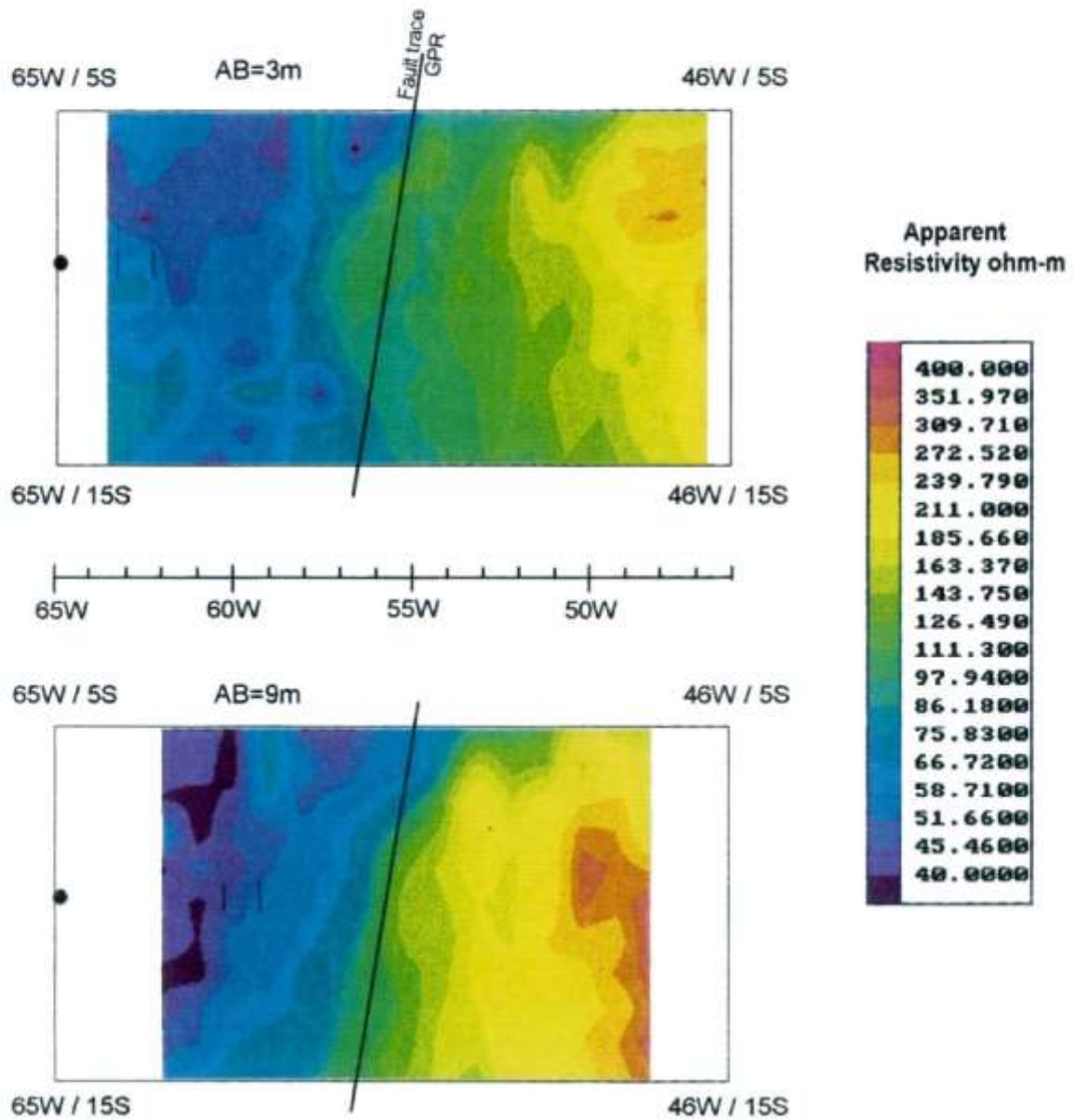


Figure 4 *rsc.* Test Site 2.1. Variable response from different depths of investigation (proportional to AB).



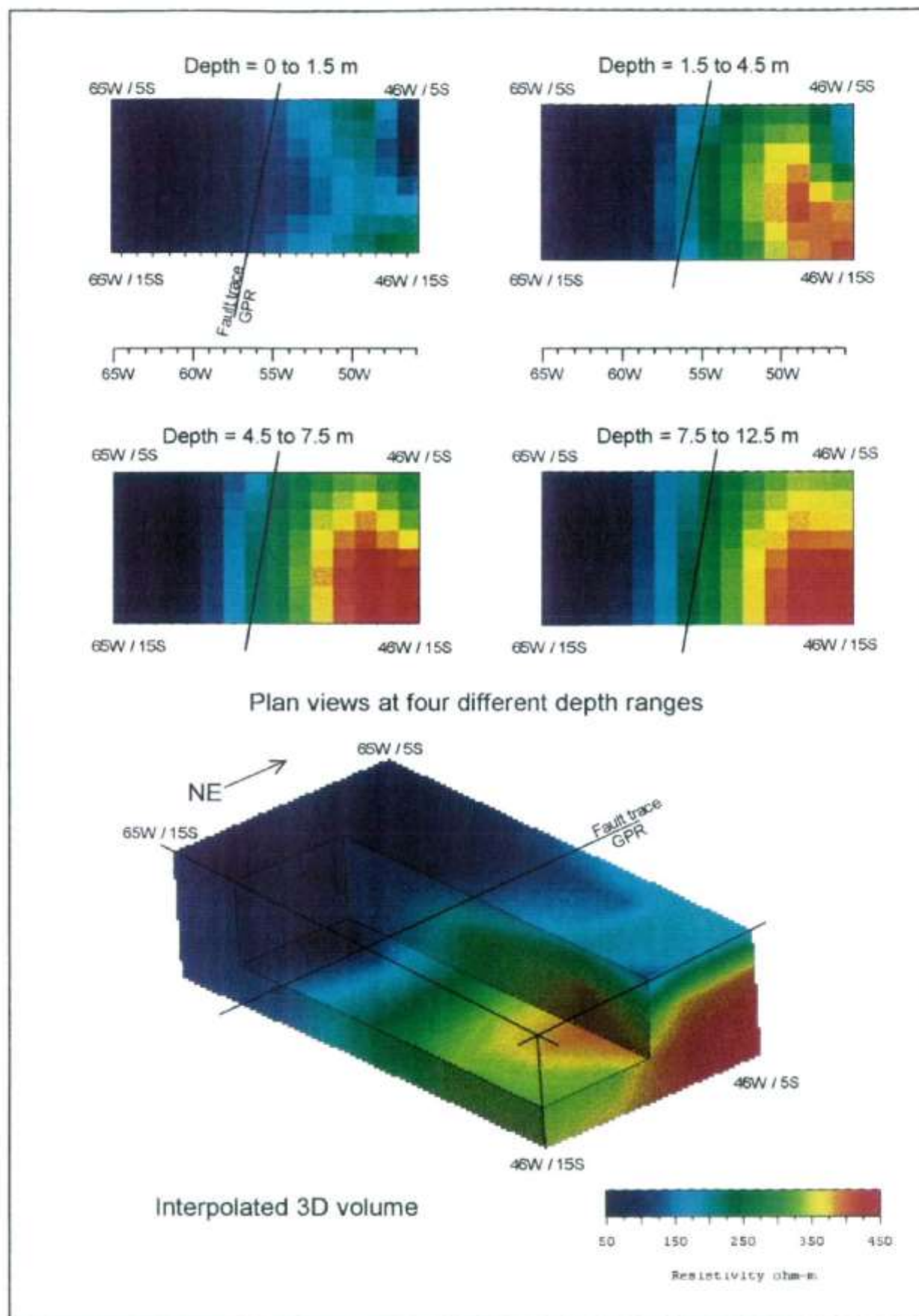
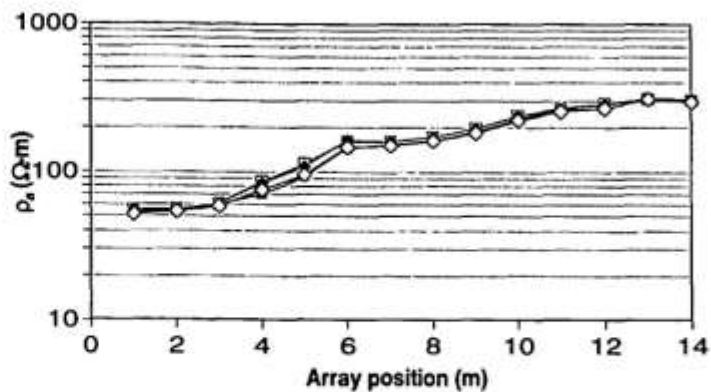
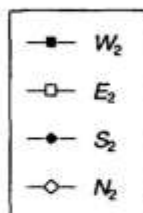


Figure 5 rsc. Test Site 2.1. Smooth inversion of resistivity data illustrating the 3D nature of the geological structure.

Focused apparent resistivity



Pole-pole apparent resistivity

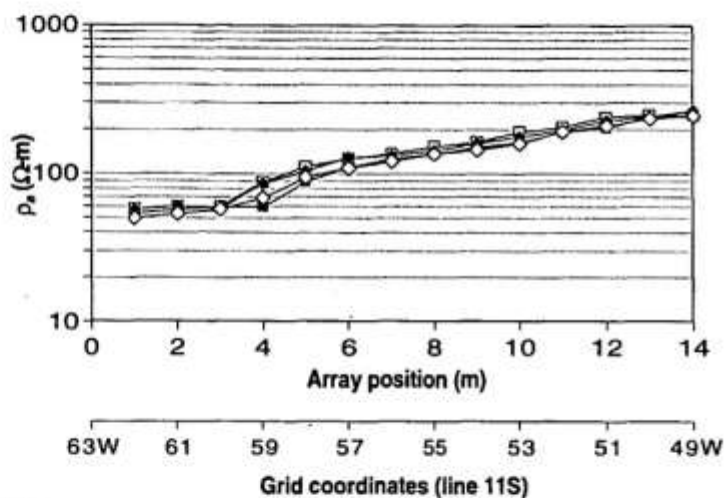


Figure 20 *rsc.* Apparent resistivity traverses.

Balance currents

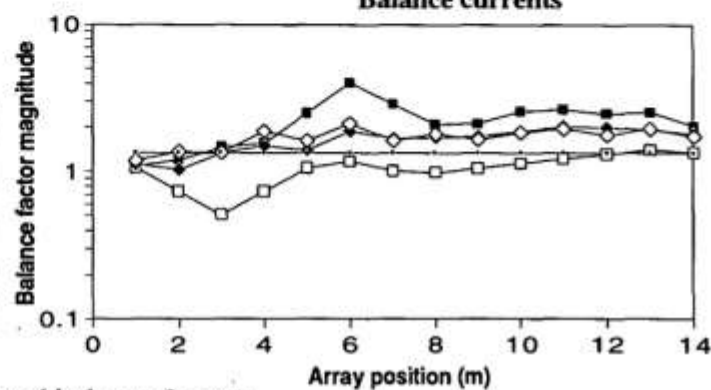
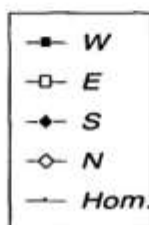


Figure 21 *rsc.* Test Site 2.1. Line 7. Focussed balance factors.

Balance currents

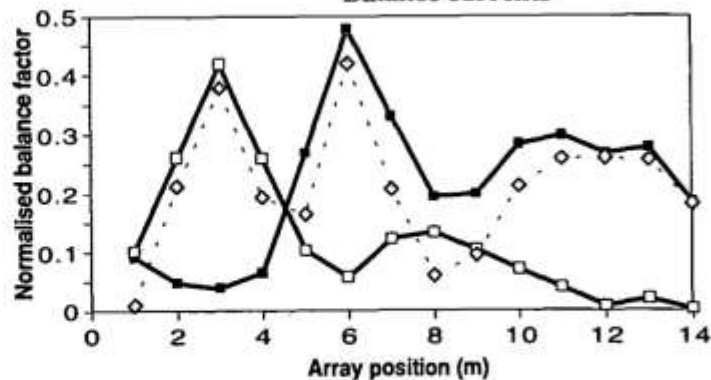
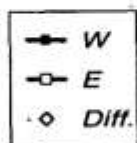


Figure 22 *rsc.* Test Site 2.1. Line 7. Normalised W-E balance factors.

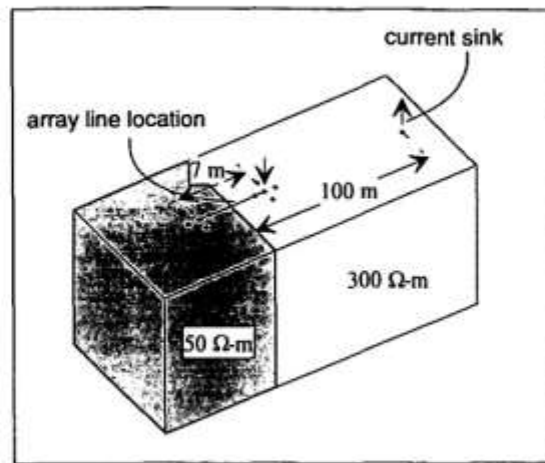


Figure 23 rsc. Idealised model of a vertical face.

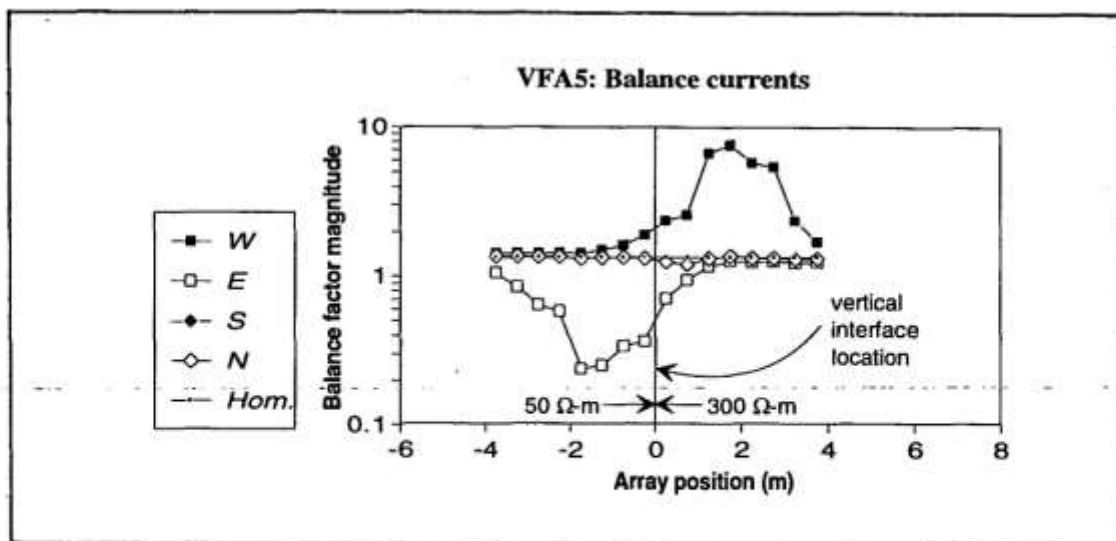


Figure 24 rsc. Vertical interface model results, Focussed balance factors.

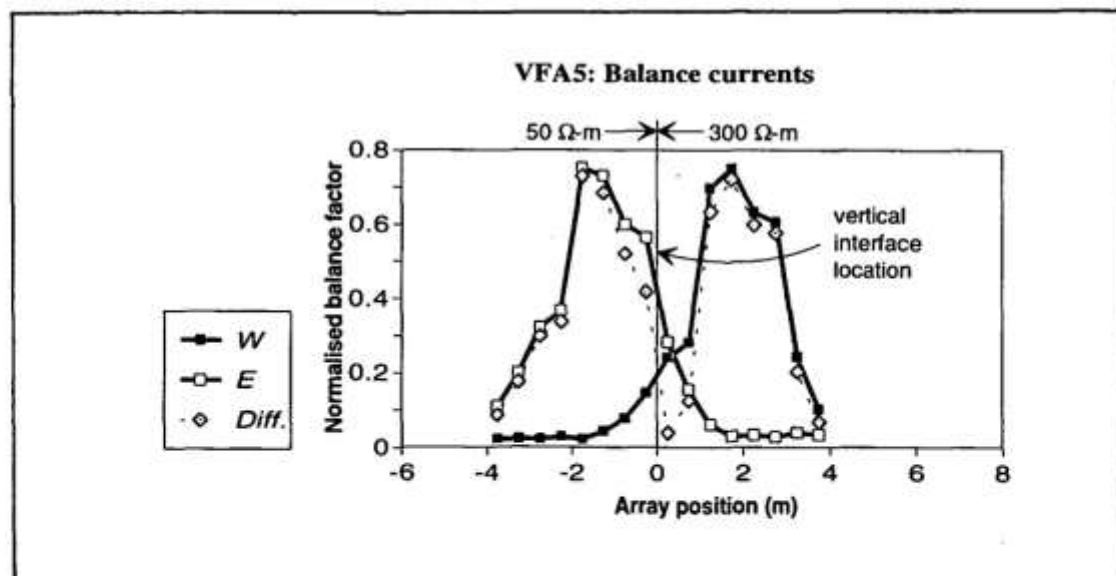


Figure 25 rsc. Vertical interface model results, Normalised W-E balance factors.



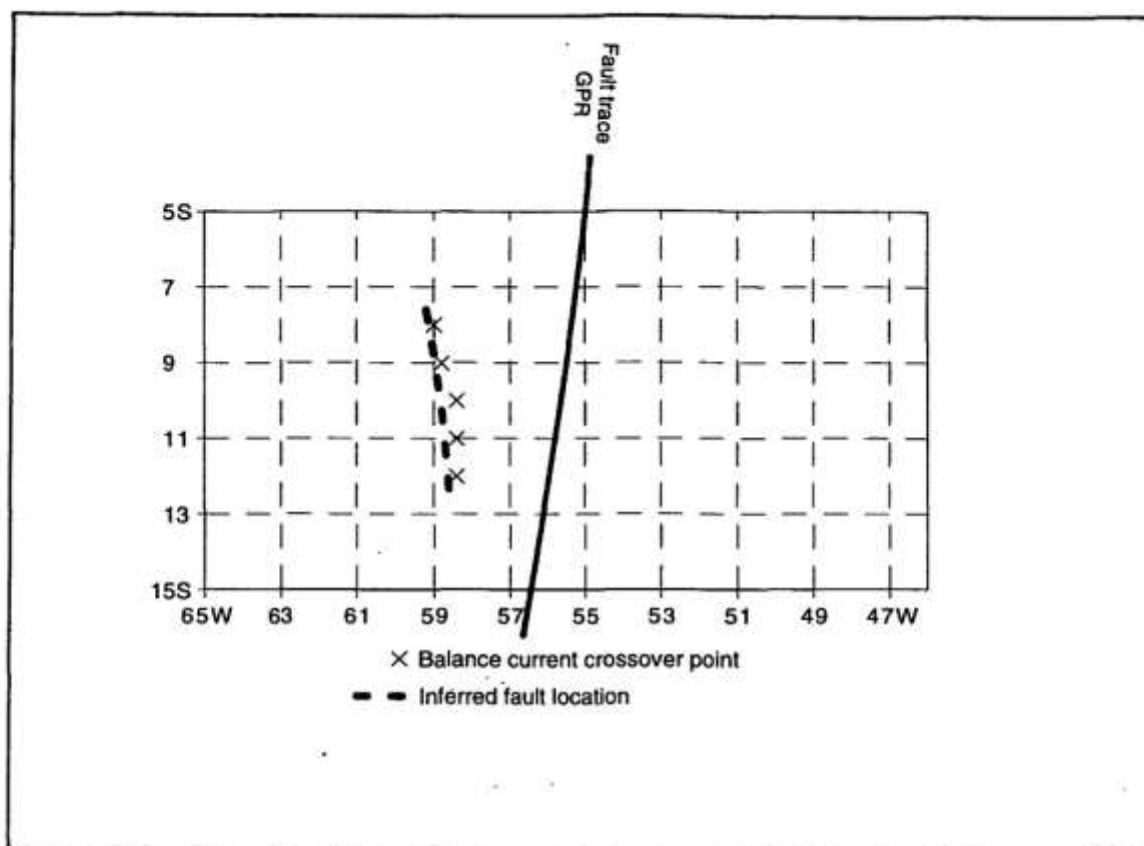
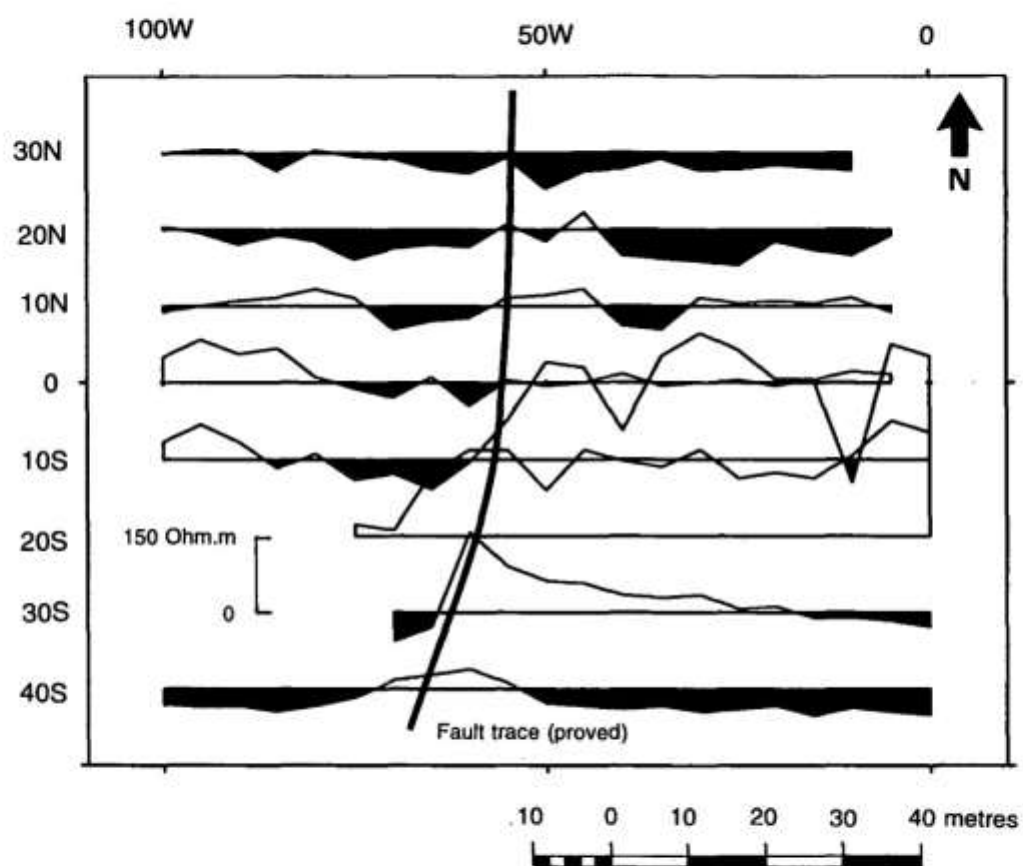
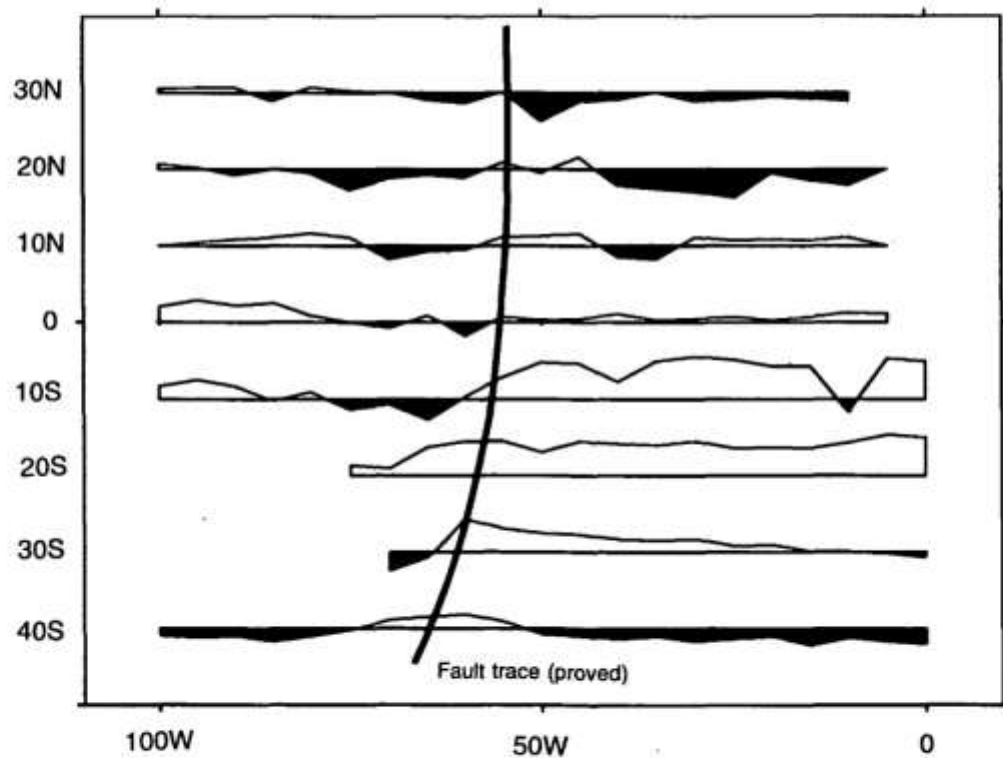


Figure 26 *rsc.* Test Site 2.1. Inferred surface location of fault trace.



A. Arithmetic scale. Scale datum 100 Ohm.m



B. Logarithm scale. Scale datum 90 Ohm.m

Figure 20 *vlf*. Test Site 2.1. VLF R-field (Interuran data) profiles and proved fault trace.

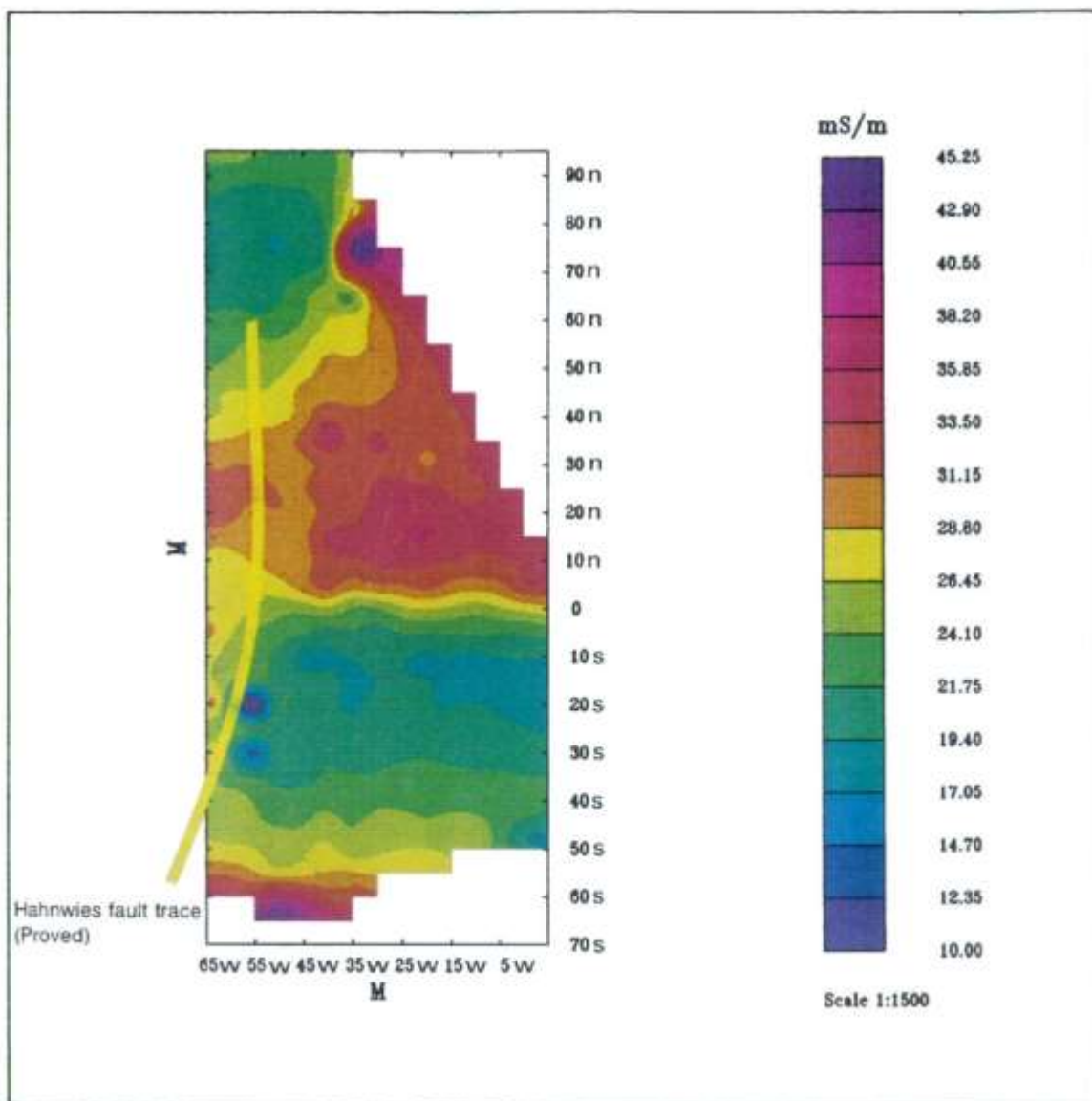


Figure 8 *em.* Test Site 2.1. Apparent conductivity contours (EM31 horizontal dipole).



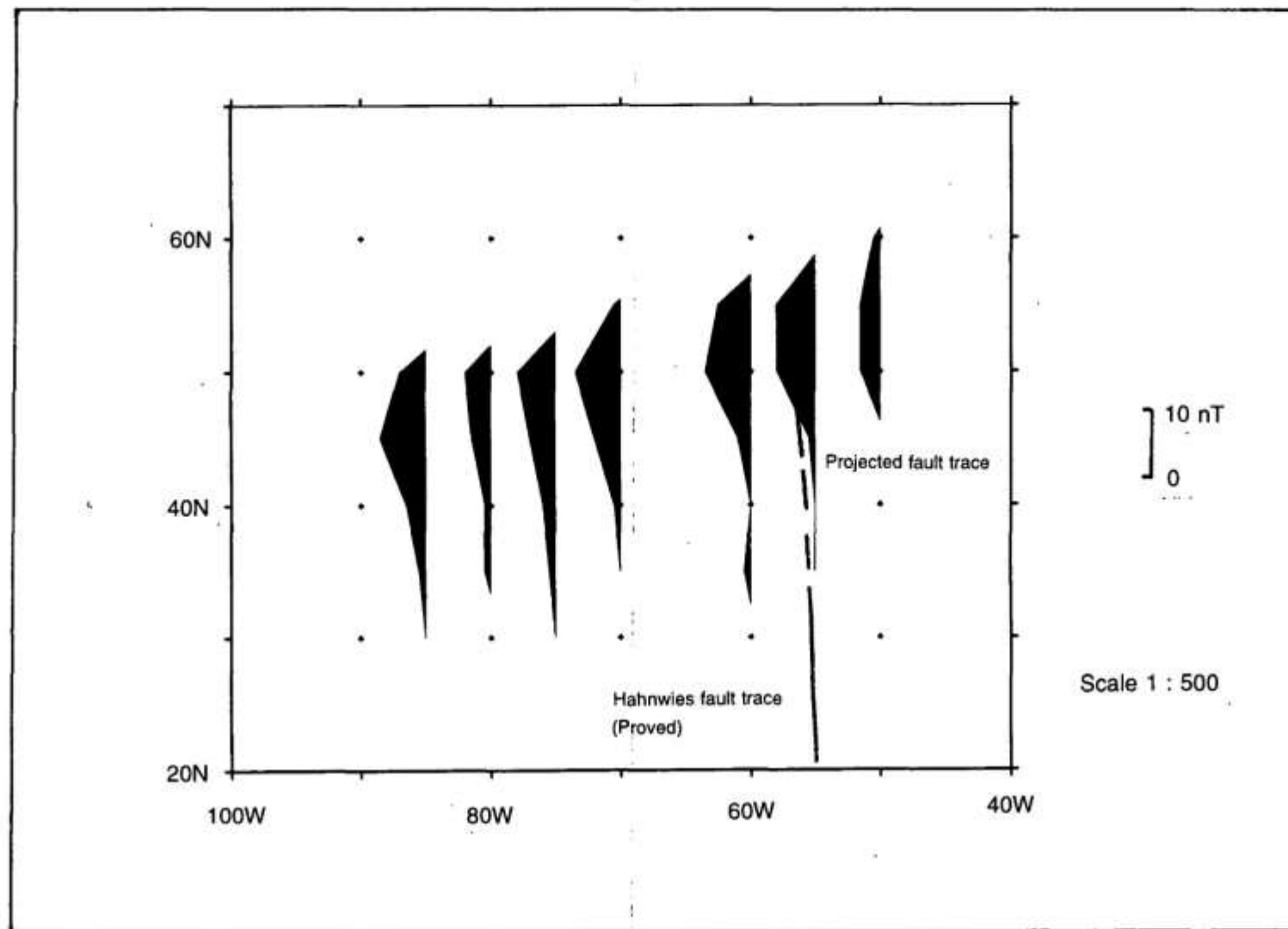


Figure 1 *mag.* Test Site 2.1. Total field magnetic profiles.

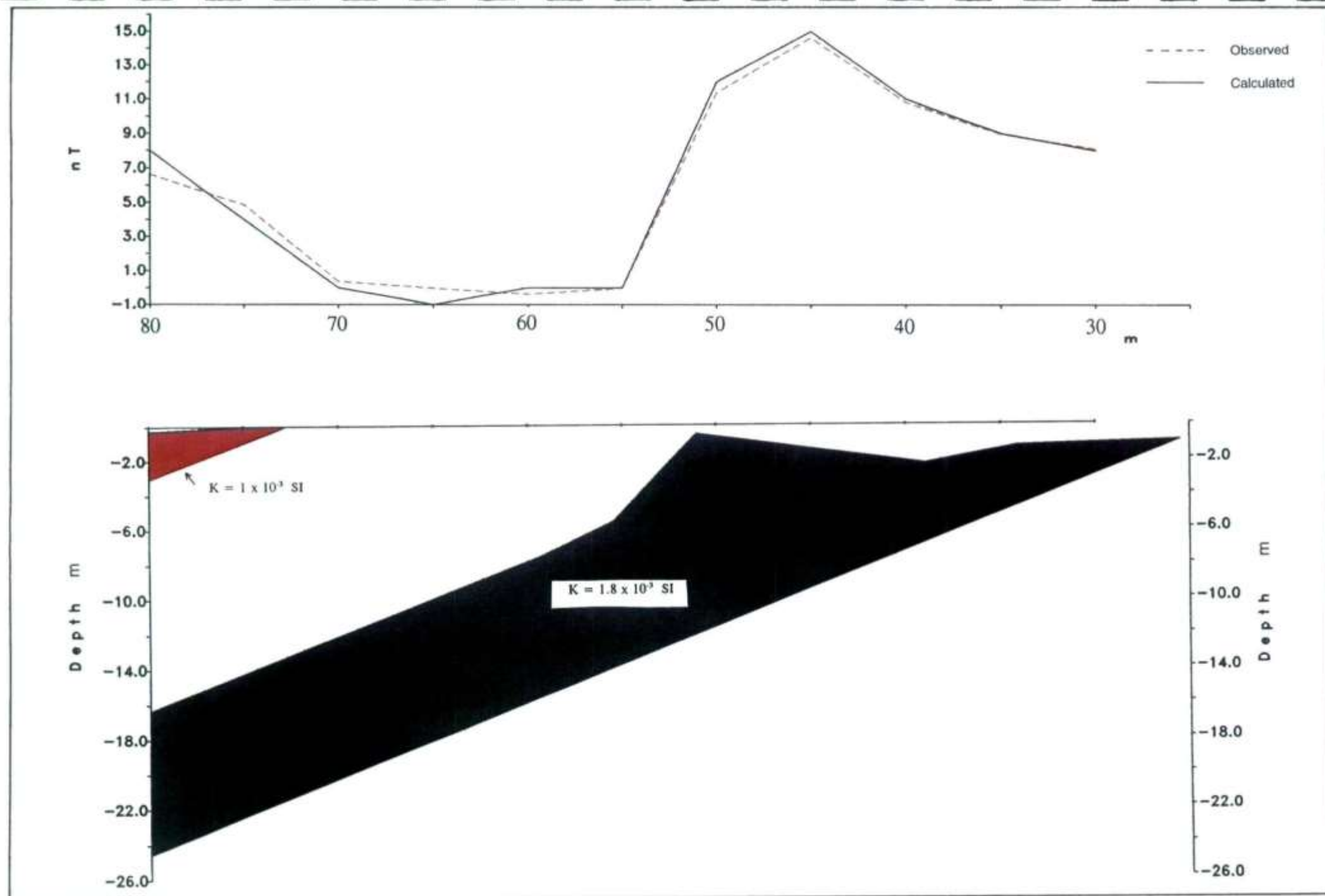


Figure 2 mag.

Test Site 2.1. Magnetic model line 85W.

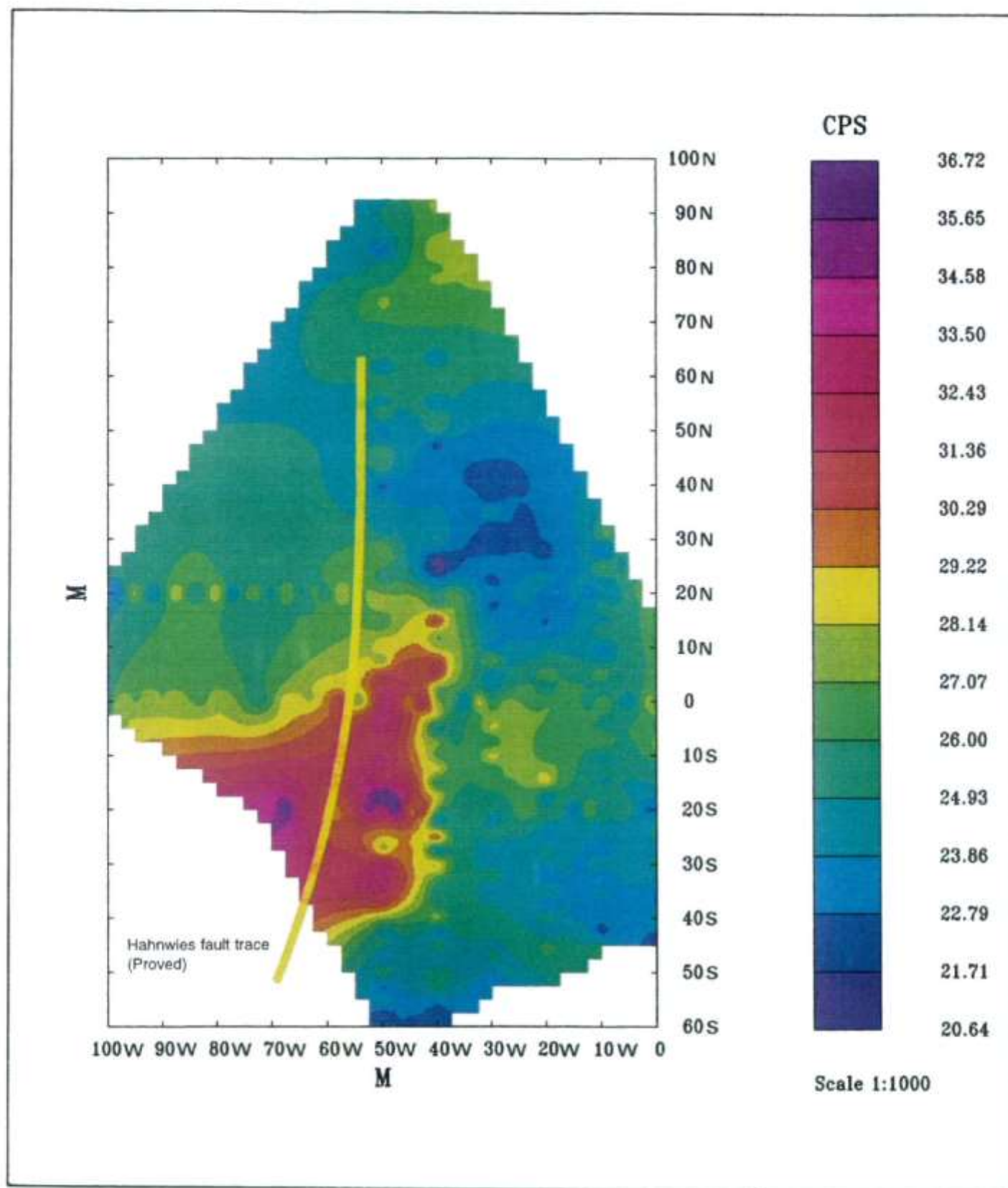


Figure 3 gam.

Test Site 2.1. Natural gamma surface mapping.



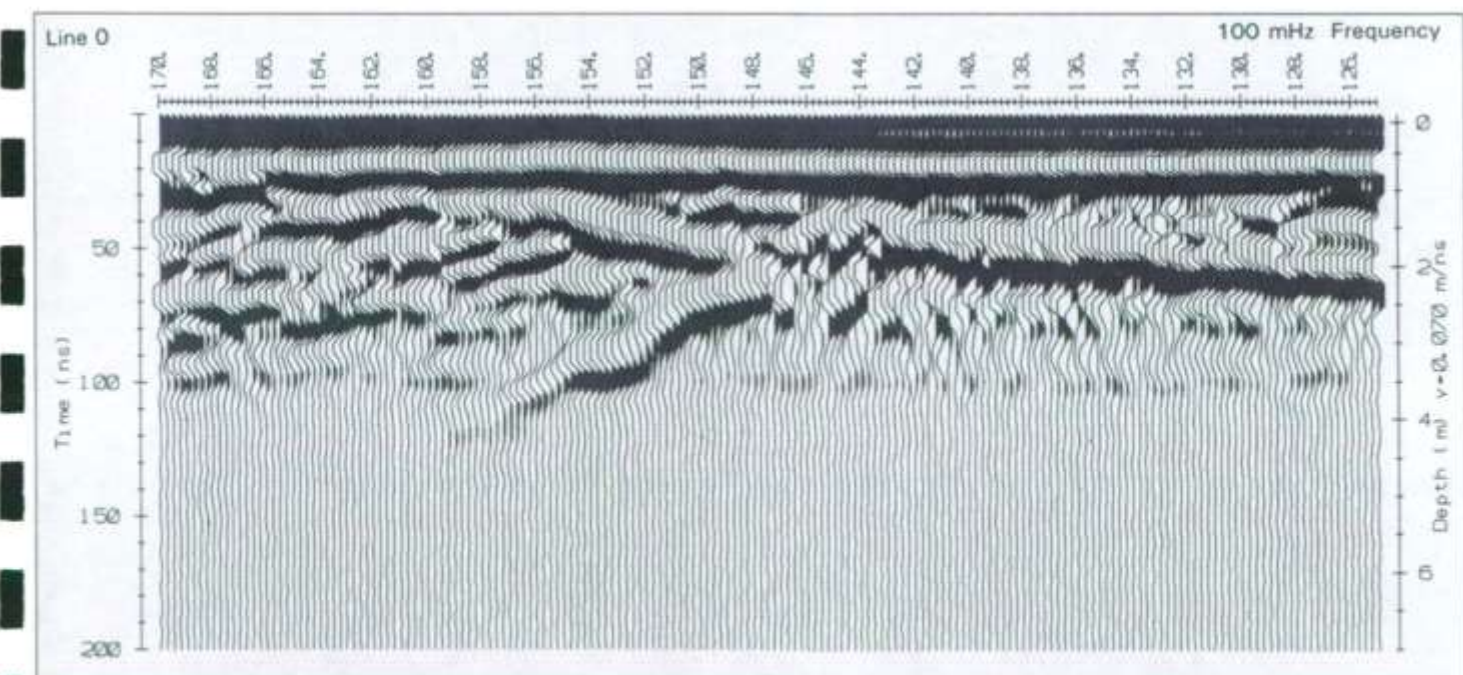
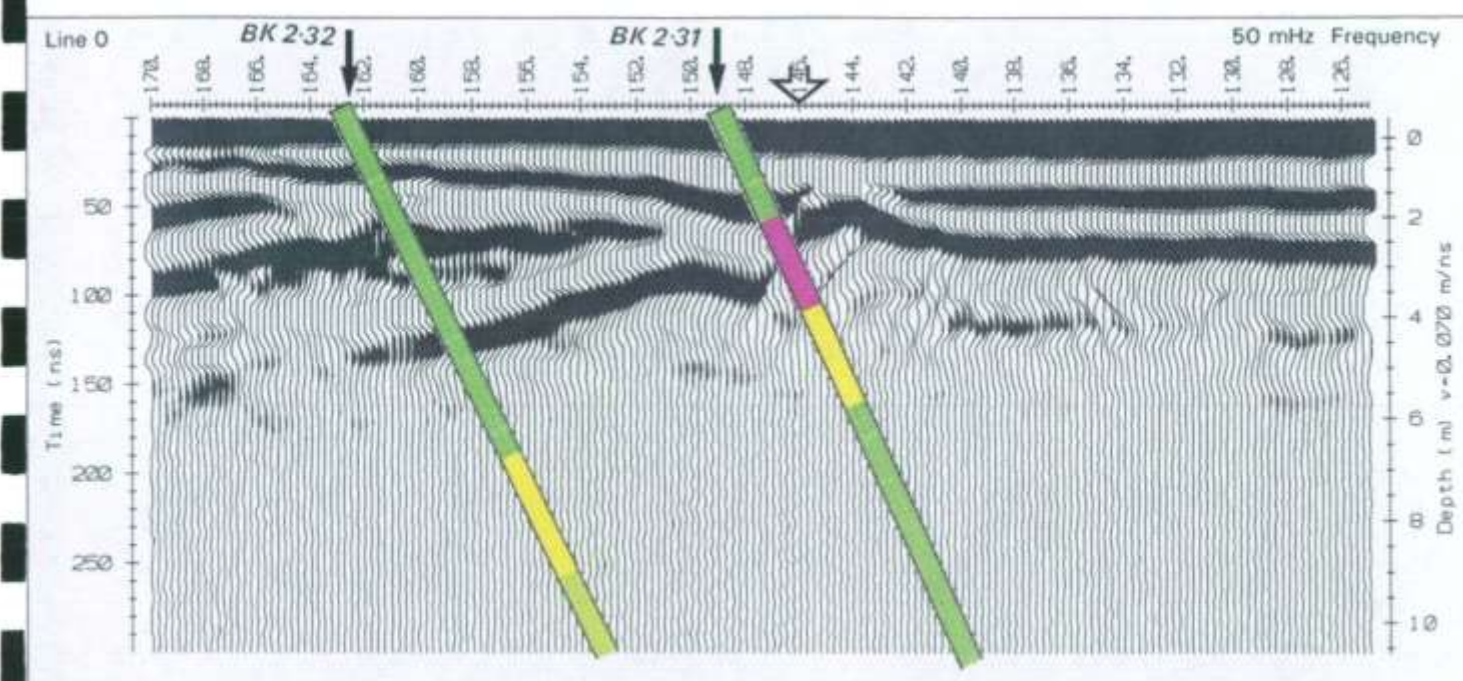
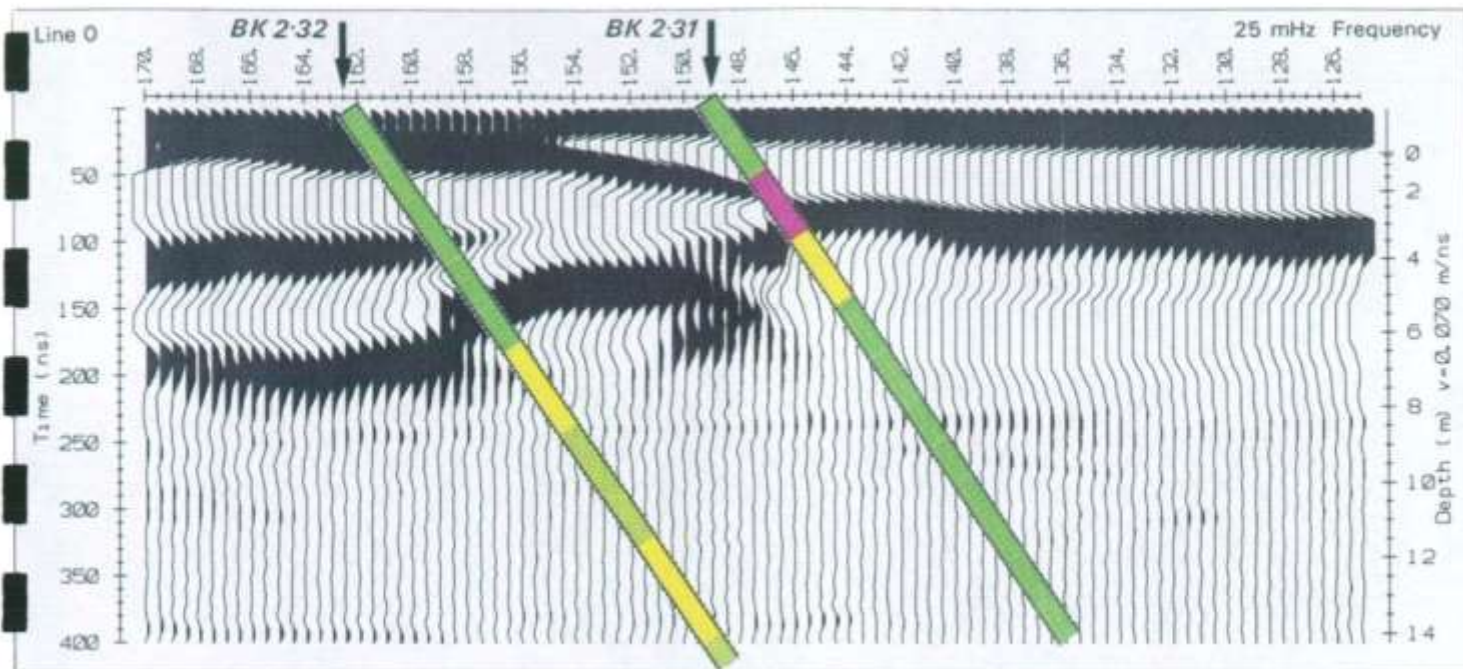


Figure 21 *gpr*. Test Site 2.3. GPR profile for line 0. Comparison of 25, 50, and 100 MHz antennae frequencies.



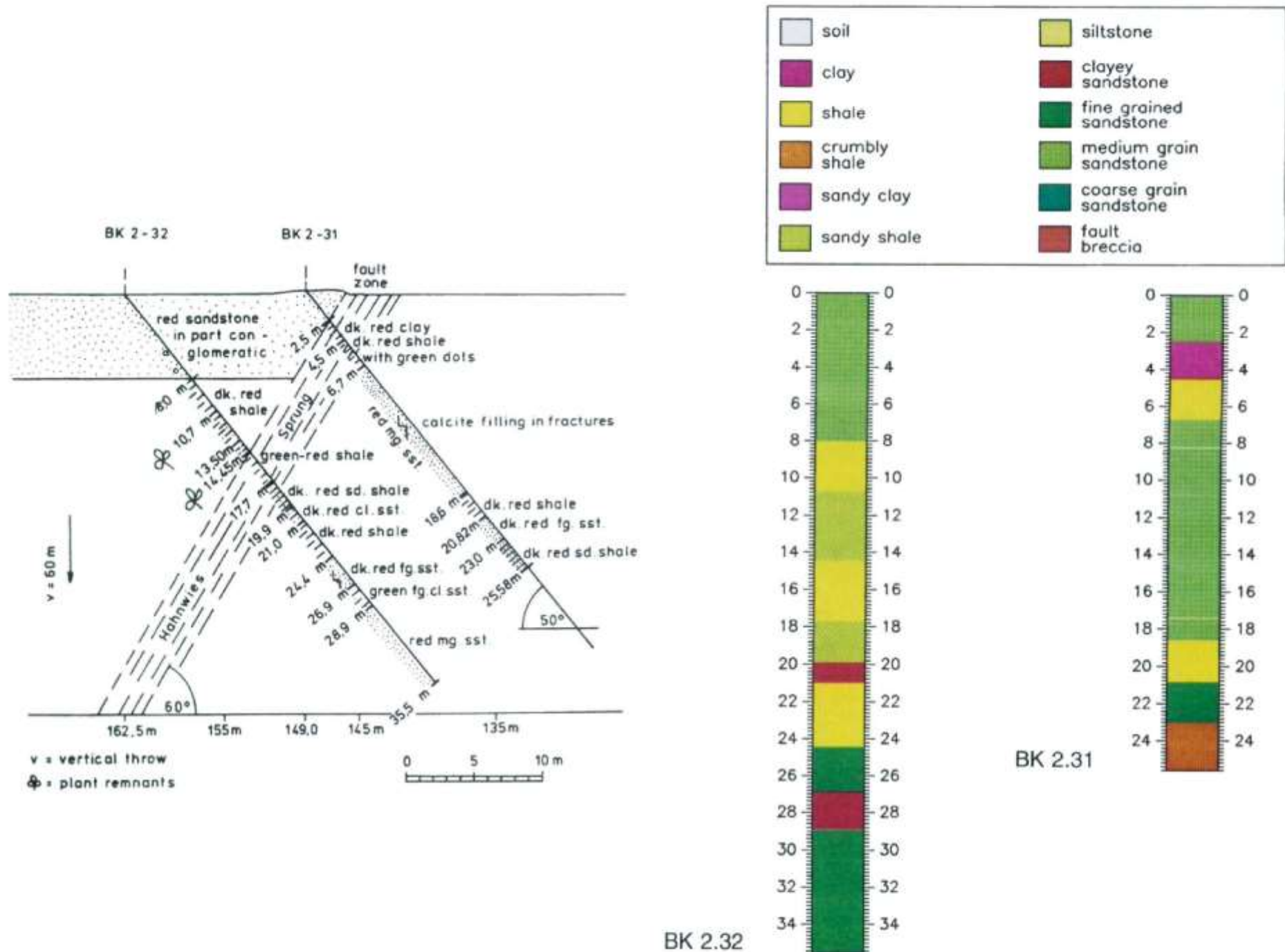


Figure 20. Test Site 2.3. Geological section: boreholes BK2.31 and BK2.32.

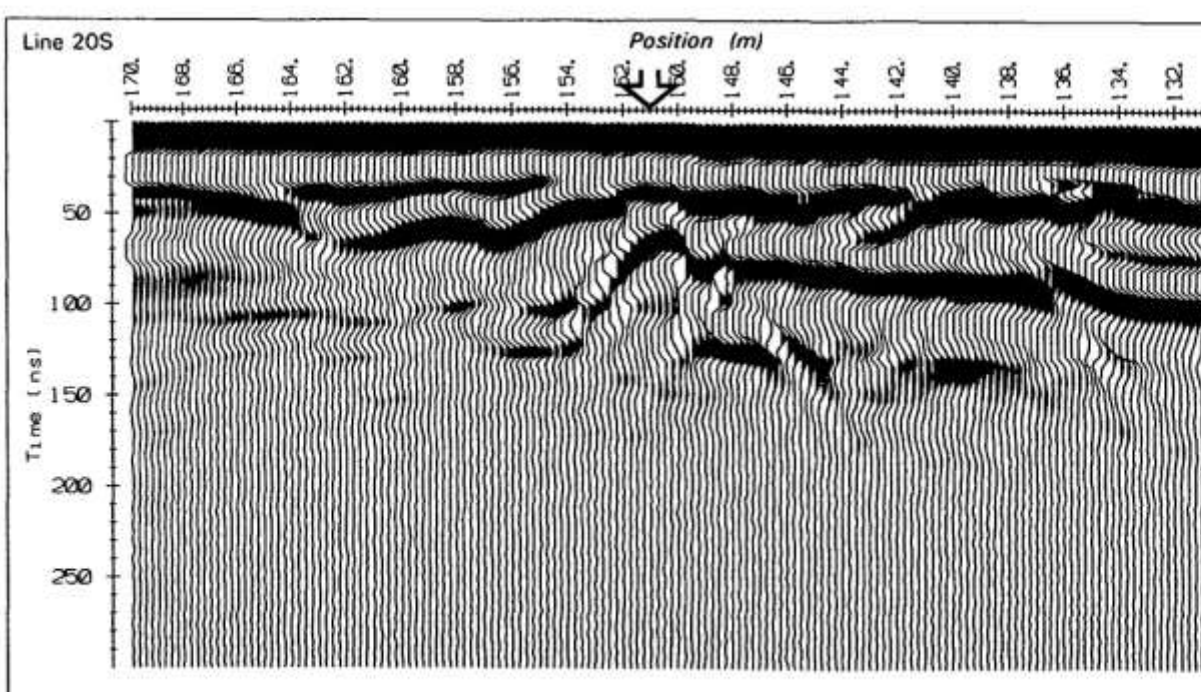
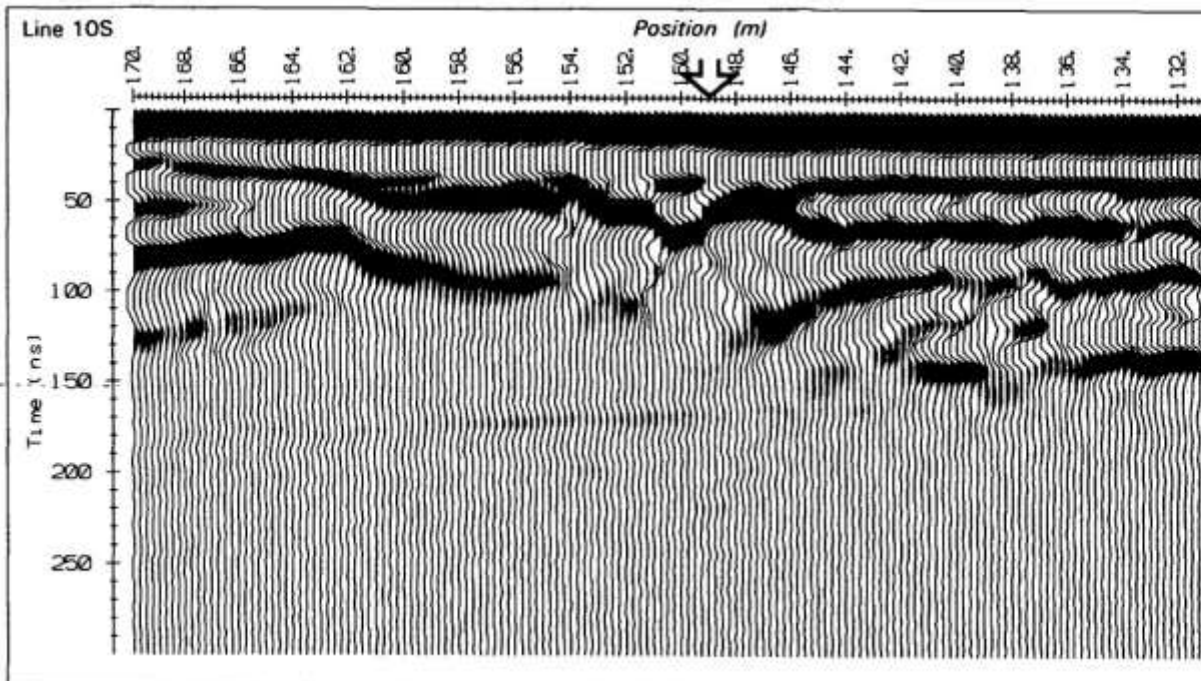
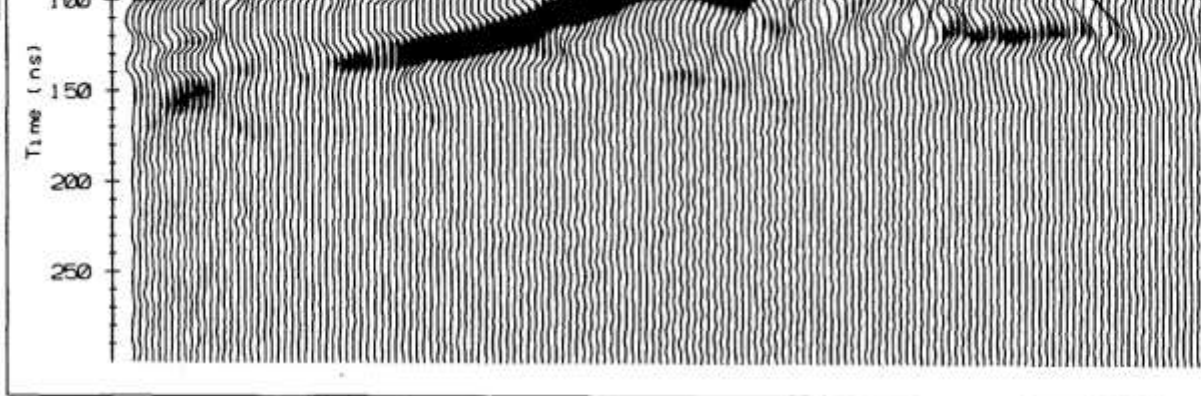


Figure 22 *gpr*. Test Site 2.3. GPR profiles for lines 0, 10S, and 20S. 50 MHz



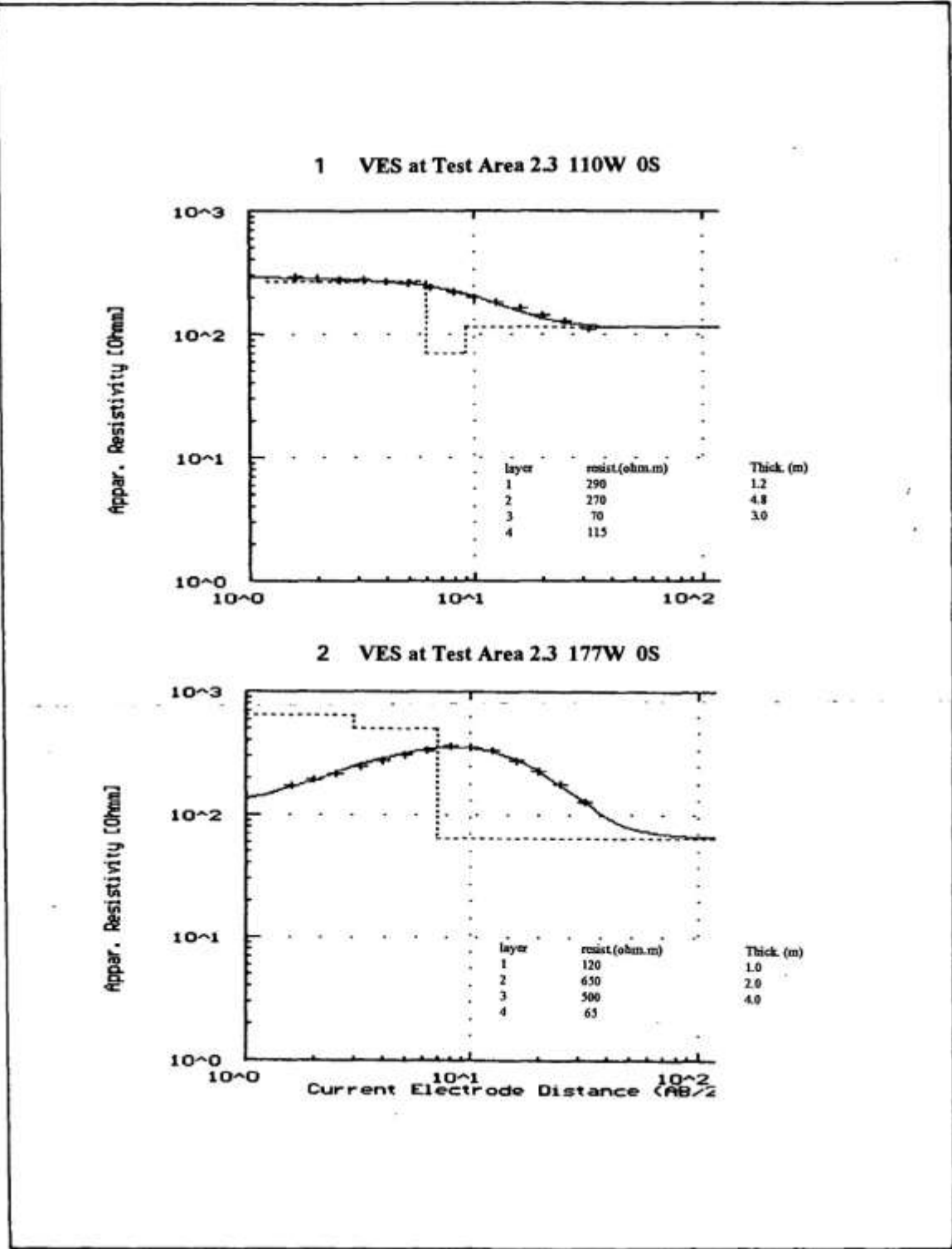


Figure 11 res.

Test Site 2.3. Interpretation of VES 1, and 2.

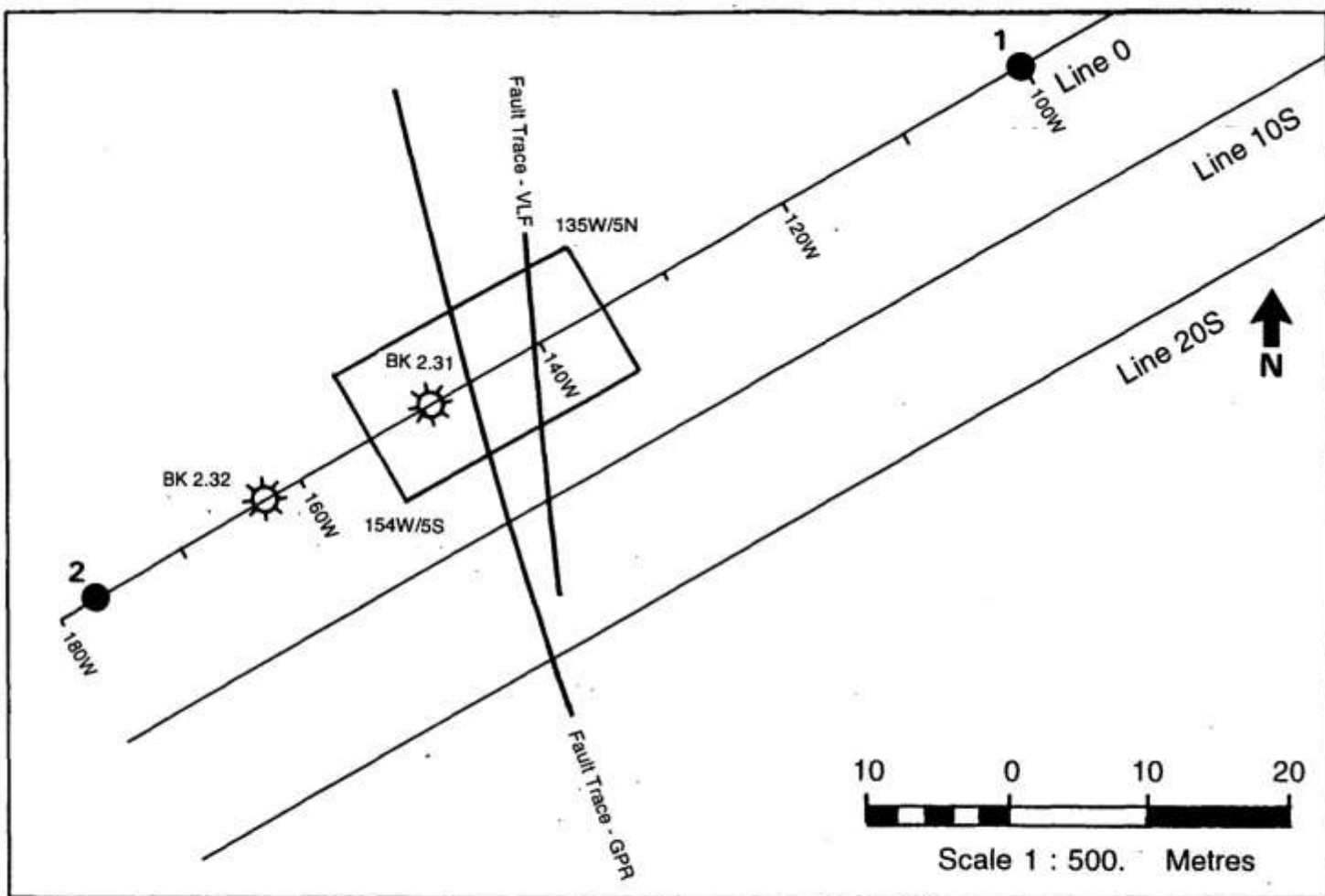


Figure 32, *rsc.* Test Site 2.3. Plan (partial)-of site showing location of RESCAN grid.

# Half - Schlumberger Apparent Resistivity Style B AB = 3 and 9 m

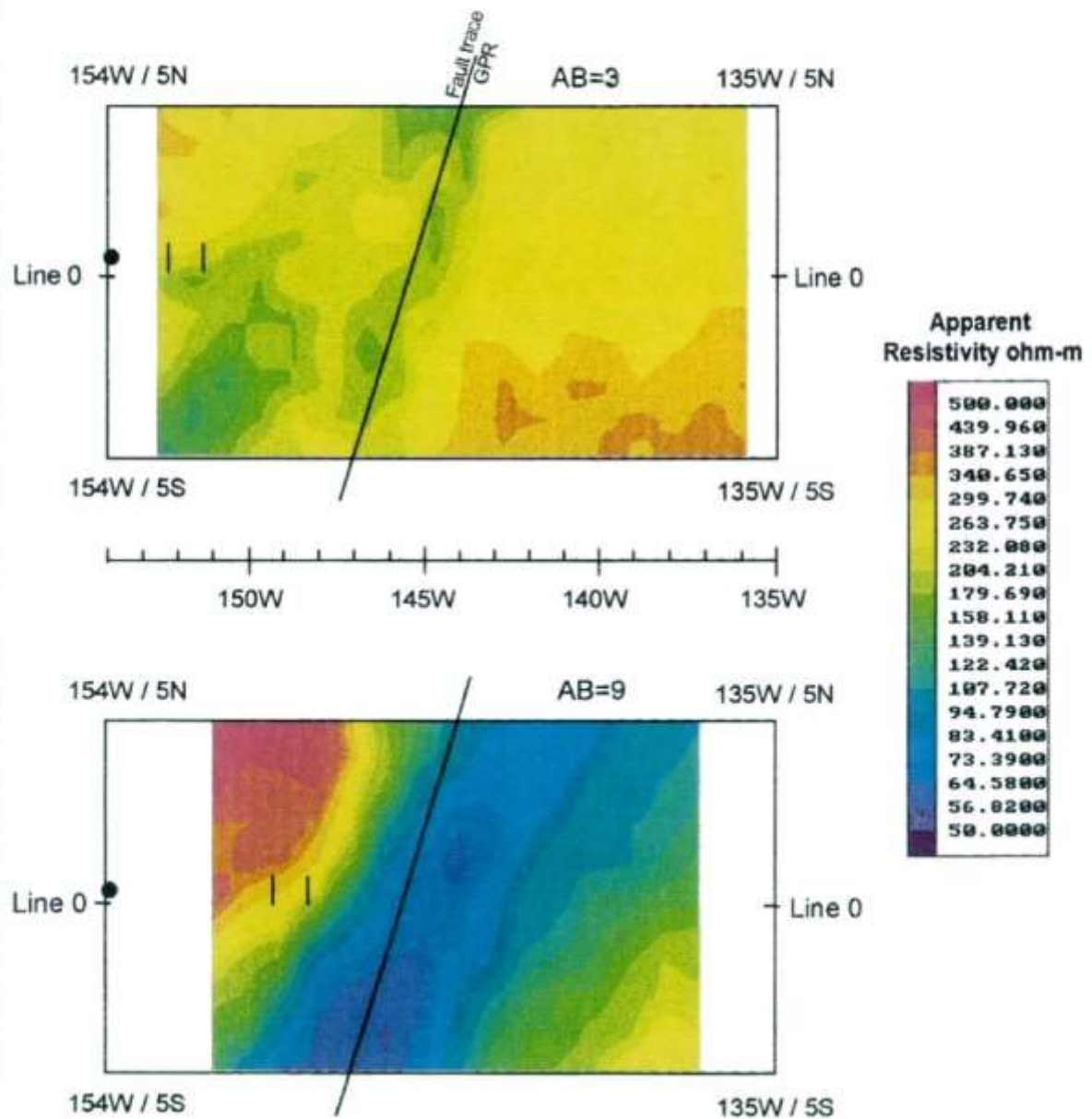
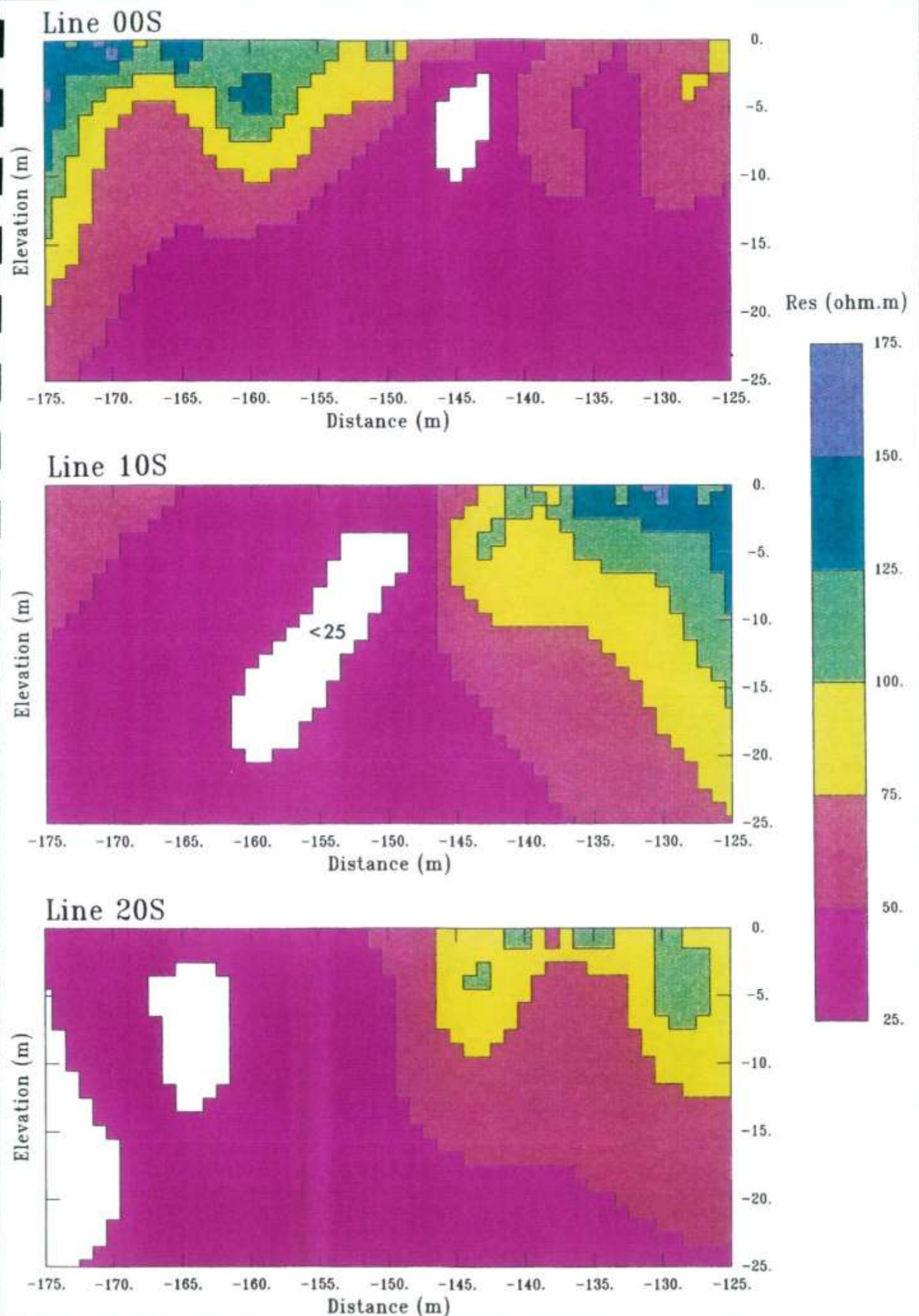


Figure 6 *rsc.* Test Site 2.3. Apparent resistivity maps for two depths of investigation.





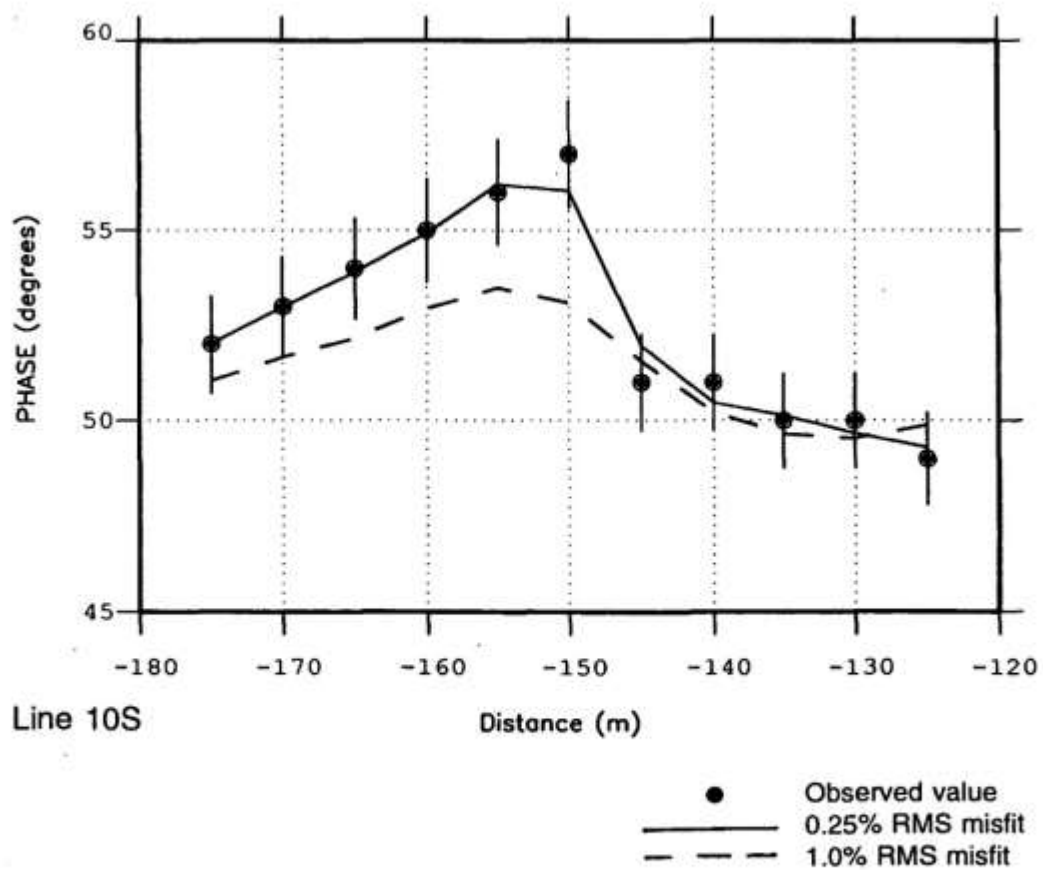
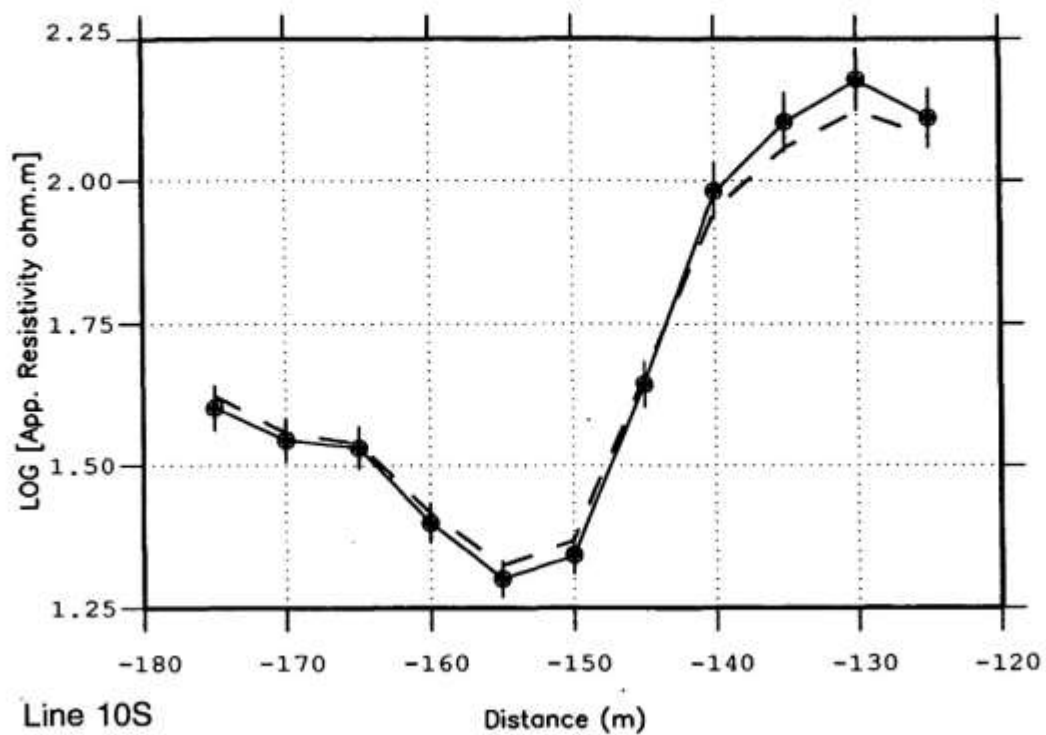


Figure 22 *vlf*. Test Site 2.3. Occam inversion: levels of fit of models to observed data.

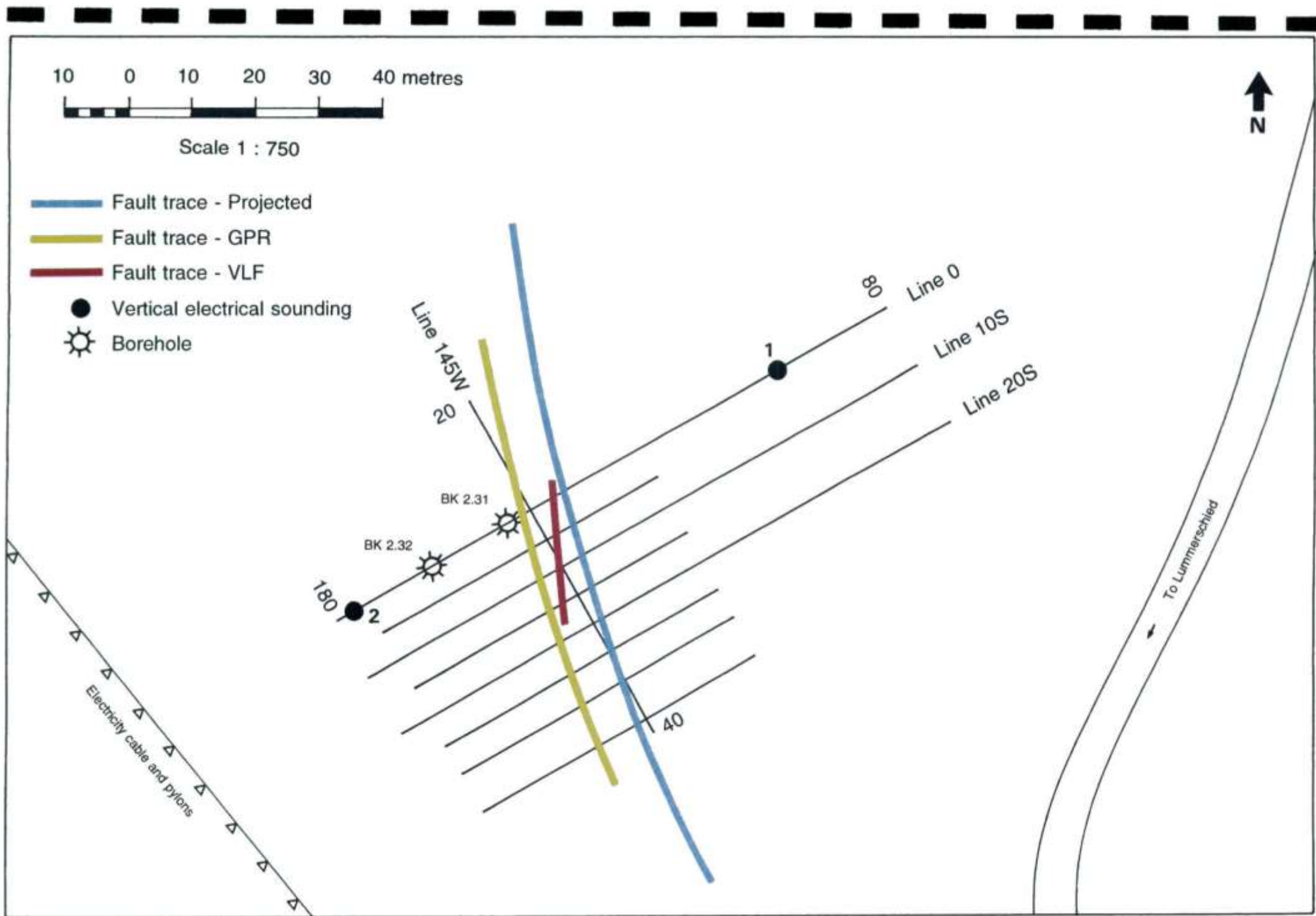
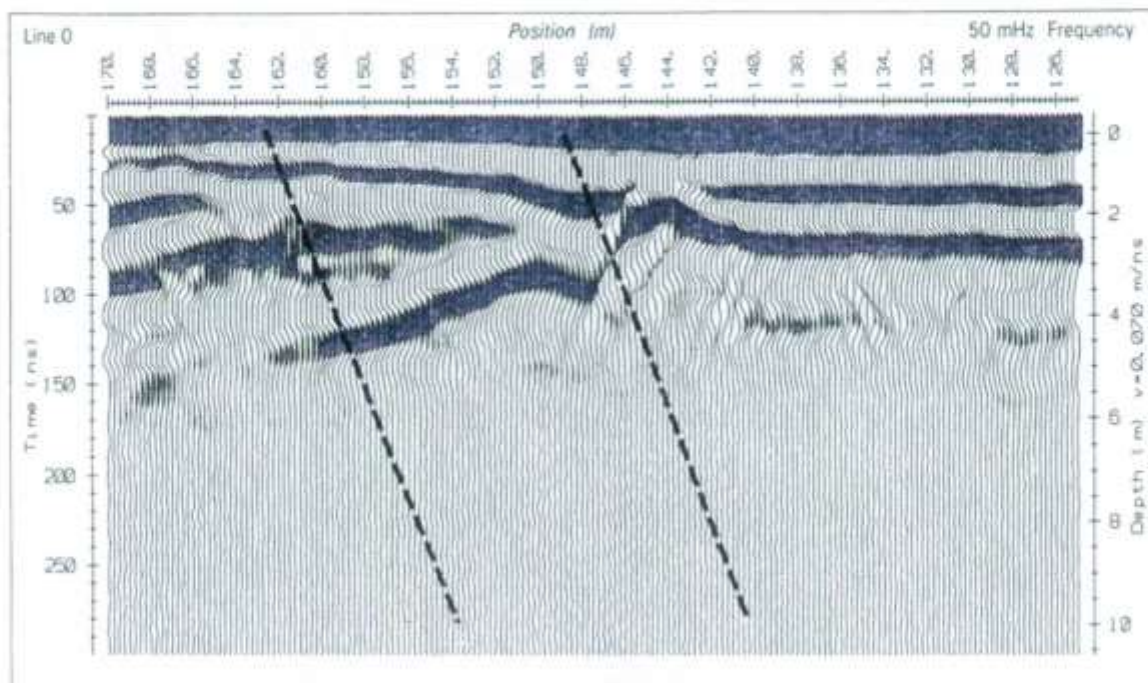
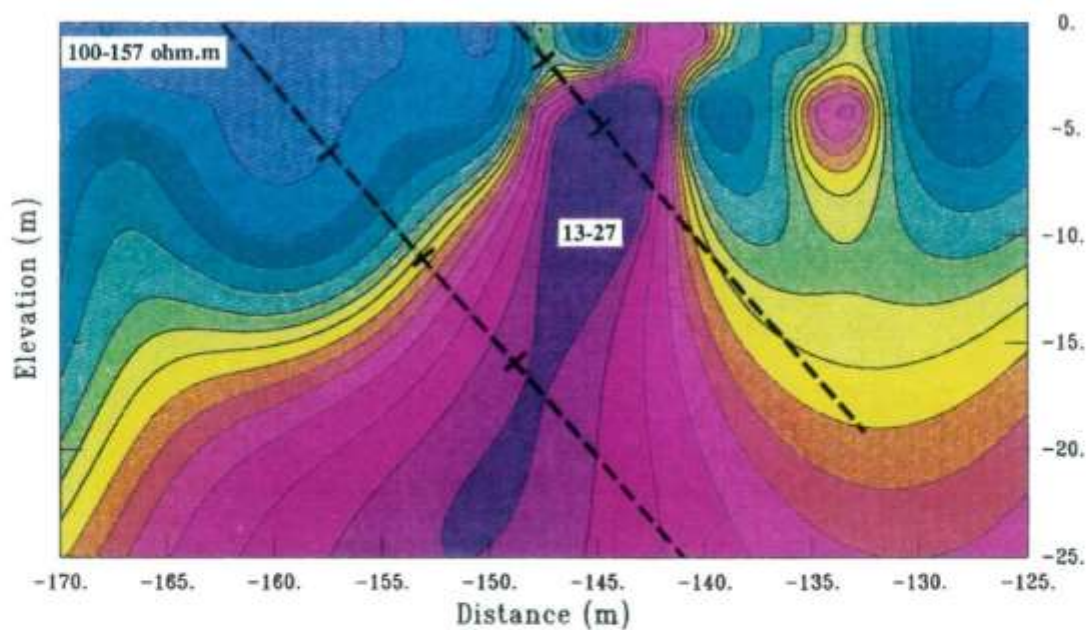


Figure 19. Test Site 2.3. Geophysical grid, borehole locations, and interpretation.





**Ground Probing Radar (50MHz)**  
 $dx = 0.25\text{m}$ , V.E.  $\times 2.3$



**VLF (16kHz) Resistivity Model (Equal Area Colour)**  
 $dx = 5\text{m}$ , True Scale

Figure 23 vlf. Test Site 2.3. Coincident GPR and VLF resistivity cross sections for line 10S.

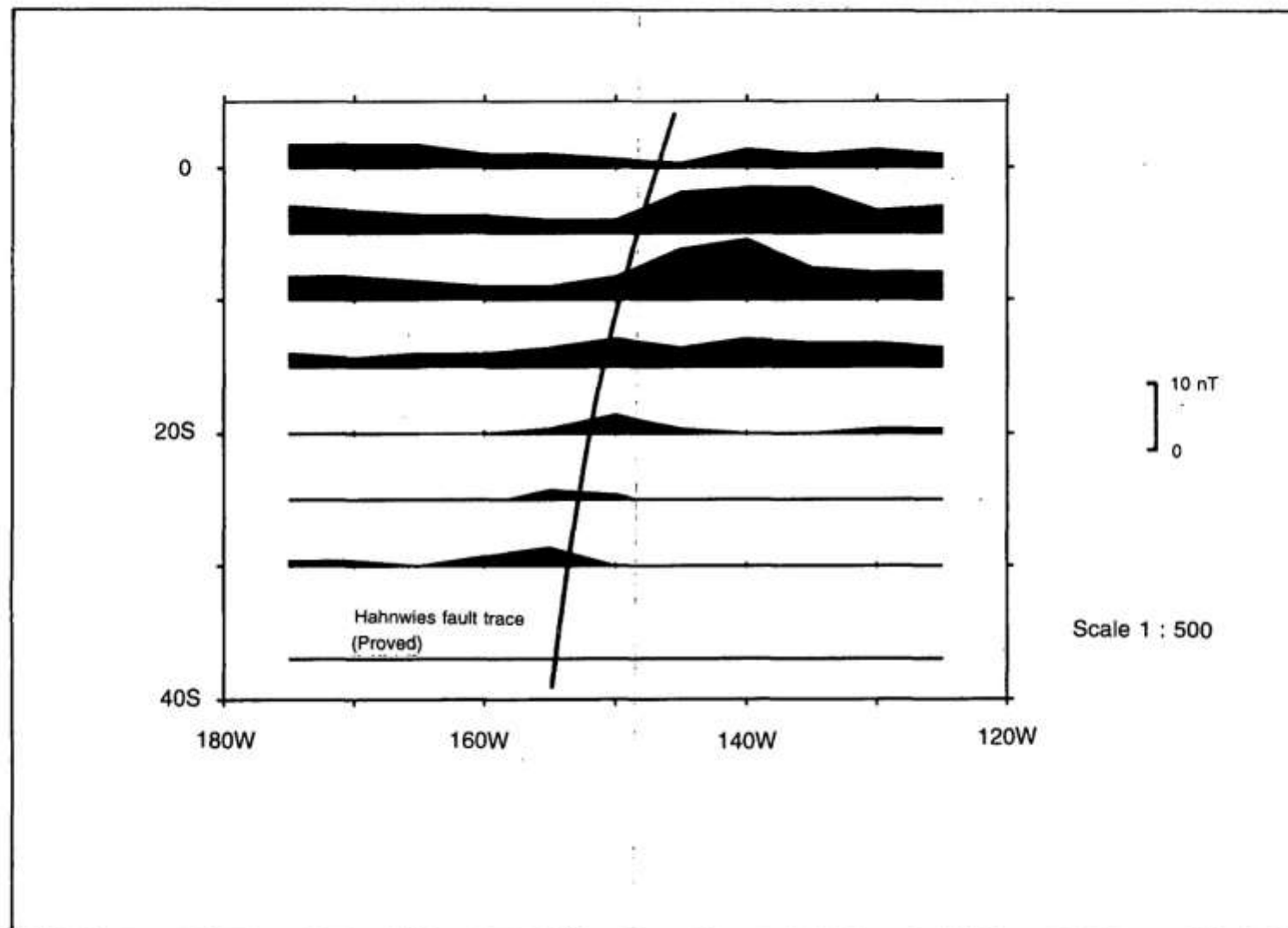


Figure 3 mag. Test Site 2.3. Total field magnetic profiles.

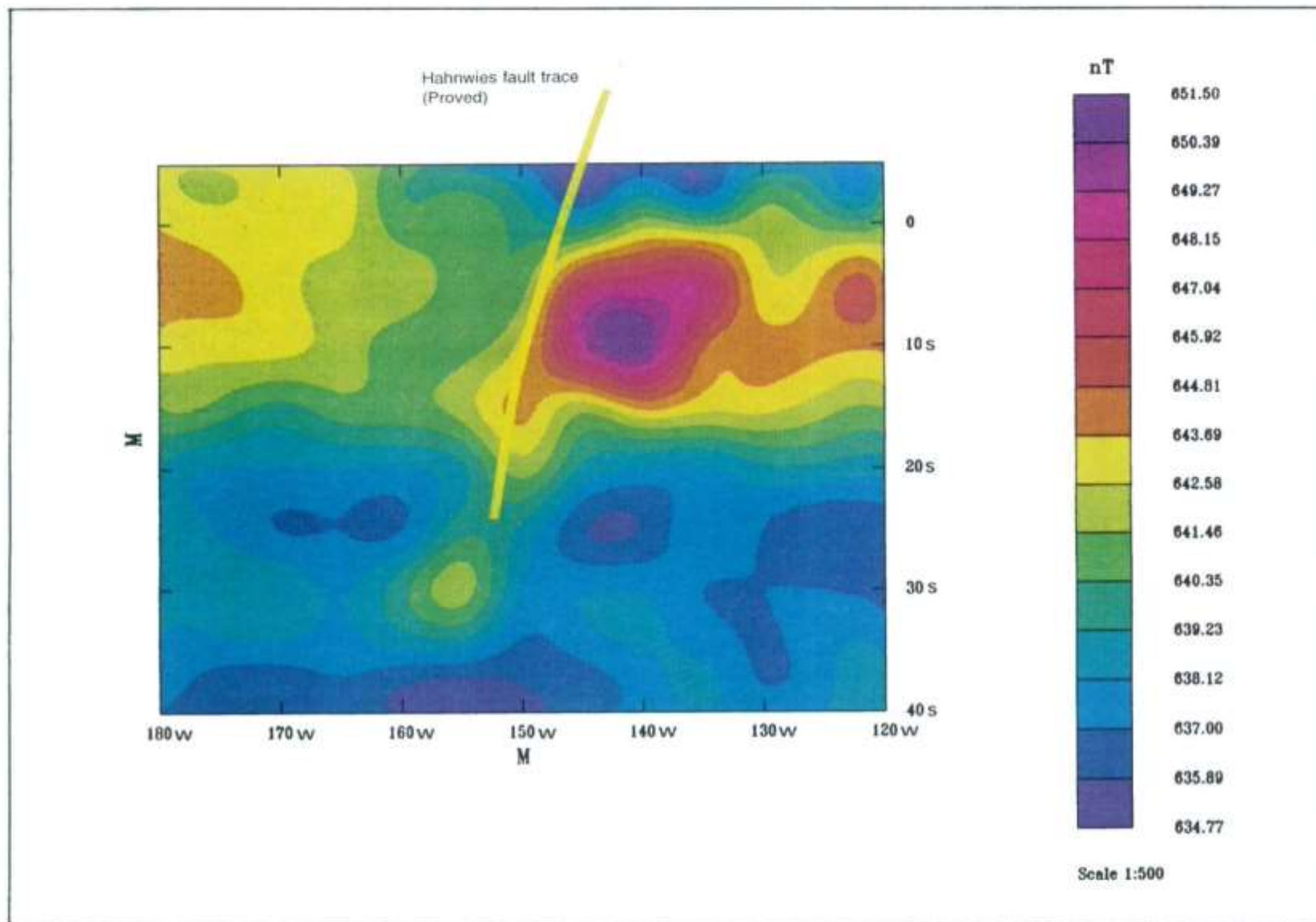


Figure 4 *mag.* Test Site 2.3. Total field magnetic contours.



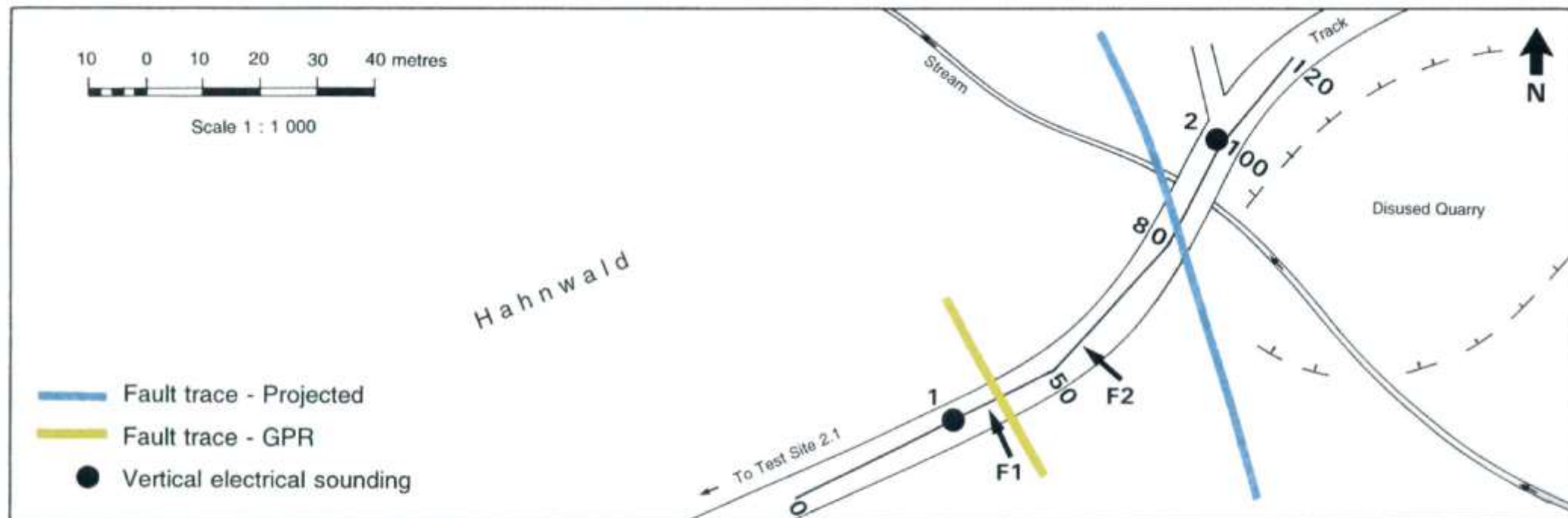


Figure 21. Test Site Hahnwald. Hahnwald traverse and interpretation.

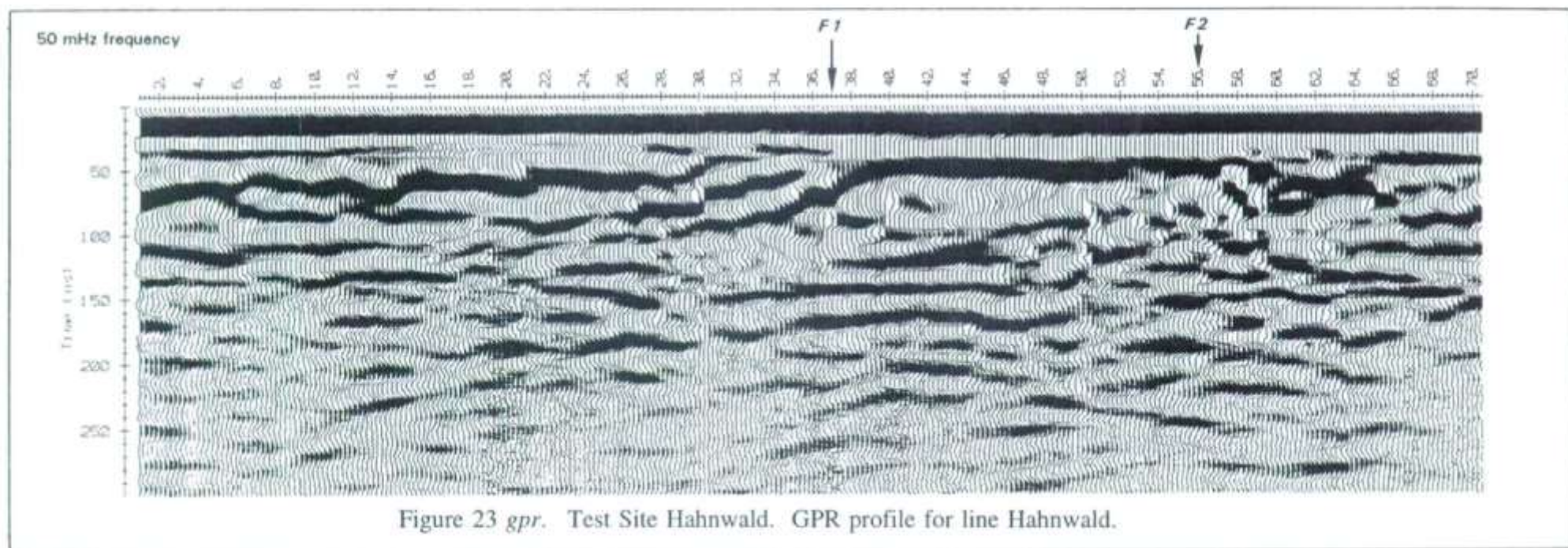
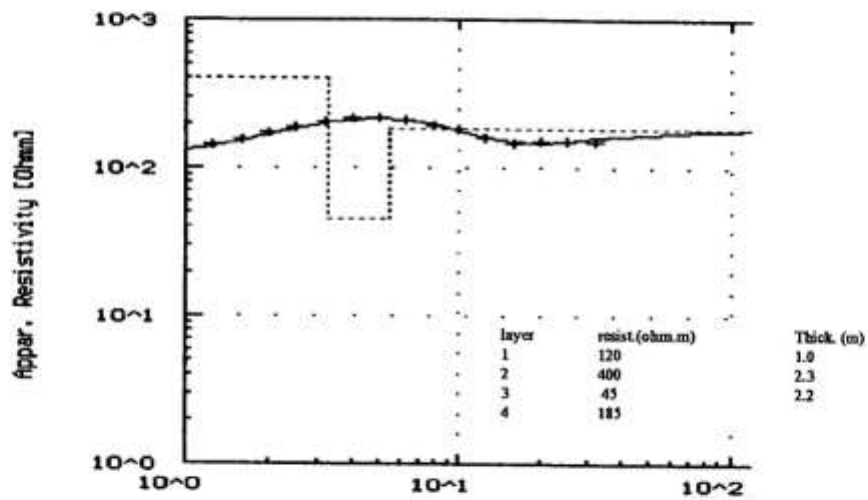


Figure 23 *gpr*. Test Site Hahnwald. GPR profile for line Hahnwald.

# 1 VES on Hahnwald track at 30E



# 2 VES on Hahnwald track at 100E

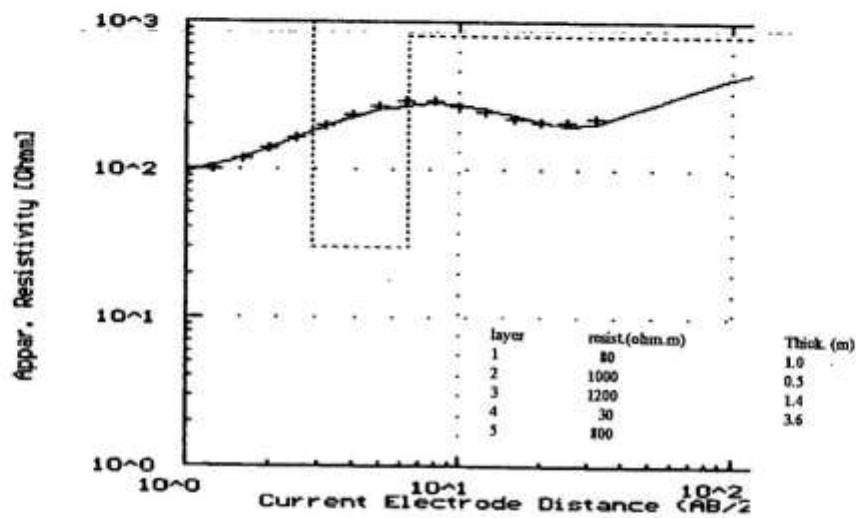


Figure 12 res.

Hahnwald track. Interpretation of VES 1, and 2.

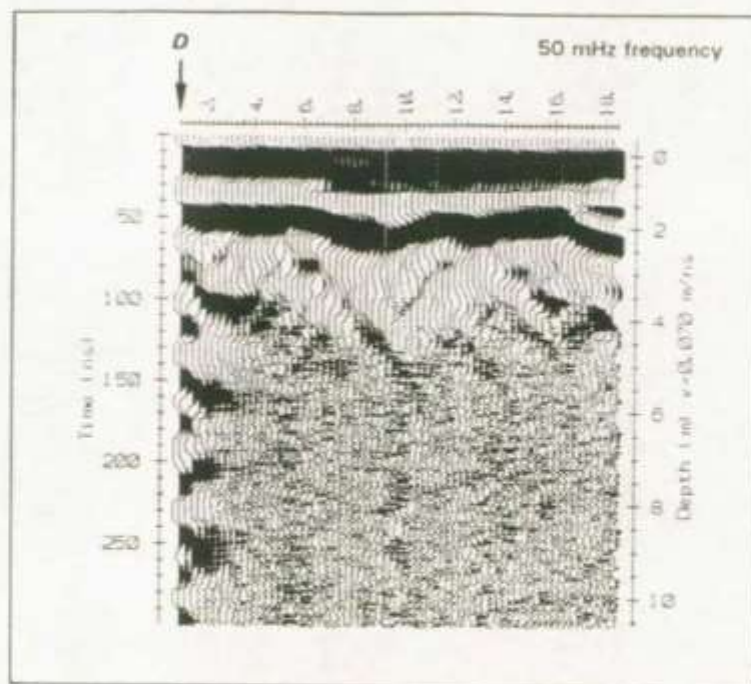
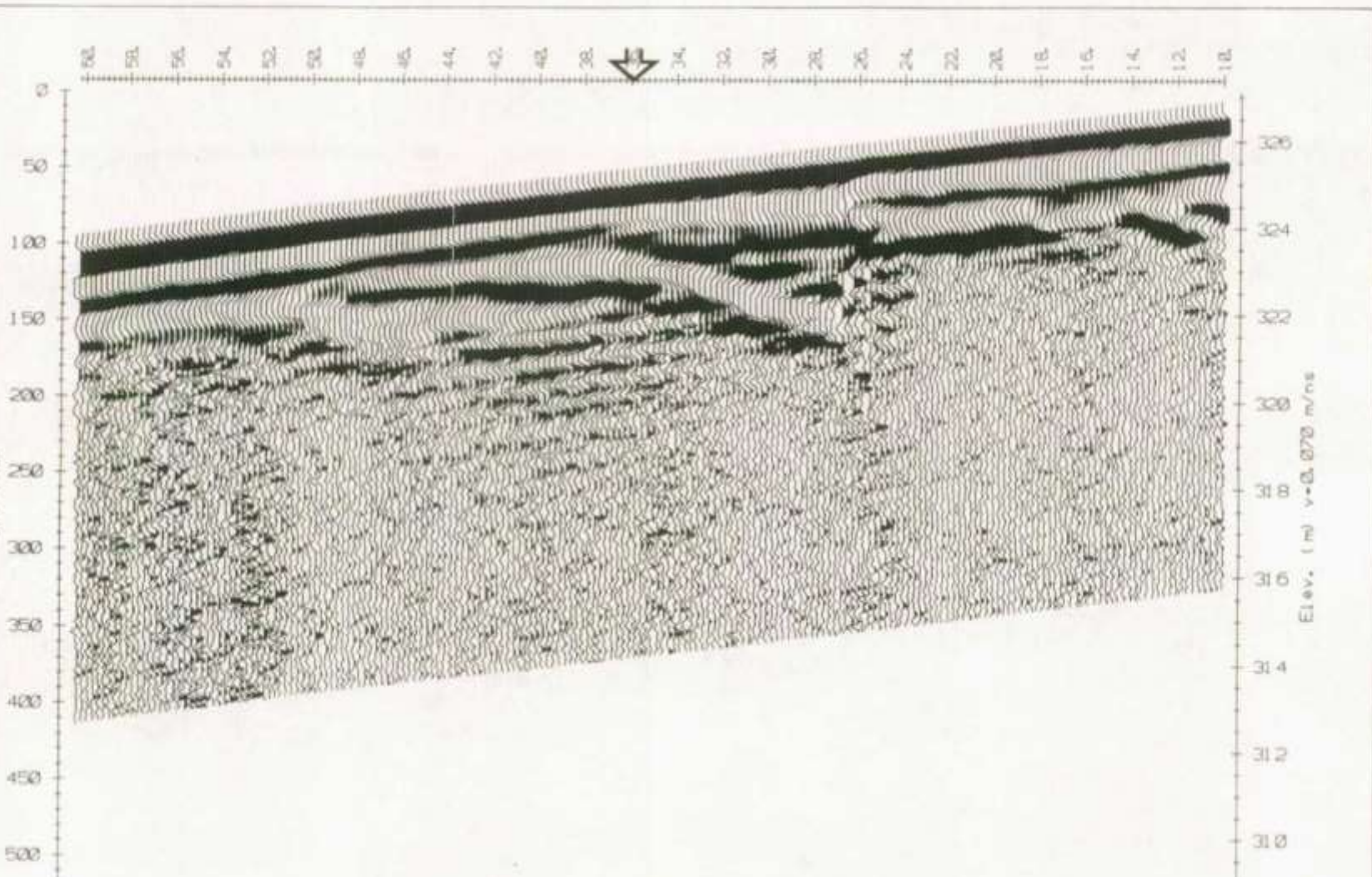


Figure 24 *gpr*. Test Site 2.5. GPR profile for line Fence.





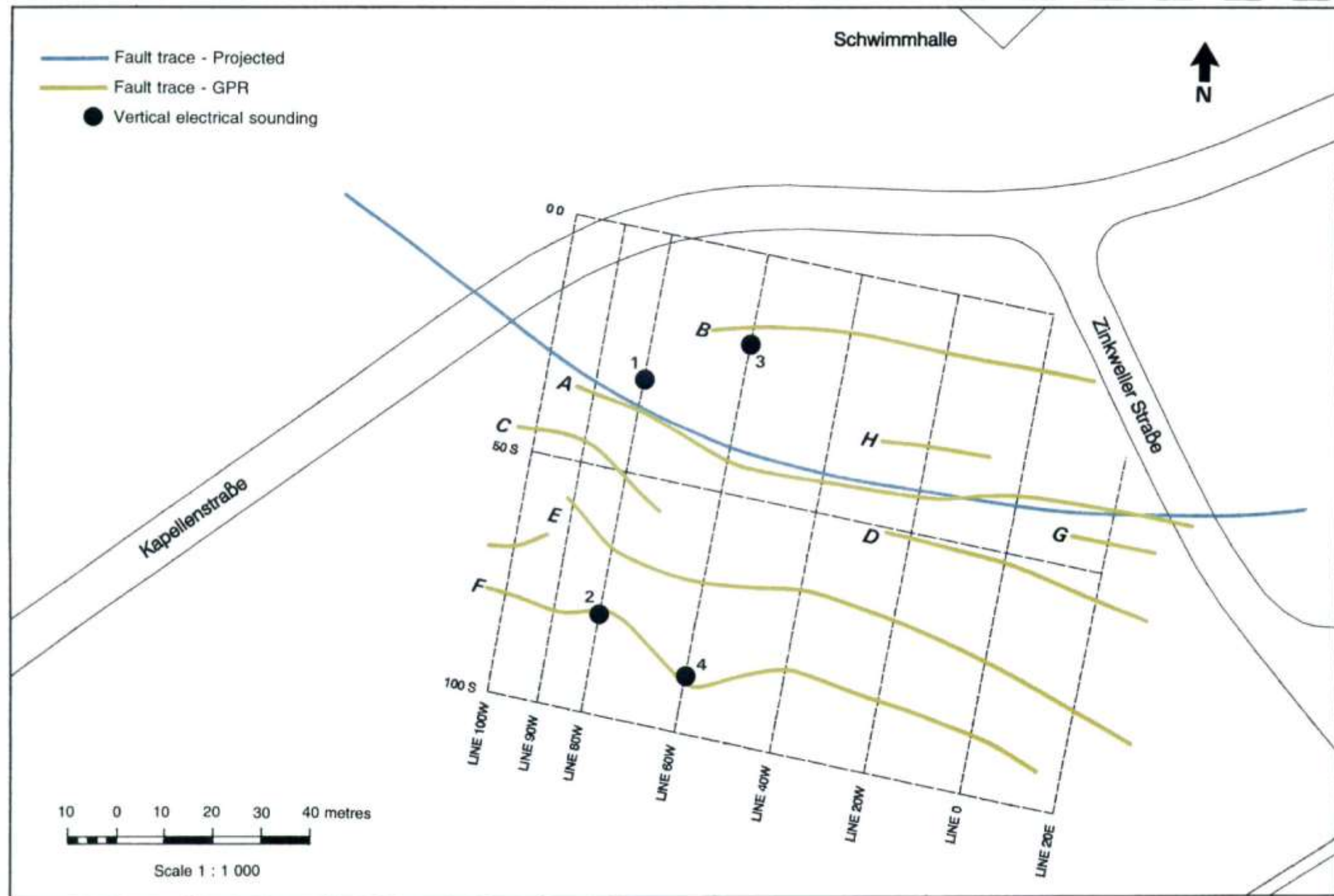


Figure 22. Test Site 3.1. Geophysical grid and interpretation.

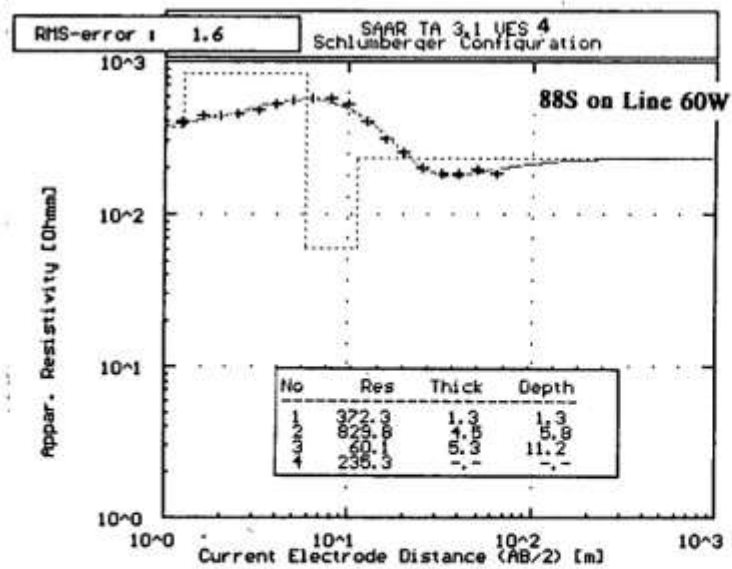
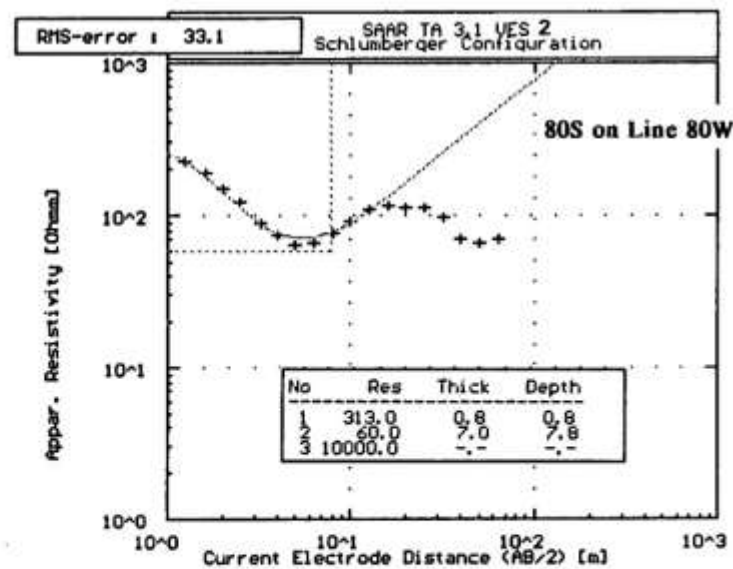
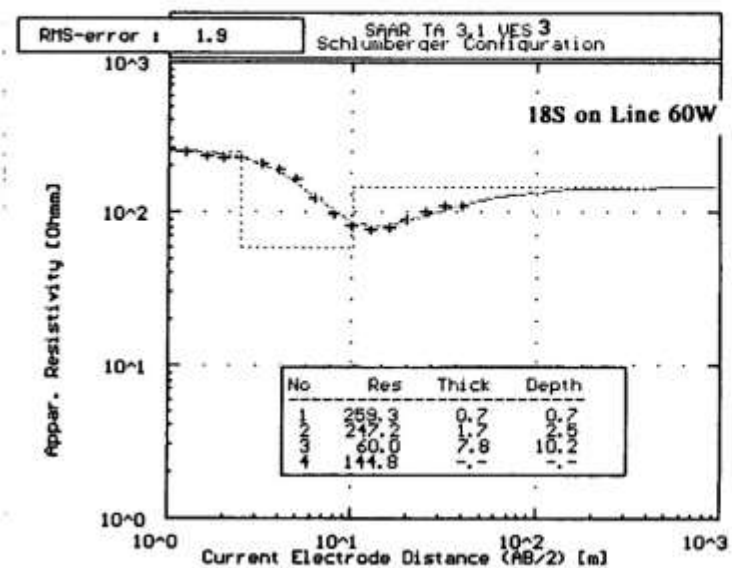
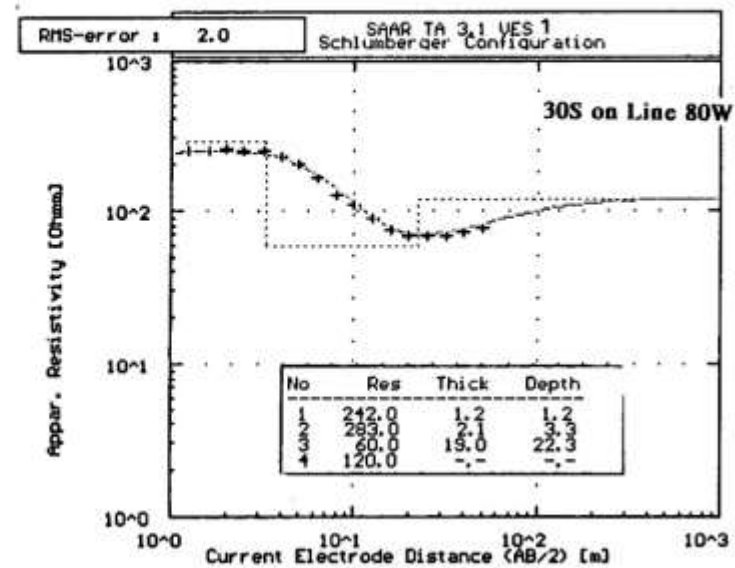
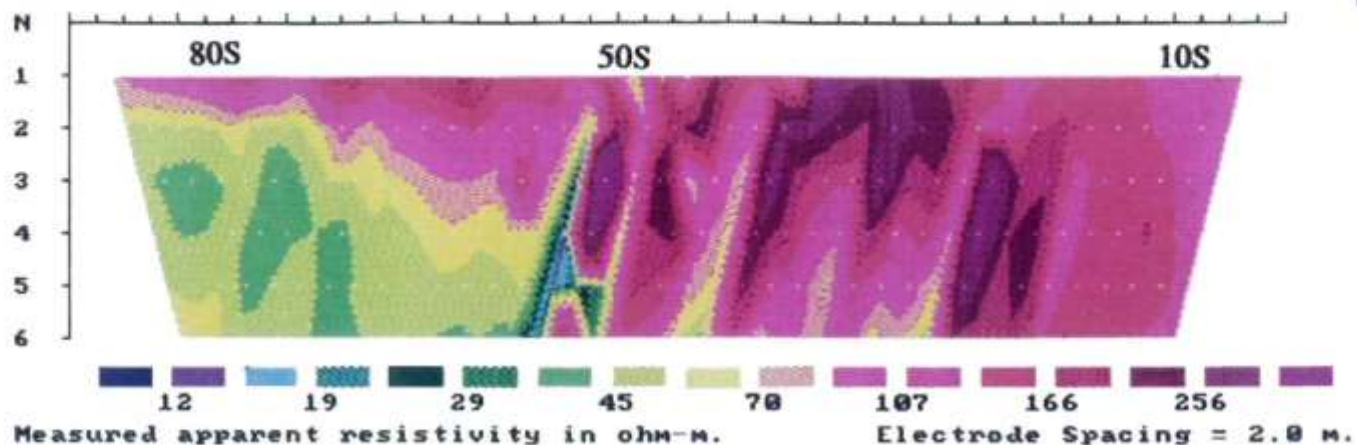


Figure 14 res.

Test Site 3.1. Interpretation of VES 1, 2, 3, and 4.





Iteration 6 completed with 27.7 % RMS Error

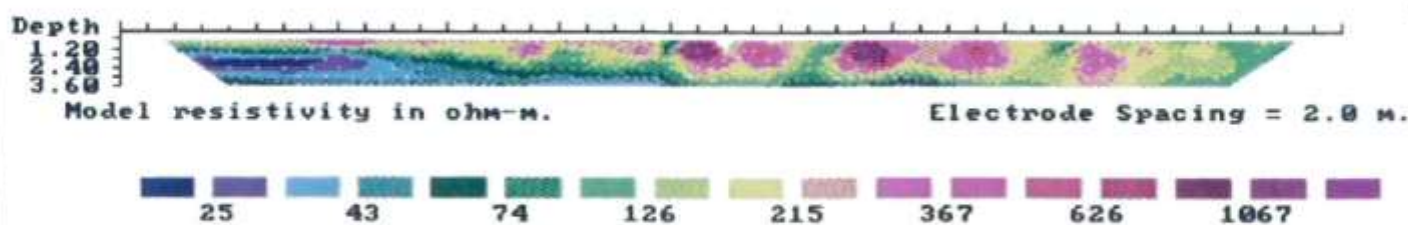
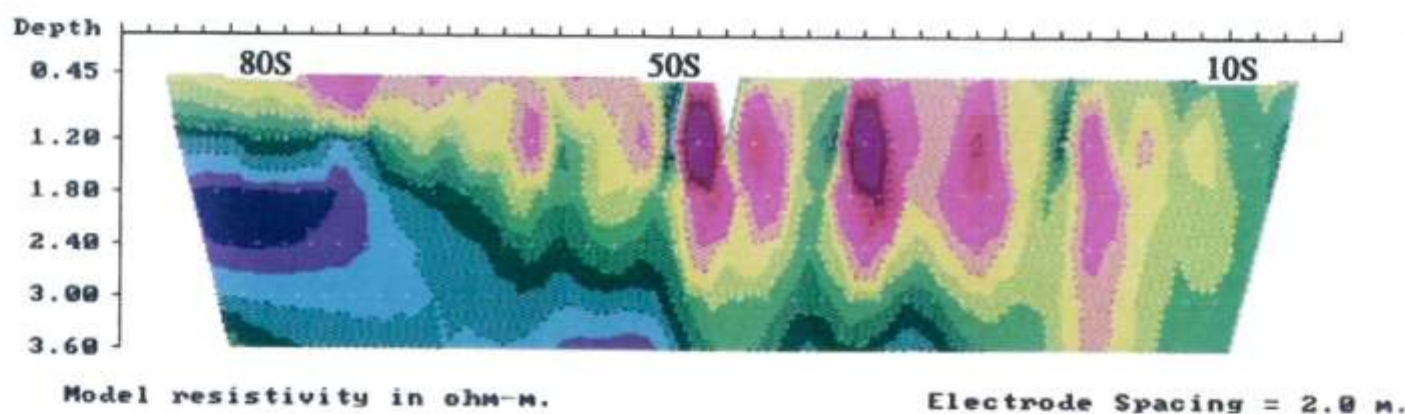
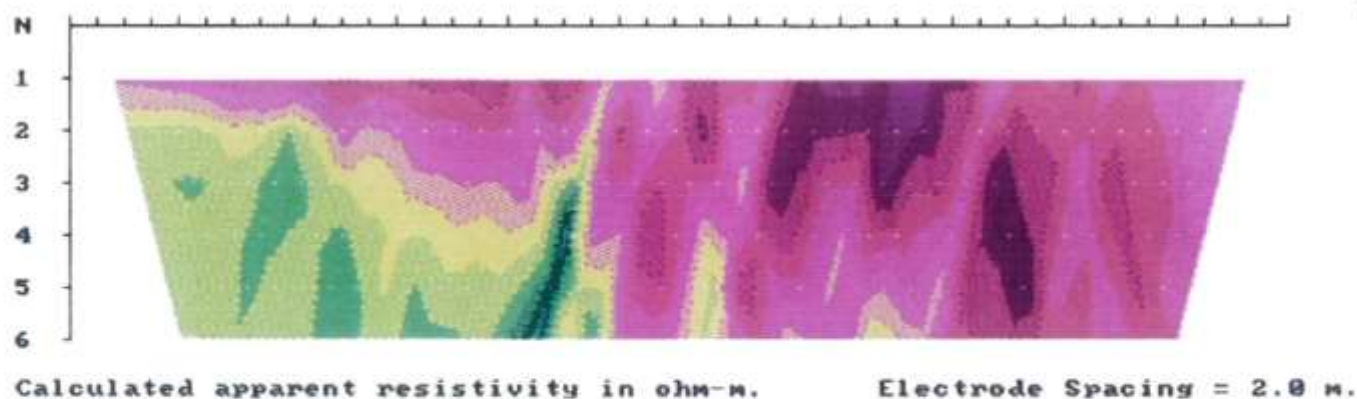


Figure 13 res. Test Site 3.1, Line 80W, Dipole-dipole resistivity data.

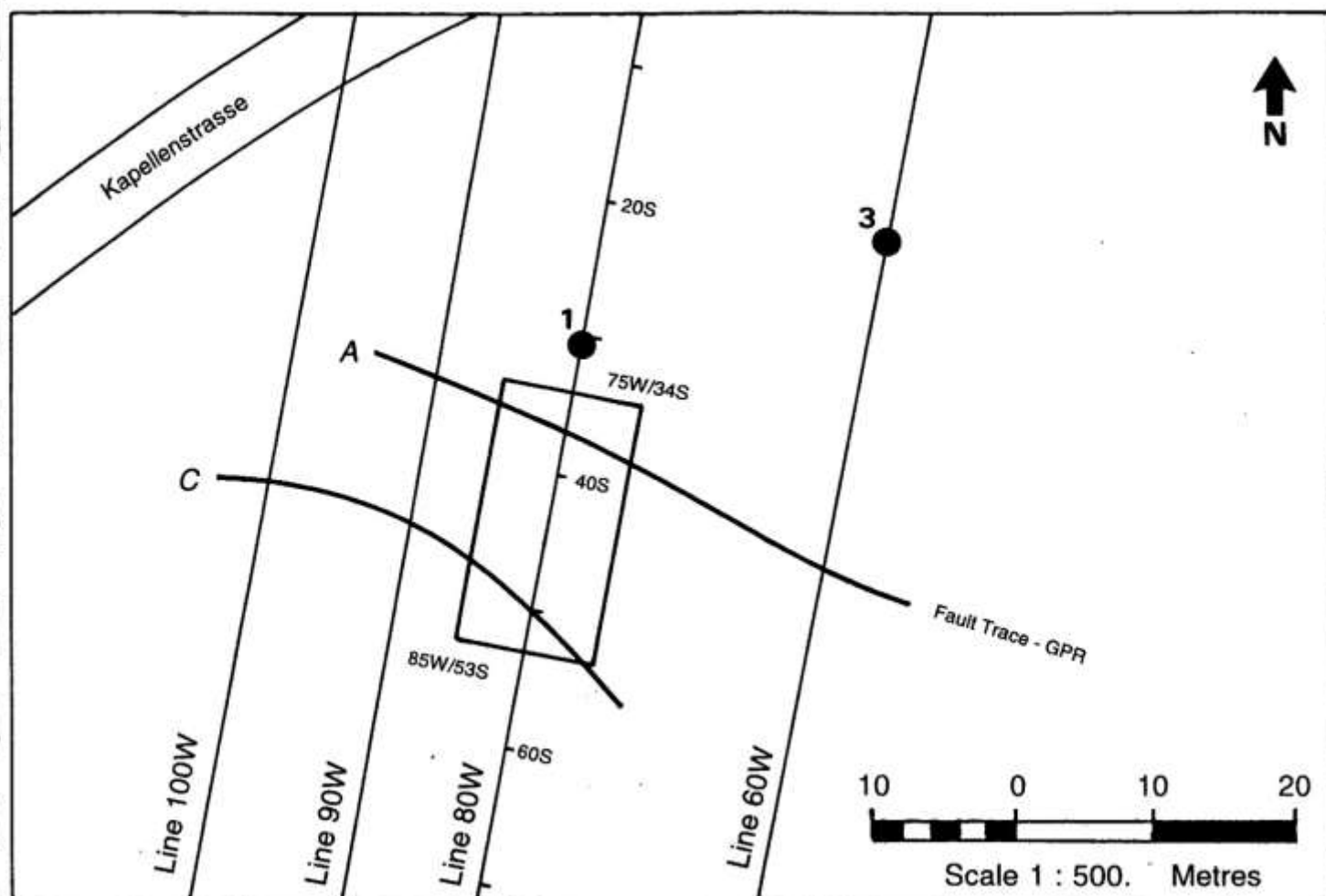


Figure 11 rsc. Test Site 3.1. Plan (partial) of site showing location of RESCAN survey grid.

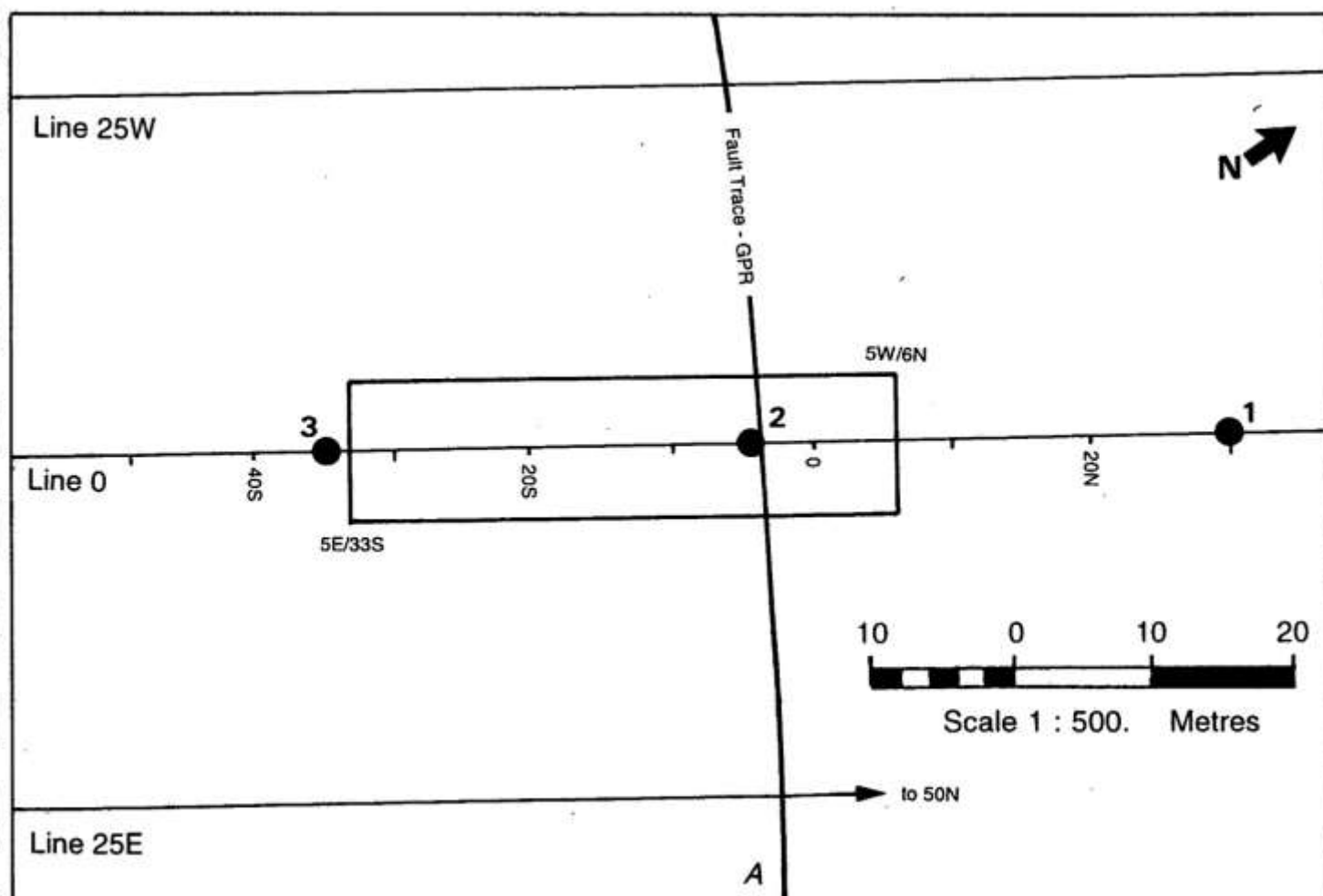


Figure 13 rsc. Test Site 3.2. Plan (partial) of site showing location of RESCAN survey grid.

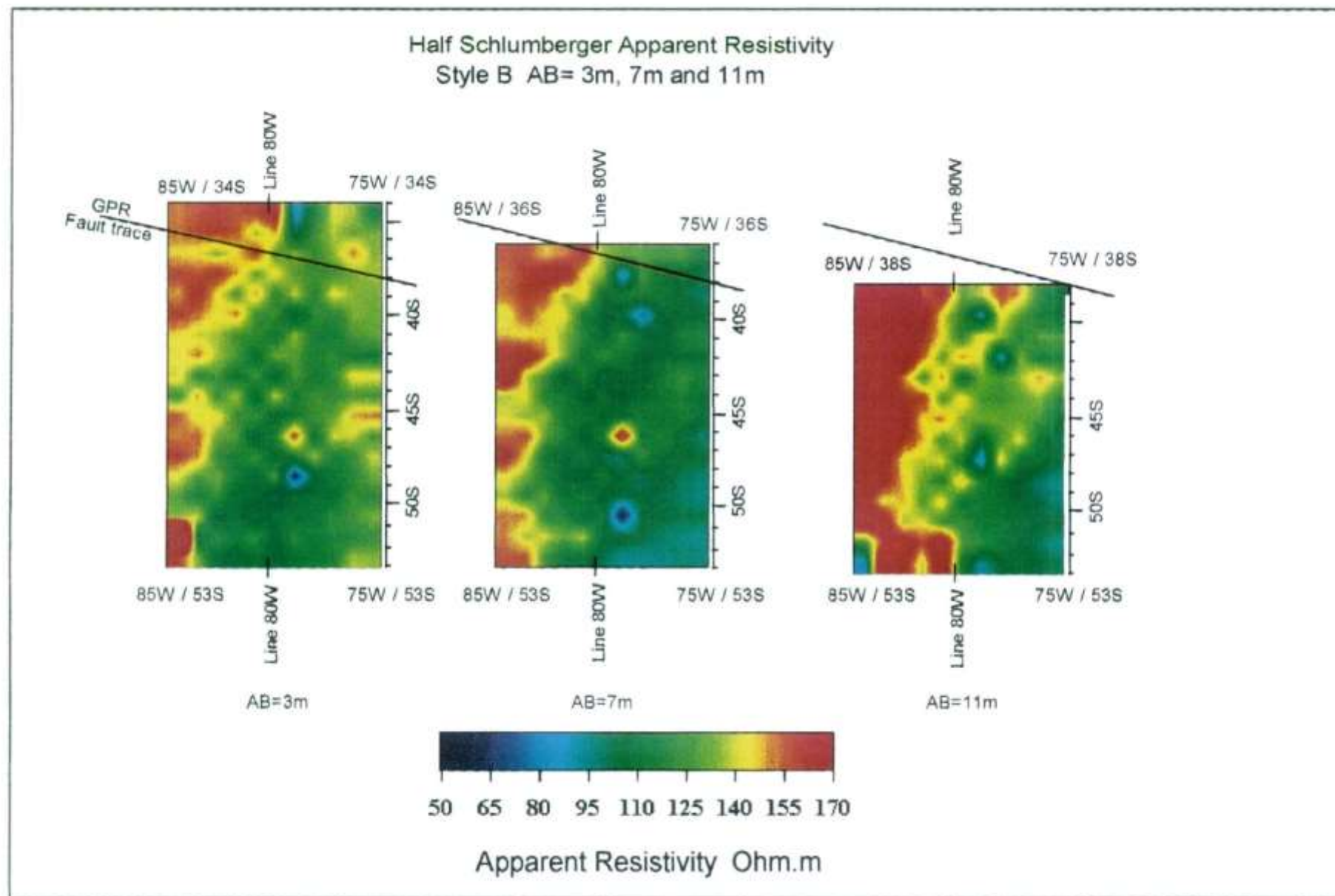


Figure 12 *rs.c.* Test Site 3.1. Apparent resistivity data, showing projected position of the fault.



Line orientation N10E, 16kHz E-field at N123E

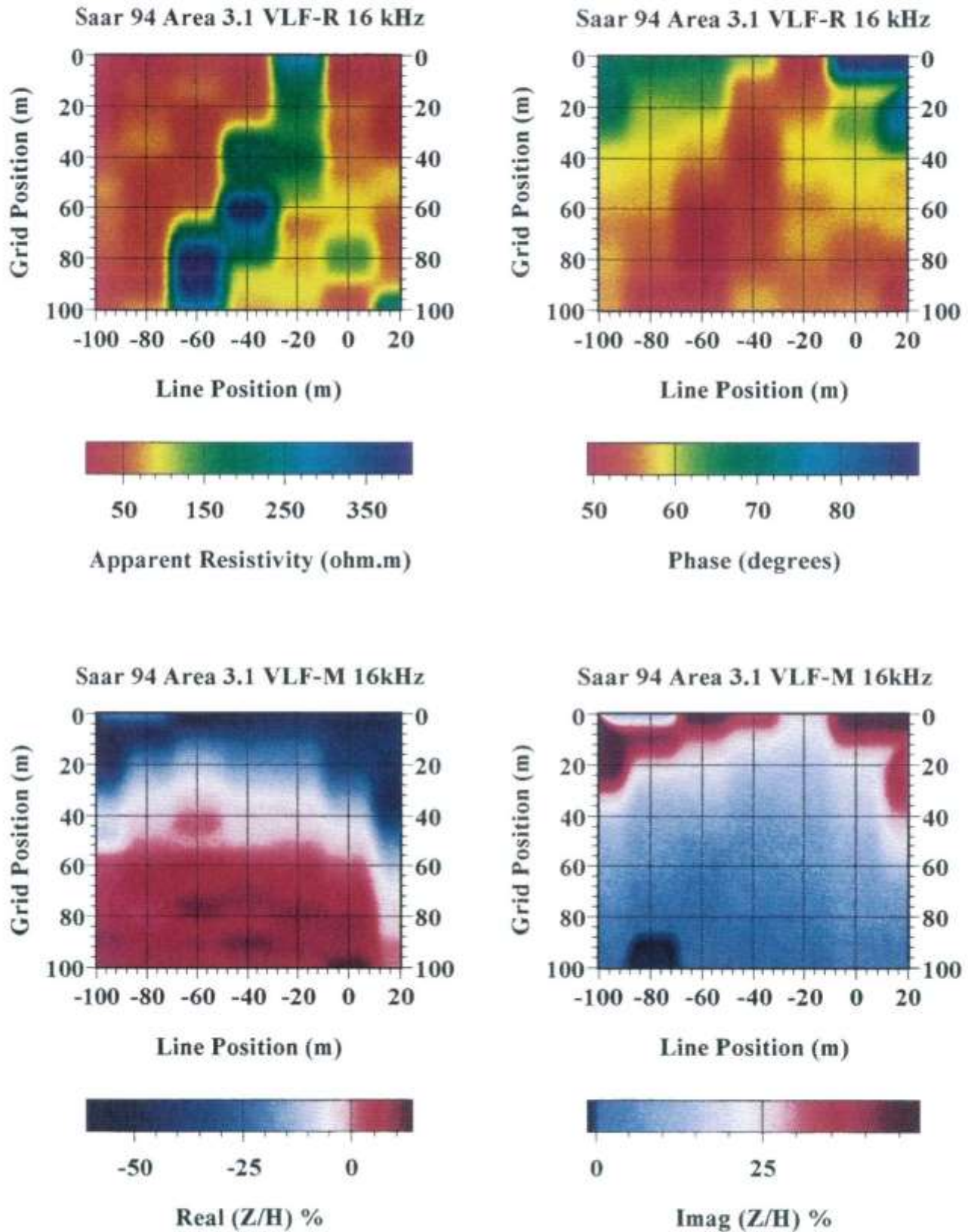


Figure 24 vlf. Test Site 3.1. VLF-R and VLF-Z field data for 16 kHz transmitter.

# Line orientation N10E, 24kHz E-field at N85E

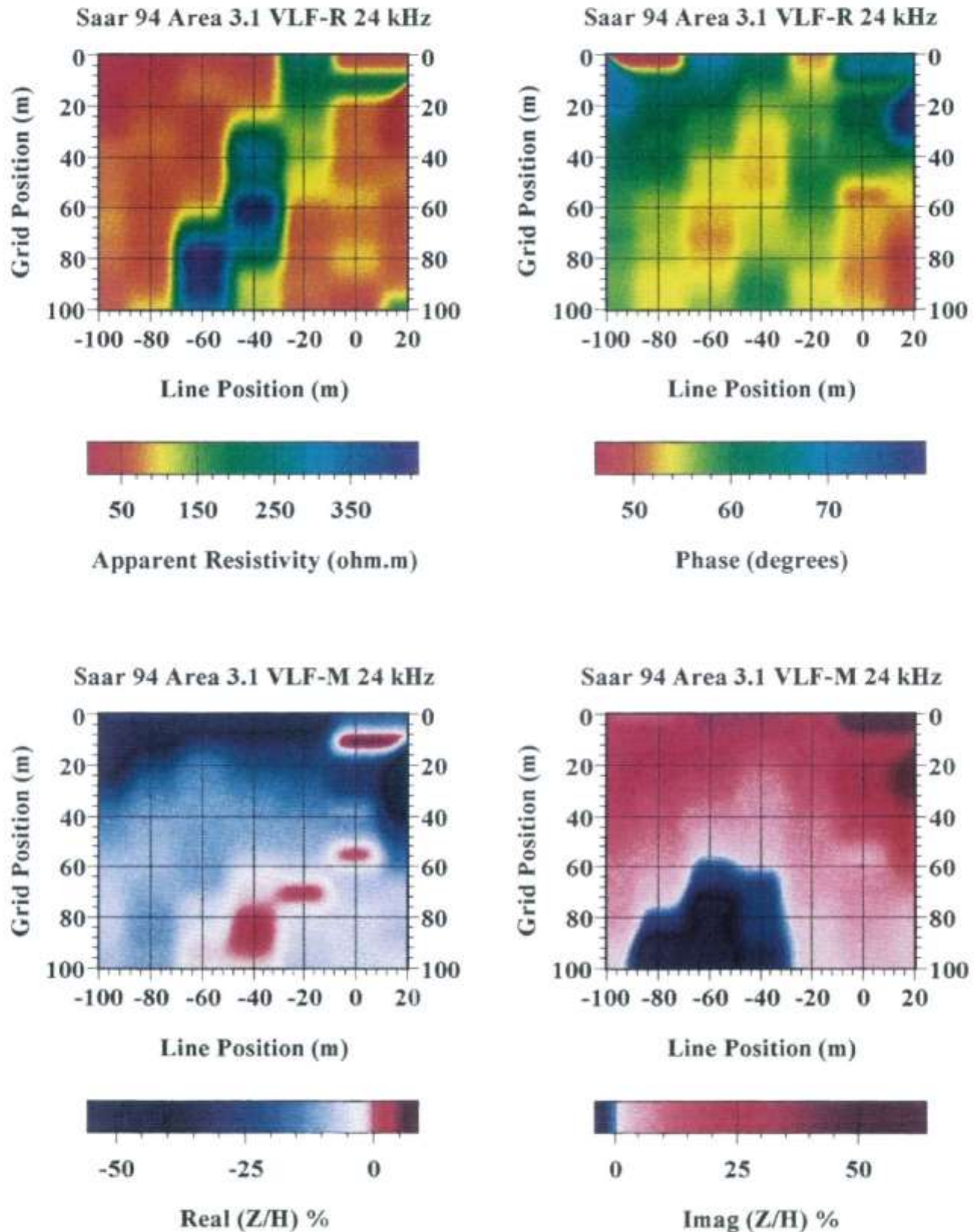


Figure 25 vlf. Test Site 3.1. VLF-R and VLF-Z field data for 24 kHz transmitter.



Line orientation N10E, 24kHz E-field at N85E  
16 kHz E-field at N123E

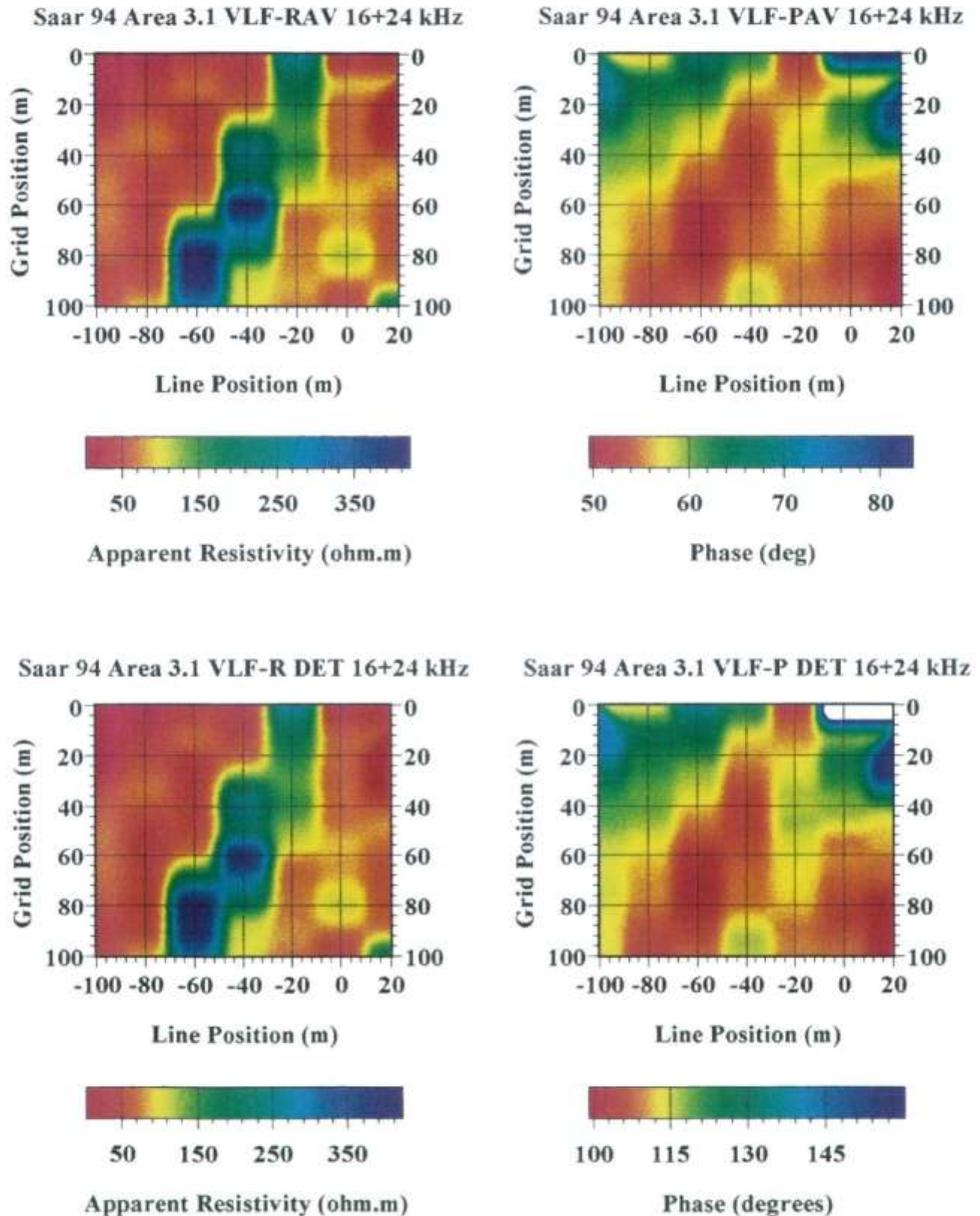


Figure 26 *vlf*. Test Site 3.1. Invariant mapping: 16 kHz and 24 kHz transmitters.



Line orientation N10E, 16 kHz E-field at N123E  
24kHz E-field at N85E

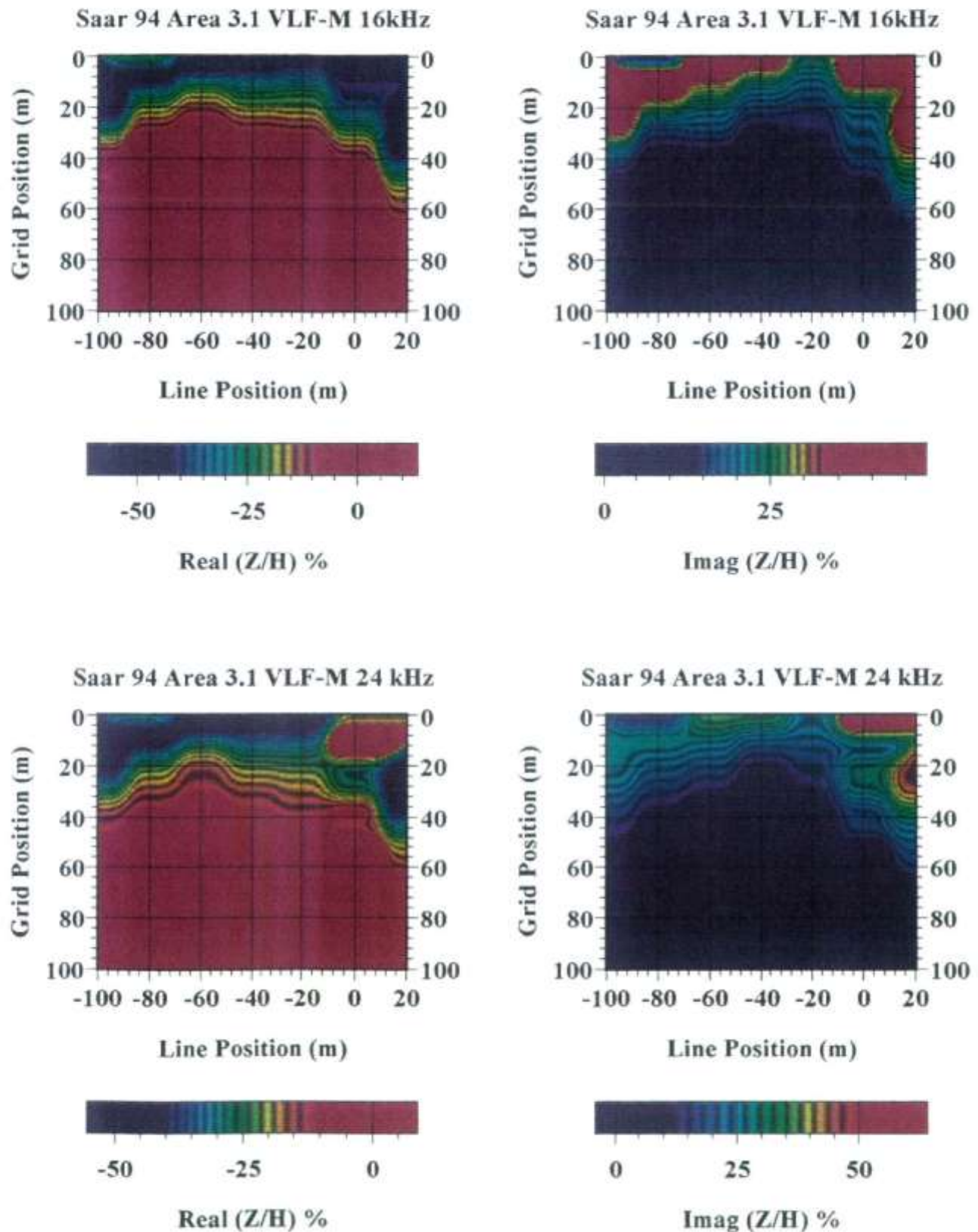


Figure 27 vlf. Test Site 3.1. VLF-Z field data using banded contour scale.

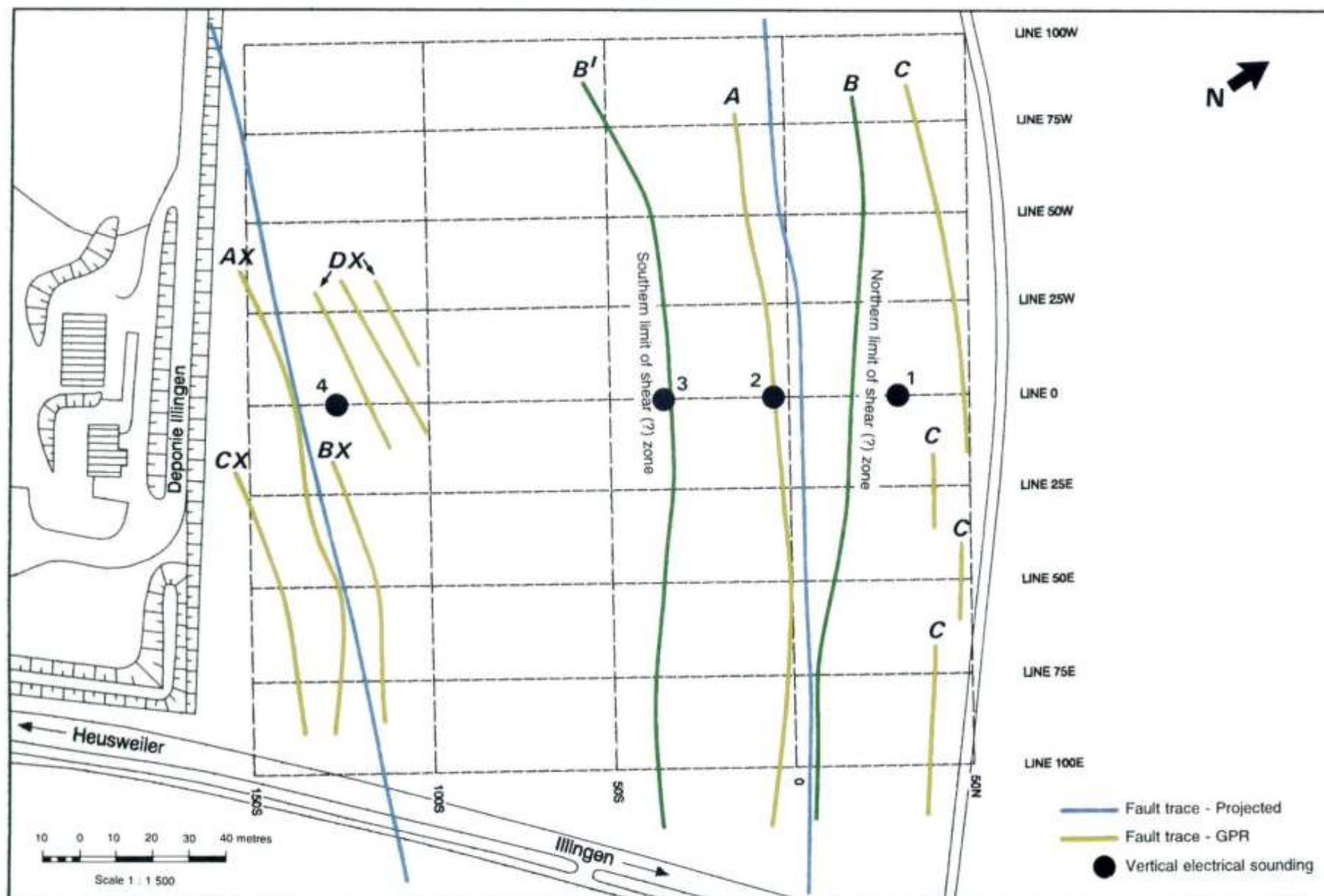
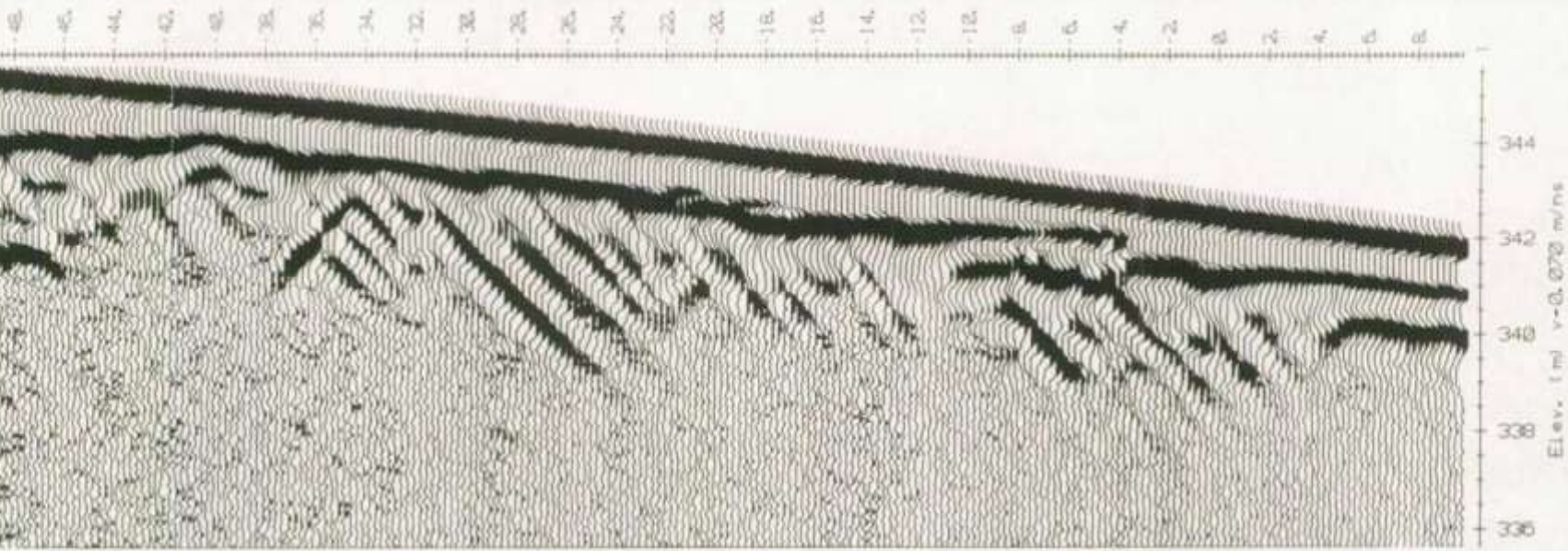


Figure 23. Test Sites 3.2 and 3.2 (Ext). Geophysical grid and interpretation.







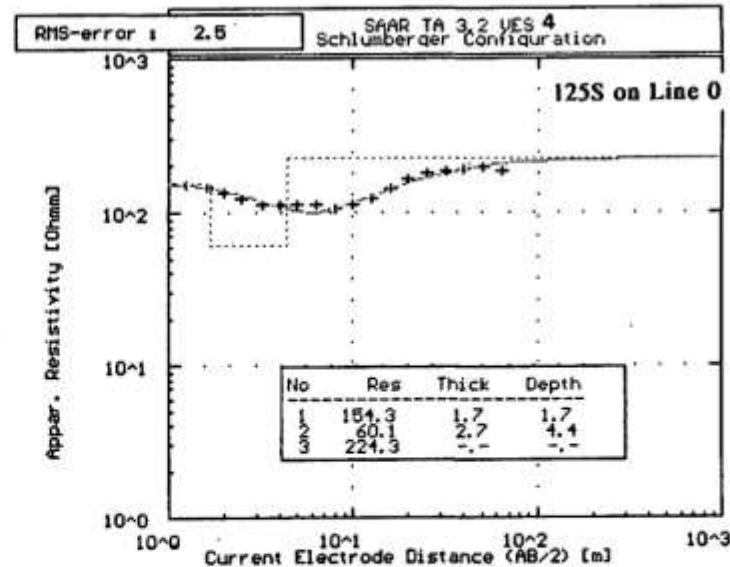
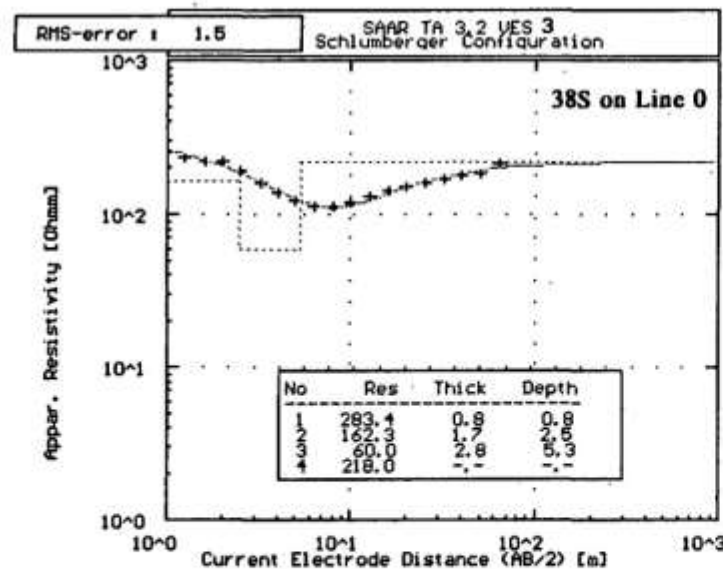
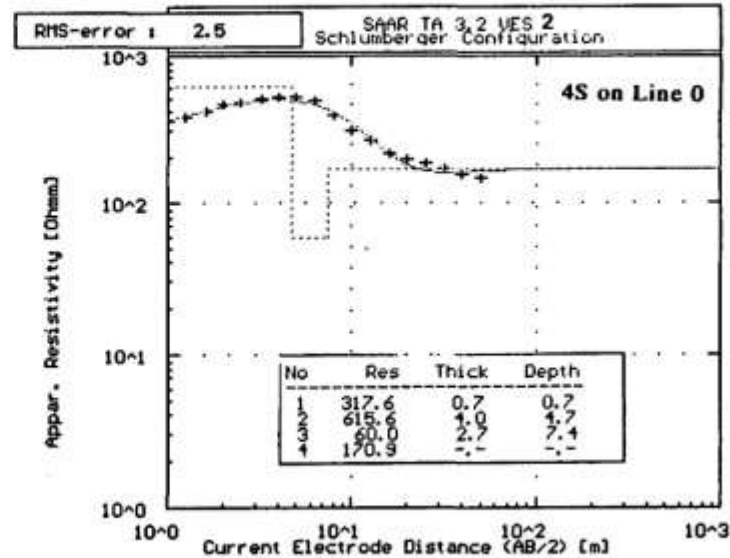
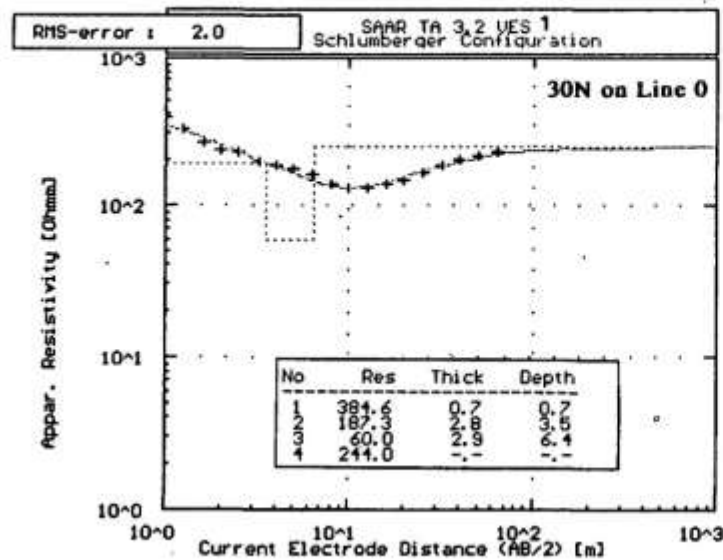


Figure 16 res.

Test Site 3.2. Interpretation of VES 1, 2, 3, and 4.

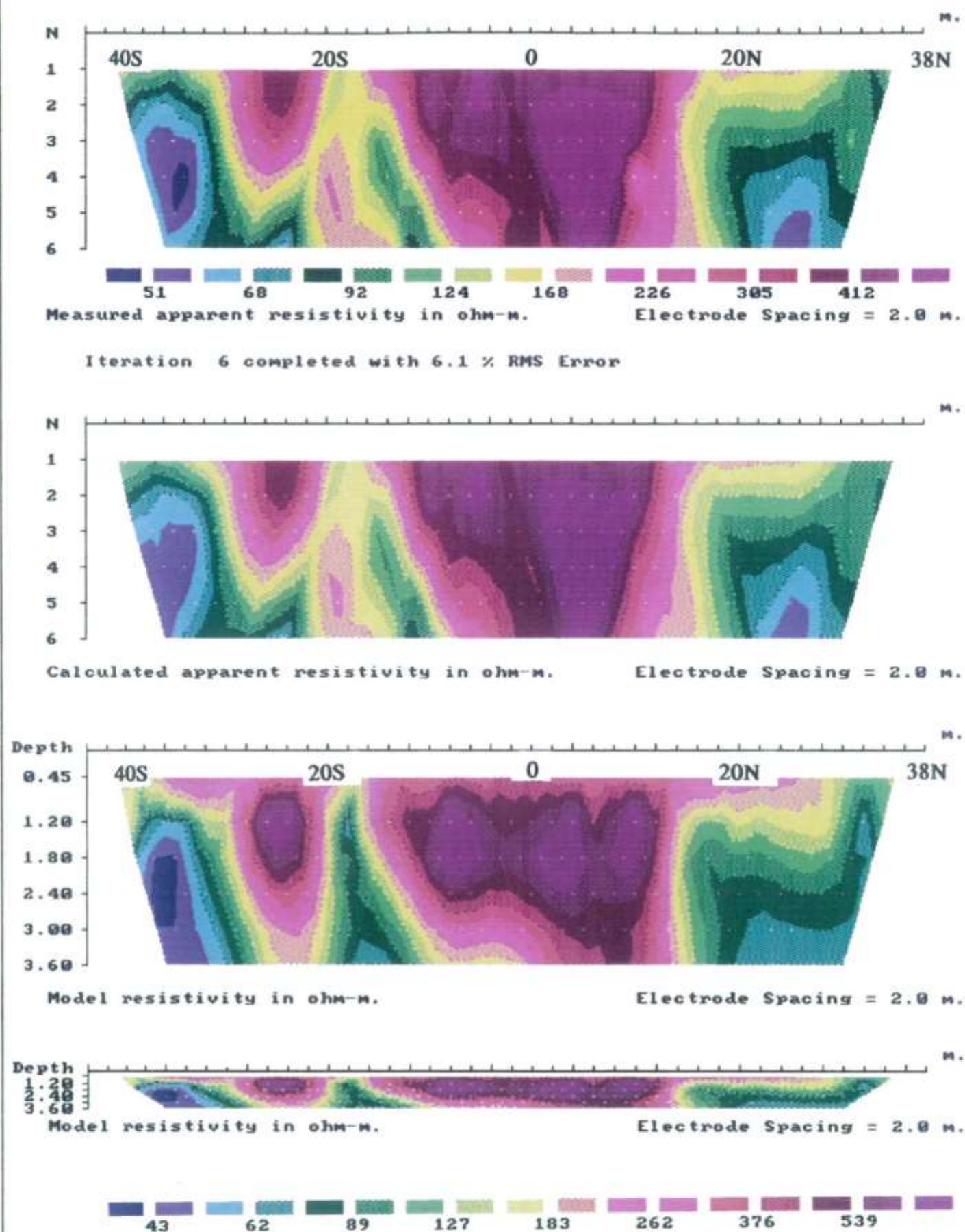


Figure 15 *res.*

Test Site 3.2. Line 0. Dipole-dipole resistivity data.

Half - Schlumberger Apparent Resistivity Style B AB=3m

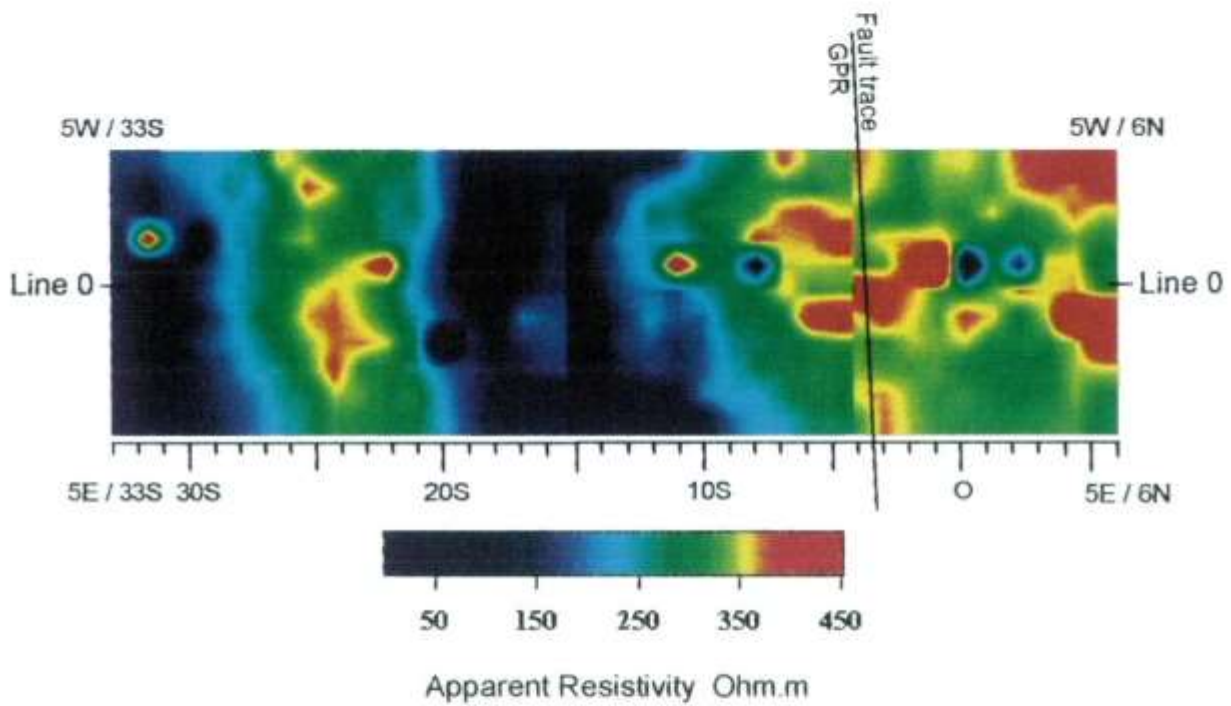
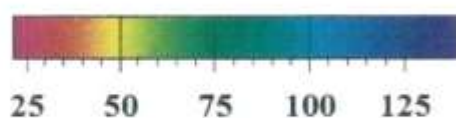
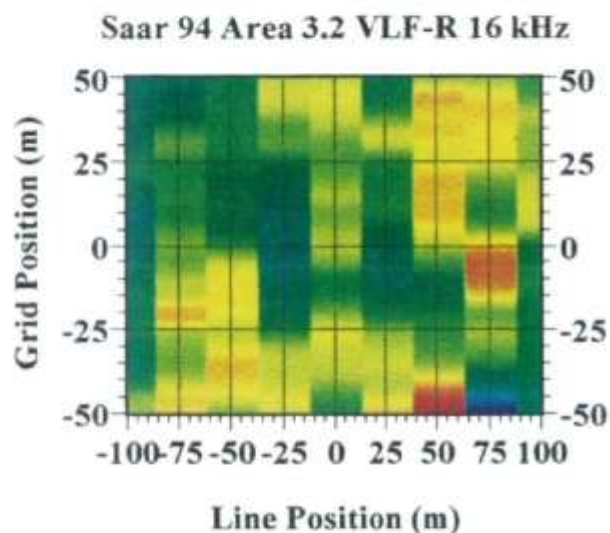


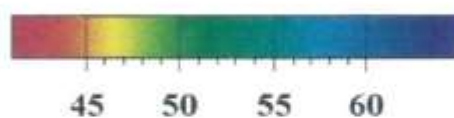
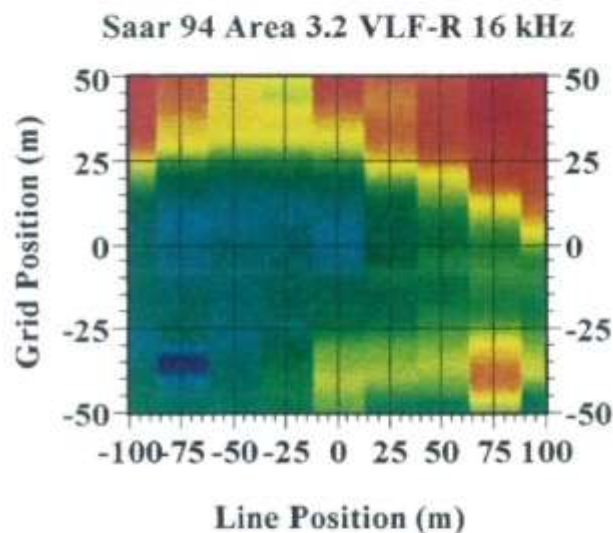
Figure 14 *rsc.* Test Site 3.2. RESCAN apparent resistivity maps for three overlapping sections.



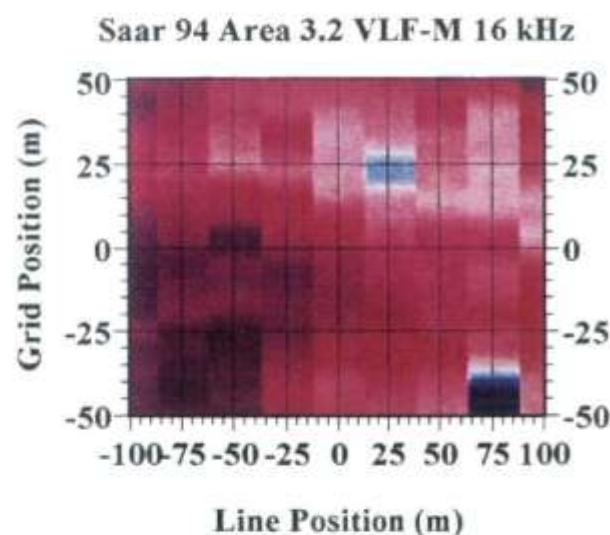
# Line orientation N30E, 16kHz E-field at N123E



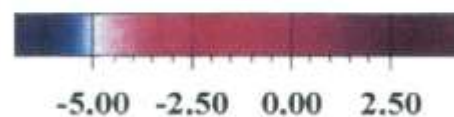
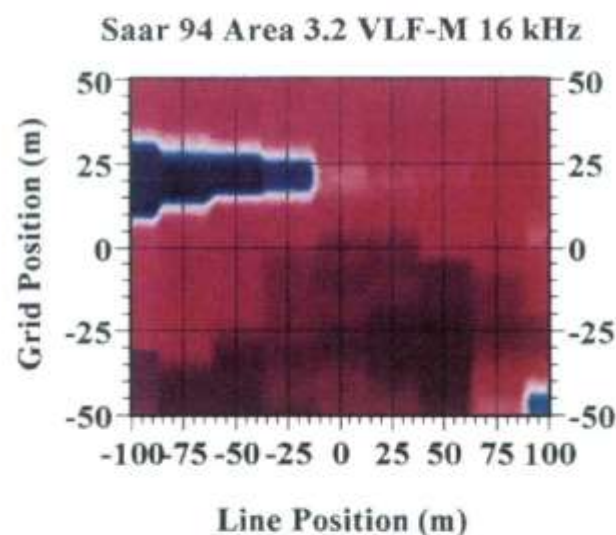
Apparent Resistivity (ohm.m)



Phase (degrees)



Real (Z/H) %



Imag (Z/H) %

Figure 28 *vlf*. Test Site 3.2. VLF-R and VLF-Z field data for 16 kHz transmitter.

# Line orientation N30E, 24kHz E-field at N85E

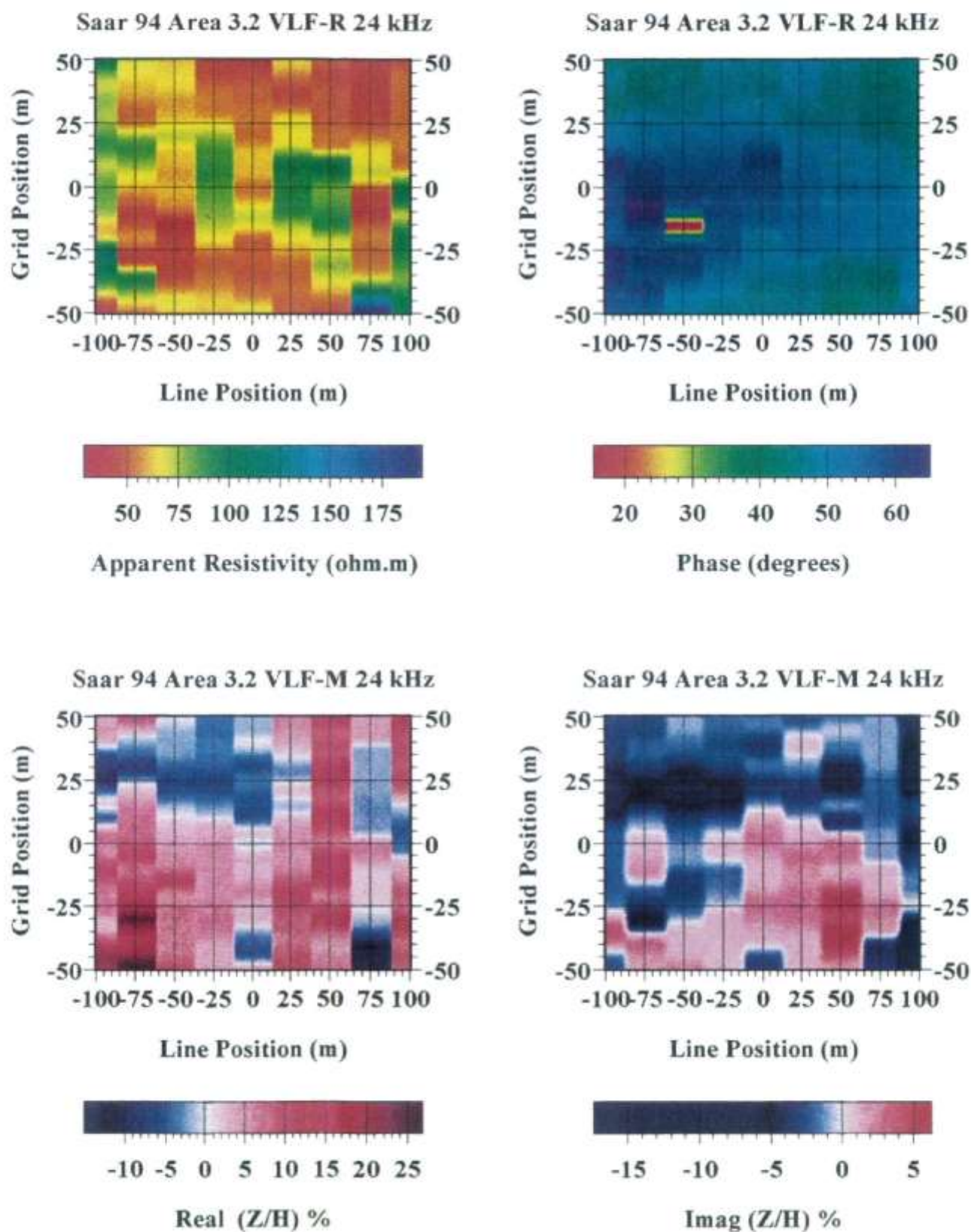


Figure 29 *vlf*. Test Site 3.2. VLF-R and VLF-Z field data for 24 kHz transmitter.



Line orientation N30E, 16 kHz E-field at N123E  
24 kHz E-field at N85E

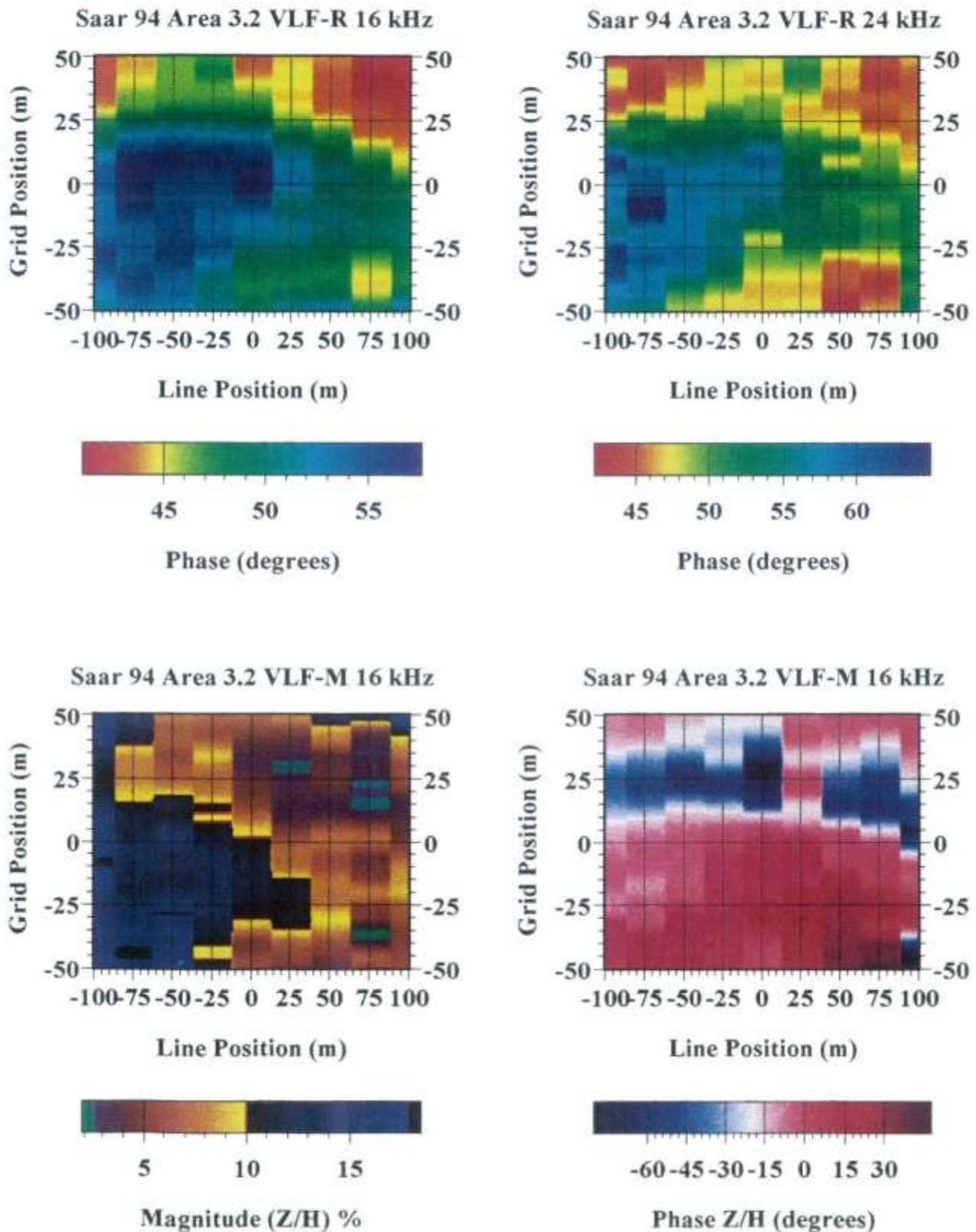


Figure 30 *vlf*. Test Site 3.2. VLF-R (phase) for 16 and 24 kHz transmitters and VLF-Z (converted magnitude and phase) for 16 kHz transmitter.



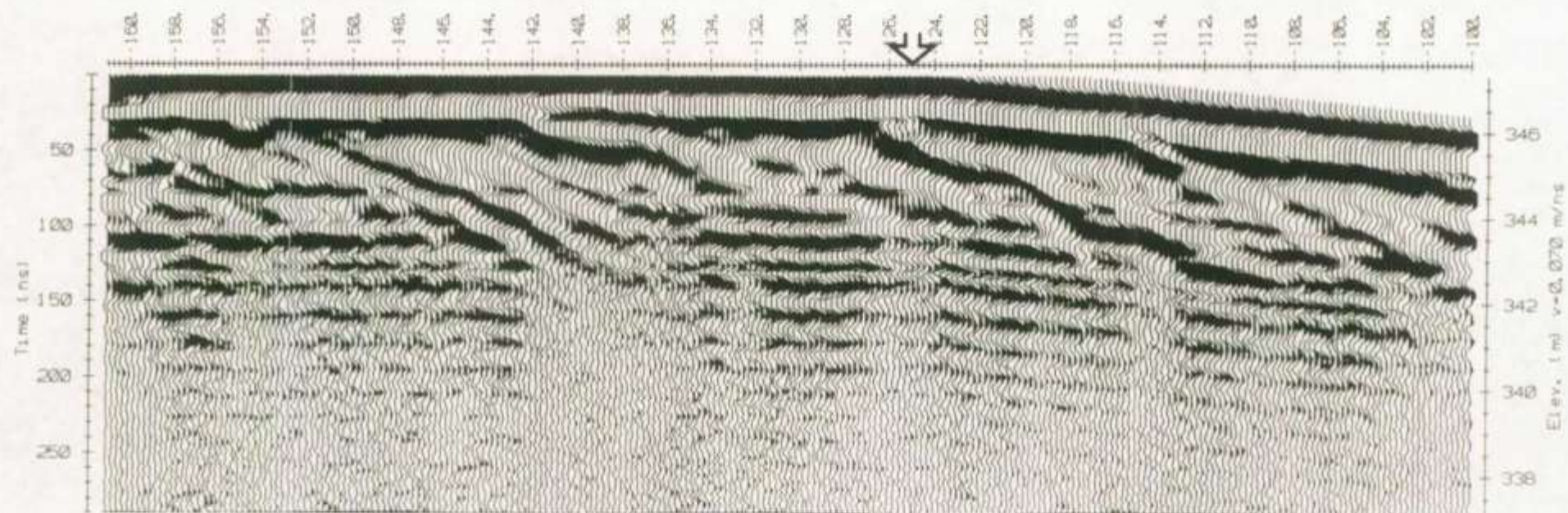


Figure 27 gpr. Test Site 3.2 (Ext). GPR profile for line 50EX. 50 MHz antennae.

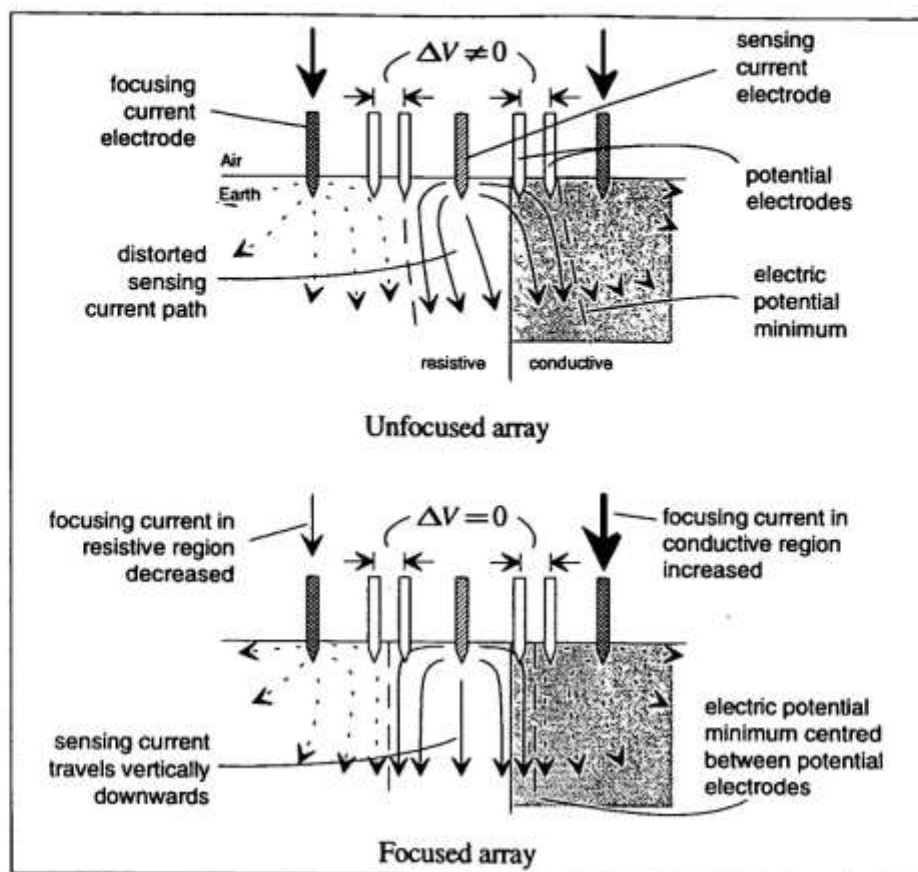


Figure 15 rsc. Focussed currents over a conductive/resistive boundary (schematic).

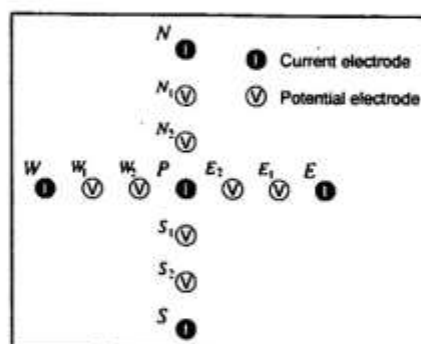


Figure 16 rsc. Electrode configuration (schematic) for a 'double laterolog' focussed array proposed by Jackson (1981).

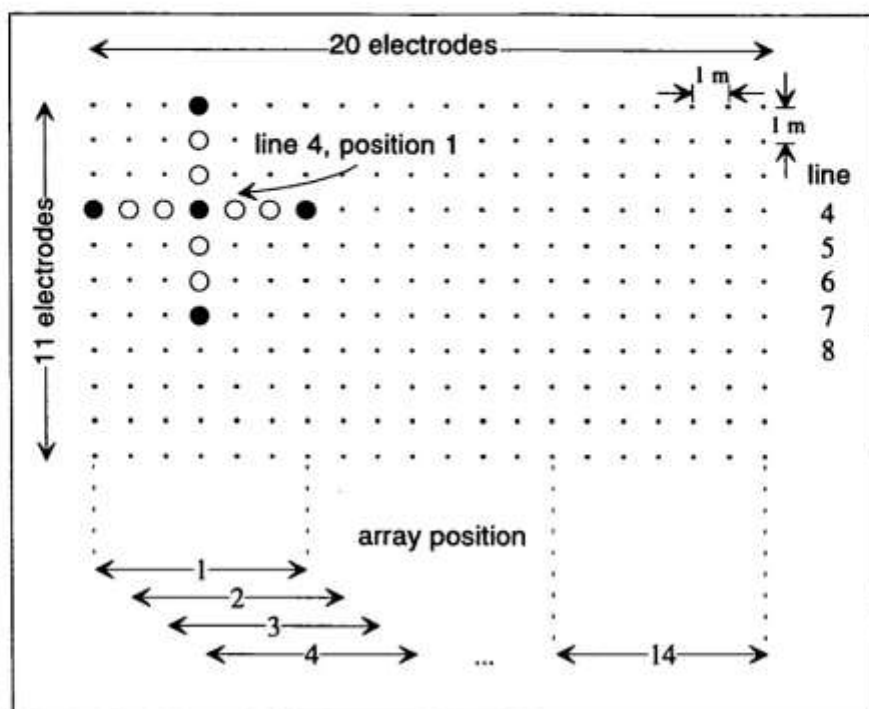


Figure 17 *rsc.* RESCAN electrode grid and focussed array positions.

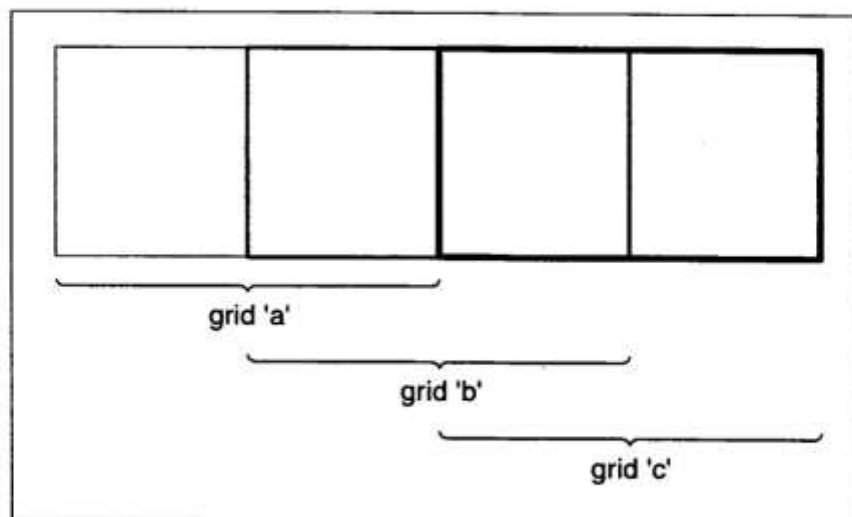


Figure 18 *rsc.* Adjacent grids.



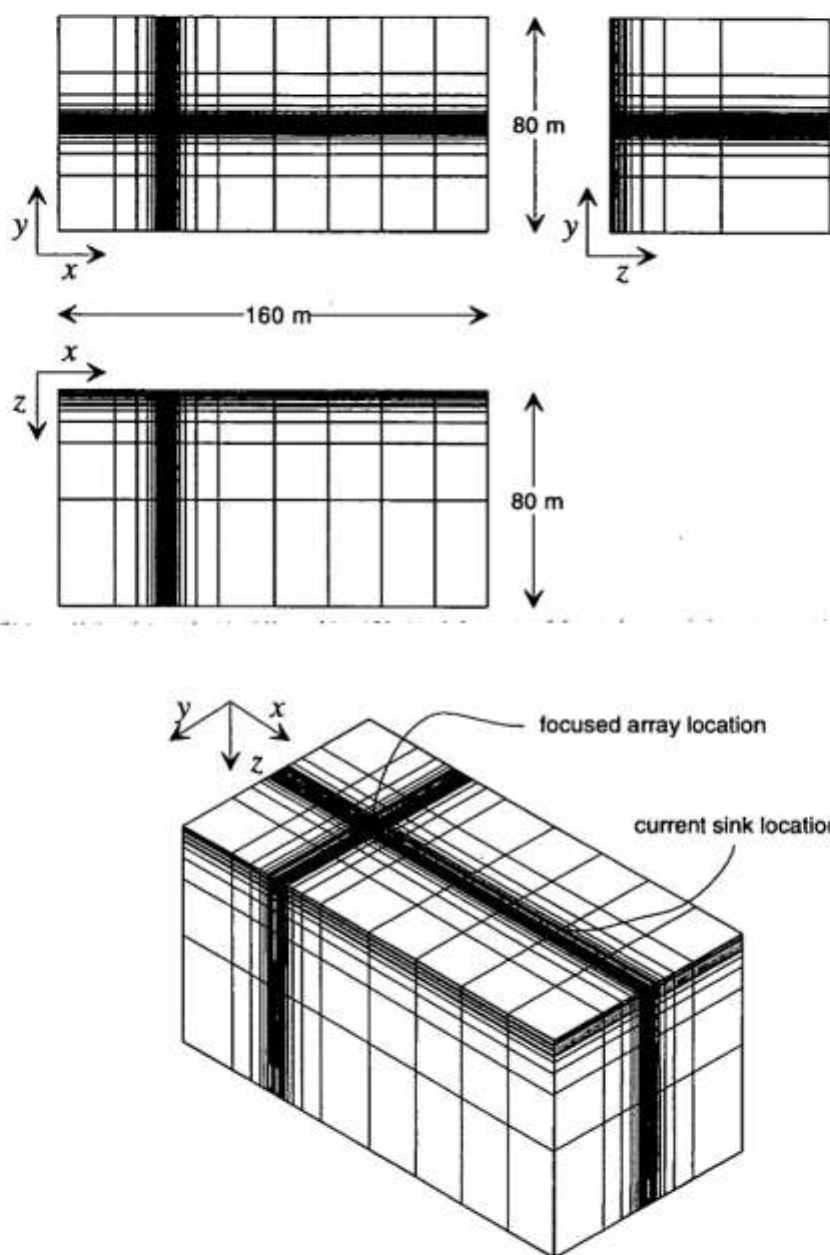


Figure 19 rsc. Model grid used in simulations of the focussed array.

